Emulsion transport in two-dimensional porous media : influence of geometric and surface heterogeneities

Elliot Speirs

▶ **To cite this version:**

Elliot Speirs. Emulsion transport in two-dimensional porous media : influence of geometric and surface heterogeneities. Fluid mechanics [physics.class-ph]. Université de Rennes, 2023. English. NNT : 2023URENS081 . tel-04506267

HAL Id: tel-04506267
https://theses.hal.science/tel-04506267

Submitted on 15 Mar 2024

HAL is a multi-disciplinary open access archive for the deposit and dissemination of scientific research documents, whether they are published or not. The documents may come from teaching and research institutions in France or abroad, or from public or private research centers.

L'archive ouverte pluridisciplinaire **HAL**, est destinée au dépôt et à la diffusion de documents scientifiques de niveau recherche, publiés ou non, émanant des établissements d'enseignement et de recherche français ou étrangers, des laboratoires publics ou privés.

COLLEGE SCIENCES DE LA MATIERE
DOCTORAL DES MOLECULES
BRETAGNE ET MATERIAUX

Université de Rennes

ifp Energies nouvelles

THESE DE DOCTORAT DE

L'UNIVERSITE DE RENNES

ECOLE DOCTORALE N° 638
Sciences de la Matière, des Molécules et Matériaux
Spécialité : *Physique*

Par
Elliot SPEIRS

Transport d'émulsions en milieux poreux bidimensionnels :

Effets d'hétérogénéités de géométrie et de surface

Thèse présentée et soutenue à Rueil-Malmaison, le 22 novembre 2023
Unité de recherche : Institut de Physique de Rennes UMR 6251

Rapporteurs avant soutenance :

Benjamin Dollet	Chargé de recherche, CNRS, Université de Grenoble Alpes
Benoit Scheid	Directeur de recherche, Université Libre de Bruxelles

Composition du Jury :

Président :	Anne-Virginie Salsac	Directrice de recherche, CNRS, Université de Technologie de Compiègne
Examinateurs :	Dominique Heitz	Chargé de recherche, INRAE
	Florent Malloggi	Ingénieur de recherche, CEA
	Benjamin Dollet	Chargé de recherche, CNRS, Université de Grenoble Alpes
	Benoit Scheid	Directeur de recherche, Université Libre de Bruxelles
Dir. de thèse :	Marie-Caroline Jullien	Directrice de recherche CNRS, Université de Rennes 1

Invités :

Nicolas Pannacci	Ingénieur de recherche, IFP Energies nouvelles
Maxime Moreaud	Ingénieur de recherche, IFP Energies nouvelles

Acknowledgments

The completion of this thesis represents not only my own efforts but also the contributions and encouragement of many individuals whom I am privileged to acknowledge.

First of all, I would like to express my sincere gratitude to my supervisors Nicolas Pannacci, Maxime Moreaud, and Marie-Caroline Jullien, whose expertise, insightful feedback, and guidance throughout this thesis have been indispensable. Thank you for introducing me to so many fascinating physical phenomena and analytical methods, and for instilling in me a rigorous research approach.

Furthermore, I would like to thank the members of the jury Benjamin Dollet, Benoit Scheid, Anne-Virginie Salsac, Dominique Heitz, and Florent Malloggi for kindly taking the time to assess this work, and for their thoughtful remarks. Thanks are also due to Hugues Bodiguel and Laurent Courbin, members of my CSI, for their advice, encouragement, and contributions throughout.

I am also grateful for my colleagues at IFPEN, whose kindness, generosity, and good humour greatly enriched my PhD experience. In particular, thanks to Sabine Martin, Guillaume Batôt, Sylvie Perrin, and Marie Marsiglia for their consistent help across all aspects of the thesis. Thanks to Matthieu Mascle, John Armitage, and Guillaume Berthe, who supported me with thoughtful conversations, plenty of sport, and a poncirus that will unfortunately never see these words. Thanks also to Camille Brigodiot for her contributions to this thesis and her constant enthusiasm. Lastly, thanks to all the "Thésards qui dépotent", particularly Valentine Combaudon, Emma Ollivier–Triquet, and Anne-Sophie Esneu for their camaraderie, not to mention the regular supply of chocolate and cakes. I forgive you for the Roquefort.

Whilst my visits to IPR were infrequent, each one was a source of great enjoyment and appreciation for the welcoming atmosphere. Thanks also to Antoine Ouvrans, always an impeccable and passionate host.

To my friends and family, I thank you for your encouragement to pursue this PhD and for putting up with me through it all. Your belief and advice have been a constant source of strength, and I am profoundly grateful to have you all in my life.

Finally, and most importantly, for her unwavering support and encouragement, her many sacrifices and boundless patience, as well as the hope and love she imparts in me, I thank my wife, Marie-Anne Speirs. My primary aspiration is to make you proud.

Table of contents

Nomenclature **vii**

1 Introduction **1**

2 Generalities **11**
2.1 An Introduction to Microfluidics 12
2.1.1 Hydrodynamics of Confined Systems 15
2.1.2 Surface Effects 19
2.1.3 Dispersions 26
2.2 Characterising Porous Media 31
2.2.1 Macroscopic Porous Media Parameters 33
2.2.2 Microscopic Porous Media Parameters 37
2.2.3 Simple Permeability Models for Porous Media 38
2.3 Conclusion and Objectives 40

3 Droplet Transport in Simple Porous Media **41**
3.1 Introduction 42
3.1.1 Droplet Generated Pressure Drops 44
3.1.2 Droplet Dipolar Perturbations 49
3.1.3 Capillary Pressure 51
3.1.4 Studies in Model Porous Media 52
3.2 Materials and Methods 54
3.2.1 Fabrication of Microfluidic Devices 54
3.2.2 Microfluidic Devices 57
3.2.3 Fluids Studied 62
3.2.4 Experimental Procedure 64
3.2.5 Data Analysis 67
3.3 Results 76

3.3.1 Initial Observations . . . 76
3.3.2 Analysing the Radial Flow Heterogeneities . . . 83
3.3.3 Pressure Measurements within the Radial Porous Media . . . 101
3.3.4 Towards Modelling the Droplet Transport . . . 103
3.4 Conclusion and Perspectives . . . 105

4 Droplet Size Evolution in Porous Media 107
4.1 Introduction . . . 108
4.1.1 Droplet Coalescence in Porous Media . . . 108
4.1.2 Droplet Breakup in Porous Media . . . 113
4.1.3 Size Dependant Droplet Transport . . . 118
4.1.4 Conclusion . . . 118
4.2 Results . . . 119
4.2.1 Initial Observations . . . 119
4.2.2 Influence of the Injection Capillary Number . . . 122
4.2.3 Influence of D/d . . . 125
4.2.4 Influence of the Geometry . . . 128
4.2.5 Influence of Droplet Concentration . . . 131
4.3 Discussion . . . 133
4.3.1 Stationary Droplet Size . . . 133
4.3.2 Stationary Droplet Size Variation . . . 135
4.4 Conclusions and Perspectives . . . 136

5 Influence of the Wettability 139
5.1 Introduction . . . 140
5.1.1 Surface Treatment Methods . . . 141
5.1.2 Influence of Wettabilities on Porous Media Fluid Flow . . . 143
5.2 Materials and Methods . . . 148
5.2.1 Making the COC Micromodels . . . 149
5.2.2 COC Surface Treatment Methodology . . . 152
5.3 Results . . . 155
5.3.1 Quality of the surface treatments . . . 155
5.3.2 Final Contact Angles . . . 161
5.3.3 Fluid Flow in Micromodels with Variable Wettability . . . 162
5.4 Discussion . . . 169
5.4.1 Summary and Perspectives . . . 171

A Angular Variations in the Permeability of Regular Porous Media 177
A.1 Introduction . . . 177
A.2 Experimental Measures . . . 181
A.2.1 Straight Channel . . . 182
A.2.2 Porous Media Measurements . . . 182
A.3 Numerical Measures: COMSOL . . . 184
A.3.1 Straight Channel . . . 184
A.3.2 Size Invariability and Mesh Dependence . . . 185
A.3.3 Porous Media Measurements . . . 186
A.4 Numerical Measures: Lattice Boltzmann . . . 188
A.4.1 Straight Channel . . . 188
A.4.2 Size Invariability . . . 189
A.4.3 Porous Media Measurements . . . 189
A.5 Discussion . . . 192

B Droplet Formation and Injection: Experimental Procedure 195

C Morphological Modelling of Random Lattice Geometries 197

D Chapter 4: Additional Information 199
D.0.1 Additional TEOS Deposit Characterisation . . . 199
D.0.2 Protocol and Results: AA photo-polymerisation on PDMS . . . 200

References 203

Nomenclature

Roman Symbols

A	Area
Bo	Bond number
Ca	Capillary number
$\overline{Ca}$	Capillary number at the mid-radius in the radial porous media ($r = R/2$)
D	Apparent droplet diameter in a channel
D_p	Post diameter in the porous media
D'	Diameter of a droplet having the same volume but a spherical form
$\underline{f}$	Volume forces acting on a fluid
g	Acceleration due to gravity
h	Thickness of a liquid lubrication film
H_{dg}	Height of the channels in the droplet generators
H	Channel height
k	Permeability
L'	Effective length of a channel, accounting for the increased resistance in the presence of a confined droplet
L_c	Characteristic length of a microfluidic channel
L_d	Droplet Length
L_E	Euclidean length

L	Channel length
L_G	Geodescic length
L_{inc}	Incubation length
M	Viscosity ratio $= \eta_d/\eta_c$
P	Pressure
P_0	Atmospheric pressure
P_{Breth}	Bretherton pressure drop induced by a droplet or bubble
P_c	Capillary pressure
Q	Volumetric flow rate
r	Radius of a fluid interface
R_0	Hydrodynamic resistance of a channel void of droplets
R_d	Hydrodynamic resistance of a single droplet
Re	Reynolds number
$\overline{Re}$	Reynolds number at the mid-radius in the radial porous media ($r = R/2$)
R_h	Hydrodynamic resistance
S	Specific surface area
T	Geometric tortuosity
$\underline{v}$	Fluid velocity vector
$\overline{v}$	Average velocity across an image series
V_c	Volume of the continuous phase
V_d	Volume of the dispersed phase
V_{drop}	Volume of a droplet
v_{max}	Maximum instantaneous droplet speed during an image series
V_{solid}	Volume occupied by the solid structure in a porous medium

V_{tot}	Total volume
V_v	Volume fraction
V_{void}	Volume occupied by the pore space in a porous medium
w_{dg}	Width of the flow-focusing channel constriction in the droplet generators
W	Channel width

Greek Symbols

η	Dynamic viscosity
η_c	Dynamic viscosity of the continuous phase
η_d	Dynamic viscosity of the dispersed phase
γ	Interfacial tension
ϕ	Porosity
Π_{disj}	Disjoining pressure
Π_{elec}	Electrostatic term (DLVO)
Π_{steric}	Steric term (DLVO)
Π_{vdW}	Van der Waals term (DLVO)
ψ	Confinement of a droplet = D/D'
ρ	Density
τ	Duration of an image series
τ_{ads}	Surfactant adsorption time scale
τ_{cap}	Viscous-capillary time scale
τ_d	Time in movement of a droplet in an image series
τ_{dr}	Film drainage time scale
τ_{form}	Droplet formation time scale

θ_c	Contact angle

Acronyms / Abbreviations

AA	Acrylic Acid
CMC	Critical micelle concentration
CNN	Convolutional Neural Network
COC	Cyclic Olefin Copolymer
EDS	Energy Dispersive Spectroscopy
FDTS	Perfluorodecyltrichlorosilane
FTIR	Fourier Transform Infrared Spectroscopy
HMDSO	Hexamethyldisiloxane
KDE	Kernel Density Estimation
LBM	Lattice Boltzmann Method
OTS	Octadecyltrichlorosilane
PDMS	Polydimethylsiloxane
PECVD	Polymer Enhanced Chemical Vapor Deposition
PEG	Poly(ethylene Glycol)
PFTE	Polytetrafluoroethylene
PGMEA	Propylene glycol methyl ether acetate
PIV	Particle Image Velocimetry
PMMA	Polymethyl Methacrylate
REV	Representative Elementary Volume
RICM	Reflection Interference Contrast Microscopy
RSA	Random Sequential Addition

RTV	Room Temperature Vulcanisation
SDS	Sodium dodecyl sulfate
SEM	Scanning Electron Microscopy
TEOS	Tetraethyl Orthosilicate

Chapter 1

Introduction

Contexte Général

Lorsque nous entreprenons un voyage en voiture, nous avons tendance à penser que l'autoroute est le chemin le plus rapide vers notre destination. C'est le chemin le plus direct, sur lequel nous pouvons rouler à la plus grande vitesse. Cependant, les petites routes secondaires peuvent parfois s'avérer plus rapides. Cela est souvent dû à la configuration des routes, ainsi qu'à l'influence des autres voitures sur la route par la création de trafic, comme lorsque l'on quitte une grande ville le vendredi soir avant les vacances scolaires. La dynamique du trafic qui en résulte est complexe et intermittente, comme en témoigne l'évolution constante des heures d'arrivée estimées ou des itinéraires proposés lors de l'utilisation d'un logiciel de navigation.

Ce même comportement peut être observé lorsque des fluides s'écoulent dans un milieu poreux, un matériau solide contenant un réseau interconnecté d'espaces ouverts au sein de sa structure. Les fluides simples, tels que l'eau ou l'air, s'écoulent principalement dans les canaux les plus larges, car la résistance à l'écoulement y est la plus faible. Toutefois, lorsque deux fluides non miscibles (qui ne se mélangent pas), tels que l'eau et l'huile ou l'eau et l'air, s'écoulent simultanément à travers un réseau poreux, les mécanismes régissant l'écoulement et l'hydrodynamique qui en résulte sont beaucoup plus complexes. Par exemple, le système multiphasique peut s'écouler préférentiellement dans les canaux les plus petits, à l'instar des voitures qui empruntent les petites routes pour éviter les autoroutes encombrées.

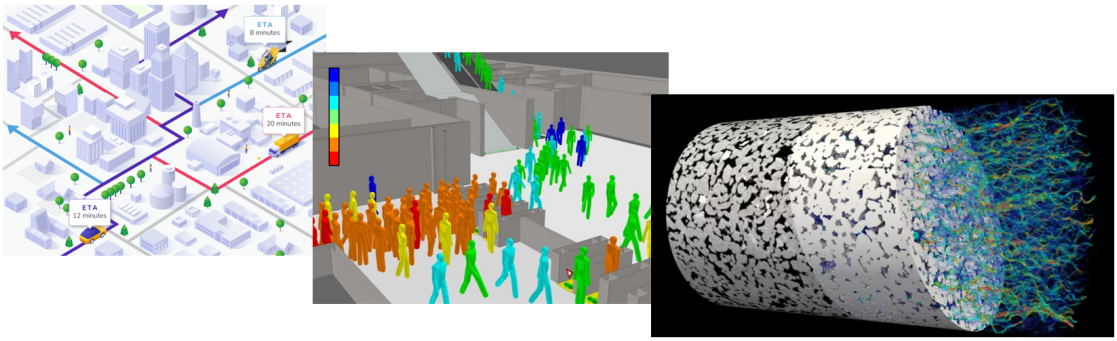

Fig. 1.1 Exemples de scénarios impliquant le transport à travers des réseaux complexes. Gauche) Optimisation des itinéraires de voitures [1]. Au milieu) Simulations de suivi de piétons. La couleur indique le degré de fluidité de chaque piéton, du plus élevé (bleu) au plus faible (rouge) [2]. À droite) Images numériques d'une roche utilisées pour modéliser le transport des fluides dans l'espace interstitiel [3].

Les systèmes fluides multiphasiques étudiés dans cette thèse sont connus sous le nom de dispersions. Une dispersion est un système dans lequel de petites particules ou gouttelettes d'une substance sont dispersées ou distribuées au sein d'une autre substance sans être chimiquement liées entre elles. Ces particules ou gouttelettes peuvent se présenter sous la forme d'un solide, d'un liquide ou d'un gaz et sont généralement appelées la "phase dispersée", tandis que la substance dans laquelle elles sont dispersées est appelée la "phase continue". Les dispersions sont couramment rencontrées dans la vie quotidienne, par exemple lors de la formation d'une crème Chantilly, de la préparation d'une vinaigrette pour une salade ou même de la prise de photos avec un appareil-photo à pellicule. Néanmoins, les propriétés des dispersions présentent une physico-chimie très riche. On peut se demander, par exemple, pourquoi il est plus facile de faire une Chantilly avec certaines crèmes qu'avec d'autres ? Plus curieux encore, comment se fait-il qu'en ajoutant de l'air à la crème visqueuse, le système obtenu soit rigide avec une viscosité bien supérieure à celle de l'air et de la crème réunies ?

Les dispersions jouent un rôle central dans une multitude de processus industriels et naturels, en particulier dans le domaine des géosciences. Par exemple, des dispersions de bulles d'air dans des solutions aqueuses peuvent introduire de l'oxygène dans les eaux souterraines ou les sols contaminés pour améliorer les efforts de remédiation [4]. En outre, les émissions anthropiques de CO_2 peuvent être capturées et séquestrées dans des aquifères salins profonds, un facteur important dans la transition mondiale vers une infrastructure énergétique à faible teneur en carbone [5]. Dans ce dernier cas, le CO_2 injecté peut passer continuellement d'un état gazeux à un état liquide ou supercritique en fonction des conditions de pression et de température dans le sous-sol, le point critique du CO_2 se situant aux alentours de 31°C et 80 bars. Le CO_2 injecté peut également se fracturer en gouttelettes ou en bulles, formant respectivement une émulsion ou une mousse, ce qui a un fort impact sur son transport à travers les aquifères poreux.

Dans le cas d'une dispersion de petites gouttelettes liquides dans un autre liquide non miscible, qui sont ensuite généralement stabilisées à l'aide d'un agent émulsifiant, le terme "émulsion" est employé. Le transport des émulsions dans les milieux poreux, tels que les sols, les aquifères, et les formations rocheuses, introduit des interactions complexes entre les gouttelettes d'émulsion, la matrice poreuse et les fluides résidents. La compréhension et le contrôle du transport des émulsions dans ces environnements complexes sont complexes. La visualisation directe de la structure des fluides et

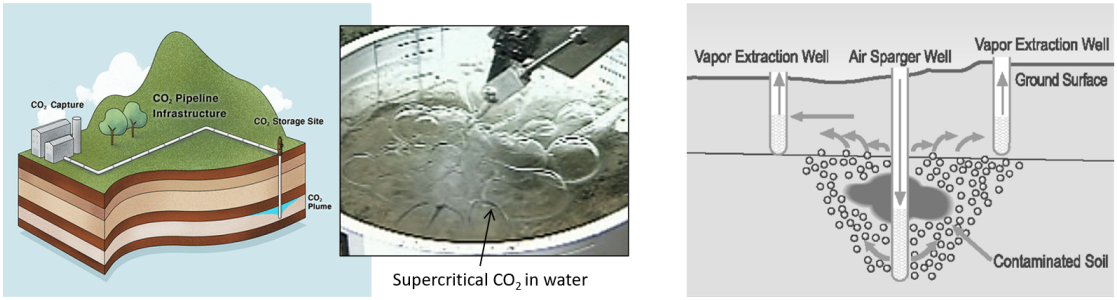

Fig. 1.2 Applications de dispersions dans la séquestration du CO_2 et la remédiation des sols contaminés. Gauche) Exemple d'infrastructure pour le captage et le stockage du CO_2, adapté de Tao *et al.* [6]. L'encart montre du CO_2 supercritique dans un bassin marin profond qui, dans l'eau, se comporte comme une huile et forme de grosses gouttelettes (image de l'IFPEN). À droite) Schéma d'un système d'aspersion d'air de Kim *et al.* [7].

de la dynamique de l'écoulement est essentielle pour comprendre et éventuellement manipuler ces influences. Cependant, l'opacité des milieux poreux réels rend cette visualisation très difficile. Une façon possible d'observer les écoulements multiphasiques à l'échelle des pores est d'utiliser des dispositifs microfluidiques constitués de canaux micrométriques transparents ou de réseaux d'obstacles à travers lesquels les fluides s'écoulent. Ces dispositifs permettent une excellente visualisation de l'écoulement à l'aide de microscopes optiques et de caméras à grande vitesse, tandis que les techniques de microfabrication existantes permettent un grand contrôle des géométries étudiées. Alors que les expériences traditionnelles sur les milieux poreux utilisant des carottes de roche peuvent prendre jusqu'à trois semaines, les nouveaux dispositifs microfluidiques peuvent être fabriqués, les expériences réalisées, et les images analysées en une seule journée.

Plan du manuscrit

L'objectif de ce travail est d'étudier le transport d'émulsions dans des milieux poreux modèles transparents. Nous nous concentrons sur l'influence des hétérogénéités dans les milieux poreux, à la fois en termes de leur géométrie ou de la mouillabilité des surfaces du micromodèle. Le manuscrit est composé des quatre chapitres suivants :

- Le premier chapitre présente les principes physiques et les techniques de modélisation nécessaires pour la compréhension des écoulements de fluides multiphasiques dans les milieux poreux. À l'échelle microscopique, la physique n'est pas la même qu'aux échelles macroscopiques auxquelles nous sommes habitués dans la vie quotidienne. Nous présentons certains des principes généraux régissant l'hydrodynamique des écoulements de fluides confinés au sein de dispositifs microfluidiques. L'influence des forces de surface, qui deviennent prépondérantes à l'échelle microscopique, est également abordée, ainsi que quelques généralités sur les dispersions. Enfin, les paramètres macro- et microscopiques importants pour décrire les milieux poreux, nécessaires pour corréler l'écoulement des fluides à l'influence de la géométrie, sont présentés.

- Le deuxième chapitre étudie le transport de gouttes microfluidiques à travers des réseaux contrôlés d'obstacles à mouillabilité homogène. Les études pertinentes récentes sur le transport de gouttes, dans des géométries allant de canaux rectilignes à des structures complexes basées sur des images de roches réelles, sont présentées. Les matériaux et la méthodologie de formation et d'injection des émulsions, utilisés dans les chapitres 2 et 3, sont présentés. Enfin, une variation systématique de plusieurs paramètres régissant le transport des gouttes, concernant à la fois l'écoulement du fluide et la géométrie du milieu poreux, est présentée. Dans ces expériences, nous observons la formation de chemins préférentiels d'écoulement lors d'injections radiales, qui dépendent de la tortuosité géométrique des réseaux.

- Dans le troisième chapitre, les expériences du chapitre 2 sont réexaminées, cette fois dans le but d'évaluer la stabilité des émulsions. La littérature sur la rupture et la coalescence de gouttes dans des géométries microfluidiques est présentée. Les distributions de diamètre des gouttes, à la fois à la sortie du milieu poreux et à des endroits spécifiques dans le milieu poreux, sont étudiées en fonction des paramètres de l'injection et des géométries. Nous constatons que le diamètre moyen des gouttes sortant du milieu poreux atteint un plateau à $Ca \approx 10^{-3}$, quel que soit le diamètre moyen des gouttes à l'entrée, dans le cas où les diamètres des gouttes sont beaucoup plus grands que les largeurs des pores. Cependant, il n'y a que peu ou pas de rupture lorsque les gouttes sont plus petites que la largeur du pore.

- Enfin, le quatrième chapitre présente une tentative de fabrication de micromodèles présentant des hétérogénéités spatiales de mouillabilité. Ce travail fait partie

d'une collaboration avec Chimie Paris Tech et a été réalisé pendant le stage de Camille Brigodiot. Plusieurs procédures de fabrication ont été testées et les résultats de chacune d'entre elles ont été discutés. Des injections de fluides, qu'il s'agisse de fluides monophasiques ou d'émulsions, ont été réalisées dans les géométries et les résultats ont été présentés. Nous constatons que la formation des chemins préférentiels d'écoulement décrits au chapitre 2 dépend fortement de la taille et de l'emplacement des zones de mouillabilité modifiée.

General Context

When undertaking a journey by car we tend to assume the motorway will be the fastest route to our destination. It is the most direct path, on which we can travel at the greatest speeds. However, sometimes the smaller side roads can prove to be quicker. This is often due to the layout of the roads, as well as the influence of the other cars on the road through the creation of traffic, such as when leaving a big city on the Friday evening before the school holidays. The resulting traffic dynamics are complex and intermittent, as evidenced by the constantly evolving estimated arrival times or proposed routes when using navigation software.

This same behaviour can be observed when fluids flow through a porous medium, a solid material containing an interconnected network of open spaces within its structure. Simple fluids, such as water or air, will primarily flow through the widest channels as the resistance to the flow is lowest. However, when two immiscible (unmixable) fluids such as water and oil or water and air simultaneously flow through a porous network, the mechanisms governing the flow and the resulting hydrodynamics are much more complex. For instance, the multiphase system can preferentially flow in the smaller channels, much like cars taking the smaller roads to avoid congested motorways.

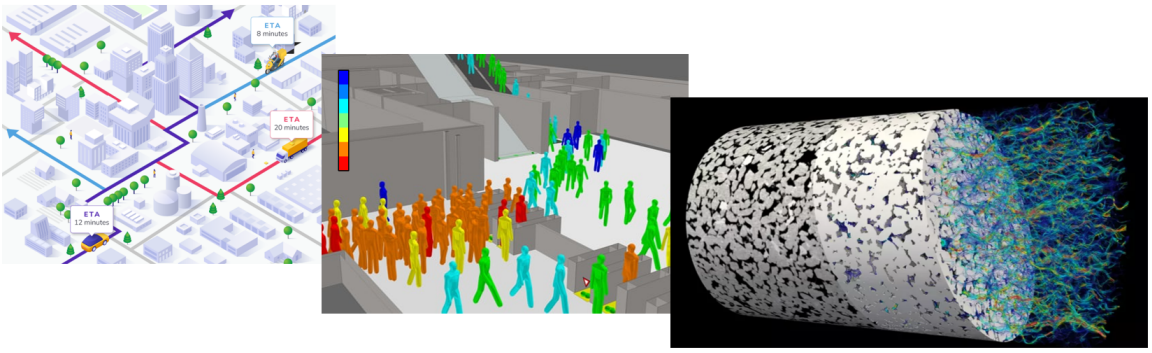

Fig. 1.3 Example scenarios involving transport through complex networks. Left) Driver route optimisation [1]. Middle) Pedestrian tracking simulations where the colour indicates the degree of fluidity from highest (blue) to lowest (red) of each pedestrian [2]. Right) Digital rock images used to model fluid transport in the pore space [3].

The multiphase fluid systems considered in this thesis are known as dispersions. A dispersion is a system in which small particles or droplets of one substance are dispersed or distributed within another substance without being chemically bonded together. These particles or droplets can be in the form of solid, liquid, or gas, and

they are typically called the "dispersed phase," while the substance in which they are dispersed is known as the "continuous phase." Dispersions are commonly encountered in everyday life, such as when forming a Chantilly cream, preparing a vinaigrette for a salad, or even taking photographs with a film camera. Nonetheless, the properties of dispersions present some very rich physico-chemistry. We might wonder, for instance, why it is easier to form a Chantilly with certain creams over others? More peculiar still, why is it that by adding air to the more viscous cream, the resulting system is stiff with a far greater viscosity than that of the air and the cream combined?

Dispersions play a pivotal role in a multitude of industrial and natural processes, particularly in the realm of geosciences. For example, dispersions of air bubbles in aqueous solutions can introduce oxygen into ground water or contaminated soils to enhance remediation efforts [4]. Furthermore, anthropogenic CO_2 emissions can be captured and sequestered in deep saline aquifers, an important factor in the global transition to a low-carbon energy infrastructure [5]. For the latter, the injected CO_2 can continuously transition from a gas to a liquid or supercritical state depending on the pressure and temperature conditions involved in the subsurface, with the critical point of CO_2 being around 31°C and 80 bar. The injected CO_2 can also fracture into droplets or bubbles, forming an emulsion or a foam respectively, which has a strong impact on its transport through the porous aquifers.

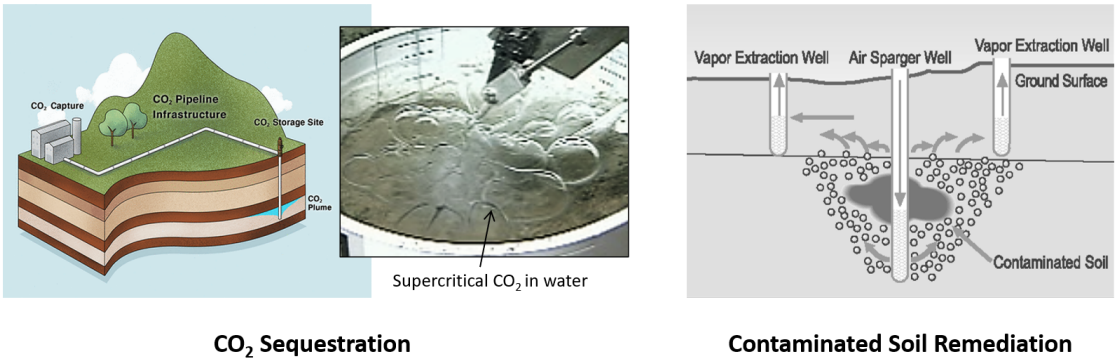

Fig. 1.4 Applications of dispersions in CO_2 sequestration and the remediation of contaminated soils. Left) Example infrastructure for CO_2 capture and storage, adapted from Tao *et al.* [6]. The insert shows supercritical CO_2 in a deep-sea basin which, in water, behaves like an oil and forms large droplets (image courtesy of IFPEN). Right) Diagram of an Air Sparging system from Kim *et al.* [7].

In the case of a dispersion of small liquid droplets in another immiscible liquid, which are then usually stabilised using an emulsifying agent, the term "emulsion" is employed. The transport of emulsions in porous media, such as soils, aquifers, and rock formations, introduces complex interactions between the emulsion droplets, the porous matrix, and the resident fluids. Understanding and controlling emulsion transport in these intricate environments is complex. Direct visualisation of the fluid structure and flow dynamics is critical for understanding and eventually manipulating these influences. However, the opacity of realistic porous media makes such visualisation very challenging. One possible way to observe multiphase flows at the pore-scale is by using microfluidic devices consisting of transparent micrometric channels or networks of obstacles through which fluids flow. The devices allow for excellent flow visualisation using optical microscopes and high speed cameras, whilst existing microfabrication techniques permit great control and customisation of the geometries studied. Whereas traditional porous media experiments using core-flood apparatus can take up to 3 weeks, new microfluidic devices can be manufactured, the experiments performed, and the images analysed all in a same day.

Outline of the Manuscript

The objective of this research is to study the transport of emulsions in transparent model porous media. We focus on the influence of heterogeneities within the porous media, both in terms of their geometry or of the wettability of the micromodel surfaces. The manuscript is composed of the following four chapters:

- The first chapter presents the necessary physical principles and modelling techniques applied to multiphase fluid flows in porous media. At the microscale, the physics is not the same as at the macroscopic scales we are accustomed to in everyday life. We introduce some of the general principles governing the hydrodynamics of confined fluid flows in microfluidic devices. The influence of surface forces, which become preponderant at the microscale, is also discussed, as well as some generalities on dispersions. Finally, the important macro- and microscopic parameters for describing porous media, necessary for correlating the fluid flow to the influence of the geometry, are presented.

- The second chapter studies the transport of microfluidic droplets through controlled lattices of obstacles of homogeneous wettability. The recent relevant

studies on droplet transport, in geometries ranging from straight channels to complex structures based on real rock images, are presented. The materials and methodology form the formation and injection of the emulsions, used in both Chapter 2 and Chapter 3, are introduced. Finally, a systematic variation of several parameters governing the droplet transport, concerning both the fluid flow and the geometry of the porous media, is presented. In these experiments we observe the formation of preferential flow paths under radial injections that arise as a function of the geometric tortuosity of the lattices.

- In the third chapter the experiments of Chapter 2 are re-examined, this time with the aim of assessing the stability of the emulsions. The literature on droplet breakup and coalescence in microfluidic geometries is presented. The diameter distributions of the droplets, both at the outlet of the porous media and a specific locations throughout the porous media, are studied as a function of the injection and geometric parameters. We find that the mean diameter of the droplets exiting the porous media plateau at $Ca \approx 10^{-3}$, regardless of the mean droplet diameter at the inlet in the case where droplets diameters are much larger than the pore widths. However, little to no breakup occurs when the droplets are smaller than the pore width.

- Finally, in the fourth chapter, an attempt at fabricating micromodels bearing spatial heterogeneities in wettability is presented. This work was part of a collaboration with Chimie Paris Tech and performed during the internship of Camille Brigodiot. Several fabrication procedures were tested and the results of each discussed. Fluid injections, of both single-phase fluids and emulsion, were performed in the geometries and the results presented. We find that the formation of the preferential flow paths discussed in Chapter 2 is highly dependant on the size and location of the zones of modified wettability.

Chapter 2

Generalities

2.1 An Introduction to Microfluidics

Microfluidics is the science of controlling and manipulating fluid flows that are geometrically constrained to a small scale, typically hundreds of micrometres or less. Over the past thirty years, microfluidics has evolved rapidly and has been implemented in a wide range of scientific and industrial contexts, such as high-throughput chemical screening, drug discovery, point-of-care diagnostics, and environmental monitoring [8, 9]. Some example microfluidic devices are shown below in Figure 2.1, used in applications such as single cell analysis, blood-glucose measurement, and droplet formation.

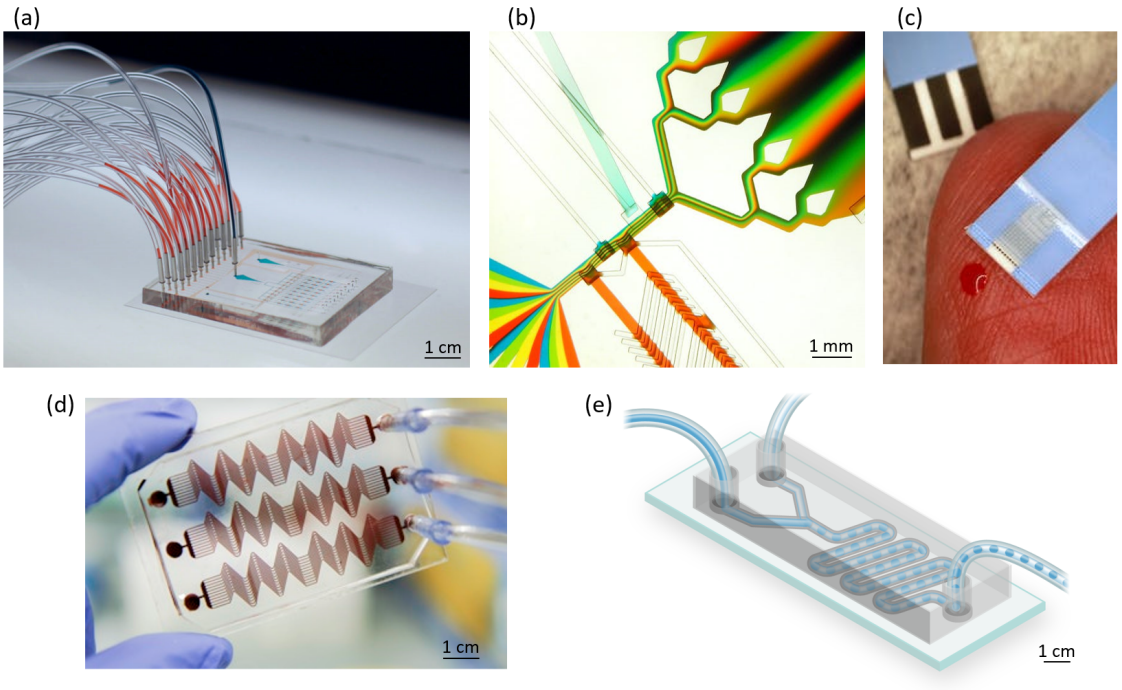

Fig. 2.1 Examples of microfluidic devices. a) Microfluidic device for single cell analysis [10]. b) Coloured streams of liquid enter a single channel from the bottom left, but very little mixing occurs due to the laminar flow at microscales, only that due to diffusion perpendicular to the flow [11]. c) Example glucose strip: a microfluidic device requiring a tiny amount of blood from the tip of a finger that produces results in seconds [11]. d) Microfluidic device for studying blood clogging [12]. e) Microfluidic device for generating monodisperse droplets (in blue) [13].

Microfluidics has become widespread in recent years, but what exactly is the appeal in working at such small scales? Given that the microscale corresponds to the size of cells, capillaries in our bodies, trees and plants, or pores in rocks, there is often a strong desire to observe phenomena occurring at these scales. The transparency and

the planar, quasi-2D geometries of micromodels allows for excellent visualisation of the flow behaviour using standard optical microscopy. Microfluidic devices also tend to be inexpensive and quick to implement. This facilitates frequent design iterations and testing. The precise geometries of micromodels can be finely tuned to enable continuous control and variation of parameters directly influencing the flow.

In the context of our study, we aim to produce a series of highly monodisperse droplets for injection into model porous media. At microscopic scales, capillary forces become dominant, enabling the generation of highly monodisperse dispersions with precise control over both droplet size and generation frequency. Figure 2.2 illustrates an example geometry for reliably creating monodisperse droplets within a microfluidic device.

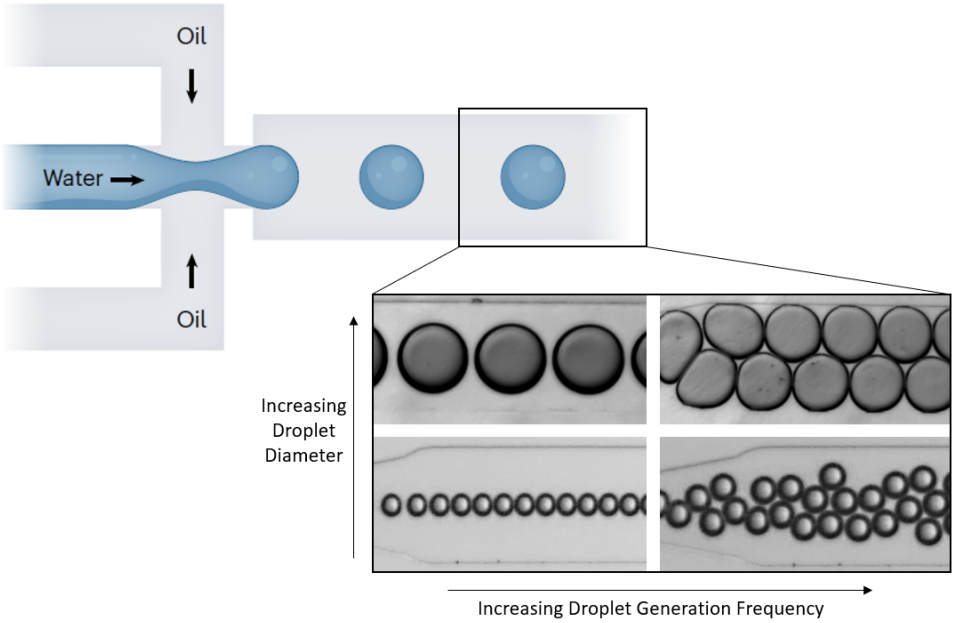

Fig. 2.2 Passive droplet generation in microfluidics. Top Left) Schematic of a flow-focusing geometry adapted from Moragues *et al.* [14]. Pressure and viscous stresses act to elongate the water phase, which subsequently breaks up into a stream of monodisperse droplets. Bottom Right) Examples of droplets produced during this thesis of varying droplet diameter and generation frequency. The width of the channels at the widest point is 300 µm.

Additionally, a diverse array of microfluidic geometries and devices has been developed, enabling controlled operations such as droplet sorting, splitting, fusion,

incubation, and many others. The ability to integrate these operations on a single microfluidic chip has significantly expanded the range of applications for microfluidic studies. For example, streams of droplets with varying chemical compositions can be rapidly generated, allowing hundreds of experiments under different chemical conditions to be conducted within a short period using a single device (Figure 2.3, left). Chemical reactions can also be initiated by merging two droplets with different compositions, and the resulting drops can be continuously observed to quantify the reaction (Figure 2.3, top-right) [15]. Other microfluidic geometries have been employed to passively separate blood components by size and filter circulating tumor cells or malaria-infected red blood cells from blood samples at high throughput rates, facilitating rapid diagnoses [16, 17]. Consequently, microfluidics has emerged as an excellent tool for a wide range of scientific studies.

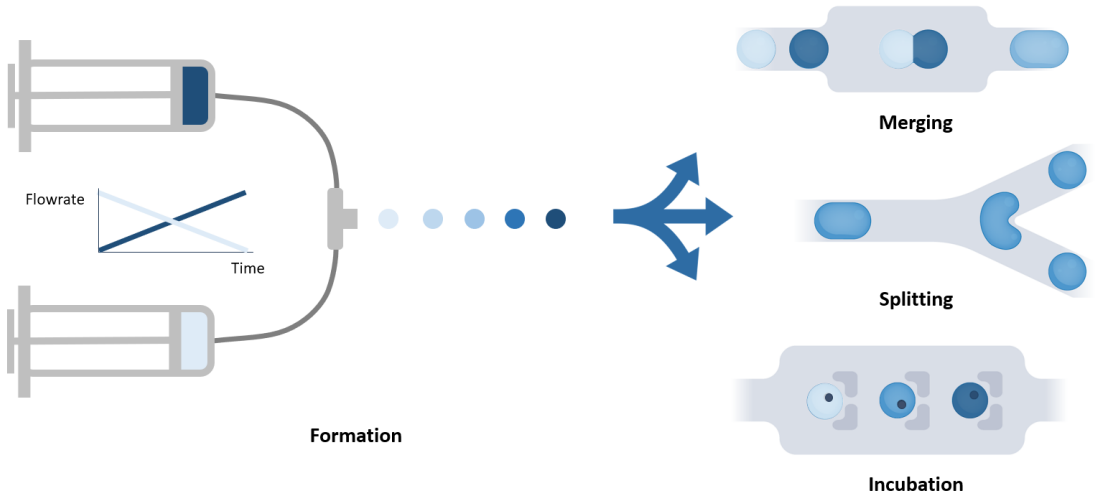

Fig. 2.3 Examples of the versatility of microfluidic operations, from easily producing droplets with varying concentrations of multiple solutions for rapid testing (left) to precisely manipulating existing droplets. Adapted from Moragues *et al.* and 'The Lutetium Project' [14, 18].

In this chapter, we delve into the physics of small-scale fluid flows in microfluidic devices. We explore the new force equilibria that arise in at these small scales, aiding our comprehension of the fluids behaviour. We also introduce key concepts of Newtonian fluid hydrodynamics within microfluidic devices and explore crucial interfacial effects, central to dispersions, the thesis's primary focus. Lastly, we cover practical considerations for the production of droplets.

2.1.1 Hydrodynamics of Confined Systems

Navier-Stokes and Stokes Equations

With a characteristic length scale ranging from tens to hundreds of microns, the fluid system within most microfluidic devices is sufficiently large to be treated as a continuum. Consequently, the motion of an incompressible Newtonian fluid in a microfluidic device can be formally described by the Navier-Stokes and continuity equations. These equations express the conservation of momentum and mass, respectively:

$$\rho\frac{\partial \underline{v}}{\partial t} + \rho(\underline{v}\cdot\underline{\nabla})\underline{v} = -\underline{\nabla}P + \eta\nabla^2\underline{v} + \underline{f} \tag{2.1}$$

$$\underline{\nabla}\cdot\underline{v} = 0 \tag{2.2}$$

where ρ is the fluid density, $\underline{v}$ the velocity field of the fluid, t the time, P the pressure, η the dynamic viscosity of the fluid, and $\underline{f}$ the sum of the volume forces acting on the fluid, such as gravitational or electromagnetic forces.

The Navier–Stokes equations describe the physics of a wide range of phenomena, from the swimming of bacteria at the microscale to the behaviour of ocean currents and the movement of glaciers at the kilometre scale [19]. However, they are inherently nonlinear, and obtaining an exact solution requires applying simplifying assumptions. One common approach involves the use of dimensionless numbers to compare the relative contributions of each of the various physical ingredients captured by the equations to the flow behaviour under specific flow conditions. For instance, by taking the ratio of the inertial term of Equation 2.1, $\rho(\underline{v}\cdot\underline{\nabla})\underline{v}$, to the viscous term, $\eta\nabla^2\underline{v}$, we arrive at the dimensionless quantity known as the Reynolds number (Re):

$$Re = \frac{[\rho(\underline{v}\cdot\underline{\nabla})\underline{v}]}{[\eta\nabla^2\underline{v}]} = \frac{\rho v L_c}{\eta} \tag{2.3}$$

where v is the flow speed and L_c is the characteristic length of the channel through which the fluid is flowing, generally its smallest dimension as this is the one that induces the greatest shear stresses. Figure 2.4 demonstrates the physical consequences of Re on the behaviour of the fluid flow. We see that at low Re ($Re \ll 1$) the flows in Figure 2.4a and Figure 2.4b remain undisturbed across the entire length of the channels, even in the presence of an obstacle in the centre of the channel in (b). As Re increases ($Re \gg 1$) in (a) and (c) the flow becomes increasingly turbulent and

chaotic, as evidenced by the motion perpendicular to the primary flow direction and the formation of von Kármán vortices in Figure 2.4c.

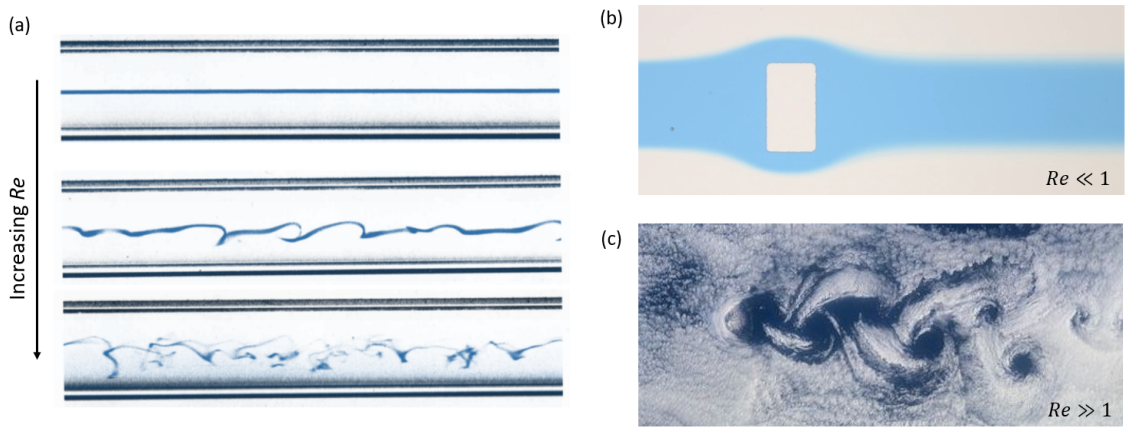

Fig. 2.4 Demonstrations of the influence of the Reynolds number (Re) on a fluid flow. All flows are from left to right. (a) Repetition of Osborne Reynolds' famous 1883 experiment. A filament of coloured water (in blue) extends undisturbed at low Re but becomes turbulent as Re increases. Image adapted from van Dyke [20]. (b) Low Re flow in a microfluidic channel around a rectangular obstacle, primarily as a result of the small channel dimensions on the order of 100 µm. Image adapted from 'The Lutetium Project' [18]. (c) High Re flow leading to the formation of von Kármán vortices downstream from the volcanic island of Rishiri in Japan. Flows are on the order of 100 km. Image adapted from NASA, 2001.

For the flows considered in this work, with $L_c \sim 100$ µm and $v \sim 100$ µm/s, we see that $\boldsymbol{Re \sim 10^{-3}}$. The inertial terms of the Navier-Stokes equations can, therefore, be considered negligible and the flow considered laminar. In the absence of body forces, Equation 2.1 simplifies to:

$$\underline{\nabla} P = \eta \nabla^2 \underline{v} \tag{2.4}$$

This equation is known as the Stokes equation, and unlike the Navier-Stokes equation it is linear and stationary, making it possible to derive analytical solutions. We now consider some typical solutions derived from Stokes equation for Poiseuille flows in microfluidic channels.

Practical Poiseuille-Flow Solutions

Most fabrication methods for microfluidic devices result in microchannels with a rectangular cross-section, as depicted in Figure 2.5 below, of height H and width W with generally $W > H$:

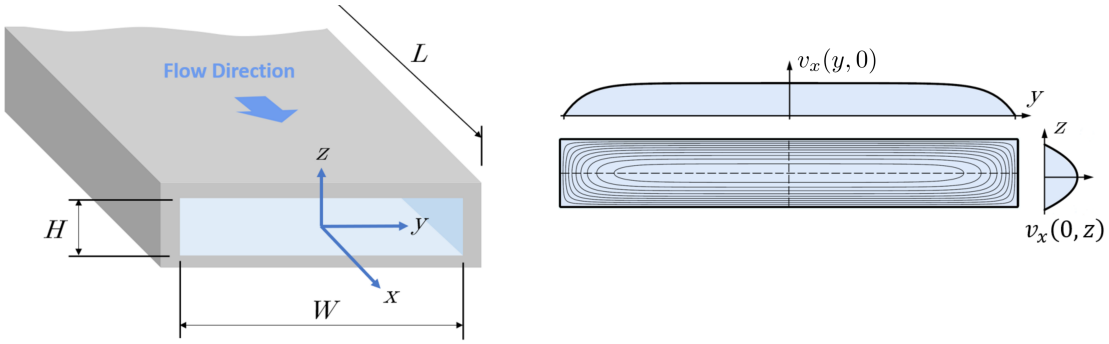

Fig. 2.5 Left) Closed rectangular channel containing a fluid flow. Right) Contour lines of the velocity field $v_x(y,z)$ for Poiseuille flow. Each line represents a step of 10% of the maximal value of $v_x(0,0)$. The plots of $v_x(y,0)$ and $v_x(0,z)$ are also included above and right of the contour plot respectively. Adapted from Bruus [21].

The Stokes equation and the associated boundary conditions for Poiseuille-Flow in such channels are therefore:

$$\left[\partial_y{}^2 + \partial_z{}^2\right] v_x(y,z) = -\frac{\Delta P}{\eta L}, \quad \text{for} \quad -\frac{1}{2}W < y < \frac{1}{2}W, \;\; 0 < z < H \tag{2.5}$$

$$v_x(y,z) = 0, \qquad \text{for} \quad y = \pm\frac{1}{2}W, \;\; z = 0, \;\; z = H \tag{2.6}$$

Despite of the high symmetry of these channels, no analytical solution for Poiseuille-flow through a rectangular channel is known [21]. Using a Fourier sum we can, however, derive the following pressure-flow rate relation [21]:

$$\Delta P = \frac{12\eta L}{WH^3}\left[1 \; - \sum_{n,\,odd}^{\infty} \frac{1}{n^5}\frac{192}{\pi^5}\frac{H}{W}\tanh(n\pi\frac{W}{2H})\right]^{-1} Q \tag{2.7}$$

Equation 2.7 can be significantly simplified in the case of a flat, wide channel, as illustrated in Figure 2.5 where $W \gg H$, a common condition in microfluidics. The pressure-flow rate relationship is considerably simplified, as demonstrated below, and the error resulting from this assumption is only 0.2 % when $W = 2H$ [21].

$$\Delta P = \frac{12\eta L}{WH^3}\left[\frac{1}{1-0.63(H/W)}\right]Q \tag{2.8}$$

Furthermore, given the linear and stationary nature of Stokes equation, a constant pressure drop across a microfluidic channel ΔP will result in a constant flow rate Q. This result can be summarised by the Hagen-Poiseuille law such that:

$$\Delta P = R_h Q \tag{2.9}$$

$$R_h = \frac{12\eta L}{WH^3}\left[\frac{1}{1-0.63(H/W)}\right] \tag{2.10}$$

where R_h is the hydrodynamic resistance, a constant of units Pa.s.m^{-3}, whose value depends on the viscosity of the fluid and the geometry of the channels. Equation 2.9 is analogous to Ohm's law, $\Delta V_e = R_e I_e$, in linear electricity where the pressure drop across a channel plays the role of the electrical potential ΔV_e along a wire and the flow rate that of the electrical current I_e.

This analogy with linear electricity proves highly valuable for tackling more complex geometries. Take, for example, the network of channels shown in Figure 2.6, where the fluid can choose one of two paths. The pressure drop across the system ΔP is the same for both branches. By applying an analogy akin to Kirchhoff's law in linear electricity, we can determine the flow rates in each branch based on their hydrodynamic resistances. For a Newtonian fluid flowing through channels of constant cross-section, the flow rate in each channel simply depends on its length. This relationship holds significant practical importance in the design of microfluidic devices.

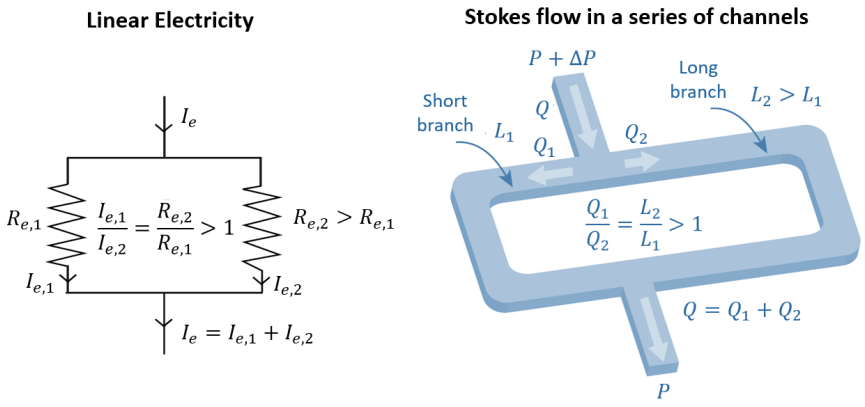

Fig. 2.6 Analogy between linear electricity and linear Stokes flow in a channel network.

2.1.2 Surface Effects

So far, we have only considered the flow of a monophasic fluid. Many applications of microfluidics, however, require the use of several immiscible fluids, often in the form of droplets or bubbles. The presence of fluid interfaces complicates the analysis, introducing time-dependence and non-linear laws into the otherwise stationary, linear Stokes flows. Before discussing the flow of dispersions in Chapter 3, we will provide an overview of capillarity – the study of interfaces between two immiscible liquids, or between a liquid and a gas – as well as some of the other rich physics of multiphase fluid systems.

We mentioned earlier two primary advantages of working with microfluidics as a result of the small scale of the flows. The first, as we have just explored, results from the linear and laminar flows that generally allow for precise control of Newtonian fluids. The second arises from the increased surface-to-volume ratio at small scales, as demonstrated using a simple scaling law:

$$\frac{\text{Surface}}{\text{Volume}} \sim \frac{{L_c}^2}{{L_c}^3} = {L_c}^{-1} \tag{2.11}$$

As the characteristic length L_c of a system decreases, the surface-to-volume ratio increases and capillary phenomena become preponderant over inertial forces. This, in part, explains how coffee can rise up through a sugar cube despite gravity's best efforts, and how some insects can walk on water with little apparent concern for the laws of physics. In this section we explore some of the capillary phenomena that are essential in understanding multiphase fluid flows in micromodels which is at the heart of this study.

Interfacial Tension

The main modification that droplets bring to fluid flows comes through the introduction of interfacial tension, γ, also commonly referred to as the surface tension. In a liquid that is in equilibrium, molecules far from any interface benefit from cohesive interactions (attractive, repulsive, and thermal) with neighbouring molecules in all directions, leading to a force equilibrium. A molecule at the interface with another immiscible phase, however, loses half of its attractive cohesive interactions, placing it in an unfavourable, higher energy state [22]. In the case of two immiscible fluids A and B this additional energy per unit surface area is represented by the interfacial tension,

γ_{AB}, with units J/m^2 or N/m. The origin of the interfacial tension is represented schematically in Figure 2.7.

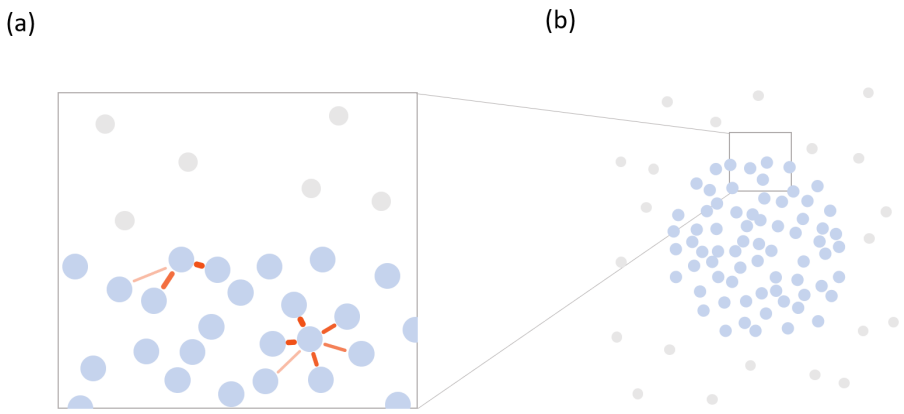

Fig. 2.7 Schematic representation of molecules of one phase (blue) prioritising cohesive bonding over adhesive bonding with molecules of another immiscible phase (grey), leading to the formation of a sphere.

In order to minimise its free energy, the interface between two immiscible fluids will change shape to form the smallest interfacial area possible. Consequently, an isolated droplet or bubble will tend to form a sphere, the shape with the smallest area for a given volume, as shown in Figure 2.7. The action of the interfacial tension and the resulting curvature of the interface leads to a pressure jump between the inside and the outside of a droplet or bubble. Known as the Laplace pressure, it is written as:

$$\Delta P = \gamma_{AB} \left(\frac{1}{r_1} + \frac{1}{r_2} \right) \tag{2.12}$$

where $\Delta P = P_B - P_A$ is the pressure difference between the two immiscible phases, and r_1 and r_2 are the principal radii of curvature of the interface, as in Figure 2.8. In the case of droplets in a continuous immiscible phase, the pressure inside the droplets will be greater than that of the surrounding continuous phase, with smaller droplets exhibiting a greater pressure difference than larger ones. The principal radii can also vary greatly across a single droplet, such as when it is being squeezed through a small microfluidic channel or rock pore, inducing pressure variations along the droplet. We discuss the consequences of this phenomenon in greater detail in Chapter 3.

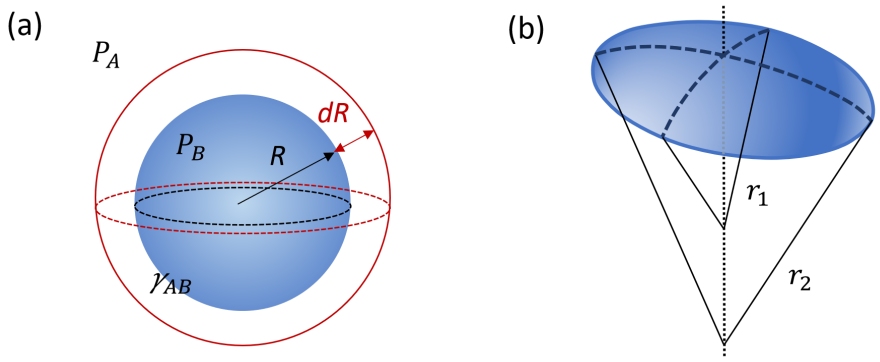

Fig. 2.8 (a) Diagram of an isolated, spherical droplet formed between two immiscible phases. (b) Principal radii of a non-spherical curved interface.

The principal radii can also vary in the case where a droplet is flattened by gravity, as in Figure 2.9. In this study we ignore the effects of gravity since the Bond number, comparing the impact of gravity to interfacial tension, is much less than one:

$$Bo = \frac{\Delta\rho g {L_c}^2}{\gamma} \ll 1 \tag{2.13}$$

where $\Delta\rho$ is the difference in densities of the two phases and g is the acceleration due to gravity.

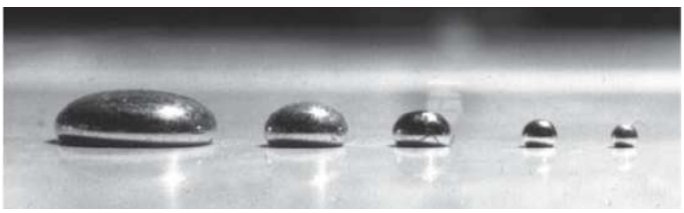

Fig. 2.9 Varying deformation of mercury drops on a glass slide under gravity as a function of their size and the resulting Bond number (Bo). The smallest drop forms an almost perfect sphere 2 mm in diameter. Adapted from Guyon *et al.* [19].

This leaves interfacial tension and viscosity in competition with each other, the relative strength of which is expressed by the capillary number, Ca, such that:

$$Ca = \frac{\text{viscous shear stress}}{\text{capillary stress}} = \frac{\eta v / L_c}{\gamma / L_c} = \frac{\eta v}{\gamma} \tag{2.14}$$

where η is the dynamic viscosity, typically that of the external phase, U the flow speed, and L_c the characteristic length scale. The capillary number can equally be interpreted as the deformability of a droplet under the given flow conditions. $Ca < 1$ indicates that the effect of interfacial tension dominates that of the viscosity and drops flowing under such conditions are able to maintain a spherical shape, minimising their interfacial energy at all times. In the opposite case of $Ca > 1$, viscous stresses dominate and droplets can be observed to undergo large deformations and exhibit highly asymmetrical shapes. In our study, $\boldsymbol{Bo \sim 10^{-1}}$ and $\boldsymbol{Ca \sim 10^{-3}}$.

Interfacial tension can be measured in a variety of ways, depending on the nature of the fluids and the stability of the interface under deformation [22]. In this study a force tensiometer was used following the Wilhelmy plate or the Du Noüy ring methods, whereby a small metallic plate or ring is submerged in the liquid then partially removed while measuring the force exerted on it [23]. Care must be taken when performing measurements as the interfacial tension is temperature dependant and the presence of impurities on the interface can cause measured interfacial tensions to vary significantly from theoretical ones.

Wettability

When a drop of water is placed on a very clean glass surface it spreads out completely, forming a thin liquid film. In this case we can say that the water drop wets the surface totally, or that the surface is very hydrophilic. This property is often desirable, such as when rainwater forms a thin layer on glasses giving uniform optical properties or in coating applications where a thin, even layer is desired. However, if the same drop is deposited on a sheet of plastic it assumes the shape of a spherical cap resting on the surface with a contact angle θ_c. If the surface's affinity for the droplet is sufficiently weak the droplet can simply roll of the surface without contaminating it.

In general, when a droplet is positioned on a flat surface we have either total wetting ($\theta_c < 10°$), partial wetting ($10° < \theta_c < 150°$), or non-wetting ($\theta_c > 150°$) [22]. When $\theta_c < 90°$ the surface is considered hydrophilic and when $\theta_c > 90°$ it is considered hydrophobic whilst when $\theta_c \approx 90°$ the affinity of the surface is considered neutral. The aforementioned wetting scenarios are summarised in Figure 2.10.

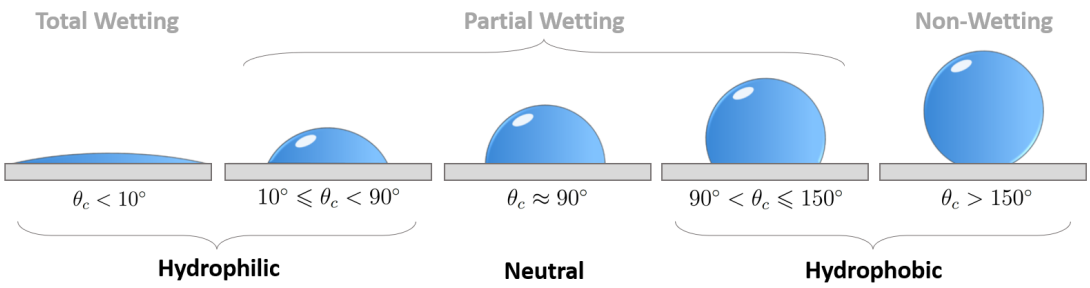

Fig. 2.10 Schematic of wetting for a 3-phase system: solid in grey, dispersed liquid in blue, and the surrounding continuous fluid (liquid or gas) in white. Adapted from [24].

Much like the interfacial tension, wettability results from local interactions between immiscible phases. The main difference with wettability is the presence of the third phase: the solid substrate upon which the droplets are placed. In the case of the water drop on the clean glass surface, where the cohesive interactions between the water and the glass are significantly stronger than the interactions between the water and the surrounding air, the water seeks to maximise its contact area with the glass substrate, minimising its surface energy [22]. The contact angle is determined as the equilibrium of interfacial tensions among the three phases using Young's relation, as shown in Figure 2.11 [25]:

$$\gamma_{SG} = \gamma_{SL} + \gamma_{LG} \cos \theta_c \tag{2.15}$$

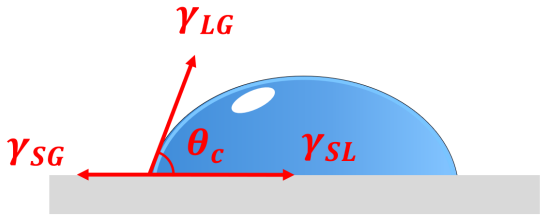

Fig. 2.11 Young's relation for a 3-phase system: solid (S) in grey, liquid (L) in blue, and the surrounding gas (G) in white. This relation also applies when the surrounding phase is an immiscible liquid.

As with interfacial tension measurements, contact angles can vary significantly with temperature or due to the presence of impurities at the interfaces. Wetting properties are also influenced by the micrometric roughness of the surface. This can be observed in nature, with the micron-scale hairs on the legs of water striders providing the necessary hydrophobicity to walk on water, or when considering the water-repelling surface of

Lotus leaves, as in Figure 2.12 [26, 27]. Furthermore, the wettability of a surface can be modified through chemical treatments whereby substrate molecules, when grafted on to the surface, are able to increase or decrease the surface energy at the solid/liquid interface.

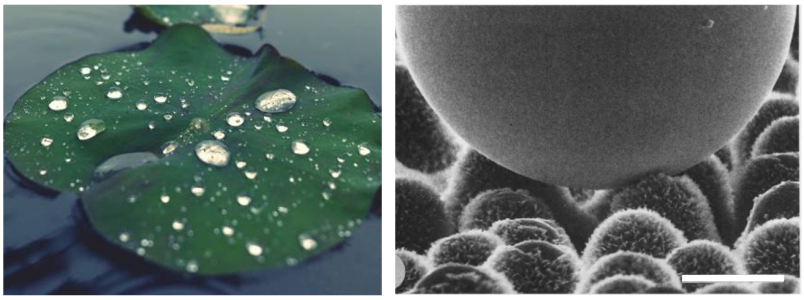

Fig. 2.12 Super-hydrophobicity of Lotus leaves owing in part to their complex surface microstructure. Left) Water drops on a Lotus leaf [28]. Right) Mercury droplet on the surface of a Lotus leaf. Scale bar is 20 µm. Adapted from Barthlott and Neinhuis [29].

Capillary Pressure

One of the most striking consequences of liquids maximising their contact area with wetting surfaces can be observed when a sugar cube is dipped in a cup of coffee. The coffee, which preferentially wets the sugar, defies gravity and naturally permeates the pore space in the sugar cube. More generally, when a capillary is inserted in a liquid that predominantly wets it, the liquid will spontaneously invade the capillary, as shown in Figure 2.13a [30]. Conversely, when a liquid strongly does not wet a capillary, it will resist entering that capillary when the capillary is submerged within it. This can be observed, for instance, when a glass capillary is submerged in liquid mercury.

The fluid interface within the capillary is curved, as visible in Figure 2.13a. We can determine the resulting pressure difference across the interface, fittingly known as the capillary pressure, P_c, and given by the Laplace pressure from Equation 2.12. For a capillary of radius r:

$$P_c = P_0 - \frac{2\gamma \cos\theta_c}{r} \tag{2.16}$$

where P_0 is the surrounding pressure, equal to atmospheric pressure in the case of Figure 2.13. The nature of the capillary action is determined by the contact angle

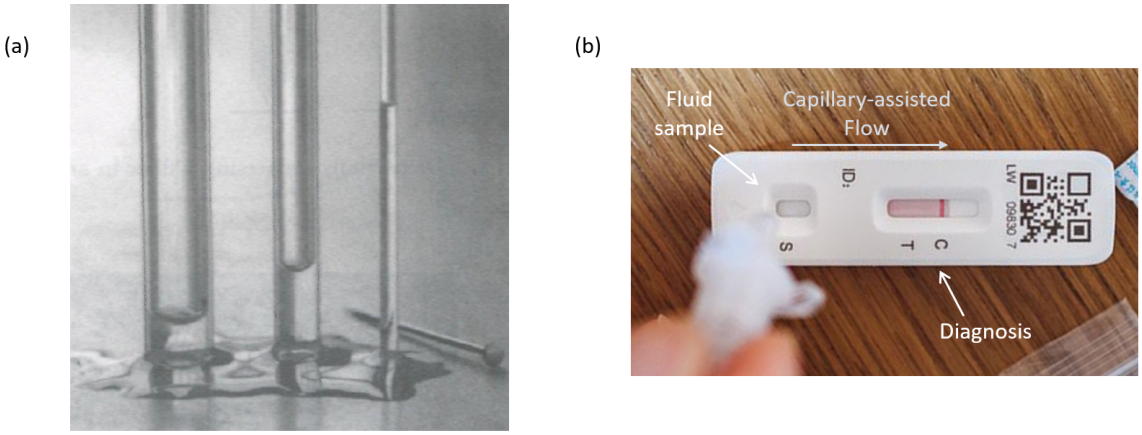

Fig. 2.13 Demonstrations of capillary action. (a) Capillary rise increases as the radius of the tube decreases. Adapted from Wick [31]. (b) Paper-based test providing a fast, low-cost diagnosis of COVID-19 (SARS-CoV-2 virus). The fluid sample flows through a series of testing strips by capillarity. Adapted from [32].

between the fluid and the capillary. When $\theta_c < 90°$, $\cos\theta_c > 0$ and $P_c < P_0$ with the resulting pressure drop in the capillary causing the fluid to spontaneously invade it. When $\theta_c > 90°$, however, $P_c > P_0$ and the local pressure increase acts to prevent the fluid entering the capillary.

As the capillary pressure is inversely proportional to the size of the capillary, this effect plays an important role in microfluidic flows. Many analytical devices, such as blood glucose meters and cheap at-home COVID-19 tests harness this principal to generate flows without the need for any external actuation or expensive laboratory equipment in general (Figure 2.13b).

In addition to spontaneous capillary action, capillary pressure plays an important role when fluids are actively injected into porous media. These flows can be classified based on whether the fluid injected into the medium, known as the invading fluid, is the wetting or the non-wetting phase.

- **Imbibition:** When a wetting fluid is injected, displacing the stationary non-wetting fluid already present in the medium, the flow is referred to as imbibition.
- **Drainage:** In the case where the invading phase is the non-wetting fluid, the process is called drainage. In drainage, capillary forces oppose the advancement of the invading phase. Consequently, the fluid will only enter a capillary when the pressure difference across the pore (ΔP) exceeds the capillary pressure (P_c).

It's worth noting that, in both imbibition and drainage, the effects are more pronounced for smaller pores, as indicated by Equation 2.16. In real porous media bearing a wide distribution of pore sizes, the flow can be highly heterogeneous with certain pathways through the porous medium being completely inaccessible to the invading phase. Imbibition and drainage flows at the pore scale in a rectilinear capillary are illustrated in Figure 2.14.

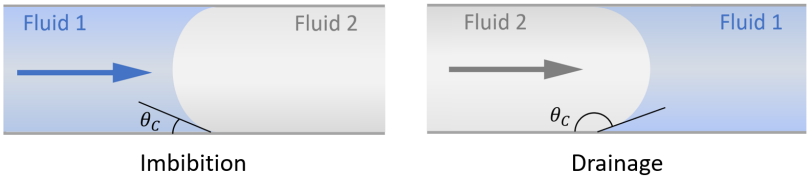

Fig. 2.14 Schematic of imbibition and drainage. Fluid 1 is the wetting phase (blue, $\theta_c < 90°$) whilst fluid 2 is the non-wetting phase (grey, $\theta_c > 90°$).

2.1.3 Dispersions

A dispersion is a general term used to describe a system in which one substance is fragmented into small particles that are dispersed throughout a continuous phase of another substance. For instance, a gas can be dispersed in a liquid, a gas can be dispersed within a liquid, as seen in the case of air in soapy water, forming a foam. Similarly, a liquid can be dispersed in another immiscible liquid, like water or vinegar dispersed in oil, forming an emulsion (Figure 2.15). We encounter dispersions in our everyday lives. They can be natural or synthetic products, such as food products, pharmaceuticals, or cosmetics, sought after for their inherent properties. Conversely, they may be the undesirable by-product of industrial processes.

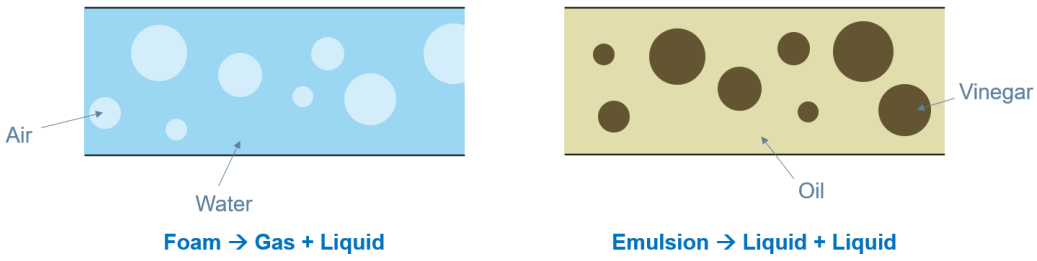

Fig. 2.15 Examples of dispersions.

An important parameter for determining the nature of the dispersion is the volume fraction of the dispersed phase, V_v, sometimes referred to as the 'quality' of the dispersion, such that:

$$\mathrm{V_v} = \frac{V_d}{V_{tot}} \tag{2.17}$$

where V_d is the volume of dispersed phase, and V_{tot} the total volume of the two phases. At low volume fractions the droplets or bubbles can be spherical whilst at higher volume fractions they form polyhedral shapes, separated by thin liquid films known as lamellae and forming ordered structures when confined in tubes. Some examples of the various structures a dispersion can take in a microfluidic channel are shown in Figure 2.16.

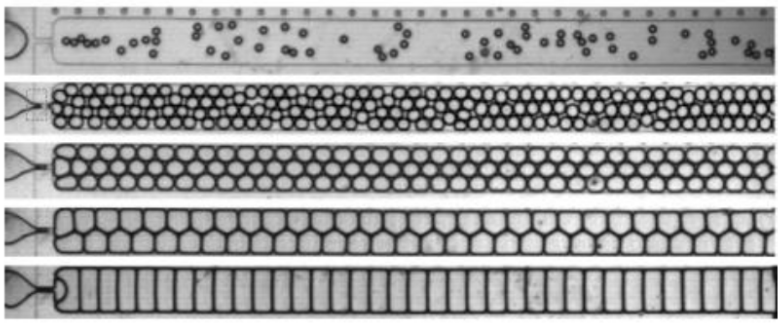

Fig. 2.16 Changes in foam structure in a microfluidic channel for increasing foam quality and bubbles size (from top to bottom). Adapted from Marmottant and Raven [33].

Dispersion Stability

In microfluidics, once a dispersion has been formed, the droplets or bubbles are transported along microfluidic channels. One of the primary challenges when working with dispersions is preventing the droplets or bubbles from recombining or merging back together instantaneously. This is because a dispersion is a thermodynamically unstable system: when two droplets come into contact, merging together to form a single, larger droplet reduces the total interfacial area, and thus the free energy of the system. This continuous process of droplets merging together is known as coalescence and is depicted in Figure 2.17 for a dispersion flowing from left to right in a channel.

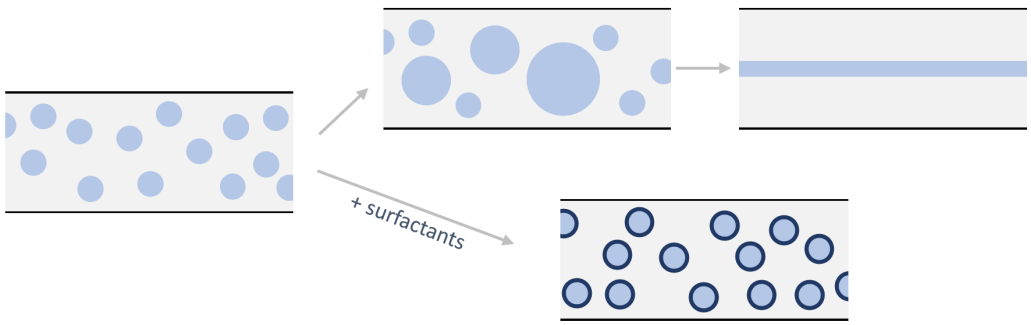

Fig. 2.17 Dispersion flow through a channel tends towards coalescence versus stabilisation when surfactant molecules (dark blue) are added. Flow is from left to right.

To stabilise dispersions, it is essential to prevent coalescence events, and in microfluidics this is done by:

- Choosing a material for the microfluidic channel such that the continuous phase is the one that most strongly wets the channel walls. Otherwise any contact between the channel walls and the dispersed phase can trigger coalescence events.
- Adding surfactants to the continuous phase of the dispersions.

Surfactants are amphiphilic molecules, composed of a hydrophilic head (affinity for water) and a hydrophobic tail (affinity for oil), as illustrated in Figure 2.18. As a result, surfactant molecules preferentially position themselves at fluid interfaces. The cohesive interactions of the molecules at the interface become less isotropic and maintaining the dispersed structure is more favourable energetically.

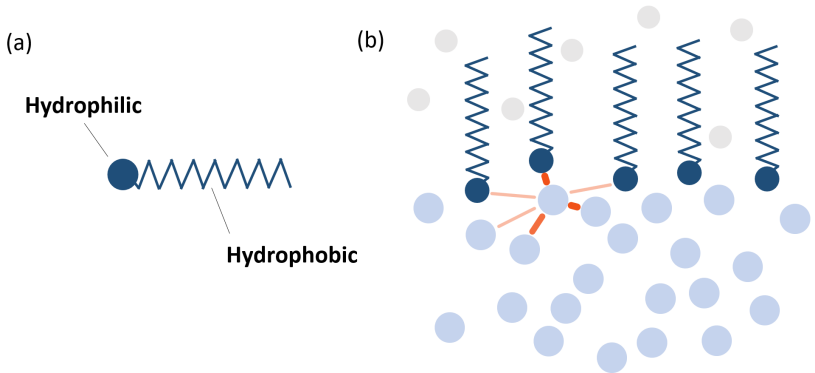

Fig. 2.18 (a) Diagram of an amphiphilic molecule. (b) Preferential positioning of amphiphilic molecules (dark blue) at the interface of two immiscible fluids (molecules in light blue and grey as per Figure 2.7).

Furthermore, the intermolecular interactions between two neighbouring droplet interfaces, which involve steric, electrostatic, and van der Waals interactions, act to prevent coalescence events between droplets. This is known as the disjoining pressure, P_{disj}, which is given by Equation 2.18. The disjoining pressure is a consequence of molecular interactions occurring between the two interfaces [34]. It typically only becomes significant for films of thickness $h < 100$ nm. Most of the time, the emulsion is stabilised through the electrostatic interactions between two adjacent interfaces covered by surfactant molecules, or by the steric repulsion at very high confining pressures.

$$\Pi_{disj} = \Pi_{elec} + \Pi_{vdW} + \Pi_{steric} = -\frac{1}{A}\left(\frac{\partial E}{\partial x}\right)_{T,\,P,\,A} \tag{2.18}$$

When an interface is completely covered with surfactants, the interfacial tension reaches its minimum value. The minimum concentration of surfactants in the continuous phase required to achieve this minimum interfacial tension is referred to as the critical micelle concentration (CMC). An example plot illustrating the interfacial tension as a function of the concentration of dilute surfactants in the continuous phase is presented in Figure 2.19. The relationship between interfacial tension and the local surfactant concentration is nonlinear and is sometimes described using the Langmuir model [22].

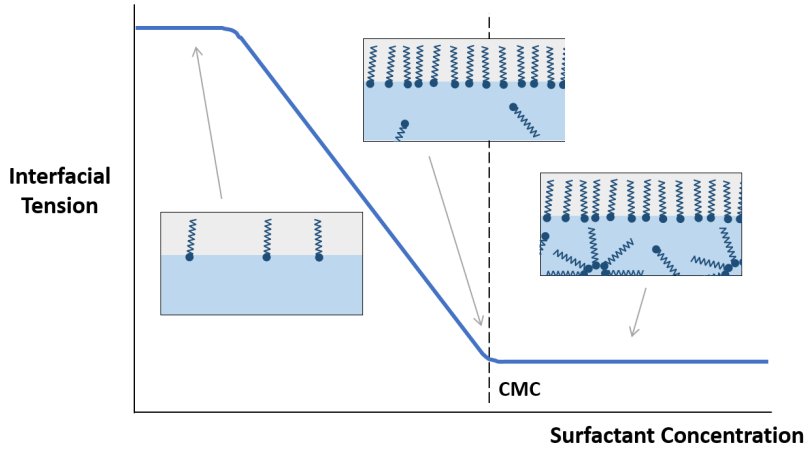

Fig. 2.19 Evolution of the interfacial tension of a fluid system as a function of the surfactant concentration.

The time required for surfactant molecules to diffuse and reach saturation at the interface can be significant and depends on the affinity of the surfactant for the fluids in question. In microfluidics, characterised by high confinement and large surface-to-volume ratios, this diffusion time is not negligible. If this diffusion time is much longer than the time it takes for two adjacent droplets to contact each other, they may still coalesce despite the potential presence of a high concentration of surfactants. The implications of this phenomenon on the stability of droplets in microfluidic systems are further explored in Chapter 4.

In general, an uneven distribution of surfactants across the interface can lead to spatial imbalances in the interfacial tension. These imbalances in interfacial tension can induce flows along the interface, moving from regions of low interfacial tension to areas of high interfacial tension. The resulting surface flows lead to a homogenisation of the interfacial tension and can, through momentum transfer, give rise to bulk flow in the system. The stress driving these flows, known as the Marangoni stress, $\boldsymbol{\sigma_M}$, is written as:

$$\boldsymbol{\sigma_M} = \vec{\boldsymbol{\nabla}}\gamma \tag{2.19}$$

An additional factor influencing droplet stability is the dispersity in droplet sizes. As demonstrated by Equation 2.12, droplets of greater curvature exhibit a larger Laplace pressure. As a result, the dispersed phase in smaller bubbles tends to diffuse into larger neighbouring bubbles of lower Laplace pressure. This mechanism, known as Ostwald ripening, leads to a coarsening of the dispersion [35]. Due to the time scale required for diffusion of the continuous phase this phenomena is of primary concern for stationary or slowly moving droplets, such as those trapped in place (further discussed in Chapter 4).

2.2 Characterising Porous Media

A porous medium is any solid or semi-solid material that contains void spaces, referred to as pores. Most materials are in fact porous to some degree, and generally owe their mechanical properties to their porous nature. For instance, building materials such as bricks, concrete, or wood, can effectively provide thermal insulation thanks to their air-filled pores. Tissue paper and sponges owe their absorbency in part to their highly porous nature. Finally, soil and the ground can hold water and air in the pore spaces and thus sustain life, whilst solid particles can be filtered out of water when it passes through beds of sand, rendering it potable.

The internal arrangement of void spaces in porous media forms vast networks of interconnected channels with nonuniform shapes and sizes. The geometrical properties of these pore networks vary greatly across different types of porous media. In certain cases, porous media may exhibit heterogeneities across multiple length scales. For example, in geological porous media, there can be geological faults at a kilometer scale and intragranular micropores at a nanometer scale. An illustration of the diversity of pore scales within Fontainebleau sandstone is provided in Figure 2.20.

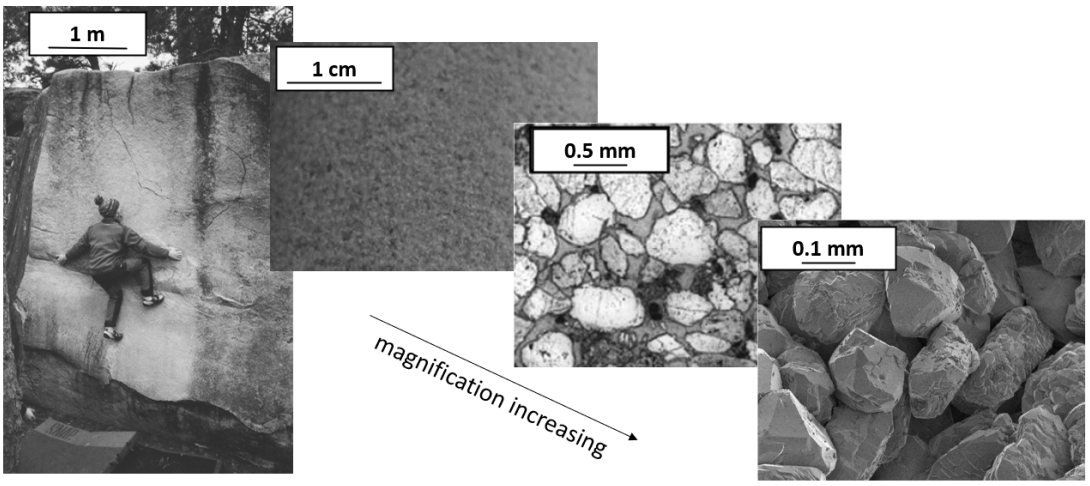

Fig. 2.20 The geometrical features of sandstone, ranging from metre-long cracks to microscopic grains. Images from left to right: Fontainebleau sandstone boulder in Rocher d'Avon, sandstone core sample by Emadi [36], sandstone optical micrograph by Louis *et al.* [37], and a scanning electron microscope image of a Fontainebleau sandstone taken at IFPEN [38].

In order to model fluid flows through different porous media, it is necessary to characterise the geometric properties of the specific porous medium in question. We will first describe some macroscopic properties, such as the porosity and the permeability. These properties are often derived using a continuum approach, which involves averaging the contributions of all the pores in the sample.

An important consideration when characterizing the macroscopic properties of a porous medium sample is to assess its representativeness. The distribution of pore sizes, shapes, and connectivity can vary significantly throughout porous media, sometimes spanning several orders of magnitude, as shown in Figure 2.20. Furthermore, many porous media exhibit anisotropic properties, meaning that their characteristics and behavior differ along different directions.

In general, we can consider a sample of a porous medium to be homogeneous for a given property, and thus representative of the medium at large, when the measurement of the property remains constant as the sample size increases [39]. The smallest sample size that satisfies this requirement is considered statistically representative of the porous media considered at the scale of interest and is known as the Representative Elementary Volume (REV). Throughout the remainder of this chapter, we assume that all macroscopic measurements are conducted on sample sizes greater than that of the REV.

In practice, measuring macroscopic pore properties can can be quite challenging due to the complexity of porous media structures and their often opaque nature. The ability to derive these properties from the various interconnected microscopic properties, obtainable through traditional imagery methods, is highly advantageous. Working at the pore scale also provides insights into many of the observed phenomena that result from the properties of the microscopic channels and the behaviour of the fluids at the microscopic scale [39]. Some microscopic properties will too be discussed in the following sections.

2.2.1 Macroscopic Porous Media Parameters

Porosity

A porous medium is most commonly characterised by its porosity, ϕ, the ratio of the bulk volume occupied by pores, or void spaces:

$$\phi = \frac{V_{void}}{V_{tot}} = 1 - \frac{V_{solid}}{V_{tot}} \tag{2.20}$$

where V_{void} and V_{solid} are the volumes occupied by the pore space and the solid structure respectively, such that $V_{void} + V_{solid} = V_{tot}$, the total bulk volume of the sample. V_{void} typically only accounts for the volume of the interconnected pore space directly accessible by a fluid from outwith the sample, as isolated pores don't contribute to the transport of matter across non-deformable porous media.

Permeability

Knowing only the porosity of a porous medium does not provide a direct indication of how easily a fluid can flow through it, which is often the primary concern. To address this, the conductivity of a porous media with respect to sufficiently slow, unidirectional flow of a Newtonian fluid was investigated experimentally by Darcy who derived a linear law relating the volumetric flow rate Q to the pressure drop ΔP. This relationship is analogous to Ohms law of resistance or Fourier's Law of heat conduction, where the proportionality constant is instead the permeability of the porous medium k, such that:

$$q = \frac{Q}{A} = \frac{k}{\eta L}\Delta P \tag{2.21}$$

q is, therefore, equal to the volumetric flow rate Q normalised by the cross-sectional area of the porous medium perpendicular to the flow A, referred to as the Darcy velocity, η the fluids dynamic viscosity, and L the length of the porous media along which the pressure drop is applied. In the case of a radial outward flow, Darcy's law is expressed as:

$$Q = \frac{2\pi k H}{\eta \ln \frac{r_{in}}{r_{out}}}\ \Delta P \tag{2.22}$$

where r_{in} and r_{out} are the radii at the inlet and outlet of the porous medium sample, and H the height perpendicular to the flow. The average interstitial velocity of the fluid in the pore space, v, is inversely proportional to the porosity of the medium:

$$v = \frac{q}{\phi} \tag{2.23}$$

The permeability, like the porosity, is a purely geometric parameter and is independent of the viscosity of the fluid. It has units of m^2 although a practical unit which is well-adapted to the order of magnitude of permeabilities in naturally occurring porous media is the darcy, defined as:

$$1\ [\text{darcy}] = \frac{1\ [\text{cm}^3/\text{s}]\ 1\ [\text{cP}]}{1\ [\text{cm}^2]\ 1\ [\text{atm/cm}]} \tag{2.24}$$

i.e. the permeability of a cube of sides 1 cm in length and containing a fluid with 1 cP viscosity when an applied pressure difference of 1 atm induces a flow rate through the cube of 1 cm^3/s. It then follows that 1 darcy = 0.987 μm^2.

Several studies have established links between permeability and porosity in different porous media [39–43].For instance, Chilingar demonstrated that grouping sandstones by grain sizes reveals distinct but intricate and non-linear trends where permeability increases with increasing porosity (Figure 2.21) [40]. Moreover, even an increase in porosity of just a few percent can result in a significantly higher permeability. These trends generally hold true for most porous media [39, 44].

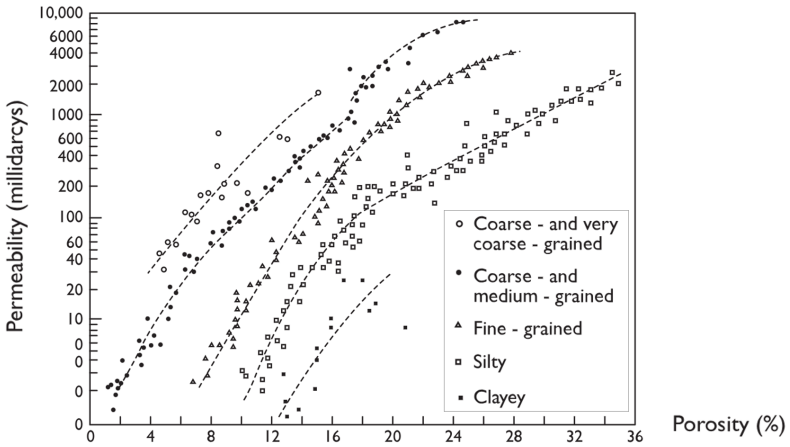

Fig. 2.21 Relationship between permeability and porosity for sandstones of various grain-sizes (from Chilingar [40], adapted by Freeze and Cherry [45]).

The permeability of a porous medium can be determined by flowing a fluid of known viscosity through a sample of the porous medium with known dimensions. This can be done by either applying a constant pressure drop across the porous medium sample and measuring the resulting flow rate or by generating a fixed flow rate and measuring the resulting pressure drop. The only unknown remaining in Darcy's law (Equation 2.21) is the sample's permeability.

In practice, multiple measurements are performed at various applied pressure drops or flow rates. The corresponding data points of flow rates vs. pressure drops can be plotted and a straight line fitted to the data points. If Darcy's law is obeyed, this line should pass through the origin, allowing for the determination of permeability from the gradient of the line. In the case of deformable porous media higher pressures can lead to significant deformation of the pore matrix and hence a non-linear pressure-flow rate relationship [46–48]. Furthermore, in many porous media, such as in most rocks, the permeability can be anisotropic. In such cases measurements are conducted in several directions and directional permeabilities are defined accordingly.

Geometric Tortuosity

In addition to the size and the abundance of pores, their connectivity and resulting topology also has a strong influence on fluid transport. Even simple porous media can provide the fluid with an almost infinite number of paths to traverse the porous media. The geometric tortuosity T provides a measure of the complexity of the pathways across the pore space:

$$T = \frac{L_G}{L_E} \tag{2.25}$$

L_G is the geodesic distance (the length of the shortest path through the porous medium between the start and end points) and L_E the Euclidean distance (the length of a straight line) between the two points [49]. As demonstrated in the schematic of Figure 2.22, straight paths through a porous medium give a tortuosity of $T = 1$ whereas $T > 1$ for paths of greater curvature.

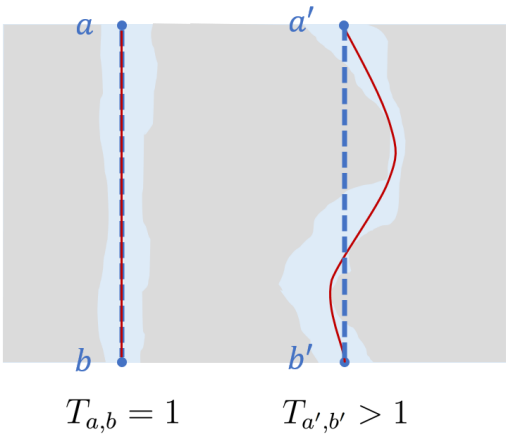

Fig. 2.22 Illustration of the geometric tortuosity as the ratio of the geodesic distance L_G (red lines) to the Euclidean distance L_E (blue dashed lines). The solid material is in grey and the pore space in blue.

By default, calculations of geometric tortuosity assume all available paths within the porous medium are equally viable. However, when considering the transport of multiphase fluids, certain narrower paths may become less favorable or even inaccessible due to the increased capillary pressure required for the objects to pass through these narrow gaps. To account for this, penalties can be applied to geometric tortuosity in relation to pore narrowness at all points along a given path [50]. The consequence of increasing the magnitude of this penalty is illustrated for a simple 2D pore structure in the schematic of Figure 2.23.

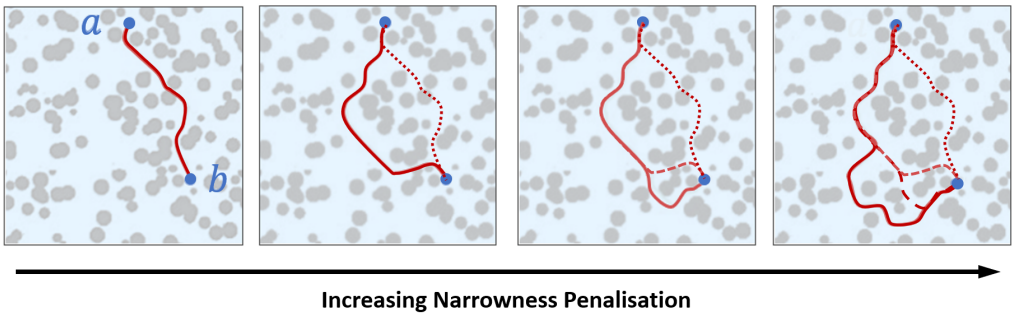

Fig. 2.23 Extension of the geometric tortuosity in a 2D pore structure from point ‘a’ to point ‘b’ by applying a narrowness penalty to the initial geodesic distance to account for narrowness between pores [51]. The solid material is in grey and the pore space in blue.

2.2.2 Microscopic Porous Media Parameters

Pore and Throat Sizes

Another crucial parameter of porous media is the size of individual pores and the distribution of pore sizes within a given medium. It's easy to envision that the flow in a single pore will have different properties (such as mean velocity and flow structure) compared to a collection of thousands of smaller pores with the same total cross-sectional area as the single pore. However, determining where one pore ends and the next begins can sometimes be a somewhat arbitrary task.

In general, an individual pore is defined as a portion of void space bounded by solid surfaces and planes erected at the locally narrowest points, which are referred to as the pore throats, as in Figure 2.24 [52]. The graph highlighting all of the possible paths between the pores through the pore network is also indicated.

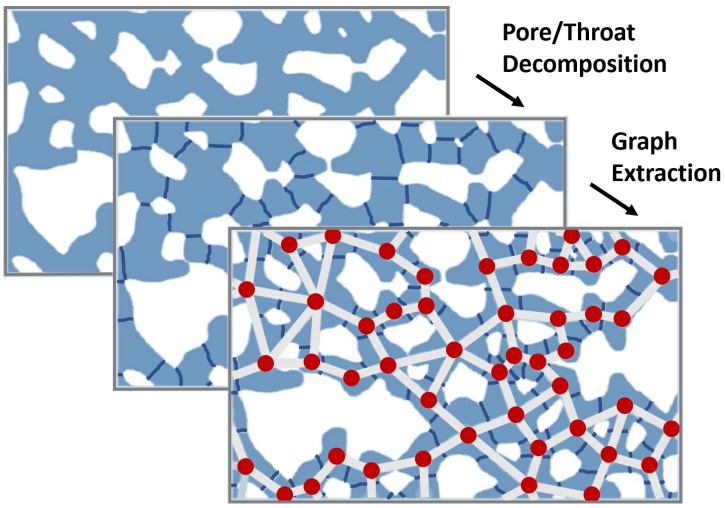

Fig. 2.24 Illustration of the delineation of an example pore space (blue) between a series of grains (white) with the pore throats indicated (dark blue lines). The pores can then be graphed to indicate their connectedness. Adapted from Yeates *et al.* [52].

2.2.3 Simple Permeability Models for Porous Media

As discussed earlier, the permeability of a porous medium is a critical parameter for understanding fluid flow structure and properties within it. Given the difficulty of obtaining permeability measures experimentally, many studies have aimed to produce simple models to estimate permeabilities based on the other aforementioned parameters.

System of Undulating Capillaries

In porous media bearing well-connected pores of relatively uniform cross-sections, the medium can be represented by a series of N undulating capillaries, each of diameter $2r$ and length L_G, as in Figure 2.25:

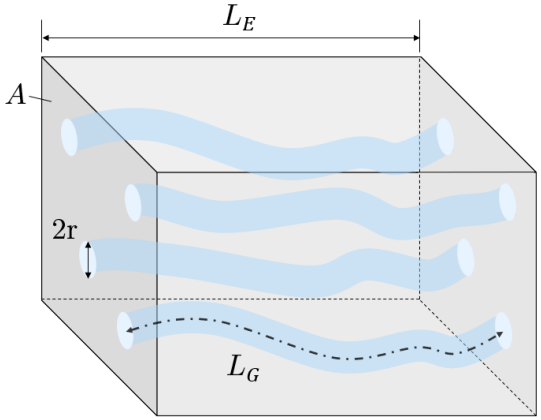

Fig. 2.25 Model of a porous medium in the form of undulating capillaries. Based on Guyon *et al.* [19]

The total flow rate per unit area can then be calculated using the Hagen-Poiseuille equation:

$$Q = N\delta Q = N\frac{\pi r^4}{8\eta}\frac{\Delta P}{L_G} \tag{2.26}$$

where δQ is the flow rate for a single cylindrical capillary and η the dynamic viscosity of the fluid. By substituting in Darcy's law (Equation 2.21) as well as the expressions for the porosity of this system $\phi = N(\pi r^2)L_c/(AL_E)$ and its tortuosity $T = L_G/L_E$, we get:

$$k = \frac{\phi r^2}{8T^2} \tag{2.27}$$

The influence of the throat size on fluid transport in porous media can be better understood by considering such a porous media. For a given porosity, Darcy's Law (Equation 2.21) and the Hagen-Poiseuille equation (Equation 2.26) can be used to determine that the permeability of this porous medium is proportional to the square of the capillary diameter, $(2r)^2$. Halving the capillary diameter whilst maintaining a constant porosity decreases the permeability by a factor of 4 [19].

Kozeny-Carmen Equation

Equation 2.27 requires the diameter of the pores to be estimated, something that is almost impossible to do without any ambiguity [19]. A widely used equation to predict the permeability of porous media, based on experimentally measurable physical quantities such as the porosity and the specific surface area S, was developed by Kozeny and later modified by Carman [53]:

$$k = c_0 \frac{\phi^3}{T^2 S^2} \tag{2.28}$$

where c_0 is a dimensionless constant depending on the channel geometry. The Kozeny-Carman equation or its many variants and extensions have been used for many different types of porous materials [54]. Carman proposed that for a wide-range of porosities, T^2 can be assumed constant ($\approx 5/2$), however it has since been shown that in low porosity media, T^2 can be as high as 50 [55].

2.3 Conclusion and Objectives

The objective of this research is to study the transport of emulsions in porous media. In particular, we seek to better understand how heterogeneities within the porous media, both in terms of their geometry or the wettability of the micromodel surfaces, influence the transport and stability of the emulsion.

In this chapter, we explored the fluid dynamics that arise at the pore-scale within porous media, with the small scales leading to laminar flows and a preponderance of surface effects. We have also presented the necessary tools to characterise the complexity of porous media, which is essential if we are to understand the flows that arise within them.

In our study, we follow a primarily experimental approach using microfluidic porous media devices, allowing for the creation of controlled and simplified porous media as well as excellent visualisation of the resulting emulsion flow *in situ*. We also benefit from existing microfluidic technologies that allow for precise control over the properties of the emulsion, such as the mean droplet diameter, the volume fraction of the droplets. With the emulsion formed on a separate microfluidic device, the properties of the emulsion are decoupled from its injection flow rate in the porous media. Therefore, we seek to assess the influence of the properties of the porous media and of the injected emulsion on the resulting transport, both through the analysis of the macroscopic transport behaviour and the pore-scale mechanisms influencing the emulsion's transport and stability.

Chapter 3

Droplet Transport in Simple Porous Media

3.1 Introduction

Many natural and industrial processes involve the transport of particle or droplet suspensions through networks of channels or obstacles. Examples include blood microflows, particle filtration, droplet microfluidics, subsurface CO_2 injection, and even road traffic or the transport of pedestrians through buildings and other public spaces. The resulting transport in these scenarios is significantly influenced by three key factors: the geometry of the medium, the nature of interactions between the particles, and the interactions between the particles and the network. As we will explore in this chapter, these three factors are in fact strongly interconnected.

Numerous studies have revealed the highly complex and collective behaviour that such systems can exhibit, even in simple geometries. An illustrative example is the experimental study conducted by Sugiyama *et al.*, which examined the formation of traffic jams on a simple circular road with no bottlenecks [56]. In droplet flows, there exists a multitude of interactions droplets can undergo between each other, including inter-droplet collisions, long-range hydrodynamic feedback, and local flow field perturbations [57–60].

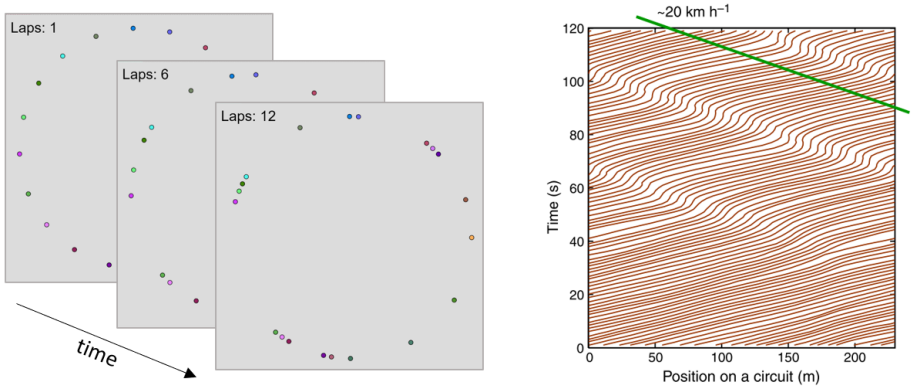

Fig. 3.1 The transport of cars around a circular loop, based on the work of Sugiyama *et al.* [56]. Despite all cars trying to respect the same speed of approximately 30 km/h, traffic jams form due to slight variations in speeds between cars resulting from user error. The simple model on the left, created by A. Averchi, illustrates this problem [61]. The spatiotemperal map on the right, created by Sugiyama *et al.*, highlights the presence of a traffic wave travelling at 20 km/h in the negative direction.

This chapter presents an experimental investigation in which a monodisperse water-in-oil emulsion is injected into the centre of a model porous medium. The porous media consist of a Hele-Shaw cell filled with cylindrical posts arranged in regular lattices, around which droplets must navigate. The size of the geometry is such that thousands of droplets can be present in the porous media at the same time.

We first present some of the literature on the transport of small numbers of droplets in simple geometries, ranging from single straight channels to small networks of interconnected channels. These studies enable a better understanding of the mechanisms governing droplet transport in porous media. We then examine studies of emulsion injection in more complex model porous media and utilise the previous findings to provide the most comprehensive explanation for the observed droplet transport. Following this, we present the results of our study on droplet transport in model porous media under both linear and radial injections, the latter having received limited attention in the literature. We systematically vary several of the most important parameters of the flow, such as the pore structure of the model porous media and the injection capillary number of the emulsion, as well as the size and volume fraction of the droplets in the injected emulsion.

In the case where the droplets diameters are much smaller than the channel height, $D \ll H$, the droplets act like tracers without perturbing the flow of the continuous phase, provided the Reynolds number is much less than 1 and droplet sedimentation or buoyancy is negligible [62, 63]. They are, therefore, assumed to flow at the local velocity of the carrier fluid, meaning droplets nearer the channel centreline will flow faster than those close to the edges. For such flows in more complex geometries, the droplets also tend to follow the streamlines of the external phase, which, therefore, dictates the path they adopt through the geometry.

When $D \approx H$ or $D > H$, droplets are confined within the channel walls, and the flow is strongly modified by capillary effects and the deformability of droplet interfaces. We primarily focus on this case, presenting three hydrodynamic properties that govern confined droplet transport: the pressure drop that arises across droplets, the dipolar perturbations induced by droplets on the flow field of the continuous phase, and the capillary pressure. We present each of the three properties individually and discuss some of the ways they can impact droplet transport in porous media.

3.1.1 Droplet Generated Pressure Drops

In most real porous media, there exist almost infinite interwoven paths for droplets to travel through. Every time a droplet arrives at an intersection between two or more channels, it must decide which path to flow into. Numerous micromodel studies have demonstrated that a droplet arriving at a junction of two diverging paths will choose the path of lower hydrodynamic resistance, i.e., the one through which the continuous phase flows the quickest, as demonstrated previously in Figure 3.2 [58, 63–65]. The simplest example of this is an asymmetric loop consisting of two channels of constant cross-section but of different lengths, as depicted in Figure 3.2. In this geometry, and in the absence of other droplets in the loop, a droplet will always choose to travel through the shorter branch since it has a lower hydrodynamic resistance than the longer one.

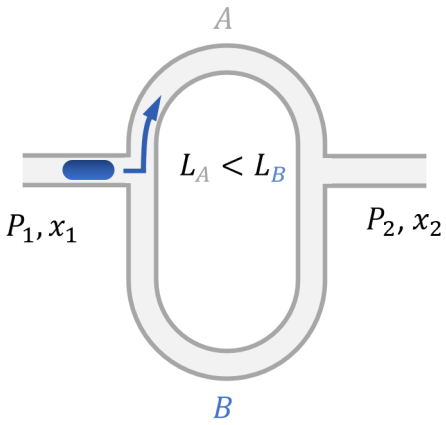

Fig. 3.2 Asymmetric loop of channels of equal cross section and of lengths L_A and L_B. When otherwise void of droplets, an incoming droplet (in blue) will always flow through the shorter of the two branches, in this chase branch 'A'.

However, the presence of droplets under confinement in a channel increases the hydrodynamic resistance of the channel in which they flow. This excess resistance can be very significant: Jakiela *et al.* reported that for a water-in-oil droplet flowing under confinement in a microfluidic channel, an 80% increase in pressure than that needed for oil alone had to be applied in order to obtain the same flow rate, despite the water having a viscosity three-times lower than the oil phase [66]. This can be understood by considering Figure 3.3a. The pressure drop across each of the channels in the figure is the same ($\Delta P = P_2 - P_1$). In the channel containing droplets, however, a significant portion of the pressure drop is concentrated across the individual droplets. The pressure drops across the remaining sections of the continuous phase are lower

than in the channel without droplets, and the corresponding flow rate through the channel containing droplets is reduced by the presence of the droplets.

Droplets, therefore, reduce the conductivity of channels in which they flow. For $n(t)$ identical droplets at time t in a channel of constant cross-section:

$$R(t) = R_0 + n(t) \times R_d \tag{3.1}$$

where $R(t)$ is the hydrodynamic resistance of the channel containing $n(t)$ droplets, R_0 is the hydrodynamic resistance of the channel void of droplets, and R_d is the contribution of a droplet to the total resistance. An interesting consequence of this hydrodynamic resistance is shown in Figure 3.3b: the presence of the droplets in branch A elevates the resistance of the branch such that the subsequent droplet preferentially enters branch B, now of lower instantaneous resistance than branch A. This can also be thought of as the droplets increasing the effective length of branch A to $L'_A > L_B > L_A$.

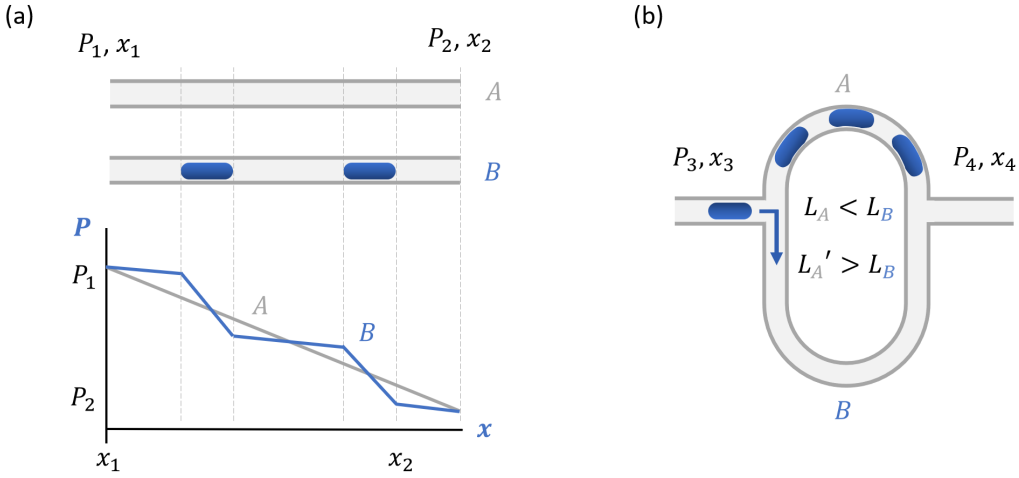

Fig. 3.3 Influence of the pressure drop induced by confined droplets flowing from left to right in a channel network on the transport of droplet trains. (a) Qualitative plot of the pressure along a microchannel containing confined droplets. Adapted from Champagne *et al.* [67]. (b) As a result of the increased hydrodynamic resistance in branch A, subsequent drops may flow instead into branch B. This can be conceptualised as the effective length of branch A having increased such that $L'_A > L_B$.

Even in a simple, asymmetrical loop as in Figure 3.3b the dynamics are highly complicated, with intricate dependencies on initial states and system parameters such

as the capillary number, the spacing between droplets, the solubility of the surfactants, and the lengths of the branches of the loop [64, 68–72].

The pressure drop induced by individual droplets or bubbles was studied by Bretherton, who considered non-wetting bubbles for which a thin film of the carrier phase is present between the bubble and the channel walls [73]. He studied large bubbles fully confined in circular capillaries, and in the absence of surfactant, at Re, Ca, and $Bo \ll 1$. By applying a lubrication analysis to the thin films, he arrived at a prediction for the thickness of the films, h:

$$\frac{h}{H} = 0.67\, Ca^{2/3} \tag{3.2}$$

where H is the diameter of the circular tube. This non-linear variability in film thickness has been shown to have a significant impact on the pressure drop induced across the droplet, commonly referred to as the Bretherton pressure drop, ΔP_{Breth}, where:

$$\Delta P_{Breth} = 4.94\, \frac{2\gamma}{H}\, Ca^{2/3} \tag{3.3}$$

Bretherton's scaling law has subsequently been adapted to account for trains of multiple bubbles [74], viscous drops as opposed to air bubbles [75], and surfactant effects [76]. Wong *et al.* also extended Bretherton's analysis to channels of polygonal cross-section, a far more common geometry in microfluidics given the fabrication techniques used most often [77, 78]. In such geometries surface tension, which tends towards a spherical droplet shape, prevents the droplet from perfectly filling the channel cross-section, leading to the formation of gutters as shown in Figure 3.4. Wong *et al.* also showed that for $Ca > 10^{-6}$ the pressure difference induced by the flow of each bubble or droplet in a rectangular channel remains proportional to $Ca^{2/3}$ with no collective effects arising between droplets. For $Ca < 10^{-6}$, however, the flow of the carrier phase through the gutters dominates and pressure difference induced by each individual droplet increases, becoming proportional to Ca.

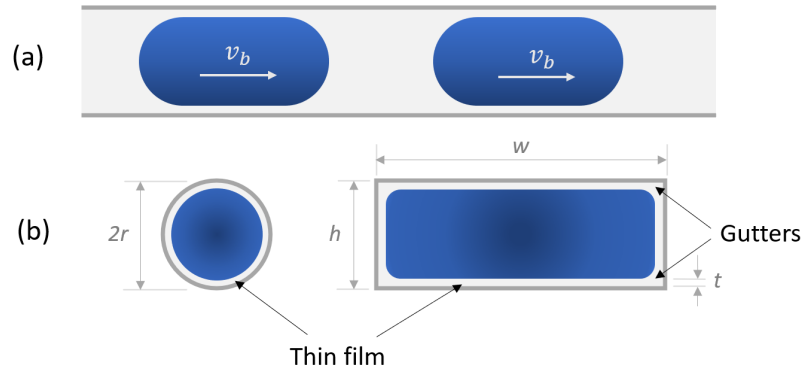

Fig. 3.4 Longitudinal (top) and cross-section (bottom) view of the transport of confined droplets in channels.

Many studies have tried to better understand the additional pressure drop induced by a single droplet in a microfluidic channel, equivalent to the hydrodynamic resistance of the droplet. Several studies have shown that the pressure drop induced by a single droplet greatly depends on a number of parameters, such as the degree of confinement of the droplet, the geometry of the channel, the viscosities of the two phases, as well as the nature and concentration of surfactant used [66, 76, 79, 80]. Furthermore, it has been shown numerically that pressure drop is not dependent on the viscous dissipation within the droplets for $Ca \ll (\eta_d/\eta_c)^{-2/3}$ [81]. However, there is still no consensus on the exact pressure drop associated to the presence of a droplet and this is still an active area of research [81–83]. Whilst it is difficult to establish generic laws to predict the pressure-drops induced by a droplet, we can at least say that the pressure drop increases with the droplet velocity.

In addition to the channel networks discussed previously, Moon *et al.* studied droplet transport through a tertiary junction, presenting three possible downstream channels for the droplet to choose, as shown in Figure 3.5. They found a dependence of the path chosen by the droplet on the capillary number of the flow [84]. At $Ca = 0.1$ and $Ca = 0.05$ the droplet followed the path of greatest flow rate (44 % inlet flow rate), whilst at $Ca = 0.025$ the droplet continued straight on along the path of lowest tortuosity, despite the lower flow rate in this path (14 % inlet flow rate). They suggested that the weaker deformability of droplets at low Ca as the interfacial tension dominates as well as the thinner Bretherton film (Equation 3.2) at lower Ca make droplets less sensitive to the flow rate disparity and more likely to choose the straightest path

through a junction in the channel network.

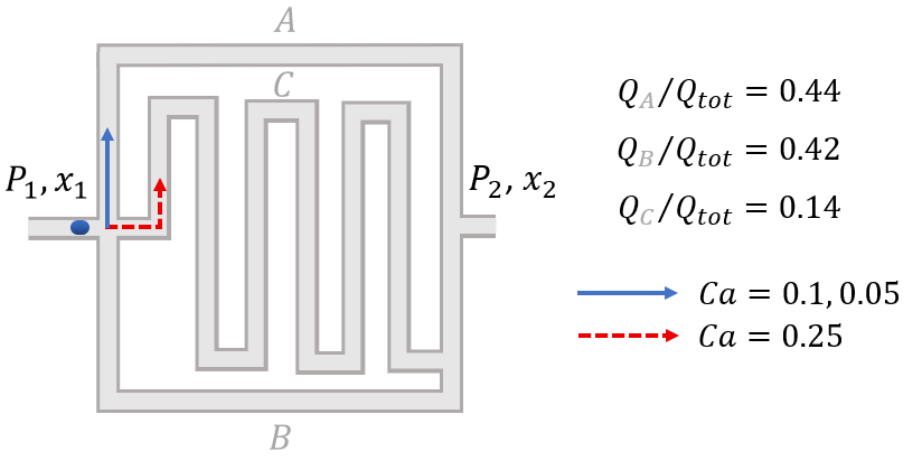

Fig. 3.5 Schematic from the study of Moon *et al.* on tertiary junctions at various injection capillary numbers [84]

Other interactions between droplets, such as collisions at the entrance to the loop, can also strongly influence the resulting path selection of the droplets, as shown in Figure 3.6 where the second droplet turns left as a consequence of the collision at the T-junction, regardless of the resistances of the channels downstream [69, 85, 86].

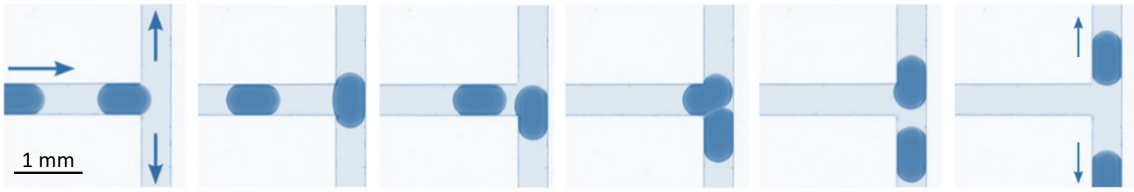

Fig. 3.6 Example of droplet collisions governing transport at a T-junction. The second droplet travels to the right as a consequence of the collision at the T-junction, regardless of the resistances of the channels downstream. Experimental images were taken with a constant time interval of 1/12 s. Adapted from Cybulski *et al.* [69].

When a large number of droplets simultaneously traverse these channel networks they in fact tend to distribute themselves among the various branches or paths in approximately the same ratio as that for the flow rate of a simple Newtonian fluid void of droplets [63]. However, in more realistic porous media with paths of varying widths, this also depends on the size of the droplets with respect to the average pore

spacing lengths L and their volume fraction V_v. For instance, Quennouz *et al.* studied a comb-type network of channels bearing two permeabilities in which a Newtonian fluid flows preferentially in the larger, central channel. When a foam is injected it initially does the same, but the accumulation of bubbles in the central leads to a large enough hydrodynamic resistance that the subsequently injected foam flows preferentially in the narrower, side channels [57]. At higher volume fractions (higher P_{gas}/P_{water} in the graph), the distribution of flow rates returned to that of a Newtonian fluid (dashed horizontal line).

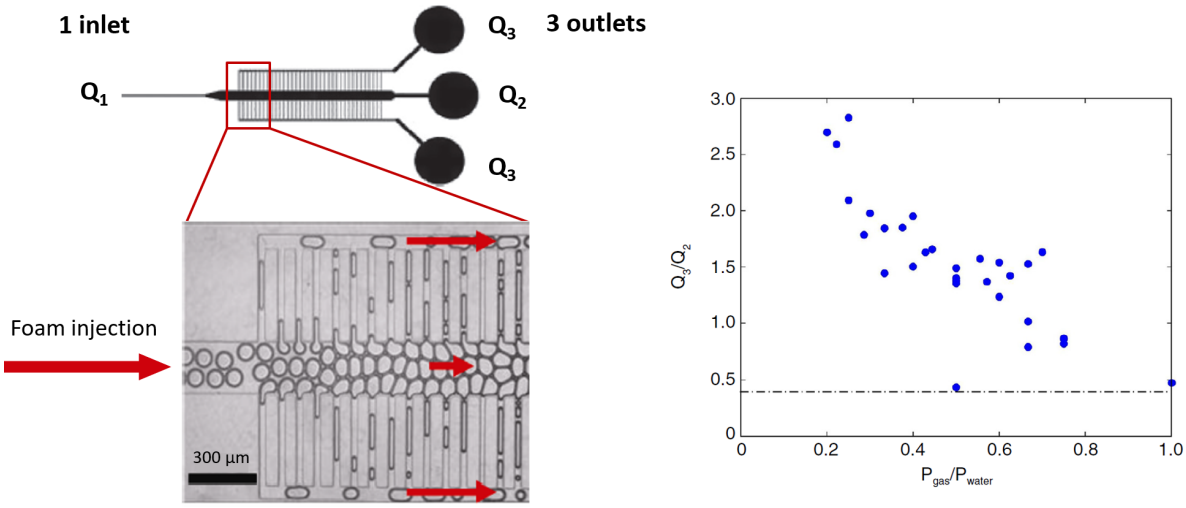

Fig. 3.7 Comb-type network of channels bearing two permeabilities. A Newtonian fluid flows preferentially in the larger, central channel but under foam injection the bubbles accumulate in the central channel, creating a large resistance. Subsequent bubbles, therefore, flow preferentially through the small side channels. The influence of the gas volume fraction on the foam diversion was also studied, as in the graph on the right. The dashed line represents the result for a Newtonian fluid measured using Particle Image Velocimetry (PIV). Adapted from Quennouz *et al.* [57].

3.1.2 Droplet Dipolar Perturbations

When a droplet flows through a microfluidic channel at $Re \ll 1$ and in which it is confined in one direction, the droplet modifies the velocity field of the continuous phase surrounding it, as in Figure 3.8a. The resulting dipolar flow field can lead to interactions between neighbouring droplets without them coming into contact with one another, as demonstrated by Beatus *et al.* for an initially 1D stream of droplets in

a straight microfluidic channel in Figure 3.8b [87].

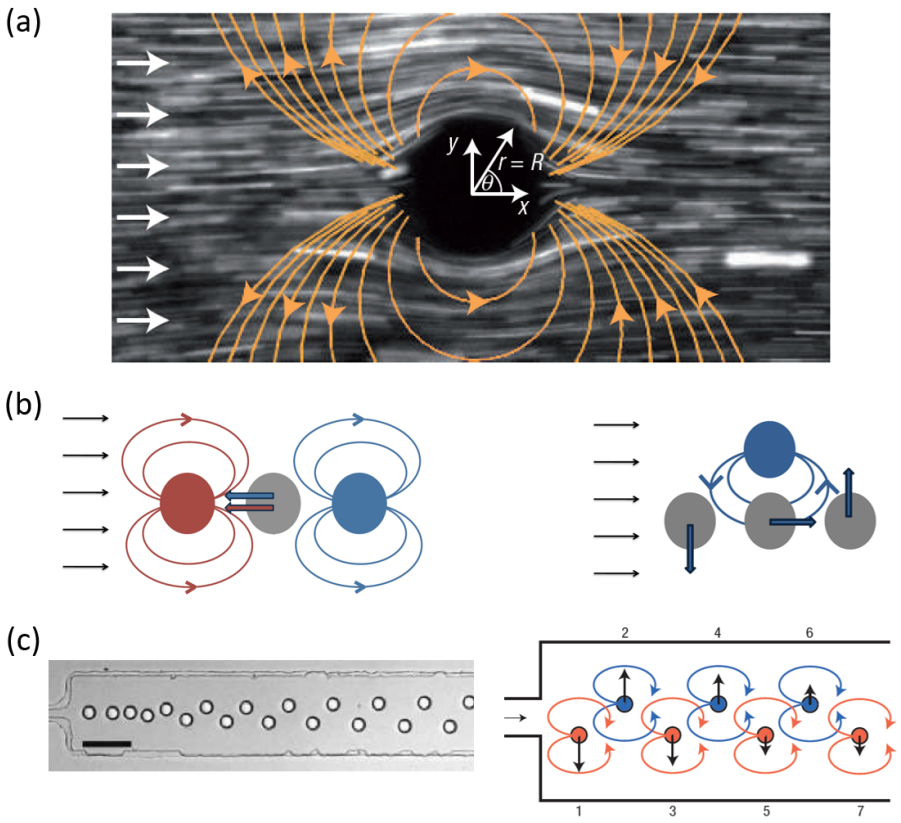

Fig. 3.8 Flow and hydrodynamic interactions between droplets. (a) Dipolar perturbation of the flow field by a confined particle in orange (adapted from Beatus *et al.* [87]). (b) Interactions between neighbouring droplets as a result of the dipole (adapted from Champagne *et al.* [67]). (c) Example of droplet transport perturbations in a simple channel (adapted from Beatus *et al.* [87]). Scale bar is 100 µm

Champagne *et al.* later studied the transport of an initially 1D stream of droplets injected in a square lattice of posts at $Ca \ll 1$. For low droplet concentrations (large separation between droplets) droplets all followed the shortest path straight through the lattice of posts (Figure 3.9a). By gradually increasing droplet concentration, droplets began to displace themselves laterally and invade more of the porous media. This diversion was largely attributed to the dipolar droplet perturbations as initially droplet spacing was sufficiently large such that collisions between droplets didn't occur. The behaviour was intermittent and cyclic, with a critical concentration of droplets following the central, straight path through the posts of 0.7 droplets/second being established.

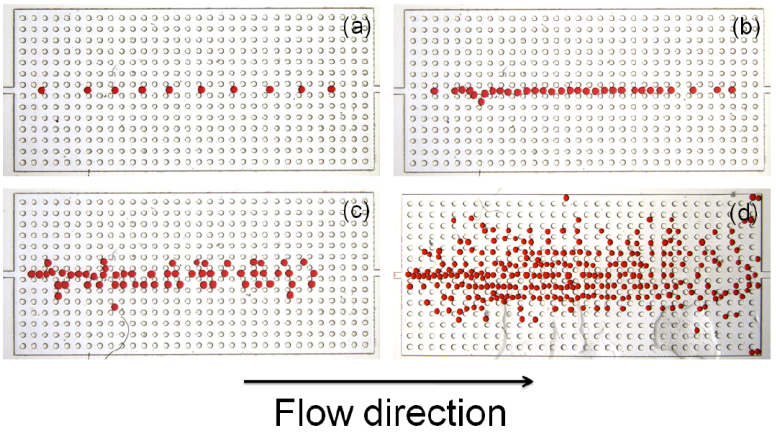

Fig. 3.9 Water droplets in hexadecane oil flowing through a square lattice of cylindrical obstacles for increasing concentrations of injected droplets (a-d). Length of the network: 9.75 mm. From Champagne *et al.* [59].

3.1.3 Capillary Pressure

In real porous media it is unlikely that the channels will be straight with uniform cross-section. Many studies have considered the flow of a droplet through a constriction in a channel, as in Figure 3.10 [88–95]. Droplets larger than the constriction must deform in order to pass through it, increasing their surface area and acting against the interfacial tension. As a result, the capillary pressure at the front of the drop is higher than that at the rear. An additional pressure drop must be applied across the constriction for the droplet to pass through it, otherwise the droplet remains trapped at the constriction entrance. This additional pressure drop is equal to the difference in the capillary pressures at the front and the rear of the droplet, $P_c = \gamma(1/H + 2/W)$, where H is the channel height and W the width of the channel constriction.

Pressure drop relationships have also been derived for channels with sinusoidal perturbations, forming a series of constrictions and providing a better approximation of the flow in real porous capillaries [96–98]. Mauray *et al.* observed that Bretherton's relation in Equation 3.3 remained valid at all Ca in channels with small constrictions where $W_{max}/W_{min} = 1.5$. For channels with larger constrictions such that $W_{max}/W_{min} = 4$ two regimes arise: the Bretherton relation is valid for $Ca > 10^{-4}$ but at $Ca < 10^{-4}$ droplet velocities become intermittent and the pressure drop remains constant, proportional to the capillary pressure P_c. It is clear, then, that Bretherton's law cannot be easily applied to more complex geometries at low capillary numbers.

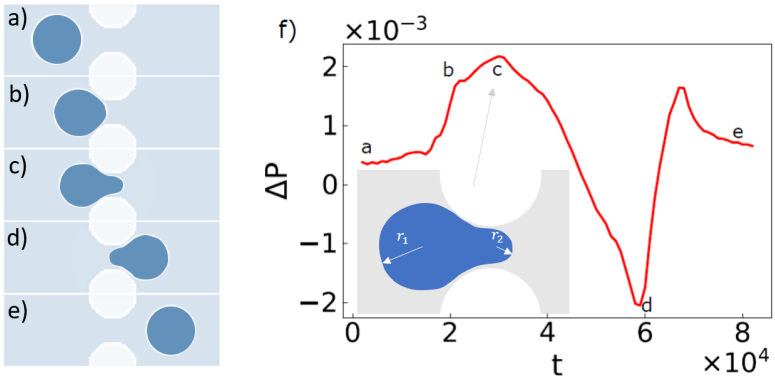

Fig. 3.10 Snapshots from a Lattice Boltzmann simulation of a droplet passing through a constriction and the pressure drop this induces. The insert in the bottom-left of the graph highlights the difference in curvature at the front and rear of the drop, corresponding to snapshot (c). Adapted from Coelho *et al.* [60]

Additionally, when one or several droplets are trapped at a constriction in a porous medium, this effectively decreases the porosity of the medium and thus increases the average bubble interstitial velocities elsewhere. Coelho *et al.* showed numerically how this increase in interstitial velocity through the unblocked pores can provide subsequent droplets with the increase in Ca required to deform and pass through pores they otherwise would have been trapped, as depicted in Figure 3.11 [60]. The resulting flows are often highly intermittent as a result [99–101].

Fig. 3.11 Schematic of a numerical image series of two droplets passing through a geometry consisting of two pores. Adapted from Coelho *et al.* [60].

3.1.4 Studies in Model Porous Media

Many studies have tried to establish links between the microstructure of more complex porous media and the transport of droplets or bubbles. For instance, Nguyen *et al.* used X-ray tomography on a core-study to highlight the presence of preferential flow paths for injected foams [102]. Several experimental studies using 2D transparent porous media showed that these preferential paths tend to arise in areas where several

large pores, relative to the average pore size, are connected to one another, representing high permeability paths, equal to the paths of lowest resistance [99–101]. Yeates *et al.* also employed a graph-based model to predict the location of these preferential flow paths. They found a strong dependence on pore diameter and the tortuosity of the flow paths at high capillary numbers, whilst at low capillary numbers foam transport was uniquely modeled by the pore diameter.

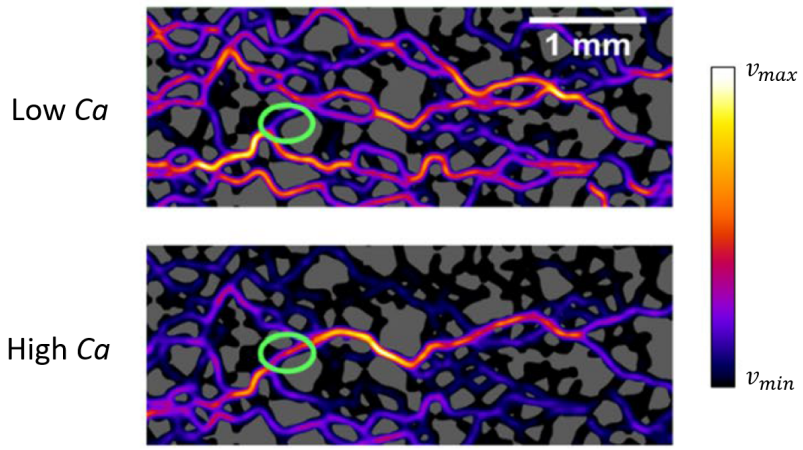

Fig. 3.12 Comparison of flow maps for foam injection in a model porous media, adapted from Yeates *et al.* [52]. Low Ca corresponds to an injection flow rate of 8.9×10^{-3} cm^3/min whilst the high Ca injection was at 2.5×10^{-2} cm^3/min. Considering the region of interest (green circle), at low Ca the preferential flow paths can be determined purely by throat size and bubbles perform an almost 180° turn. However, at high Ca the tortuosity also plays a significant role with the foam preferentially following the straightest path (lowest tortuosity) possible.

3.2 Materials and Methods

We study the transport of an initially monodisperse emulsion in model porous media: transparent, quasi-2D microfluidic flow cells containing series of cylindrical posts of constant radius. An experimental procedure allowing for fine tuning of the size and volume fraction of the droplets in the emulsion was developed using a microfluidic droplet generator. The pre-formed emulsion could then be injected into the microfluidic porous media at the controlled capillary number as determined by the total injection flow rate.

In this section, the microfluidic devices will first be described, together with the fabrication methods and some characterisations. The fluids studied and the experimental procedure for the preparation and injection of the emulsions is then presented. Finally, the data analysis methods used for the results of this chapter and Chapter 3 are discussed.

3.2.1 Fabrication of Microfluidic Devices

The microfabrication process can be divided into two main steps, the first of which involves creating a mould of the desired geometry on a silicon wafer. After the mould has been made, it can be used to prepare hundreds of PDMS micromodels across its lifespan. The second step encompasses the process for fabricating a new PDMS micromodel with the desired geometry using the mould from the first step.

Preparing the Mould

Silicon wafers are ideally suited for this application as they are smooth on an atomic scale, hence their abundant use in the microelectronics industry. A two-dimensional projection of the geometry is first designed and printed on to a transparency. All designs in this thesis were done using the CleWin5 design software from WieWeb. A silicon wafer is then spin coated with a layer of UV-sensitive resin, typically SU-8, of uniform thickness (50 ± 5 µm in this study). By exposing the wafer to UV light through the transparency, the design on the transparency can be imparted onto the wafer. As SU-8 is a negative resin only the areas exposed to UV radiation are reticulated, and the rest can be washed away in a chemical bath, typically consisting of PGMEA (Propylene glycol methyl ether acetate). We are then left with an extruded negative of

the 2D motif in solid resin. This step is summarised visually in Figure 3.13 for the fabrication of a simple microchannel bearing one inlet and one outlet. At this point the mould can optionally be silanised using FDTS (perfluorodecyltrichlorosilane) to facilitate the removal of the reticulated PDMS during the next step.

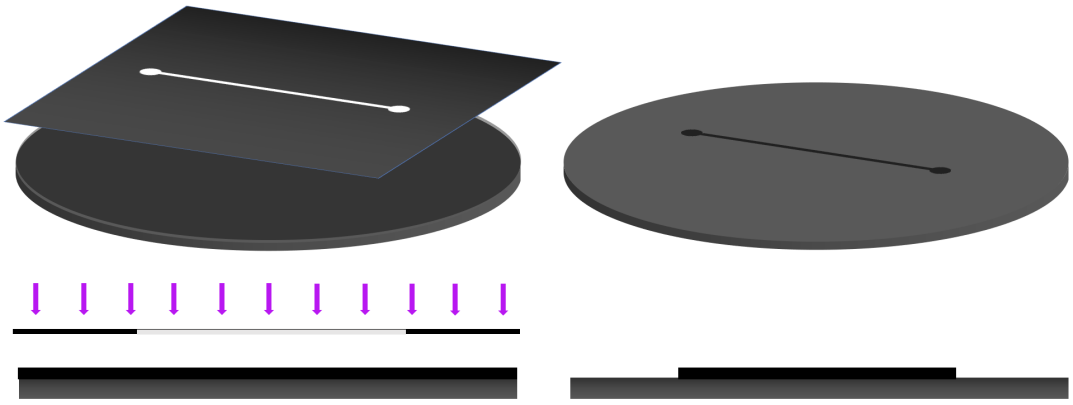

Fig. 3.13 Preparing the mould. Left: Silicon wafer spin coated with a negative resin and exposed to parallel UV rays through an opaque mask with transparent regions bearing the desired geometry. Right: After development, all non-reticulated resin is removed and the geometry of the masque has been transferred to the wafer. Dimensions are not to scale.

Preparing the mould is the most delicate of the two steps, requiring access to equipment that is not available in many laboratories. For instance, for precise reproduction of the micrometric geometries the transparency must be of excellent resolution, generally 50800 dpi or higher, often requiring specialist printing equipment. Additionally, since dust and other such particles commonly found in the air are of the micrometric scale, great care should be taken during this step to avoid polluting the micropatterns imprinted on the silicon wafer - a single strand of dust adhered to your geometry could be enough to block an entire channel. The various processes required to fabricate the mould; generally spin coating, baking, UV exposition, and chemical revelation; should be undertaken in a clean room. Nevertheless, production of the transparency and the mould can readily be outsourced if required, as was generally done for this study.

Preparing the Micromodel

First, liquid PDMS is mixed with a reticulating agent (Sylgard 184 Silicon Elastomer Kit, ratio 9:1 respectively) and degassed using a vacuum pump. The mould is placed in

a petri dish or tin-foil basket where the PDMS mix is poured over, degassed once more, and cured at 60°C for approximately one hour. Once stiffened, the micropatterned disk of PDMS can be slowly removed from the mould and cut to shape, leaving an embossed area bearing the desired geometry (cf. Figure 3.17 for an example micropatterned PDMS disk). The inlet and outlet holes are then punched to allow the fluid-carrying tubing to be inserted. Opting for tubes of external diameter slightly larger than the diameter of the hole punched means they are held in place purely by the elasticity of the PDMS with no need for external fixations. This makes using the micromodel more practical as tubing can be swapped between various systems with ease.

The microsystem can then be closed by preparing a second petri dish with the same mix of PDMS, forming a thickness of approximately 2 mm to minimise possible PDMS deformation. This second batch of PDMS is then left placed in an oven at 60°C until it is nearly fully reticulated. It should be tacky when touched, but not leave a fingerprint. The micro-patterned PDMS disk can then be gently positioned face down on top of the partially reticulated PDMS before allowing the whole to reticulate fully. By adhering the micropatterned surface face-down to a flat surface we are left with a network of channels around the cylindrical posts through which fluid can flow. This second step is shown in Figure 3.14. The resulting flow cell has channels of uniform height, equal to the depth of SU-8 resin on the wafer used, and is entirely hydrophobic as measured by a contact angle of 110°.

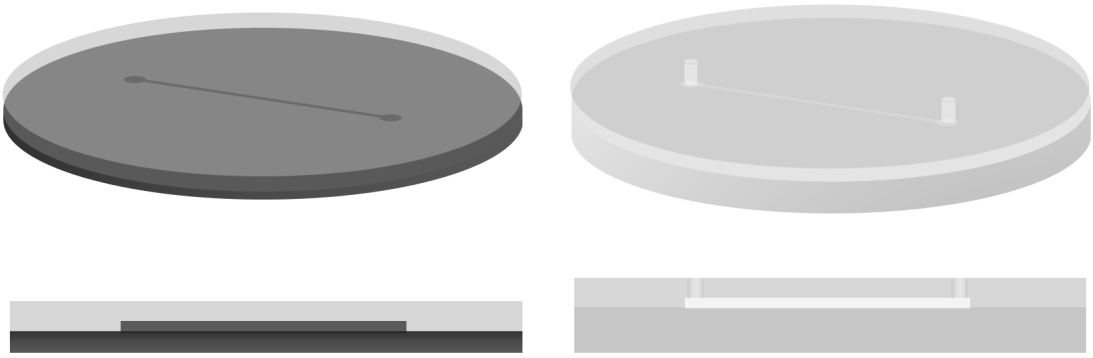

Fig. 3.14 Preparing a PDMS micromodel from the mould in Figure 3.13. Left: Liquid PDMS and reticulating agent are poured over the mould. Right: Once reticulated, the PDMS is removed from the mould, holes are punched for fluid inlet and outlet, and the micro-patterned PDMS disk is positioned on a second, partially reticulated body of PDMS. Dimensions are not to scale.

For some micromodels, such as the majority of the droplet generators discussed next, this latter stage varied slightly. The micropatterned PDMS body was instead plasma bonded to a glass slide which is easier to manipulate under a microscope. When a water-in-oil emulsion being studied, any plasma bonded devices were left for a minimum of 12 hours to return to their original hydrophobic state. Otherwise, if an oil-in-water emulsion was being considered, the channels were immediately filled with the continuous water phase following plasma bonding and experiments were performed within 10 minutes of the bonding.

3.2.2 Microfluidic Devices

Droplet Generation Devices

Emulsions were generated using microfluidic devices consisting of a flow-focusing geometry [103]. An example device, consisting of a PDMS body attached to a glass slide, is shown in Figure 3.15.

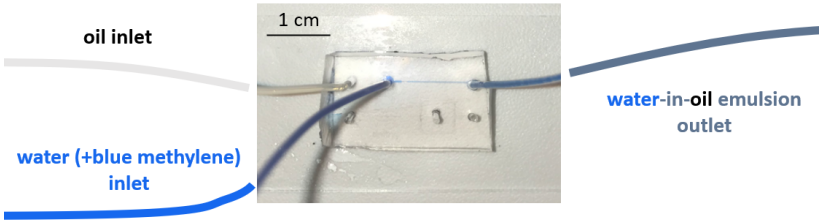

Fig. 3.15 Example of a microfluidic droplet generator.

In addition to ensuring the monodispersity of droplet sizes, it was important to have maximum versatility in the size and volume fraction of the produced droplets. To do so, several designs of varied dimensions, such as the height of the channels ($20 \leqslant H_{dg} \leqslant 100$ µm) or the width of the flow-focusing channel constriction ($30 \leqslant w_{dg} \leqslant 50$ µm), were employed. Later designs also included a comb-like system of channels to add or remove the continuous phase for additional control [86]. The addition of filters downstream of all injection points reduced the likelihood of blockages caused by microscopic dust particles or stray pieces of PDMS detached during the boring of the holes to insert the tubing, as demonstrated by Salkin *et al.* and illustrated in Figure 3.16 [104].

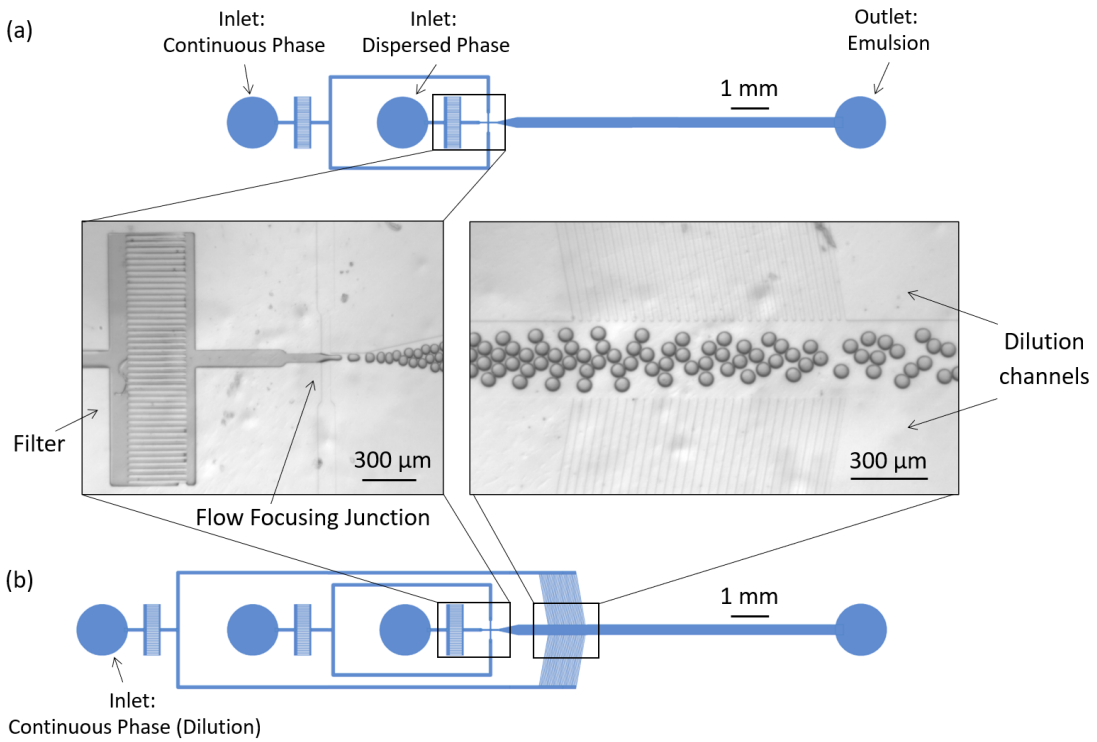

Fig. 3.16 Design of two microfluidic droplet generation devices (blue schematics) used in this study, as seen from above. (a) Device with two fluid inlets (left) and one fluid outlet (right). (b) Same device as in (a) but with a system of channels to dilute or concentrate the droplets by adding or removing the continuous phase respectively. For this, an additional continuous phase inlet was added to the far left of the geometry.

Model Porous Media

Model porous media can bear a variety of structures, from simple networks of channels of constant cross-section to real rock morphologies obtained from X-ray tomography [105]. In this study we employ simplified porous structures, enabling us to finely control the numerous parameters of the porous media. For instance, using morphological models we can quickly create several geometries of varying minimum pore size whilst keeping the porosity or other geometric parameters constant across them all, as done in this work [106]. The aim of this approach is to separate the behaviour of the dispersion from the morphology of each medium.

All geometries feature cylindrical posts 50 µm in diameter. These posts were arranged in several regular lattices (hexagonal, square, and rectangular) or randomly. For all the regular lattice geometries the porosity is kept constant at 0.60 by varying the inter-post spacing, L. For the random geometries, methods based on stochastic

placements of the cylindrical posts were employed. The positions of the posts were chosen according to probabilistic rules, which are discussed in greater detail in Appendix C. One geometry where posts were allowed to overlap one another was created, resulting in a porosity of 0.64. A series of geometries preventing post overlap were also created by varying the minimal post separation distance, L, whilst keeping the porosity as close to 0.6 as possible. The actual porosities for the non-overlapping geometries, included in Figure 3.18, ranged from 0.6 - 0.64.

A pair of scanning electron microscope (SEM) images of an example micropatterned PDMS surface are shown in Figure 3.17. The properties of all the lattice geometries considered are shown in Figure 3.18.

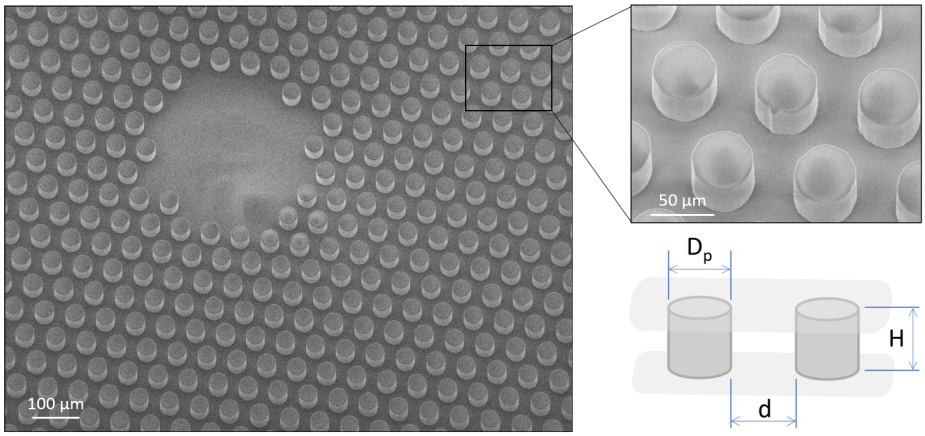

Fig. 3.17 SEM images of a micropatterned PDMS surface bearing a hexagonal lattice of posts. All posts are 50 µm in diameter, D_p, and in height, H. The channel network through which the fluids can flow is created by adhering this patterned surface to a second, flat surface.

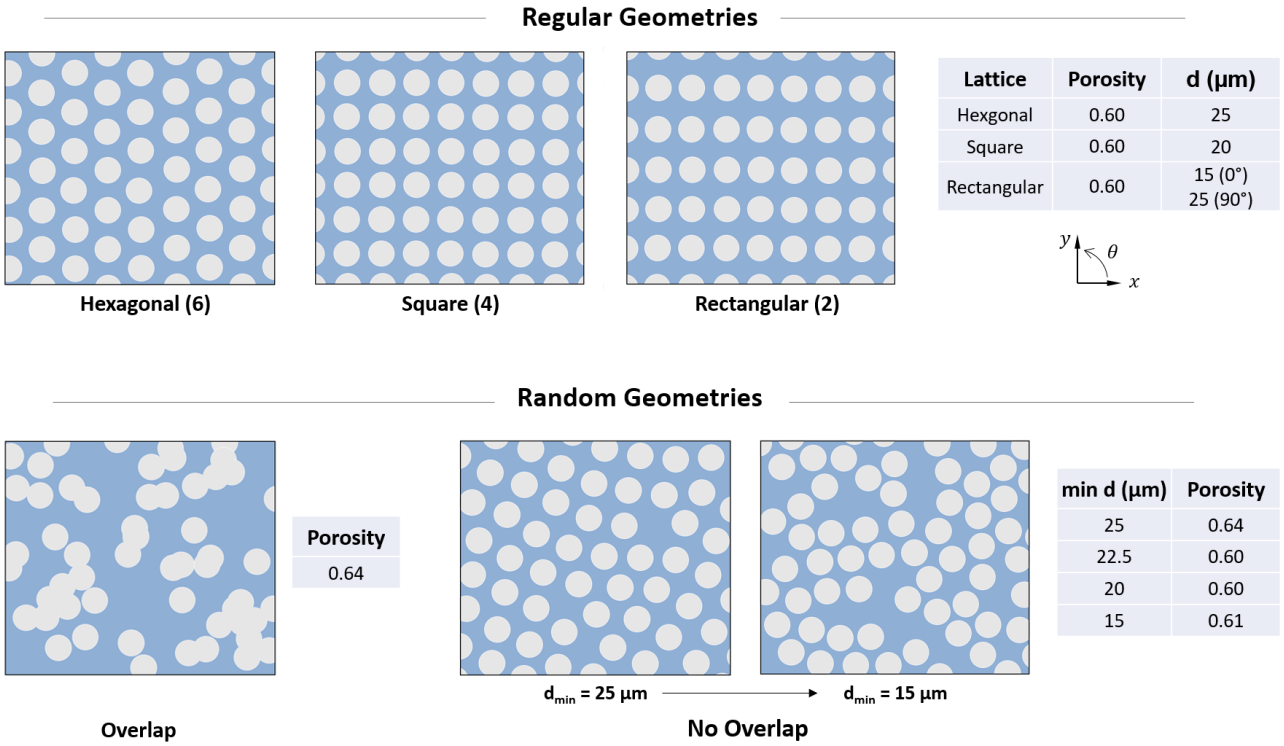

Fig. 3.18 Lattice geometries of the model porous media studied. All posts have a diameter of 50 µm. The number of planes of symmetry of each of the regular geometries are indicated in parentheses.

In addition to varying the lattice structures, several geometries of model porous media were considered, allowing both linear and radial flows to be studied, the latter being the primary interest of this study.

In the case of radial flows, our initial tests were performed on micromodels consisting of a 10x10 mm square porous region. For further radial injections we designed a circular porous region that is 13 mm in diameter, $2R$, and contains approximately 25000 posts. The porous region is surrounded by a circular exit channel of width 300 µm for more homogeneous fluid drainage. A straight observation channel of width 300 µm and length 20 mm was also added. Inlet and exit ports were bored using a 1 mm external diameter syringe, with the inlet positioned at the centre of the porous region and the exit at the end of the straight channel. The posts at the centre of the porous region were omitted to provide a visual aid whilst boring the inlet, as visible on the left of Figure 3.17.

One might wonder what influence the position of the single exit channel could have on the flow within the porous medium. By modeling half of the surrounding circular channel as a rectangular channel of length πR and cross-section 300 x 50 µm, we can compare the resistance of this channel to that of a 30° angular section of the porous region, as shown in Figure 3.19. The resistance of the rectangular channel can be determined using Equation 2.8 whilst that of the angular section can be calculated using Darcy's law in angular coordinates from Equation 3.18 and the permeability measurements of the porous region discussed in Appendix A. We find that both sections have a resistance on the order of 1×10^{14} Pa.s/m^3. We can deduce that flowing from the centre straight to the exit channel presents half of the hydrodynamic resistance as if the fluid travels in the opposite direction from the channel before exiting via the circular channel. We further discuss the impact this can have on droplet transports in Section 3.3.2.

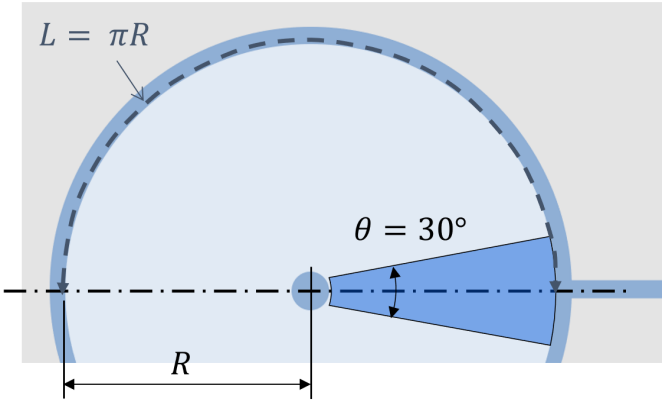

Fig. 3.19 Schematic of the radial porous media for assessing the impact of the position of the straight outlet channel on the flow within the porous medium. The resistance of the 30° angular section is found to be on the same order of magnitude as a rectangular channel of length $L = \pi R$ where $R = 6.5$ mm such that $R_h = 1 \times 10^{14}$ Pa.s/m^3.

The linear geometries consisted mainly of a rectangular porous region of length of 12 mm, approximately equal to the diameter of the circular porous region in the radial geometries, and width 3.6 mm. At either extremity of the porous region is an additional space of length 0.3 mm to allow the dispersion to enter the lattice of posts evenly across the width. The two rectangular channels are 20 mm in length, the same length as the exit channel of the radial geometries. The various microfluidic patterns are shown in Figure 3.18.

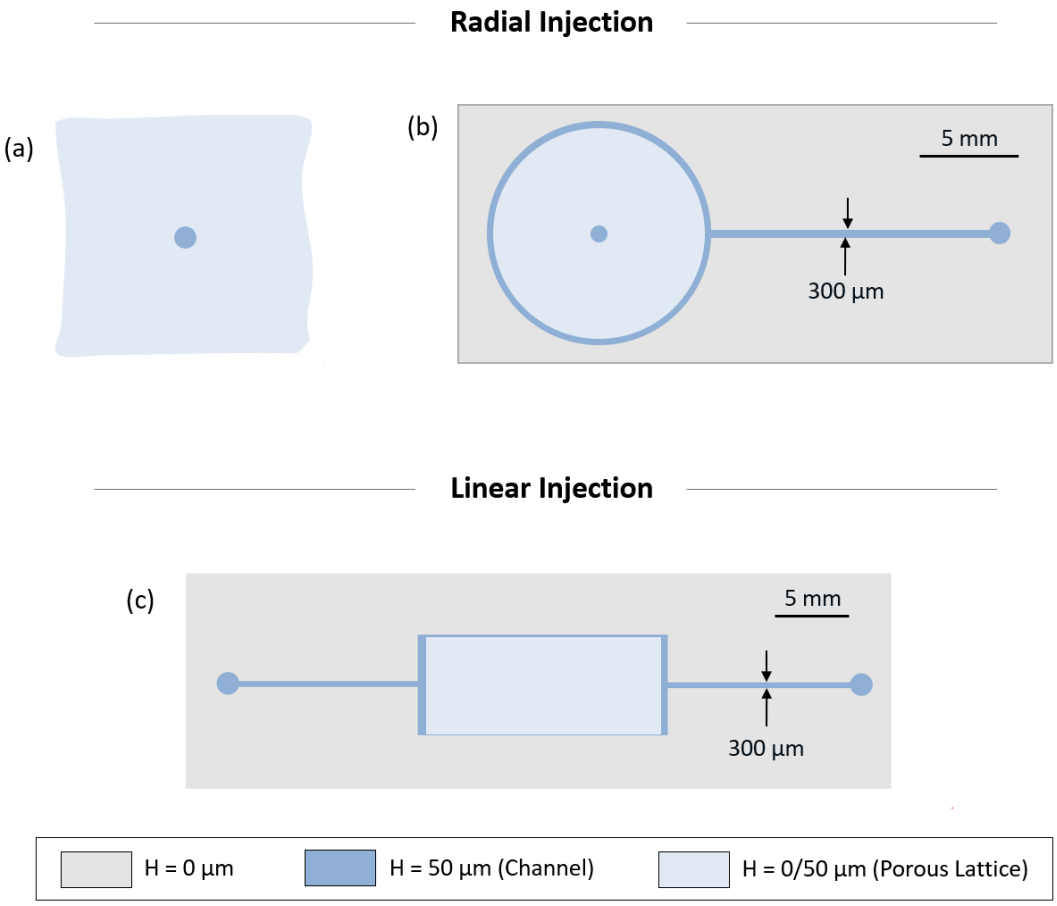

Fig. 3.20 Example geometries of the model porous media for both radial and linear injections. (a) consists purely of a porous region whilst (b) has a circular channel surrounding the porous region as well as an exit channel. (c) has a straight entrance and exit channel either side of the porous region.

3.2.3 Fluids Studied

This study focused on the injection in porous media of emulsions - dispersions of two immiscible liquid phases. Given the natural hydrophobicity of PDMS, the primary dispersion for this study was a water-in-oil emulsion - droplets of distilled water in a carrier phase of high-purity mineral oil (Alfa Aesar, dynamic viscosity 18 mPa.s). As both fluids are transparent, 1 g/L of blue methylene (Merck) was added to the distilled water to enhance visualisation. To encourage droplet formation and inhibit subsequent droplet coalescence the surfactant Span 80 (Sigma-Aldrich) was added at a concentration of 1 wt% ($\approx 2 \times 10^{-2} M$, > 60 CMC) to the oil phase, as per Bancroft's Law [107]. The interfacial tension between the aqueous phase and the surfactant-mineral oil solution at this concentration was measured to be 5 mN/m using

the Wilhelmy plate method. The graph of the interfacial tension as a function of surfactant concentration for the fluids of this study is shown in Figure 3.21.

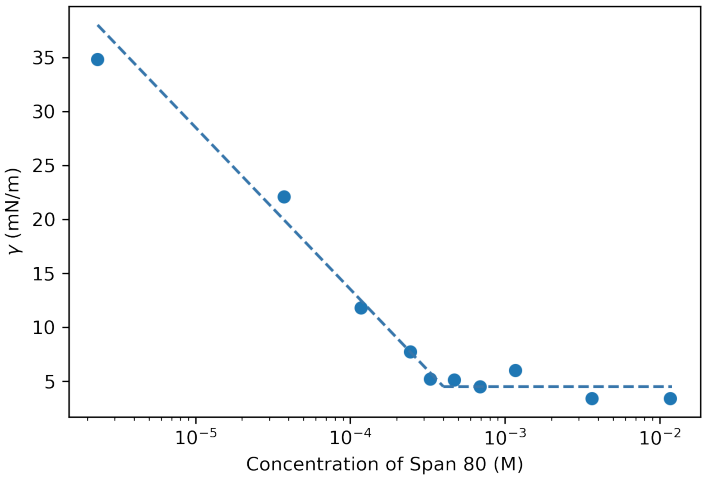

Fig. 3.21 Plot of the interfacial tension of the immiscible fluid system primarily used in this study as a function of the surfactant concentration in the oil phase. The CMC is situated at $\approx 3 \times 10^{-4}$ M.

The viscosity of the oil phase is 18 mPa.s, giving a viscosity ratio of $M = \eta_d/\eta_c = 0.06$. It has been shown numerically that the dissipation within the droplets can be assumed negligible for $Ca \ll (\eta_d/\eta_c)^{-2/3}$ [81]. In the case of water droplets in mineral oil, this applies when $Ca \sim 10^2$ so droplets can safely be assumed inviscid. In further studies the influence of the viscosity ratio of the two phases, M, was considered. For instance, a hydrophilic version of the porous media was made and the inverse emulsion, mineral oil drops in a continuous phase of water and blue methylene, was studied. In this case the droplets were stabilised by adding 1 wt% SDS (Sigma-Aldrich) to the continuous water phase. Whilst the CMC of this fluid system was not measured, the CMC of a water in hexadecane system was measured as 0.25 wt% by Salkin *et al.* and no coalescence of the droplets was observed prior to entering the porous media. Experiments using droplets of fluorinated oils (Fluo-Oil 7500, Emulseo) with 1 wt% surfactant (FluoSurf, Emulseo) in a continuous water phase were also performed. The lower density of the fluorinated oils, however, presented experimental difficulties, negatively impacting the stability of the emulsions produced before arriving at the porous media.

Although mineral oil has been observed to be absorbed by PDMS, no changes in the microsystems or the nature of the flows were observed during a typical experiment lasting several hours. Given the small ratio of post separation to height ($\frac{d}{H} \leqslant 0.5$) the porous region can be considered unaffected by the swelling. In wider channels, such as the one surrounding the porous region, an influence of PDMS swelling on droplet transport was only observed at very low flow rates ($Q \leqslant 0.5$ µL/min). In this case, droplets were observed to flow only at the edges of the channel where the swelling was the least pronounced. flow rates below this value were not considered in this study.

3.2.4 Experimental Procedure

The generic experimental set up for the experiments in this chapter and the following one is shown below in Figure 3.22.

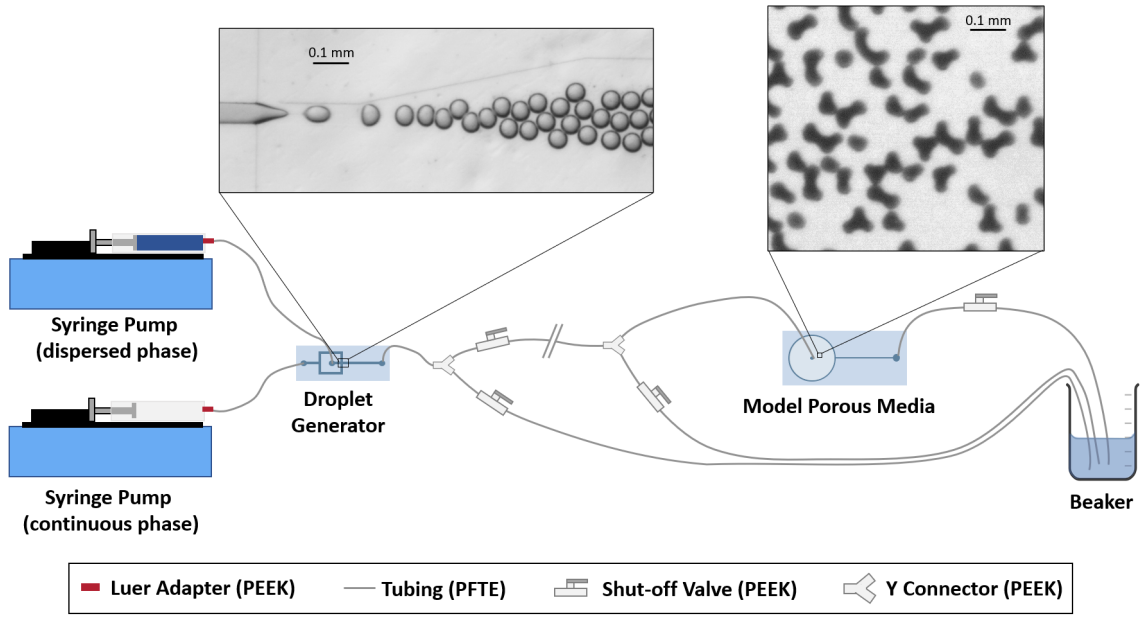

Fig. 3.22 Schematic of the experimental set-up employed for the experiments in Chapters 3 and 4. Experimental images are from the formation (left) and transport through a model porous medium (right) of different water-in-oil emulsions. The experimental apparatus is not shown to scale.

Droplet Generation

As shown in Figure 3.22, the fluid phases were injected into the droplet generator using two high-precision syringe pumps (Harvard Pico Plus Elite) and PFTE (Polytetrafluoroethylene) tubing of internal and external diameters 0.5 mm and 1 mm respectively. Flow rates were selected with respect to the desired droplet size and volume fraction. The droplet generator is positioned below an optical microscope fitted with a high-speed camera (jAi GO-2400M, monochrome) allowing for *in situ* observation of the droplets being formed.

Droplets were initially directed, using a series of valves, towards the waste beaker. After a minimum of ten minutes, the size and volume fraction of the droplets being formed were considered stable and emulsion could be redirected towards the porous medium.

Droplet Injection

The porous medium used was initially saturated with the continuous phase. It was positioned below a high-speed camera (Vieworks VC12MX, monochrome) fitted with a Tokina F2.8 FF Macro lens and above a CCS LED backlight. This set up provided a sufficiently large field of view to capture the entirety of the porous region. Two Kenko extension tubes, 36 mm and 12 mm, and a Kenko 'Teleplus HD 2x GDX' teleconverter allowed smaller regions of the porous media and the droplet circulating through them to be captured in greater resolution. The maximum resolution achievable generated pixels of approximately 2 µm in length, giving a resolution on the order of 150 pixels per cylindrical post. The porous medium was mounted at the same height as the droplet generator to reduce any influence of gravity on the emulsion being transported between the two devices. On some occasions, the porous media was repositioned below the optical microscope mention above to allow for higher-resolution pore scale observations at precise points in the porous region.

It was important to be able to separate the flow rates employed to produce the desired emulsion from those of its injection in the porous media. This allows for the exact same emulsion to be injected into the porous media at various flow rates and not simply the flow rate at which the droplets were formed. To do so, the tubing between the droplet generator and the porous medium was first filled with the emulsion being

generated. With the tubing filled with the emulsion, the flow rates could then be adjusted to produce the desired injection flow rate.

We define the injection conditions using the dimensionless capillary (Ca) and Reynolds (Re) numbers, both of which require a notion of injection speed, v. Generalising a radial flow is difficult as, due to conservation of mass, the flow speed reduces radially with distance r from the central injection point. In order to account for the different injection conditions, we define the injection capillary and Reynolds numbers at the mid-distance from the centre to the edge of the porous region ($r = R/2$) and account for the porosity of the media as follows:

$$\overline{Ca} = \frac{\eta_c v}{\gamma} = \frac{\eta_c}{\gamma}\frac{Q}{\pi R h \phi} \tag{3.4}$$

$$\overline{Re} = \frac{\rho H v}{\eta_c} = \frac{\rho}{\eta_c}\frac{Q}{\pi R \phi} \tag{3.5}$$

where η_c is the dynamic viscosity of the continuous phase, γ the interfacial tension, R the radius of the porous region, ρ the density of the continuous phase, Q the total injection flow rate, and $\overline{Ca}$ and $\overline{Re}$ are the injection capillary and Reynolds numbers respectively. The flow conditions across the experiments are summarised below in table 3.1. It is clear that the capillary and Reynolds numbers will not be homogeneous at a given radius due to the presence or not of droplets. We will discuss in this chapter the heterogeneities in the capillary number distribution with the porous media.

$M = \frac{\eta_d}{\eta_c}$	Q_{tot} (µL/min)	γ (mN/m)	$\overline{Ca}$	$\overline{Re}$
0.06	1 - 50	5	$10^{-4} - 10^{-2}$	$10^{-4} - 10^{-2}$

Table 3.1 Experimental flow conditions.

Different lengths and diameters of tubing were used to transport the emulsion between the droplet generator and the porous media, depending on the quantity of emulsion required for the experiments. The hydrodynamic resistance between the two microfluidic devices, therefore, varied slightly between experiments, which is known to have an impact on the size of the droplets being formed. We had to be careful and confirm that the droplets being observed under the microscope were indeed the same as those further downstream being injected into the porous media, and that the size

didn't vary significantly throughout the duration of an experiment. We measured the diameters of droplets (procedure shown in Section 3.2.5) produced for various tubing sizes at consistent imposed flow rates. The results indicated a variation of just 3 % between droplet diameters, which we considered negligible.

Between experiments the microfluidic devices and the connecting tubing were rinsed with ethanol before being saturated in the continuous phase ahead of a new experiment. In general the model porous media were used ten to twenty times before being replaced, the main reason being due to blockages of a few pores by dust or other particles. No differences were observed experimentally throughout the lifespan of a porous media. The droplet generators, with their larger channels and filters in the later designs, were less susceptible to blockages and could be used for up to around thirty experiments.

3.2.5 Data Analysis

The highly visual nature of 2D micromodels provides vast insights into the physical mechanisms at play. In order to quantify the phenomena on display, this visual data must be analysed using image processing techniques. The techniques used have been detailed in this section. All of them derive from the fact that, as mentioned previously, the fluid of study is a water-in-oil emulsion with blue dye added to the water whilst the oil remains transparent. This allows the droplets in each image frame to be identified based on the grey-scale value of each pixel, ranging from 0 for a pure black to 255 for a pure white. We are able to quantify the emulsions in terms of droplet size (including the dispersity of this size) and volume fraction. Additionally, tracking the displacement of droplets between frames allows their instantaneous velocity to be determined, which can be key in determining the mechanisms acting on the droplet at any point in time. We can also gain further insights on droplet transport by analysing the geometric properties of the geometries, such as their tortuosity, or by performing droplet tracking to observe the paths most frequently taken. The different methods used to perform these analyses are described in this section.

Quantifying the Dispersion

To begin with, we need to quantify the condition of the emulsion being formed *in situ* in the droplet generator. Doing so provides a basis of comparison between experiments. The shape adopted by the droplets in a channel will depend greatly on their size with respect to that of the channels, forming either a sphere, a disk, or an oblong form when confined in one, two, or three directions respectively. Figure 3.23 shows the shape of droplets in the case of confinement in one or two directions: droplets large enough to produce confinement in three directions within the droplet generators were not considered.

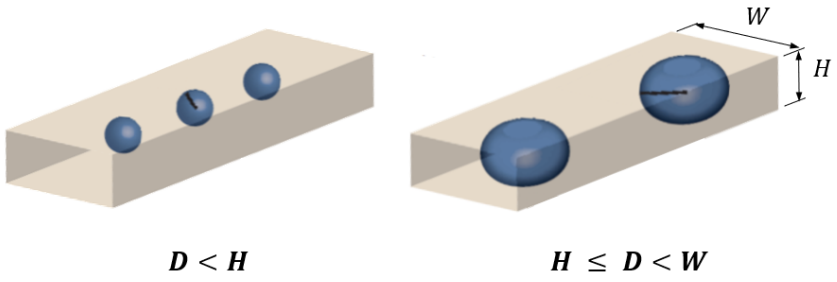

Fig. 3.23 The spherical ($D < H$) and pancake ($H \leqslant D < W$) shapes formed by droplets in a channel of width w and height H. Adapted from Panizza *et al.* [71].

Since the height H of the channels through which the droplets flow is known, by measuring the apparent diameter D of a drop as we see it, we can then determine the configuration of each individual drop and calculate droplet volume V_{drop} and the diameter for a spherical drop of the same volume D'. The confinement of the drop can also be defined as the ratio of the apparent diameter to the spherical diameter such that $\psi = D/D'$. A typical image processing workflow is shown in Figure 3.24. The images were analysed in ImageJ whilst the histograms of the droplet size distributions were generated in Python using a Gaussian Kernel Density Estimation (KDE) and the SciPy package's default bandwidth of 0.40, calculated using Scott's rule [108].

With apparent droplet diameter determined, V_{drop} and D' can be calculated. We only consider the cases where a droplet is not confined or when it is confined in only the vertical direction:

	$\boldsymbol{D < H}$	$\boldsymbol{H \leqslant D < W}$
Shape	Spherical	Pancake-shaped
$\boldsymbol{V_{drop}}$	$\frac{\pi D^3}{6}$	$\pi(\frac{D-H}{2})^2 H + (\frac{\pi H}{2})^2(\frac{D-H}{2}) + \frac{4\pi}{3}\frac{H}{2}^3$
$\boldsymbol{D'}$	D	$\sqrt[3]{\frac{6V_{drop}}{\pi}}$
$\boldsymbol{\psi}$	$\frac{D}{D'} = 1$	$\frac{D}{D'} > 1$

Table 3.2 Formulae for determining droplet size properties

We can then determine the heterogeneity between droplets diameters, called the droplet dispersity, as well as the fraction of the total volume occupied by the droplets. For the former, we can determine the coefficient of variation, CV, which is the sample standard deviation of the droplet volumes divided by the mean droplet volume $\overline{V_{drop}}$:

$$CV = \frac{\sqrt{\frac{\sum_{i=1}^{n}(V_i - \overline{V_{drop}})^2}{n}}}{\overline{V_{drop}}} \tag{3.6}$$

For the latter, we can calculate the total volume of the dispersed phase based on the number of droplets observed multiplied by their volumes, determined for each droplet configuration using the methods described above. This dispersed phase volume is expressed as a fraction of the total volume of the observed channel section ($W \times H \times L$), giving the fraction of dispersed phase present.

It is worth noting that, as discussed in Section 3.1, the thickness of the lubricating (Bretherton) film surrounding a droplet increases with its speed. In this case, the apparent droplet diameter D would also increase, as the droplet is experiencing greater confinement. Jakiela *et al.* studied droplets in a rectangular channel that were confined in both directions perpendicular to the flow [66]. They found droplet lengths increased with Ca, but that even at $Ca \approx 10^{-2}$ the difference was less than 10 % when compared to the length of the same droplets at zero velocity. For our experiments, Bretherton's law in Equation 3.2 for a channel of 50 µm in height and a flow at $Ca \approx 10^{-3}$ gives a film thickness of $h \approx 350$ nm. The difference in apparent diameter of a droplet passing from a channel of height H to one of height $H - 700$ nm, calculated using the equations for pancake-shaped droplets above, is just 0.5 %.

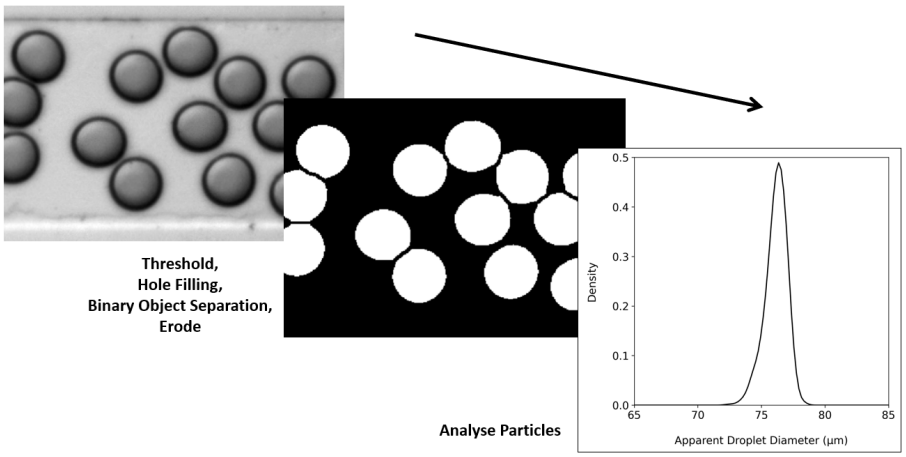

Fig. 3.24 Image processing to pass from a cropped experimental image (left) to a binarised version (centre) from which the droplet sizes can be determined and analysed (right). Image processing performed using plug im! and ImageJ [109, 110]. Droplet size data was then analysed in Python.

Quantifying the Porous Media

As mentioned in Section 3.2.2, regular lattice geometries of constant porosity were used for the majority of this experimental work. From the perspective of radial flows, the alignment of the posts as seen by the droplets varies angularly, as shown in Figure 3.25. The variation is cyclic and depends on the symmetries of the posts. This leads to angular variations in the geometric tortuosity which could impact the ease with which a droplet flows in a given direction. In this section we present the methods used to quantify these geometric differences, which will prove useful for Section 3.3. We assume that, for the regular lattices at least, the permeability does not vary angularly. For a detailed analysis of this assumption, as well as the series of experimental and numerical permeability measures performed, see Appendix A.

In Section 2.2.1 we defined the geometric tortuosity between two points as the ratio of geodesic and Euclidean distances separating them. For binary supports, the geodesic distance is the length of the shortest path between the two points, this path being constrained in one set. Considering two binary functions I, I': $\mathbb{R}^2 \to \{0,1\}$, and two bounded sets of points $S = \{x \in \mathbb{R}^2 | I(x) = 1\}$ and $S' = \{x \in \mathbb{R}^2 | I'(x) = 1\}$, as well as the complementary set S where $S^c = \{x \in \mathbb{R}^2 | I(x) = 0\}$, tortuosity T is defined as:

$$T_x = \frac{L_G(x', x)}{L_E(x', x)} = \frac{L_G(x)}{L_E(x)} \tag{3.7}$$

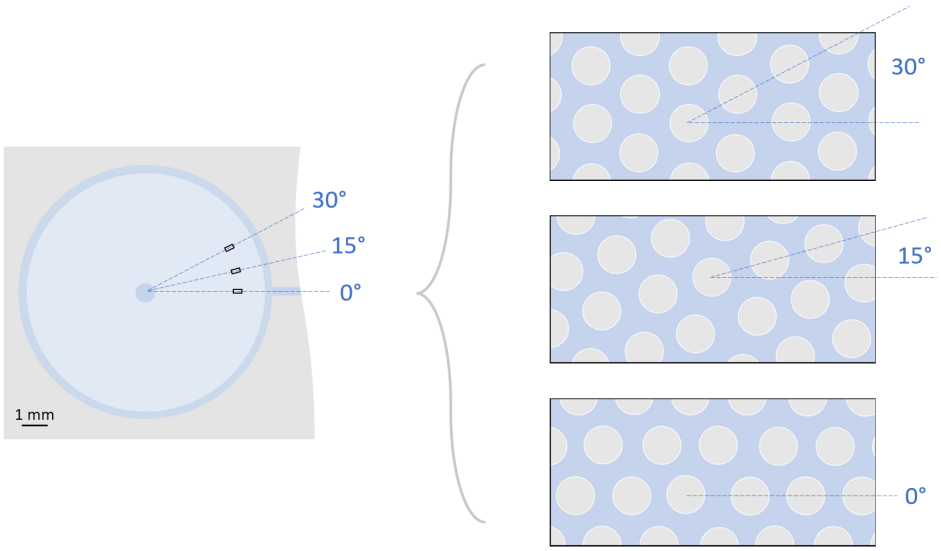

Fig. 3.25 Schematic of the radial porous media (left) and the resulting variations in the orientation of the posts (right) in the case of the hexagonal lattice. All posts have a diameter of 50 µm.

$$x'|_{min} \;\; L_E(x', x), x' \in S' \tag{3.8}$$

The set S of the function I denotes the pore space of the microfluidic system. The set S' of the function I' refers to the injection zone in the micromodel. The congestion generated by a spherical micro-droplet of radius r can be considered by dual effect [111] and is equivalent to zero congestion in a support eroded by r [51]. Considering a spherical congestion of size r, we get:

$$T_{x,r} = \frac{L_{E_{sr}}(x)}{L_E(x)} \tag{3.9}$$

$$S_r = \epsilon_r(S) = \{x \in S, \;\; L_E(x, S^c) > r\} \tag{3.10}$$

Based on these definitions, tortuosity maps be generated from binary images of the pore structure and the injection location [110]. This operation is available within plug im!, which also provides angular averages, allowing a graph of the angular variations in the tortuosity to be plotted.

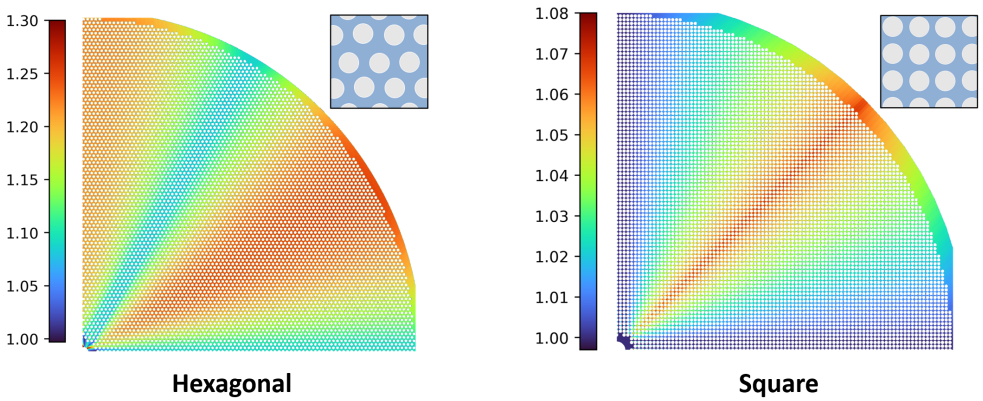

Fig. 3.26 Tortuosity maps of a quadrant of the hexagonal and square porous media. The radial geometries have a radius of 6.5 mm and the posts have a diameter of 50 µm.

Quantifying the Droplet Transport

Finally, we seek to describe the nature and behaviour of the emulsion when flowing through the porous media. The three main properties we analysed were the spatial density of the droplets throughout the porous medium, the paths followed by the droplets, and the instantaneous velocities of the droplets. We now discuss the procedure for each.

Droplet Density in the Porous Medium

Over the course of injecting droplets in a porous medium, droplets can accumulate and compact themselves to a greater degree in certain parts of the medium than others. The spatial density variations can be determined using the following method. First, a series of experimental images is binarised to separate the droplets (pixel value of 1) from the surrounding posts and continuous phase (pixel value of 0). Then, measuring the average pixel intensity across an arbitrary area containing any number of droplets gives the portion of that area occupied by droplets. By performing this measure in a systematic manner through a porous medium, we can gain quantify how homogeneously the droplets are distributed throughout the porous medium, as in Figure 3.27.

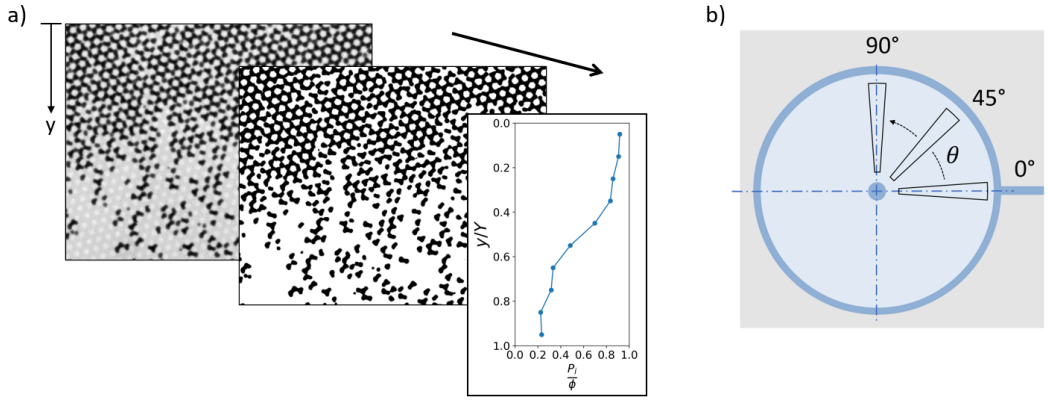

Fig. 3.27 (a) Image analysis from experimental image (left) to binarised image (centre) which can then be analysed in ImageJ to generate a graph of the spatial droplet densities. (b) Black line-sections in the schematic highlight the zones over which pixel intensities are averaged in the case of radial geometries.

Droplet Trajectories in the Porous Medium

The ImageJ plugin TrackMate was used with experimental times series to generate the trajectories of the droplets throughout the porous media [112]. The trajectories of all the droplets analysed can then be graphed such that the start of each trajectory is positioned at the same coordinates. These maps allow for a concise comparison of the trajectories of all of the droplets.

Droplet Speed Maps in the Porous Medium

When lots of droplets at low resolution are analysed using TrackMate, inaccuracies can arise. For instance, traditional tracking methods have difficulty thresholding low-resolution images of uniform colour as well as following singular events such as droplet break-up or merging. For this reason, in order to generate accurate maps of the instantaneous velocities of all of the droplets in the porous medium, we adopt a recent approach based on a Convolutional Neural Network (CNN). Upon manual comparison of droplet speeds with those predicted by the CNN, the discrepancies in droplet speeds were less than 20 %. In recent years, deep learning-based methods have shown remarkable success in solving such image registration problems [113, 114].

In this approach, a CNN estimates a registration field from two images. The network is optimised for this specific application through the learning phase. A learning

database is built digitally from images I_F taken during droplet injection experiments. A stochastic deformation field Φ is generated numerically, producing deformed image pairs I_M computed from Φ and I_F. At inference step, giving two images, the network predicts the deformation field between the image pair.

Considering two images $I_F : \Omega_F \to \mathbb{R},\ I_M : \Omega_M \to \mathbb{R},\ \Omega_F, \Omega_M \subset \mathbb{R}^2,\ \Phi$ registration field and θ learnable parameters, a registration network g is written as:

$$g_\theta(I_F, I_M) = \Phi \tag{3.11}$$

Knowing the registration fields of pairs of images of distribution D, an optimal value $\hat{\theta}$ is obtained by (cf. Figure 3.29):

$$\hat{\theta} = argmin_\theta \left[\mathbb{E}_{(I_F, I_M)\sim D} \left[\mathcal{L}(\Phi,\ g_\theta(I_F, I_M)) \right] \right] \tag{3.12}$$

The loss function is computed with expected Φ and estimated $\tilde{\Phi}$:

$$\mathcal{L}(\Phi, \tilde{\Phi}) = \frac{\left|\Phi - \tilde{\Phi}\right|}{|\Phi| + |\tilde{\Phi}|} \tag{3.13}$$

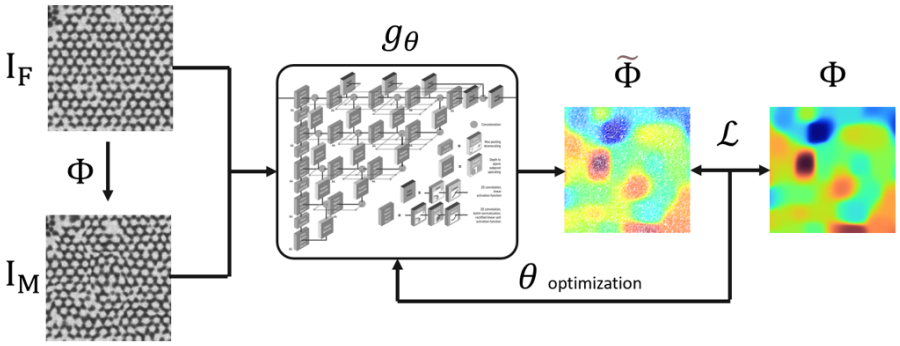

Fig. 3.28 Optimisation of g_θ for generating the deep-learning based droplet velocity maps. The architecture is shown in greater detail in Figure 3.29.

From a given image I_F and a deformation field Φ, the deformed image I_M is computed as:

$$(I_F, I_M) = (I_F, I_{F(\Phi)}) \tag{3.14}$$

$$I_F(\Phi(p)) = \sum_{q \in N_{\Phi(p)}} W_{q-\Phi(p)} . I_F(q) \tag{3.15}$$

$N_{\Phi(p)}$ is a neighbourhood around the point $\Phi(p)$ and W are weights of cubic spline interpolation.

Considering a Poisson point process $\mathcal{P}$ with density ϑ, $\mathcal{X}$ random vector, and f a smooth adaptive function imposing the congruence of the deformation field. $\Phi : \Omega_\Phi \to \mathbb{R}^2, \quad \Omega_\Phi \subset \mathbb{R}^2$, is written as:

$$\Phi = f(\cup \mathcal{X}_{c_k}) \tag{3.16}$$

$$c_k = \left\{ p \in \mathbb{R}^2, \quad d(p, p_k) < d(p, p_l), \quad p_k \in \mathcal{P}, \quad p_l \in \mathcal{P}, \quad l \neq k \right\} \tag{3.17}$$

Φ is parametrised by ϑ, f, and the maximum modulus of $\mathcal{X}$.

The architecture of g is an encoder-decoder convolutional neural network (cf. Figure 3.29). The architecture takes as an input two images of the same size, and produces as an output a deformation field, i.e. two images of similar size to the input ones. The network projects the input images into a reduced dimensional space, then reconstructs the output. Short circuits and intermediate layers improve network optimisation and predication accuracy.

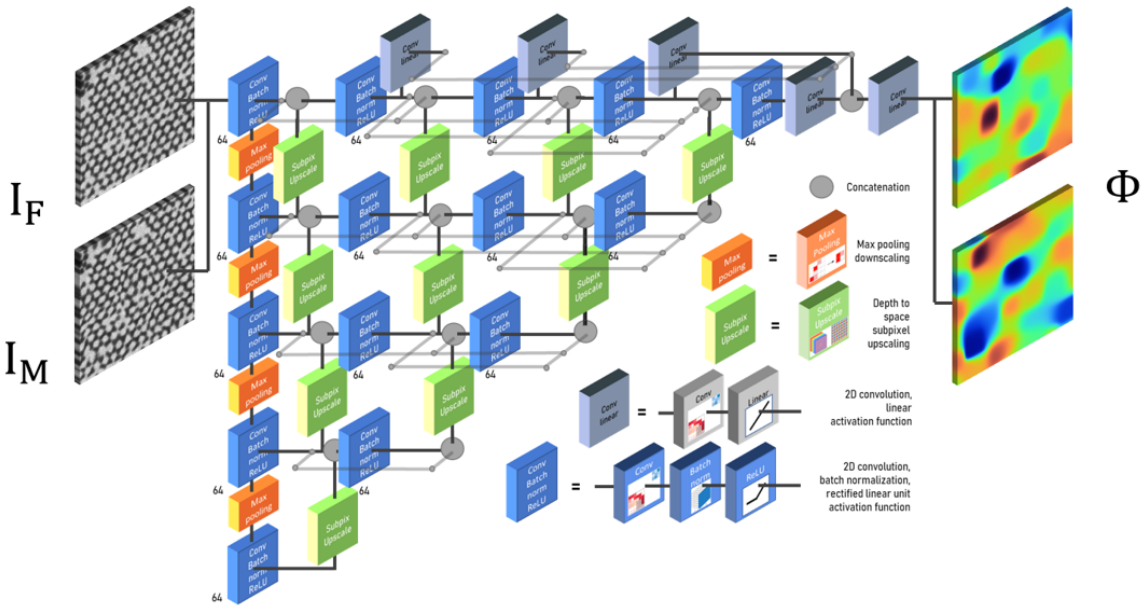

Fig. 3.29 Architecture of g_θ, with input (I_F, I_M) and output Φ.

3.3 Results

3.3.1 Initial Observations

A large portion of the research performed during this thesis was inspired by an observation made during one of the first experiments performed. A water-in-oil emulsion was injected into the centre of a PDMS micromodel consisting of a hexagonal lattice of cylindrical posts and initially saturated with the oil phase. Since both fluids are naturally transparent, blue methylene (1 g/L) was added to the water droplets to aid visualisation and thus the darker regions in any experimental images are those where the density of droplets is the highest. As can be seen in Figure 3.30a the resulting emulsion flow was largely heterogeneous. Once a stationary phase was reached, droplets flowed uniquely in the high tortuosity directions from the central injection point, as highlighted by the tortuosity map in Figure 3.30b, whilst droplets in the low tortuosity zones remained trapped in place. This counter-intuitive observation, that the preferential flow paths arose in the high tortuosity directions, incited us to try to understand the physics that could induce such a flow.

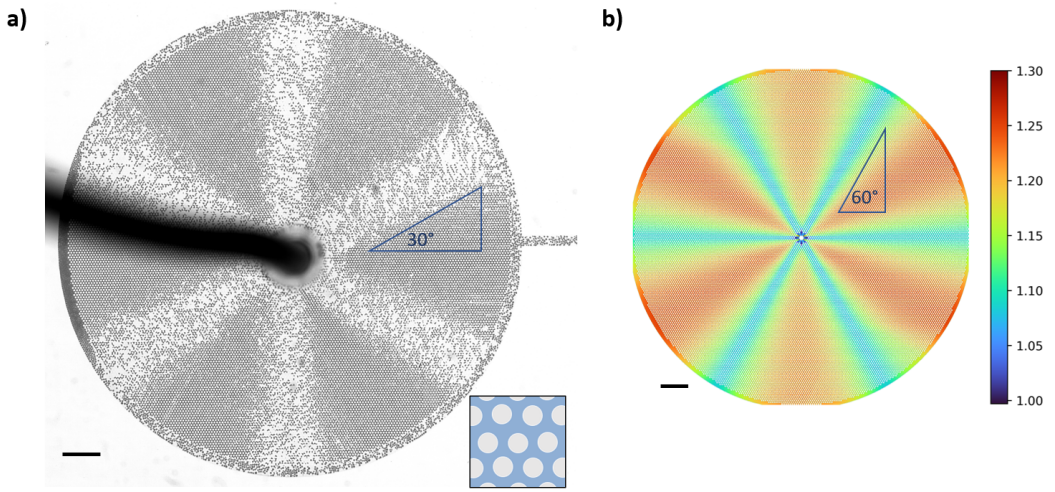

Fig. 3.30 (a) Experimental image of the radial injection of a water-in-oil emulsion in a regular PDMS porous medium at $\overline{Ca} \approx 7 \text{ x } 10^{-4}$ and $\overline{Re} \approx 9 \text{ x } 10^{-4}$. The water droplets are in grey whilst the continuous oil phase is transparent. Scale bars are 1 mm. The microstructure of the porous medium is shown in the insert at the bottom-right where the diameter of the posts is 50 µm. The unique paths of droplet flow arise at regular intervals of 60°, corresponding to the directions of high tortuosity through the microstructure. (b) Tortuosity map for a central radial injection generated as described in Section 3.2.5 using plug im!.

The following sections of this chapter consist of a systematic variation of the parameters that could influence the flow, such as the geometry of the lattice of posts, the total injection flow rate, and the volume fraction of droplets, among others. Unless otherwise stated, the ratio of the droplet diameter to the post spacing, D/d, is greater than one and so the droplets have to deform in order to pass between the rows of posts. In this section we first consider emulsion injections in rectangular geometries bearing the same lattices of posts since such flows are simpler to model and allow for some of the different mechanisms influencing the droplet transport to be more easily identified. We focus on three key aspects of the droplet transport: the paths taken by the droplets, the intermittency of the droplet velocities, and the spatial variations in droplet density that form within the porous media. We also only consider the behaviour of the droplets after the porous medium has been filled with the emulsion and a stationary phase has been reached. Afterwards, we consider more thoroughly emulsion flows in the radial geometries, both during the initial filling phase and the subsequent stationary phase.

Droplet Direction

The droplets injected were initially 75 µm in diameter such that $D/d = 3$, meaning droplets would be expected to undergo lateral displacements whilst traversing the lattice of posts. Figure 3.31 shows the droplet displacements from their initial paths for two capillary numbers ($Ca = \eta Q/\gamma wh = 10^{-2}$ and $Ca = 2$ x 10^{-3}) and for two post orientations with respect to the direction of the pressure gradient (0° and 30°). The droplet trajectories were generated by performing droplet tracking using the TrackMate plugin with ImageJ whilst the colours serve for visually differentiating droplet paths [112]. All droplet paths have been normalised so they start at the same point in the graph. Considering the 30° geometries, at both values of Ca we see a large variation in the paths taken by individual droplets as they tend follow zig-zag paths, flowing in straight lines with respect to post alignment, i.e. they flow in directions of low tortuosity within the porous medium. In fact, Figure 3.31 shows that in the 30° geometry no droplets followed directly the direction of the pressure gradient (red dotted line) despite this being the shortest path through the porous medium.

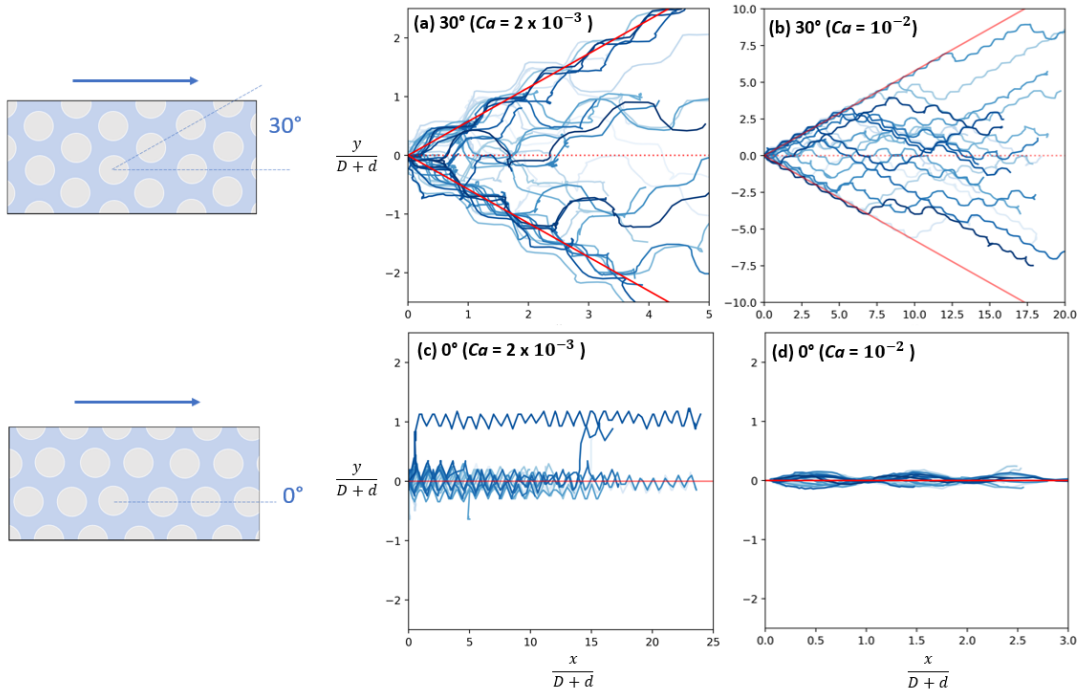

Fig. 3.31 Droplet trajectories (in different shades of blue to differentiate individual droplets) for two different post alignments and injection capillary numbers. Direction of the pressure gradient indicated by the blue arrows above the post geometries. For the posts aligned at 30° with the pressure gradient (top row) the red solid lines show the directions of 30° and the red dotted line is for zero lateral displacement. For the posts aligned with the pressure gradient (0°) the red solid line is also at 0°. Displacements in the x- and y-directions have been normalised by the distance between the centres of two consecutive posts $D + d$. Note that the x- and y-axes are not shown to scale.

For the geometries at 0° in Figure 3.31, the posts are aligned with the pressure gradient. At the higher Ca almost all droplets followed the alignment of the posts and the pressure gradient, equivalently the directions of lowest tortuosity. Droplets behaved in the same way at the lower Ca but some droplets became intermittently blocked in the porous region. Moving droplets were occasionally displaced vertically by one row in either direction to bypass the blocked downstream droplets.

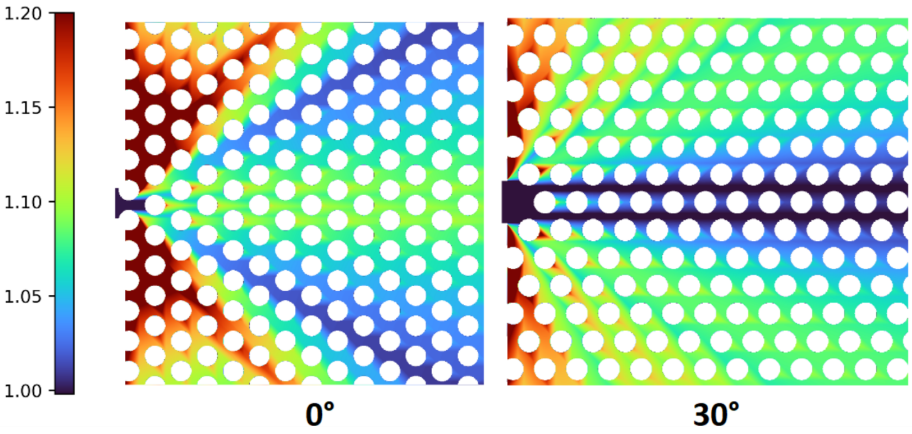

Fig. 3.32 Tortuosity maps of the entrances of the two rectangular porous media, created used the method described in Section 3.2.5.

Summary: Droplet Direction

- During the stationary phases observed in the rectangular porous media, droplets tend to flow through the porous media along the directions of **low tortuosity** at both $Ca \approx 10^{-2}$ and $Ca \approx 10^{-3}$, even if the alignment of the posts is offset from the direction of the pressure gradient by 30°.
- At lower Ca the droplet directions can become slightly more stochastic. This is because some droplets become temporarily blocked and subsequent ones bypass around them.

Droplet Mobility

From the droplet tracking mentioned above, we observed that the speeds of the droplets were highly dispersed. No droplets became permanently blocked in the porous medium, but at certain points the instantaneous droplet speed can be zero, such as when a droplet arrives at a bifurcation point around a post and must decide in which direction to move.

To quantify this speed dispersity, we used the droplet tracking data to determine the ratio of time throughout a series of 100 images (0.67 s) that the droplets were in motion (τ_d/τ). $\tau_d/\tau = 1$ means the droplet is constantly flowing through the porous region whereas $\tau_d/\tau = 0$ means the droplet is blocked during the entirety of the sampling time. Time in motion was defined as any time steps between consecutive images where the droplet displacement was greater than 1 µm, the same order of magnitude as the

uncertainty due to microscopic shaking of the camera. This same criteria, equal to less than 2 % of the length of droplets as they flowed through the porous media, was adopted for all experiments. The PDFs from the resulting histograms have been plotted in Figure 3.33. We see that at the higher Ca the behaviour in each of the geometries is rather similar, with the large majority of droplets being in motion for the entirety of the image series regardless of the orientation of the posts. At the lower Ca we find a larger degree of droplet speed dispersity. The slightly greater droplet speed dispersity in the 30° geometry could be due to the fact that the droplets follow zig-zag paths, frequently crossing paths with one another (see Figure 3.31 for droplet trajectories). This was observed to cause more collisions and instantaneous trapping of droplets as compared to 0° where droplets mostly flow parallel to one another through the porous region, following the post alignment.

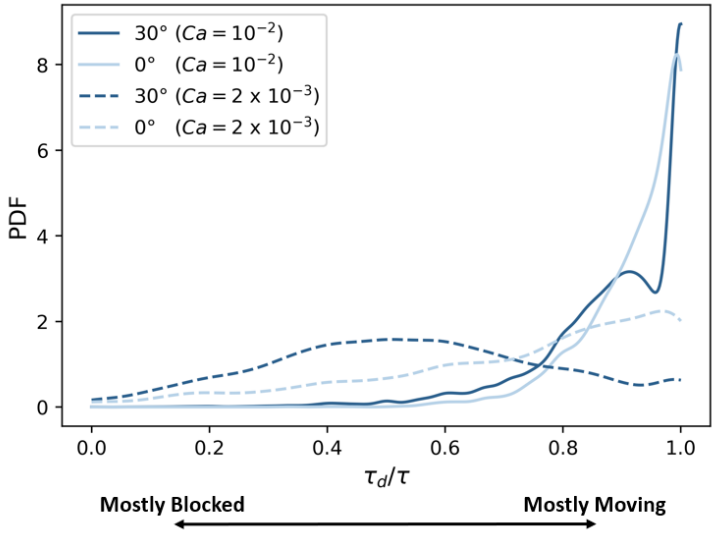

Fig. 3.33 Probability density functions of the time in movement (τ_d) of droplets normalised by the total duration of the time series considered (τ). Two Ca and two post orientations were considered. PDFs were generated as described in Section 3.2.5.

Summary: Droplet Mobility

- Droplet speed dispersity is greater at lower Ca ($Ca \leqslant 10^{-3}$)
- There is no clear tendency for droplet speed dispersity as a function of the alignment between the posts and the direction of the pressure gradient.

Droplet Spatial Uniformity

Lastly, we discuss the uniformity of the flow in the rectangular porous media during the stationary phase, both in terms of droplet speeds and concentrations throughout the porous region. As discussed in Section 3.1 complex flow patterns arise during the transport of concentrated confined droplets in porous media due to (i) collisions between droplets, (ii) the dipolar perturbations induced by the droplets on the mean flow field, and (iii) droplets seeking the local directions of least resistance (highest flow rate). The experimental images (a) and (b) in Figure 3.34 show typical spatial variations in droplet concentration for constant inlet droplet concentration with both geometries (0° and 30° respectively) and at $Ca = 10^{-2}$.

The spatial concentrations of droplets were quantified following the approach detailed in Section 3.2.5, with the resulting graph of the average spatial concentrations across all 40 images shown in Figure 3.34c. Lastly, the average speeds of all the droplets in experiment (a) throughout a time-series of 40 images (v) were measured and normalised by the maximum measured instantaneous droplet speed (v_{max}). The normalised droplet speeds were then averaged along the y-direction and plotted in Figure 3.34d.

We see for the 0° geometry in Figure 3.34a that a region concentrated with droplets forms around the lower-middle of the geometry in terms of the transverse (y-) axis. For the 30° geometry, on the other hand, as shown in Figure 3.34b, the spatial concentration of droplets was highly homogeneous with no particular regions maintaining a high concentration. Figure 3.34c highlights the peak in the concentration of droplets in the 0° geometry (blue line). In the 30° porous medium is rather uniform, albeit lower near the edges of the image than in the centre.

As shown in Figure 3.34d the average speeds of the droplets in the concentrated region of the 0° geometry are markedly lower than elsewhere in the porous medium, despite all paths between the inlet and the outlet of the porous medium having the same length, resistance, and tortuosity when void of droplets. This region remained dense in droplets throughout the entirety of the experiment. However, between experiments its exact y-position could vary slightly.

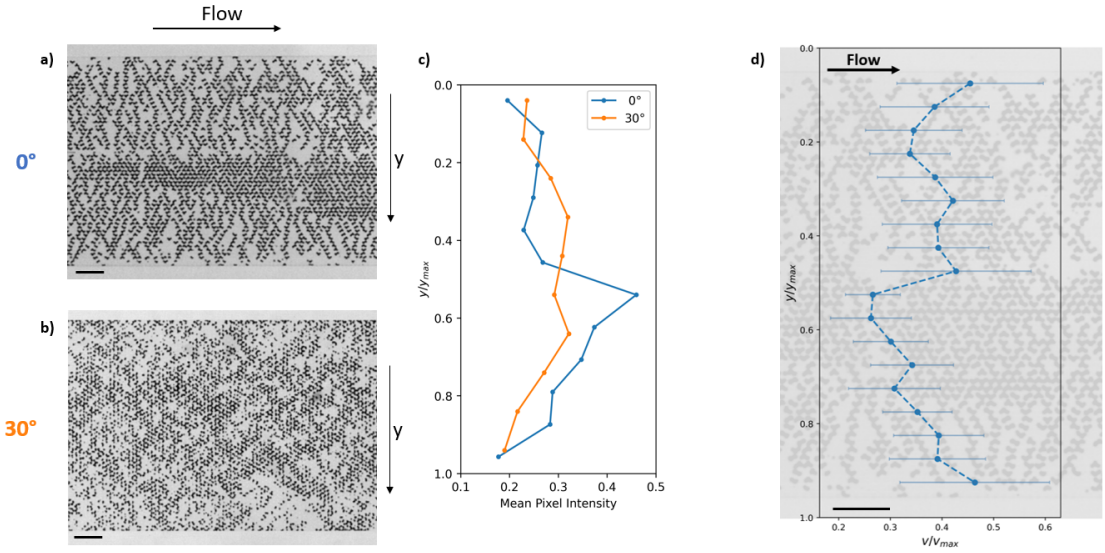

Fig. 3.34 (a,b) Experimental images of droplet flow at $\overline{Ca} = 10^{-2}$ in the 0° and 30° geometries respectively. (c) Curves of the variations in average pixel intensity in the transverse direction for binarised versions of (a) and (b) where droplets have an intensity of 1 and elsewhere an intensity of 0. Average values across all 40 experimental images were then taken. (d) Average speeds of all the droplets (v) throughout a time-series normalised by the maximum measured instantaneous droplet speed (v_{max}) for the experiment in (a) are shown along the transverse (y-) axis normalised by the width of the image (y_{max}). Both images were taken immediately downstream of the inlet channel. All scale bars are 500 µm and all droplet flows are from left to right.

Summary: Droplet Spatial Uniformity

- Even in simple, uniform porous media, areas of high droplet concentrations can form, leading to a marked reduction in droplet speed and thus Ca in these areas.
- These disparities in local droplet Ca could further impact droplet transport and speed dispersity which, as discussed above, depends on Ca.
- These disparities only tend to arise when the alignment of the pores is in the same direction as the pressure gradient of the flow.

3.3.2 Analysing the Radial Flow Heterogeneities

We now return our attention to the unexpected heterogeneities that arise during the radial injection of an emulsion in the porous medium bearing a regular hexagonal lattice of posts (Figure 3.30a). Despite the permeability of this geometry being constant in all directions from the central injection point (see Appendix A for further development of this point) droplets flowed in a limited number of directions whilst all droplets elsewhere in the medium were blocked. Furthermore, these limited flow paths correspond to the directions of high tortuosity, which is counterintuitive as we would expect droplets to take the shortest paths through the porous medium.

By performing droplet tracking we can start to better understand how these patterns arise. Figure 3.35 shows four cropped images at different time points during emulsion injection in a radial geometry at a total injection rate of 15 µL/min, giving $\overline{Ca} \approx 7 \text{ x } 10^{-4}$ and $\overline{Re} \approx 9 \text{ x } 10^{-4}$ at the mid-radius of the porous region. Furthermore, the volume fraction of the droplets $V_v \approx 0.5$. The low tortuosity directions from this central injection position are indicated with red lines in the insert in the leftmost image of the figure. Furthermore, the pressure gradient acts radially outwards in all directions from the injection point (bottom left corner of the images), unlike in the rectangular geometries discussed earlier where it only acts in one direction. The post separation in the geometry considered now is $d = 75$ µm, giving a droplet-to-pore size ratio of $D/d = 1$ and a confinement of $\psi = 1.1$. In the following sections, however, we systematically analyse the influence of these parameters amongst others such as the injection $\overline{Ca}$ and the dispersed volume fraction V_v.

We observe that the initial droplets that enter the porous media in the low-tortuosity directions (those at the base of the dark blue arrows in Figure 3.35) continue to flow along these directions of low tortuosity. This was expected and is in agreement with the observed droplet trajectories for the linear geometries at 0° in Figure 3.31 since both the posts and the pressure are aligned in this direction. As the flow continues the number of droplets flowing along these paths increases which in turn increases the hydrodynamic resistance of the paths. As a result, droplets in these paths slow down and become highly compacted. Droplets also decelerate proportionally to their distance from the centre of the porous medium as per conservation of mass for a radial flow.

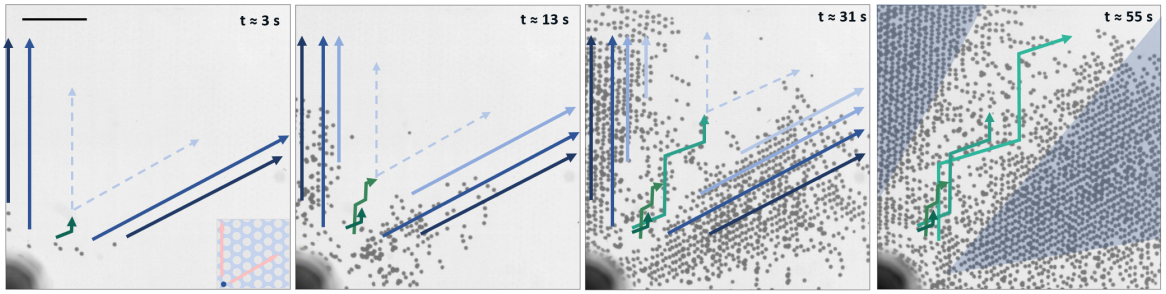

Fig. 3.35 Experimental images of droplet flow at $\overline{Ca}$ = 7 x 10^{-4} from the central injection point (bottom left). Arrows indicate droplet directions. Blue arrows indicate droplets entering the porous medium in directions where the pressure gradient is aligned with the post orientation (behaving like those in the 0° linear geometries). Green arrows indicate droplets that arrive in the porous medium in directions where the post alignment is offset from the pressure gradient (behaving like those in the 30° linear geometries). Dashed lines indicate possible future directions. Scale bar for experimental images is 0.5 mm, diameters of the posts in the insert of the leftmost image are 50 µm.

The increased resistance of the initial low tortuosity paths cause some of the subsequent droplets to seek new paths through the porous medium. Increasing numbers of droplets begin to pass through the high tortuosity regions. These droplets initially emulate the zig-zag trajectories observed in the linear geometries at 30° of Figure 3.31, preferentially following the lines of the posts and not the direction of the pressure gradient, as was also observed in the rectangular geometries. They then quickly settle on flowing in straight lines through the posts (low tortuosity - one of the two dashed light blue arrows). This behaviour repeats itself throughout the filling phase, with droplets converging on the low tortuosity regions, leading to a local increase in concentration of droplets.

It is interesting to note that in most previous studies of droplet traffic phenomena in microfluidic systems, no stationary phase is achieved, with the flow remaining intermittent and cyclic meaning the preferential flow paths constantly change [59, 60, 68, 99]. In this experiment, however, the low tortuosity paths maintained a high droplet concentration of droplets. In some experiments the low tortuosity directions were completely blocked and all droplets injected during the stationary phase passed by the high tortuosity paths.

To support this scenario, droplet tracking was performed on two separate series of 50 experimental images (5 s) in this hexagonal geometry. The image series corresponded approximately to the second and fourth images in Figure 3.35. The results are shown in Figure 3.36 where the colours in the overlay of the experimental image (left) represent the average droplet speed throughout the image series normalised by the maximum average droplet speed measured between the two images ($\bar{v}/max(\bar{v})$). During the filling phase (left) the droplets primarily flow in low tortuosity directions, with an average normalised speed when passing the dashed white arch of 0.35. During the stationary phase, the droplets at the same radial position in the low tortuosity directions have a normalised speed of approximately 0.1 whilst droplets in the high tortuosity directions have a normalised speed of around 0.65. Ultimately, at this stage of the work, we don't have a rational explanation for this droplet blockage in the low tortuosity paths and we hope we will be able to provide an explanation at the defense.

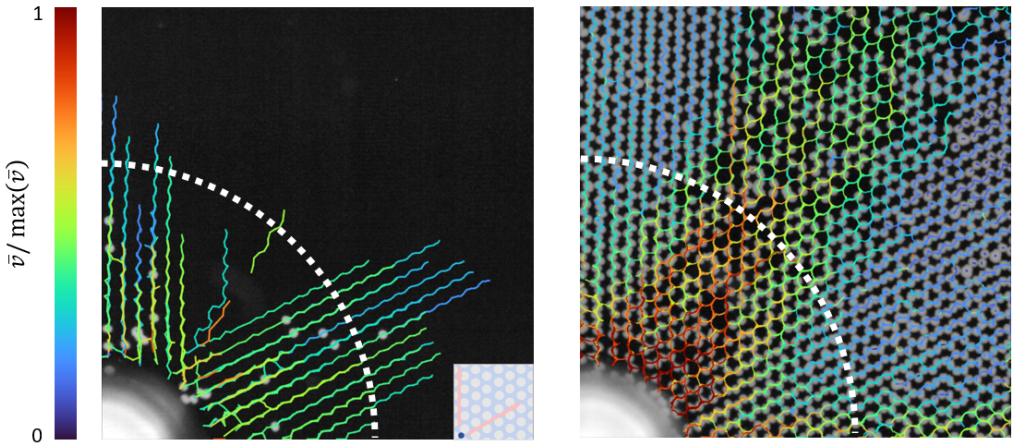

Fig. 3.36 Droplet tracking performed on two series of 50 experimental images (5 s) during the filling phase in the hexagonal geometry, corresponding approximately to the second and fourth images in Figure 3.35. Image dimensions are 2.2 x 2.2 mm. Colours in both figures correspond to the average droplet speed throughout the image series ($\bar{v}$) normalised by the maximum average droplet speed measured ($max(\bar{v})$). Time between the beginning of each image is 26 s. The white dashed-arches are a visual aid for a constant distance from the central injection point.

Summary: Radial Droplet Flows

- In the radial geometries, just like in the linear geometries, the droplets initially follow the paths of low tortuosity.
- Consequently, the droplets converge on the low tortuosity regions, increasing the hydrodynamic resistance of these regions.
- The droplets in the low tortuosity regions slow down significantly. The total resistance is too great for the droplets in the low tortuosity regions to be evacuated and a stationary phase is reached where subsequently injected droplets flow preferentially in the originally high tortuosity directions.

Role of the Pore Geometry

With the previous observations in mind, the parameters of the porous media and the emulsion injection are systematically varied in order to assess their influence on the transport heterogeneities observed. This will also allow us to ascertain the robustness of the previous observations.

We start by varying the structure of the lattice of posts, studying both regular and random geometries. Once again, a water-in-oil emulsion was prepared and injected in a series of model porous media initially saturated with the continuous phase, as described in Section 3.2.4. In the following experiments the injection capillary and Reynold's numbers were held constant at $\overline{Ca} \approx 2 \text{ x } 10^{-3}$ and $\overline{Re} \approx 1 \text{ x } 10^{-3}$ respectively. The circular geometries presented in Section 3.2.2 with minimal post spacing $d = 15 - 25\mu$m for the regular geometries and $d \leq 25\mu$m for the random geometries were used. Droplets at the inlet had a diameter of $D = 75 \pm 0.9$ µm such that $\psi = 1.1$ and depending on the geometry $D/d \approx 3 - 4$. Unless otherwise stated, the volume fraction of the droplets in the emulsion $V_v \approx 0.5$.

Regular Geometries

Figure 3.37 shows experimental images of the droplets flowing in the different micromodels during the filling (top) and stationary (bottom) phases for the three lattice structures presented in Figure 3.18. During the filling phase for each of the geometries the droplets all flowed preferentially in the low tortuosity directions, as described in

the previous section for the hexagonal geometry. With the emulsion having filled the porous media, the droplet transport in the stationary phase occurred preferentially in the high tortuosity directions (lighter grey zones in the bottom row of images). Interestingly, each of the macroscopic droplet patterns in the regular geometries bears the same number of symmetry planes as the posts in the lattice at the microscopic scale. Furthermore, leaving the experiments at $\overline{Ca} > 10^{-3}$ to run for up to one hour led to coalescence of the droplets in the dense low-tortuosity regions, after which point all subsequently injected droplets passed by the high tortuosity directions. This coalescence, however, had no influence on the pattern created by the heterogeneous transport, which arose for lower $\overline{Ca}$ in which no permanent blockage or coalescecne occurred. For further discussion of coalescence in the porous media see Chapter 3.

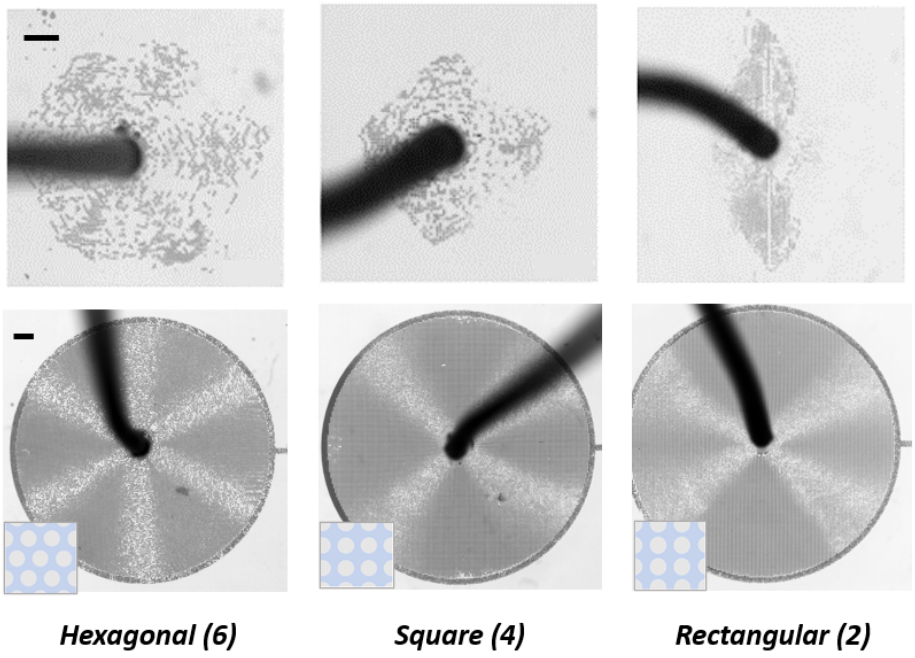

Fig. 3.37 Experimental images of emulsion injection in four porous media bearing four different lattice geometries at $\overline{Ca} \approx 2 \times 10^{-3}$. The top row depicts the transitional filling phase (droplets flow primarily in low tortuosity directions) whilst the bottom row shows the corresponding stationary phase once the emulsion had filled the geometry (droplets in low tortuosity directions are largely trapped and the injected emulsion flows primarily in the high tortuosity directions). This stationary phase lasted for the remainder of the injection. In brackets are the number of planes of symmetry of each geometry which arise in the patterns formed during the injection for both phases. All scale bars are 1 mm whilst the posts in the insert showing the lattice structure all have a diameter of 50 µm.

In addition to the lattice structure, we tested the influence of the radius R of the porous regions. Figure 3.38 shows that even for geometries with $R \approx 35(D + d)$, the smallest we were able to test experimentally, and with a radius approximately 4 times smaller than that of the geometries in Figure 3.37, the same transport patterns arose.

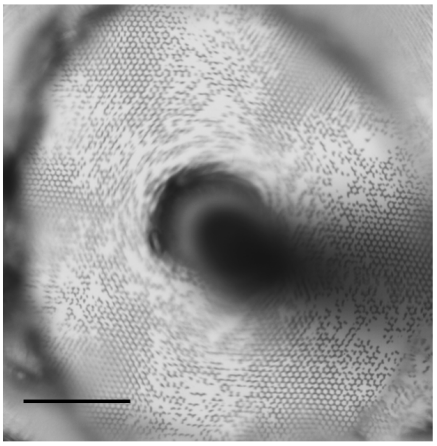

Fig. 3.38 Experimental image for the hexagonal lattice geometry in a porous medium of radius $R \approx 35(D + L)$. Scale bar is 1 mm.

Random Geometries

A series of random post lattices were created using the morphological models discussed in Section 3.2.2. We first studied a random geometry where the posts were allowed to overlap one another freely whilst maintaining a porosity of 0.64 (compared to 0.6 for the regular geometries). The resulting filling and stationary phases are shown in Figure 3.39. No preferential direction of droplet flow arose and the concentration of the droplets throughout the porous region during the stationary phase was homogeneous.

Additional random geometries, without post overlap and of varying minimal inter-post spacing, were also studied, as shown in Figure 3.40. The minimal inter-post spacing ranged from 15 µm (that of the rectangular geometry) to 25 µm (that of the hexagonal geometry). When the post spacing is the smallest (a-b) no discernable patterns arise and the droplet flow is homogeneous, as for the in Figure 3.39 for overlapping posts. Increasing the minimal post spacing whilst maintaining a constant porosity leads to fewer possible lattice geometries. As a result the geometries formed become pseudo-crystalline, with zones in the porous region almost bearing a hexagonal symmetry. Whilst less pronounced than for the original hexagonal geometry, the

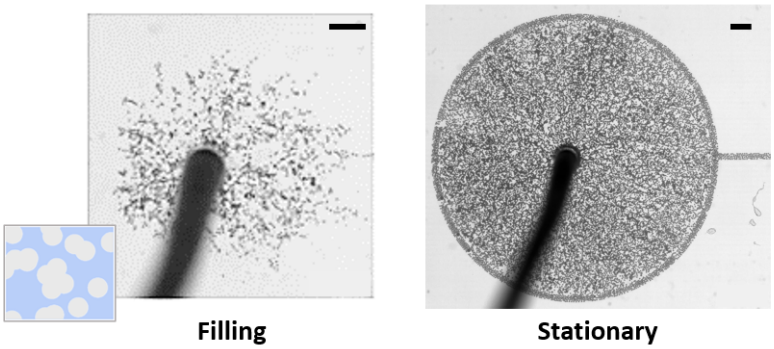

Fig. 3.39 Experimental images of emulsion injection at $\overline{Ca} = 2$ x 10^{-3} in a random post lattice (with overlap). Both scale bars are 1 mm.

same droplet transport patterns can be discerned in the case of Figures 3.40c-d. This observation provides, therefore, an indication of the robustness of the phenomena being observed, and widens the range of real-world porous media to which these observations could be applied.

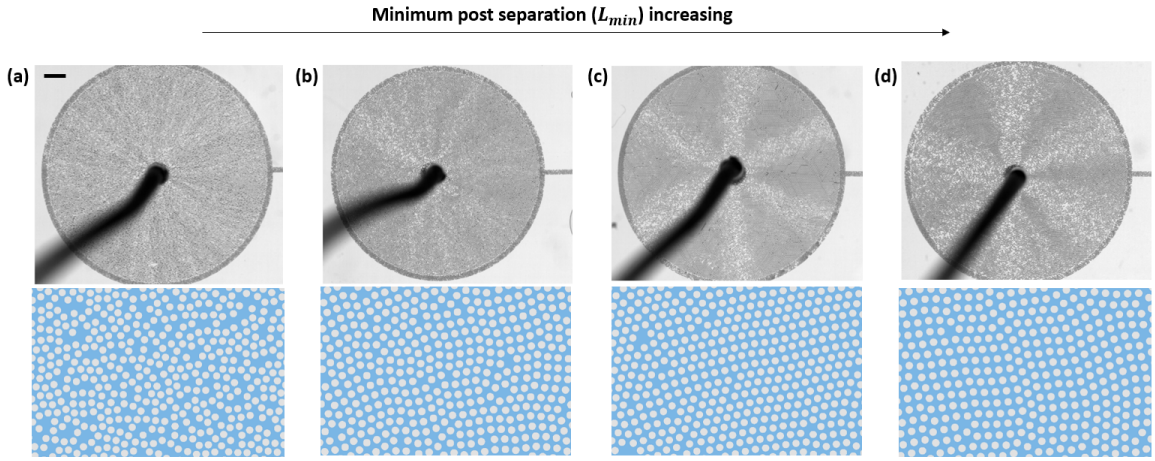

Fig. 3.40 Experimental images of emulsion injection at $\overline{Ca} = 2$ x 10^{-3} and the corresponding lattice geometry. As the lattices become increasingly crystalline the droplet transport patterns become increasingly present. Scale bar is 1 mm, all posts have a diameter of 50 µm. (a) $d_{min} = 15$ µm, $\phi = 0.61$ (b) $d_{min} = 20$ µm, $\phi = 0.60$ (c) $d_{min} = 22.5$ µm, $\phi = 0.60$ (d) $d_{min} = 25$ µm, $\phi = 0.64$.

Summary: Role of the Pore Geometry

- The influence of the lattice geometry on the transport of the droplets at $\overline{Ca} = 2 \text{ x } 10^{-3}$ as well as constant droplet size ($D/d \approx 3$) and volume fraction was studied.
- For all of the regular geometries considered, the droplets flow preferentially in the low tortuosity directions during the filling phase but in the high tortuosity directions during the stationary phase. The number of planes of symmetry in the microscopic lattice geometry are systematically reproduced in the macroscopic flow patterns.
- For purely random geometries the flow is homogeneous.
- In pseudo-crystalline geometries the flow heterogeneities from the regular geometries are identifiable albeit less pronounced.

Role of the Injection Capillary Number

The radial emulsion flows discussed until now were all undertaken at the same injection capillary number. In this subsection we present a series of experiments, using mainly the hexagonal geometry, where we systematically varied $\overline{Ca}$ whilst keeping all other parameters, such as the size and concentration of the droplets, constant. The method used to separate the formation of the droplets from their injection is described in Section 3.2.4.

Before discussing the results, it is worth noting that while the injection capillary number was varied, the capillary number inside the porous media is not homogeneous. Injected droplets travel at different speeds as a function of their distance from the centre as well as the concentration of droplets downstream along the same path.

Filling Phase

Figure 3.41 shows the filling phase for the hexagonal and square lattice geometries and at two different injection $\overline{Ca}$. The heterogeneous flows for $\overline{Ca} \approx 2 \text{ x } 10^{-3}$ discussed previously are included in Figure 3.41a. The two images for each geometry highlight the initial flow in the low tortuosity directions and the subsequent transition towards flowing preferentially in the high tortuosity directions. At $\overline{Ca} \approx 10^{-4}$, however, droplets

uniformly fill the porous media at both stages of the injection shown for each geometry shown in Figure 3.41b. The droplets form an advancing circular front, regardless of the orientation of the regular lattices of posts.

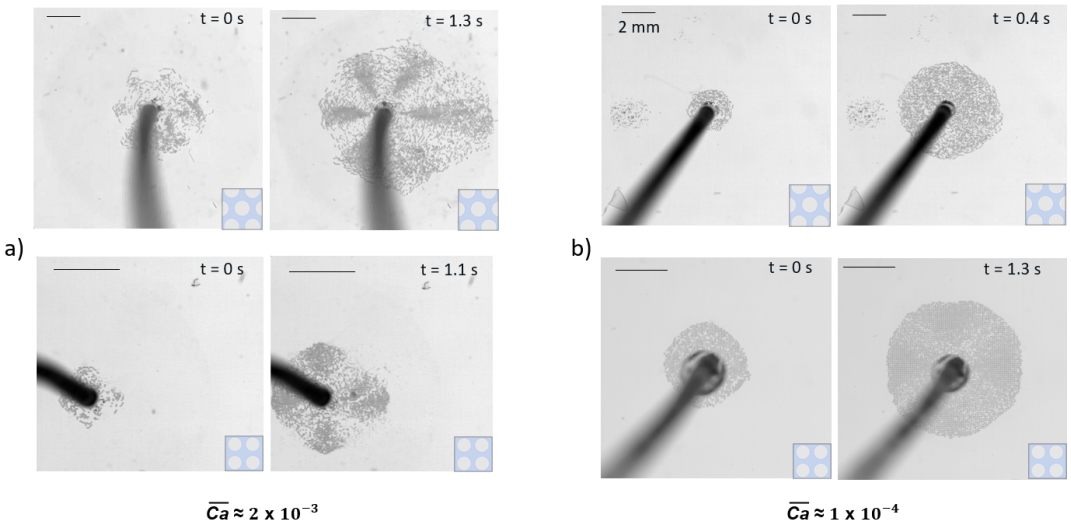

Fig. 3.41 Filling phase for the hexagonal (top) and square (bottom) lattice geometries at two different capillary numbers. All scale bars are 2 mm and the posts in the inserts showing the lattice geometries are 50 µm is diameter.

At low $\overline{Ca}$ droplets had more difficulty deforming in order to pass between the posts. After traversing just a few rows of posts droplets stop moving and become trapped. Upstream droplets are then able to flow past these droplets before themselves becoming trapped a few pore lengths later. This pattern repeats itself until the porous medium has been filled, at which point the majority of droplets spend most, if not all, of their time trapped. Many droplets also alternate brief bouts of movement and trapping. Similar droplet transport has already been observed, experimentally and numerically, such as by Champagne *et al.* or by Coehlo *et al.* respectively [59, 60].

This behaviour can be quantified through the dispersity in droplet speeds, as discussed in Section 3.3.1. Figure 3.42 shows τ_d/τ for the droplets at various stages in the filling of the porous medium. As the porous media fills, the percentage of droplets spending most or all of their time trapped increases significantly. At $Ca \approx 10^{-4}$ no distinct preferential flow zones consistently arise across repetitions of the experiment. A similar curve during the stationary phase was obtained by Coehlo *et al.* numerically in a linear porous medium [60].

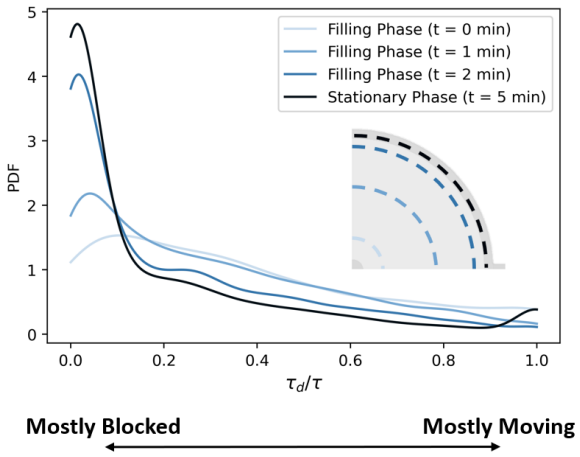

Fig. 3.42 Probability density functions of the time in movement (τ_d) of droplets normalised by the total duration of the time series considered (τ). Three intervals of 40 images at different stages during the filling phase and one interval during the stationary phase were considered (see insert for the positions in the porous region of the circular droplet front for each of the image sets). PDFs were generated as described in Section 3.2.5.

Stationary Phase

Figure 3.43 shows the stationary phase for four injection capillary numbers ranging from $\overline{Ca} \approx 10^{-4}$ to $\overline{Ca} \approx 3$ x 10^{-3} in the hexagonal geometry. We see that the heterogeneous transport patterns arise gradually with increasing $\overline{Ca}$ from left to right as increasing numbers of droplets converge in the low tortuosity regions.

We quantified the spatial variations in droplet density for each of the four experiments using the technique described in Section 3.2.5. At each $\overline{Ca}$ considered, the average pixel intensities $\bar{I}$ along the entire radius of the geometry was measured at 5° intervals, starting from the direction of the exit channel (0°). The measured intensities were averaged over six experimental images for each $\overline{Ca}$, and the resulting plots are shown in Figure 3.44. Increasing $\overline{Ca}$ leads to droplet accumulation around the zones of low tortuosity. The higher volume of dispersed phase present in the porous medium at higher Ca, proportional to the areas under each of the curves, effectively reduced the porosity of the porous medium. The thinning of the preferential flow paths with increasing $\overline{Ca}$, clearer in Figure 3.45, is also visible. This is likely to have an influence on the interstitial velocity of flowing droplets, as will now be further investigated.

Interestingly, Figure 3.44 shows that the lowest total droplet concentration present in the porous medium, indicated by the total area under each curve, occurs at $\overline{Ca} \approx 6$ x 10^{-4}. This $\overline{Ca}$ could be the most suitable when the goal is to have the lowest volume of the dispersed phase remaining in the porous medium. This is also the Ca at which the droplets appear the most mobile, unlike at both higher and lower $\overline{Ca}$ where high degrees of droplet trapping occurs.

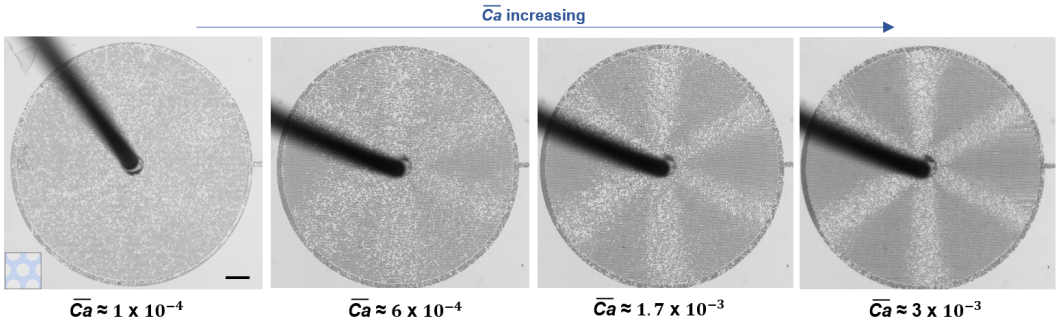

Fig. 3.43 Experimental images for increasing $\overline{Ca}$ from $\overline{Ca} \approx 10^{-4}$ to $\overline{Ca} \approx 3$ x 10^{-3} in a hexagonal lattice geometry. Scale bar is 1 mm.

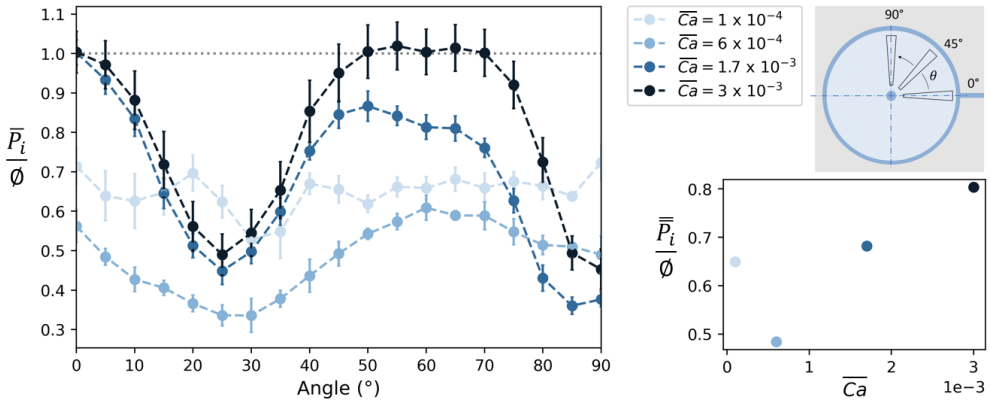

Fig. 3.44 Angular variation of the average pixel intensity $\overline{P_i}$ along the entire radius of the porous medium at 5° intervals. For each $\overline{Ca}$ considered, six binarised experimental images were considered and the averages at each 5° interval were plotted. Droplets had a pixel intensity of 1 whilst elsewhere a value of 0. Higher values, therefore, correspond to greater droplet densities. More information on the approach used can be found in Section 3.2.5. The averages of the average pixel intensities $\overline{\overline{P_i}}$ are also plotted as a function of $\overline{Ca}$. For comparison, the injected volume fraction is approximately 0.5.

In order to quantify the behaviour of the droplets, we performed large scale droplet tracking throughout a single quadrant of the geometries at each $\overline{Ca}$ using the deep-learning-based approach described in Section 3.2.5. Figure 3.45 shows the resulting velocity fields for a variety of capillary numbers. Two scale bars have been included to highlight the spatial heterogeneities in local Ca (left) determined from the local droplet speeds (right):

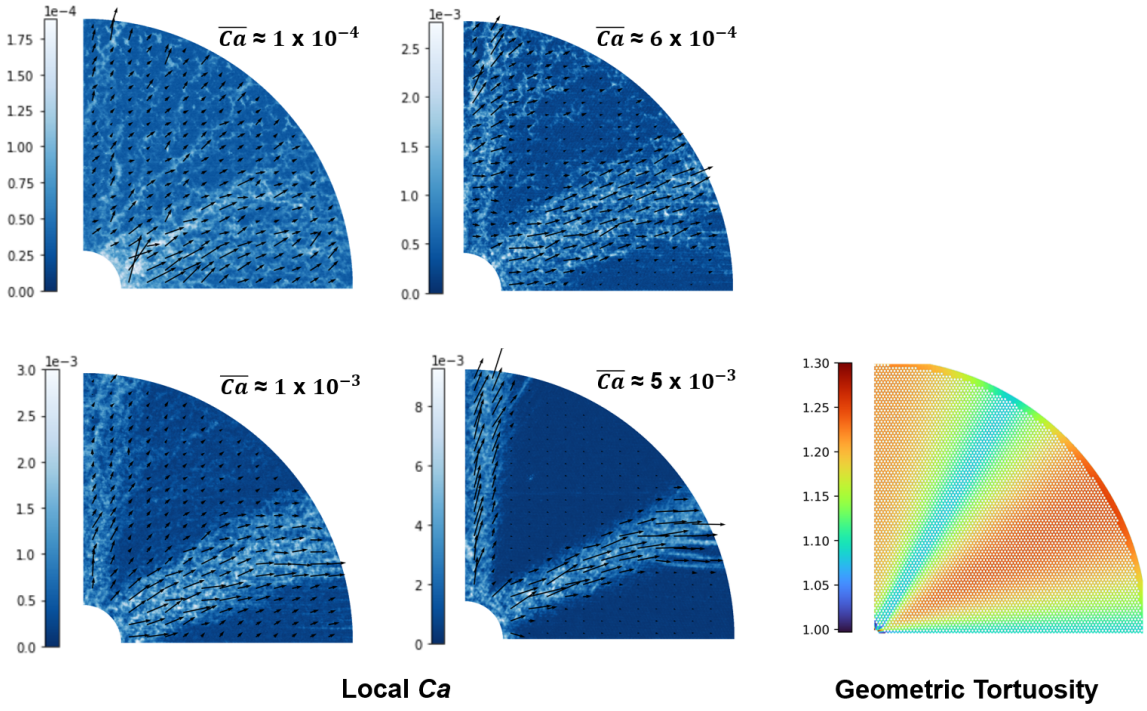

Fig. 3.45 Left) Maps showing the local Ca for experiments at four different injection $\overline{Ca}$. Maps were generated using the deep-learning-based method discussed in Section 3.2.5. Right) Tortuosity map of the hexagonal geometry from the central injection point. Radii of the porous media are ≈ 6 mm.

The angular averages of the droplet speeds are then normalised by the average velocities from 0° to 90° at the mid-radius $r = R/2$. The tortuosity map of the same geometry is also shown and the angular averages plotted for comparison in Figure 3.46:

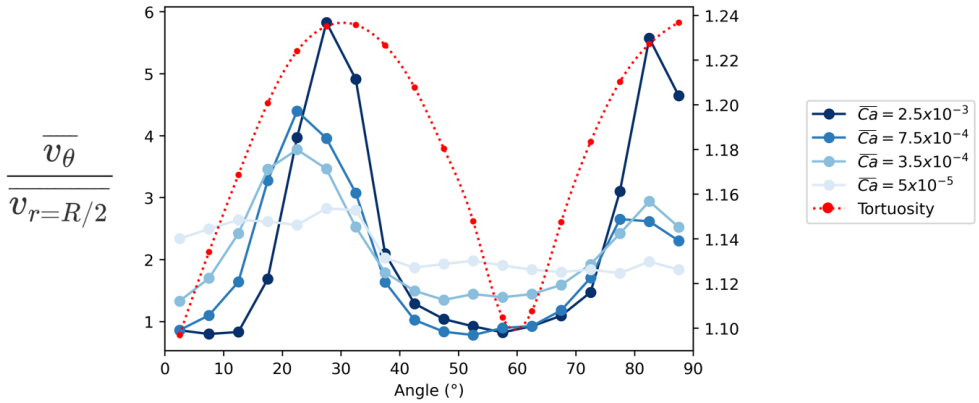

Fig. 3.46 Angular variations in average droplet velocities. The angular average of each of the velocity maps in Figure 3.45 were taken at intervals of 5° and normalised by the average velocities from 0° to 90° at $r = R/2$. Average values of the tortuosity map were also calculated the same way.

Summary: Role of the Injection Capillary Number

- During the filling phase, $\overline{Ca} \approx 10^{-3}$ leads to a highly heterogeneous droplet distribution, the geometry of which depends on that of the lattice microstructure.
- At $\overline{Ca} \approx 10^{-4}$, however, the droplets fill the micromodel uniformly, producing a homogeneous, circular front regardless of the regular lattice geometry chosen. Droplet velocities at $\overline{Ca} \approx 10^{-4}$ were also shown to be highly dispersed.
- During the stationary phase, a gradual transition from uniform to heterogeneous filling was observed with increasing $\overline{Ca}$.

Role of the Emulsion State

We can characterise the state of the emulsion injected into the porous media based on two parameters: droplet size and droplet volume fraction. Up until this point the ratios of the droplet diameter to the post spacing, D/d, have been greater than one and so the droplets had to deform in order to pass between the rows of posts.

Figure 3.47 shows the phase diagram charting the influence of these two parameters. The general trend is that at low D/d and droplet concentration the droplets fill the porous media homogeneously. As these parameters increase the droplet transport becomes highly heterogeneous. At high D/d and high droplet concentration the patterns formed by the droplet transport appear less contrasted as the porous medium becomes saturated in the dispersed phase. The gaps in the phase diagram are due to experimental difficulties in continuously varying one of the parameters whilst keeping the others constant. In the following subsections we expand on these observations for the two parameters separately.

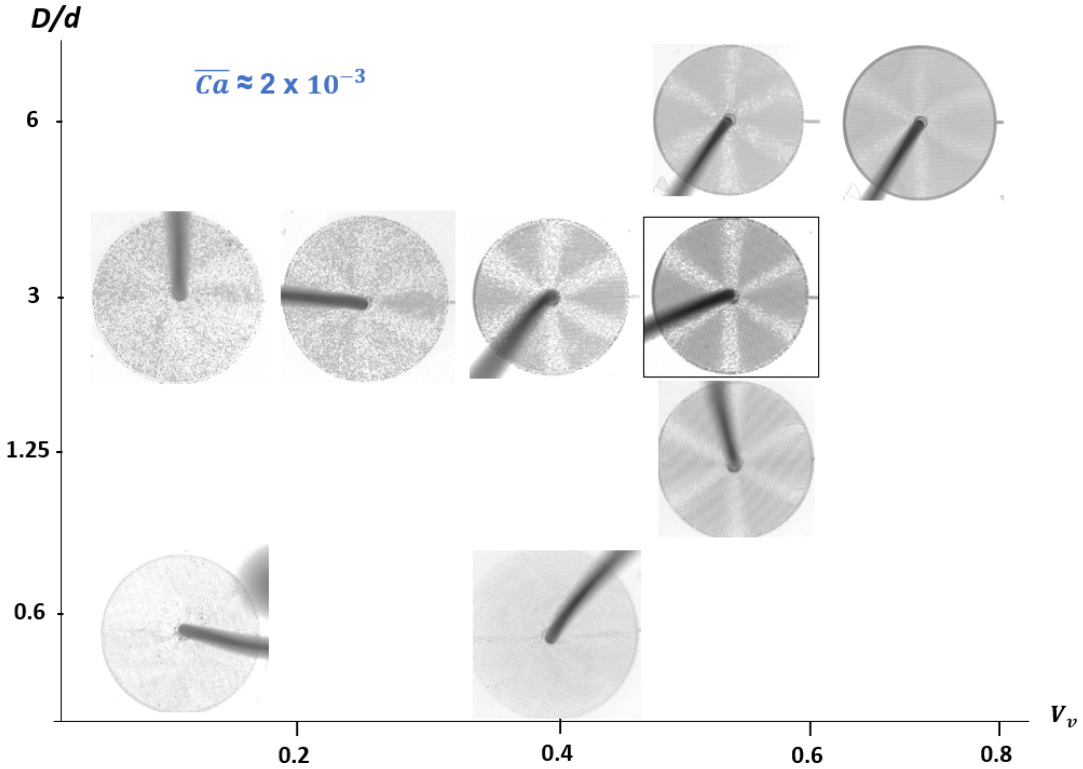

Fig. 3.47 Phase diagram for D/d and volume fraction (V_v) of the emulsion injected into the hexagonal lattice geometry at $\overline{Ca} \approx 2 \times 10^{-3}$.

Role of D/d

In all cases where $D/d > 1$ we see the same heterogeneous transport pattern. When $D/d \geqslant 3$ significant breakup of the droplet occurs when traversing the initial posts. The influence of breakup on the transport of the droplets is discussed in Chapter 3.

For droplets much smaller than the spacing between the posts and the height of the porous media, i.e. where $D/d < 1$ and $\psi < 1$ respectively, droplets filled the porous media uniformly and no flow intermittencies were observed. Several studies have in fact shown that for such 'bubbly' flows the droplets act like tracers in a Newtonian fluid [105, 63]. By tracking the motion of these small droplets we can therefore gain greater insight into the injection of a Newtonian fluid in the radial porous media. The tracking methods used previously don't work for these small droplets since the droplets aren't sufficiently contrasted for automatic detection and since droplets can overlap one another in the vertical direction making droplet detection difficult.

For the bottom left experiment in Figure 3.47 we instead took the pixel-wise differences between subsequent images in a series of 50 experimental images and then averaged the resulting images. In the final image shown in Figure 3.48 we see the unconfined droplets follow curved paths from central inlet to the outlet at the middle right of the image. These patterns resemble that of a dipolar potential flow between a source and a sink [19], which gives us the expected streamlines in the absence of the posts given the linearity of Stokes flow. This would, therefore, suggest that the flow of a Newtonian fluid injected at the centre point of the porous region is not perfectly radial and is in fact influenced by the unique exit channel to the right. The influence of these flow paths on the droplet transport has been minimal so far as the droplets were confined and considerably increase the hydrodynamic resistance of the porous region, making that of the circular channel negligible. However, as we will now see these streamlines become particularly important when the concentration of droplets injected is varied.

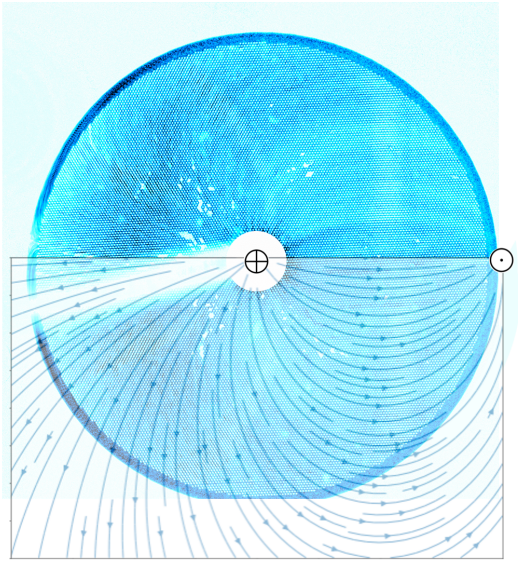

Fig. 3.48 Bottom left experiment from Figure 3.47. The pixel-wise differences between subsequent images in a series of 50 experimental images were determined. The images in the figure is the average of all the resulting images. On the bottom half, the plot of the dipolar potential flow between a uniform source ($\oplus$) and sink ($\odot$) has been superimposed for comparison.

Role of Droplet Concentration

If we consider Figure 3.47 where $D/d = 3$, as was the case in the prior experiments of this section, a continual transition between homogeneous and heterogeneous droplet patterns arises for constant $\overline{Ca}$ as the droplet concentration increases. We can deduce from this that the collective behaviour between droplets plays an important role in generating the heterogeneities.

In the case of the high concentration droplet flows, the large accumulation of droplets in the low-tortuosity zones adds significant resistance to the flow. The pressure drop across the porous media for these constant flow-rate experiments becomes far greater than in the surrounding exit channel and the resulting droplet transport exhibits little influence from the position of the sole exit as for small droplets adding little resistance in Figure 3.48.

The behaviour of the droplets in the low concentration experiment (top-left image in Figure 3.47) was considered more closely. Throughout the duration of this experiment we find no zones in the porous medium where droplets are trapped indefinitely. We have

already observed in both the linear and radial geometries that at the $\overline{Ca}$ considered here the droplets systematically follow the directions of low tortuosity. At the lower concentrations the fewer droplets across the radius of the porous medium add less resistance to the flow. We, therefore, observe droplet transport that appears to be on a spectrum from the purely dipolar streamlines for droplets of $D < d$ and the heterogeneous transport for $D > d$ and $V_v \geqslant 0.4$ where droplets primarily flow inline with the posts (low tortuosity directions). This situation is summarised in Figure 3.49. The patterns in the low concentration geometries would likely be more prominent if the flow was purely radial, i.e. if there was more than one straight exit channel. This may explain why we observe some accumulation amongst the droplets travelling at the 0° direction towards the exit at the middle-right of the porous region.

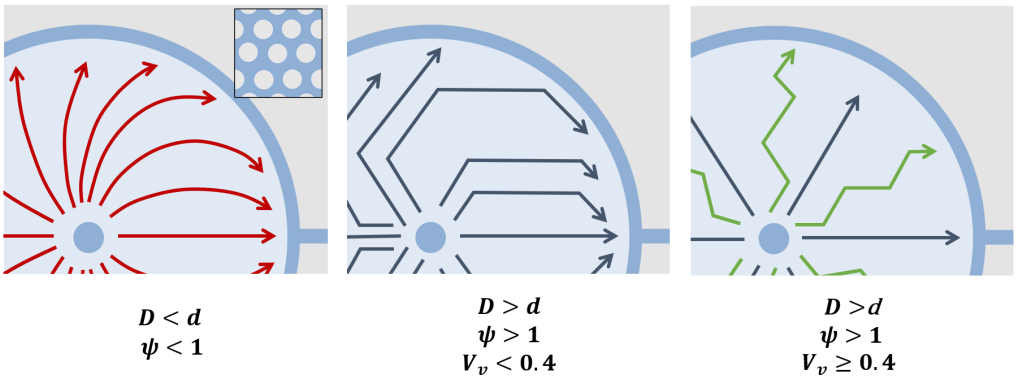

Fig. 3.49 Illustrations from droplet tracking performed on the hexagonal lattice geometries at various normalised droplet sizes and volume fractions. We observe a transition from purely dipolar transport (left, red lines) to purely following the low tortuosity directions between the posts (right).

Finally, for the two left-most experiments at $D/d \sim 3$, when $\overline{Ca}$ was subsequently increased for constant droplet size and concentration the flow become once again increasingly heterogeneous. The experiments were not tested for a long enough duration to see if coalescence could occur or if droplets were trapped for long enough periods and in close enough proximity to one another, producing an irreversible blockage.

Role of the Viscosity Ratio

The final variable considered in this chapter is the ratio of the viscosities of the dispersed to the continuous phase, $M = \eta_d/\eta_c$. A study was performed using the inverse

of the emulsion discussed thus far, i.e. drops of mineral oil in a continuous phase of water and blue methlyene ($M \approx 20$). Instead of SPAN 80, 1 wt% SDS was used as the surfactant which could be dissolved in the continuous water phase. The micromodels, bearing the same hexagonal lattice geometry, were instead plasma bonded to a glass slide and were used immediately after bonding, maintaining their hydrophilicity.

The resulting droplet flow patterns from an example experiment are shown in Figure 3.50 at $\overline{Ca} \approx 1$ x 10^{-4}, determined using the viscosity of the aqueous phase which is now the continuous phase. In previous experiments any heterogenieties in the flow presented themselves immediately. In this case, however, droplet transport was homogeneous during the filling phase and heterogeneities arose gradually over the course of approximately 60 minutes, at which point they bore a striking resemblance to those of Figure 3.43 for a water-in-oil emulsion at $\overline{Ca} \approx 1.7 \times 10^{-3}$ (insert in Figure 3.50). With the now dispersed oil phase having a dynamic viscosity roughly 20 times greater than that of continuous water phase, a greater degree of viscous dissipation occurs within the droplets [62, 75] and the pressure drop generated by a droplet passing through narrow pores is far greater than for the water-in-oil emulsion. The surfactant used is also different, since the water phase is now the continuous one, to which we add 1 wt% SDS in the water phase. During the stationary phase no droplets were observed to escape the porous region through the low-tortuosity directions. Whilst not studied systematically in this thesis, we can nonetheless deduce that the ratio of viscosities is also an important parameter in the formation of the droplet transport heterogenieties.

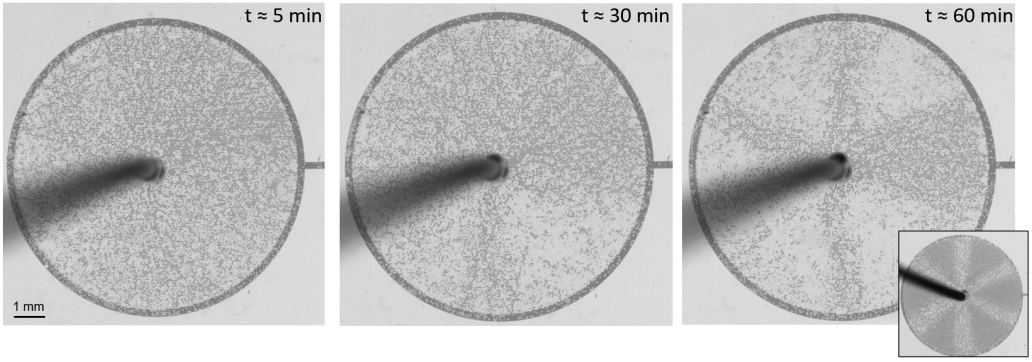

Fig. 3.50 Experimental images of an oil-in-water emulsion injected into the hexagonal geometry at $\overline{Ca} \approx 1.5$ x 10^{-3}. The oil drops are transparent and blue methylene (1 g/L) was added to the continuous phase. $M = \eta_d/\eta_c \approx 20$. $D/d \approx 3$ and the volume fraction of the droplets $V_v = 0.06$ (for which no patterns were observed in the case of the water-in-oil emulsion). Bottom-right insert is from Figure 3.43 at $\overline{Ca} \approx 3$ x 10^{-3}.

Summary: Role of the Emulsion State

- For $D/d > 1$ we see heterogeneous droplet transport, while at $D/d \ll 1$ the droplets act like tracers in a Newtonian fluid.
- As the volume fraction of the disperse phase is decreased, the blockages cause by high spatial concentrations of droplets become less severe and the flow becomes more homogeneous.
- At high $M = \eta_d/\eta_c$, the transport of the highly viscous droplets is not stationary, with the patterns changing in time. We are unable, however, to arrive at a strict conclusion on the influence of the viscosity ratio.

3.3.3 Pressure Measurements within the Radial Porous Media

All experiments in this thesis were performed at a constant flow rate $\dot{Q}$ using syringe pumps. In order to gain some insight into the pressure drop across the porous medium during the stationary phase, we undertook measures of the pressure at two different points along the radius, 4 mm apart from one another $r_2 - r_1 = 0.3R$, of the circular porous region. By using Darcy's law for radial geometries (equation 3.18) we can determine an effective viscosity of the emulsion as in equation 3.19 below:

$$Q = -\frac{kA}{\eta}\frac{dP}{dr} \tag{3.18}$$

$$\eta = 2\pi Hk\left(\frac{P_2 - P_1}{Qln(r_2/r_1)}\right) \tag{3.19}$$

We performed our measurements in three steps:

1. We first tested the calibration of the pressure sensor by connecting it directly to a fluigent pressure generator (Fluigent Flow EZ 2000mbar). Plotting the applied pressures (P_{app}) against the corresponding measured pressures (P_m), both in mbar, we obtained an equation for the corrected pressure $P_{cor} = (P_m + 17.33)/0.97$, based on the gradient of the line of best linear fit through the data points.
2. Secondly, we measured the pressure drop of the continuous phase only at two points in the porous medium, once at 0° from the exit channel in one model and then at 30° from the exit channel in a second micromodel (as was the case in

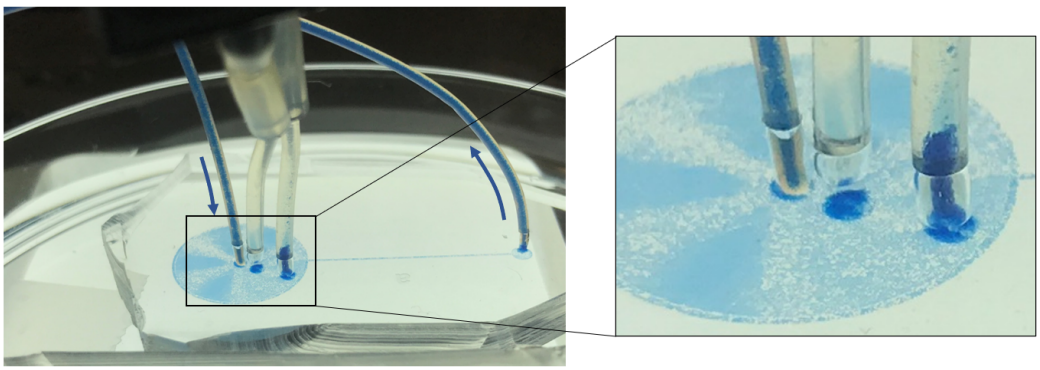

Fig. 3.51 Experimental set-up of the pressure measurement across two points in the porous medium. Both points fall on a line at 30° from the exit channel, a region normally of preferential transport (no trapping). We see the addition of the pressure tubes disturbed the normal flow behaviour, with droplets trapped below these tubes and some even entering them.

Figure 3.51). The measured viscosities at 0° and 30° were 10.4 mPa.s and 9.6 mPa.s respectively. Compared to the real viscosity of the continuous phase of 18 mPa.s, we have quite a large error of approximately 45%. Nonetheless, these measured values will allow us to determine the relative change in viscosity due to the addition of the droplets in the next step.

3. Finally, we measured the pressure drop in the geometry with the pressure points at 30° and in the case of an emulsion injection (Figure 3.51). By applying the same method as in the previous step, we determined an effective viscosity of the emulsion to be 33.9 mPa.s, over three times larger than continuous phase in the absence of droplets. We see from the image to the right of Figure 3.51 that the connection of the pressure sensor greatly influenced the flow of the droplets, with the only blockage in the same quadrant occurring directly below the tubes connected to the pressure sensor.

In order to limit the disturbance of the pressure sensor we subsequently tried connecting it using narrower tubing, however with this set up we were unable to measure stable values of the pressure drop, even for the continuous phase only. It would be interesting in future experiments to apply a constant pressure for the injection and not a constant flow rate, so as to see it's influence on the patterns formed by the droplets.

3.3.4 Towards Modelling the Droplet Transport

Furthermore, we recently collaborated with Hugues Bodiguel ("Laboratoire Rhéologie et Procédés", Grenoble INP) to see if we could create a simple model capturing the transport of the droplets and it's dependence on the different experimental parameters. We simplified the hexagonal arrangement of posts as a hexagonal mesh with rectilinear channels of constant cross-section, as can be seen to the left of Figure 3.52. Droplets enter at the bottom left node (orange) of the mesh at a prescribed frequency and capillary number and can exit at any of the outermost nodes (dark blue). For every iteration in the model the pressure differences are recalculated based on the length of the channels, the flow rates, and the number of drops in each channel. All pressure drops are calculated using the relation of Wong *et al.* assuming rectangular channel cross-sections [77, 78]. We don't account for any other interactions between droplets, such as collisions between droplets or dipolar perturbations.

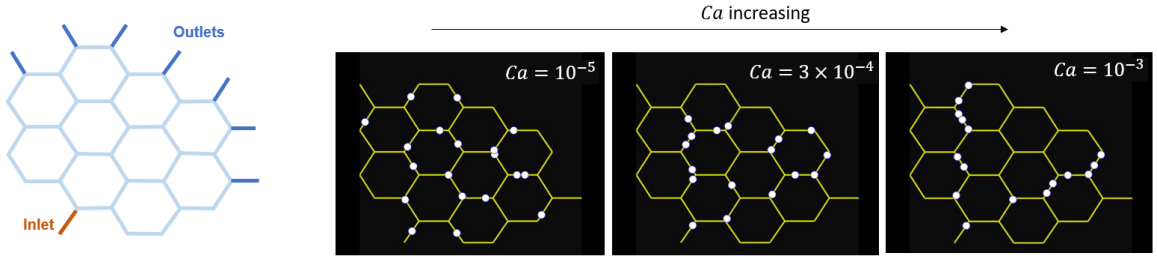

Fig. 3.52 Numerical model of the droplet flows through a simple hexagonal network of channels. Simulations performed by H. Boudigel.

Even for these simple parameters, the experimental filling phases are well produced by the model. The snapshots from the model on the right of Figure 3.52 for increasing Ca capture the same transition from homogeneous filling to heterogeneous filling in the low tortuosity directions as in Figure 3.41. Figure 3.53 also shows the DLD maps for the experiments at $Ca = 10^{-5}$ and $Ca = 10^{-3}$, clearly highlighting this transition from random path selection to preferential low-tortuosity paths.

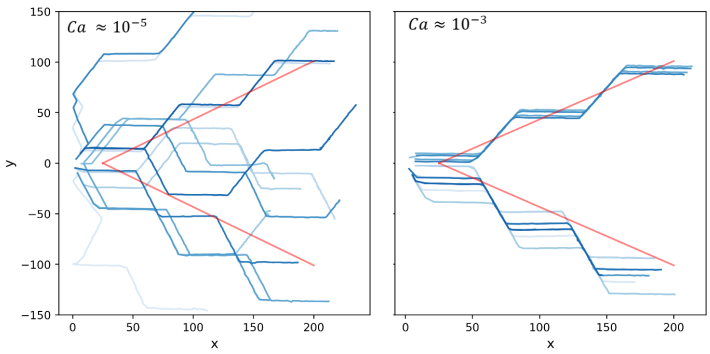

Fig. 3.53 DLD maps of the droplets at two different capillary numbers: $Ca \approx 10^{-5}$ (left) and $Ca \approx 10^{-3}$ (right). The red lines are at $\pm 30°$.

It remains to be seen, however, whether the model would be able to capture the stationary phase where the droplets in the high Ca flow block the low tortuosity paths, redirecting subsequent droplets through the high tortuosity paths. It would also be interesting to see if the influence of other parameters, such as the concentration of droplets injected, are in agreement with the corresponding experimental results described previously.

3.4 Conclusion and Perspectives

In our study we injected emulsions of monodisperse droplets into porous media consisting of varying lattices of cylindrical posts. By first considering flows through rectangular porous media, some of the main characteristics of the flow for droplets of diameter $D \geqslant 3d$ were ascertained. Firstly, the droplets flow along the directions of low tortuosity through the posts and not strictly along the directions of the pressure gradient for offsets of up to 30°. Secondly, the speeds of droplets become dispersed at $Ca \leqslant 2 \times 10^{-3}$ as droplets have greater difficulty traversing the pores. Finally, even in simple geometries the droplets don't spread out through the porous media uniformly, with areas of high droplet concentration forming. The droplets in these high concentrations zones travel markedly slower than those elsewhere in the porous media.

These results were then used to explain the striking patterns that emerged when the same droplets were injected at the centre of radial porous media. The patterns arise since droplets followed the local alignment of the posts, converging on the zones of low tortuosity which led to high droplet concentrations and significantly reduced droplet speeds in these zones. The patterns are due to heterogeneous droplet transport through the porous media and were observed to be particularly dependent on the injection capillary number ($\overline{Ca}$), the size of the droplets with respect to the channel height (ψ) and the pore widths (D/d), as well as the volume fraction of the droplets (V_v). Notably, at $\overline{Ca} \approx 10^{-4}$ confined droplets have greater difficulty overcoming the capillary pressure necessary to pass through pore constrictions, and the resulting collective droplet behaviour leads intermittent flows and a uniform filling of the porous media. At $\overline{Ca} \geqslant 10^{-3}$ confined droplets are able to flow freely through the pore constrictions and follow preferentially the paths of low tortuosity. Due to the confinement of the droplets, however, the pressure drop induced by each droplet leads to large hydrodynamic resistances in the areas of droplet congestion. A transition occurs where droplets instead flow preferentially in the directions of high tortuosity, a regime that remains stationary for the remainder of the experiment. Nonetheless, by subsequently reducing $\overline{Ca}$ the effect of the capillary pressure becomes preponderant and the droplets proceed to distribute themselves uniformly.

We subsequently studied the influence of the parameters of the porous media, such as the lattice structure, as well as the influence of the emulsion state, such as the confinement of the droplets, on the transport of the emulsion. We found that for all the regular lattice structures tested, droplets flowed preferentially in the high tortuosity

directions, as reflected by the microscopic pore structure, after having strongly concentrated in the low tortuosity directions. However, at $\overline{Ca} \approx 10^{-4}$, at droplet volume fractions $V_v < 0.2$, and for droplets of diameter $D \ll d$, the droplets filled the porous media homogeneously. For the random geometries, preferential flow paths were only observed in the pseudo-crystalline geometries that most resembled the regular lattices.

Finally, a new analytical tool was employed, based on a CNN approach, to allow for maps of droplet velocities within model porous media to be generated. This allows for the local capillary numbers at all positions in the geometry to be determined, which could correlated with the local concentration of droplets to quantify the resistance added by each droplet. Such instantaneous tracking of thousands of droplets, often of low contrast when compared to the surrounding posts, would be extremely challenging using traditional image analysis methods.

For further work, a study of droplet transport on a smaller geometry, similar in size to that of the simulations in Figure 3.52, could be performed. Reducing the complexity of the geometry and the number of droplets within it at a given time could allow for the mechanisms governing the transport to become clearer. Furthermore, adopting additional droplet formation techniques, such as using a T-junction droplet generator as opposed to the flow-focusing ones used in this study, could be tested. This could allow for lower droplet concentrations to be achieved, allowing the transport of very small numbers of droplets to be studied. Using rectangular geometries or those in Figure 3.52 would also allow for the droplet generator and the porous region to be incorporated on the same microfluidic device, simplifying the experimental procedure.

Another axis of further work would be to greater quantify the flow in the porous region. For instance, further pressure drop measurements, as in Figure 3.51, could be performed at different locations throughout the porous media. The measured pressure drops could be correlated to the positions within the porous media as well as the local concentration of droplets. Tests could be performed to isolate the influence of the vertical confinement (ψ) and the lateral confinement when passing through pore constrictions (D/d). Subsequently, the tortuosity maps could be updated to account for the reduced conductivity of the blocked passages. Injections with a pressure controller, as opposed to a syringe pump of fixed flow rate, could also give greater insight into the flow behaviour.

Chapter 4

Droplet Size Evolution in Porous Media

4.1 Introduction

As previously mentioned, microfluidic systems provide a means of producing emulsions with highly monodisperse droplets. In many microfluidics applications this droplet monodispersity is critical, such as in the formation of metamaterials or in the use of droplets as individual microreactors [8, 9]. However, if the droplets aren't stabilised by surfactants, if they encounter obstacles or undergo sharp changes in direction, or if the surface treatments of the channels through which they flow aren't adapted, the size distribution as well as the wetting of these droplets will evolve. As such, droplets can further breakup into smaller droplets or coalesce together until both phases are completely separated. Many industrial processes take advantage of the above factors to control the state of a dispersion. For instance, during high pressure homogenisation milk is forced through micrometric holes, reducing in size and uniformly dispersing the fat globules. With the fat globules small enough to be subject to Brownian motion they are less likely to adhere to one another and the stability of the dispersion is increased [115]. On the other hand, controlling the wettability of the surfaces of membranes can lead to forced coalescence of dispersed oil in water, facilitating its removal [116].

In this chapter we first present some of the literature on the breakup and coalescence of droplets or bubbles in porous media and the effect this can have on the transport of emulsions or foams respectively. We do so by first considering the behaviour of isolated droplets in simplified microfluidic systems, before moving on to the behaviour of groups of droplets in more complex porous media. The microfluidic experiments presented in Chapter 2 are then re-examined through the lens of variations in droplet size. The explanations for the stability of droplets, as well as its influence on the transport heterogeneities, are then discussed. All the experiments in this chapter involved favourable wettabilities in that the continuous phase preferentially wets the substrate as opposed to the dispersed phase. In the following chapter the influence of variable wettabilities is treated.

4.1.1 Droplet Coalescence in Porous Media

In the absence of surfactants, two essential conditions must be met for two droplets to coalesce: the droplets must come into contact with each other, and the thin film of continuous phase separating the droplets must be drained. For the film to drain, the stabilising forces arising from surface tension and lubrication must be overcome,

meaning the viscosity ratio of the two fluids also plays an important role. Furthermore, adding surfactants reduces the likelihood of coalescence by providing an electrostatic and/or steric repulsion between the fluid interfaces.

Some of the bulk mechanisms contributing to coalescence were discussed in Chapter 1. However, when droplets are under confinement at the microscale some of these mechanisms are exacerbated given the limited surfactant reservoir, large shear stresses, and high surface-to-volume ratios. Numerous microfluidic studies have been performed using controlled geometries and physico-chemical properties to better quantify the relevant pore-level mechanisms leading to droplet coalescence in porous media. Whilst many active methods for forcing droplet coalescence have been developed in recent years, we will focus solely on passive methods relying purely on the nature of the flow and the geometry.

Without Surfactants

In the absence of stabilising agents, contact between droplets is normally sufficient to induce their coalescence [117]. Even in a straight channel, preventing droplets from contacting one another is no simple task due to the hydrodynamic interactions between confined droplets discussed in the previous chapter [87].

Furthermore, if the speed of one droplet is greater than that of the next drop upstream from it then the distance between the two will diminish until they contact one another. This can occur in channels or pores of size d where $d \sim D$ when the leading droplet is larger than the following one (Figure 4.1, left) or has a greater viscosity (Figure 4.1, middle) as in both cases the leading droplets present a greater hydrodynamic resistance [118]. Additionally, when two identical droplets pass through a row of pillars where $d < D$ (Figure 4.1, right) or a channel expansion (Figure 4.2, left) the slowing of the first droplet can cause the two droplets to collide [119, 15].

In all of these studies the absence of surfactants led to the coalescence of all droplet pairs following their contact. The droplets in the first three studies coalesced immediately after contact. In the latter study the two droplets travelled a distance of $x \approx 10D$ after the collision before coalescing. Bremond *et al.* further observed that a subsequent passage of the closely-spaced droplets through a converging channel, causing the droplets to move apart from one another, led to a locally lower pressure

between the droplets and in fact forced the coalescence 10 times faster at $x \approx D$ [15].

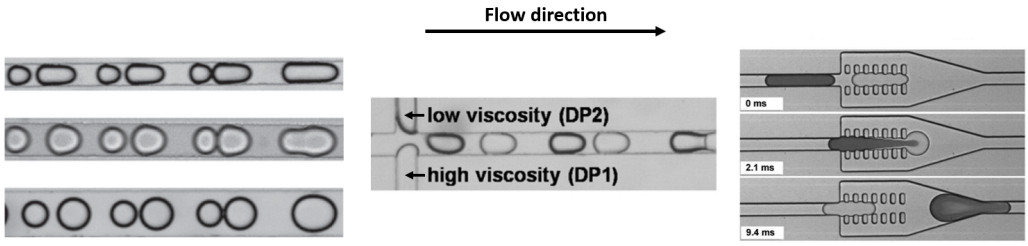

Fig. 4.1 Controlled coalescence of droplets. Coalescence induced by alternating the sizes (left) and viscosities (middle) of successive droplets [118], or when the droplets are slowed down whilst passing through an array of pillars (right) [119]. Channels (left, middle) and the entrance channel (right) have a width perpendicular to the flow of 50 µm. No surfactants were added to the fluid systems.

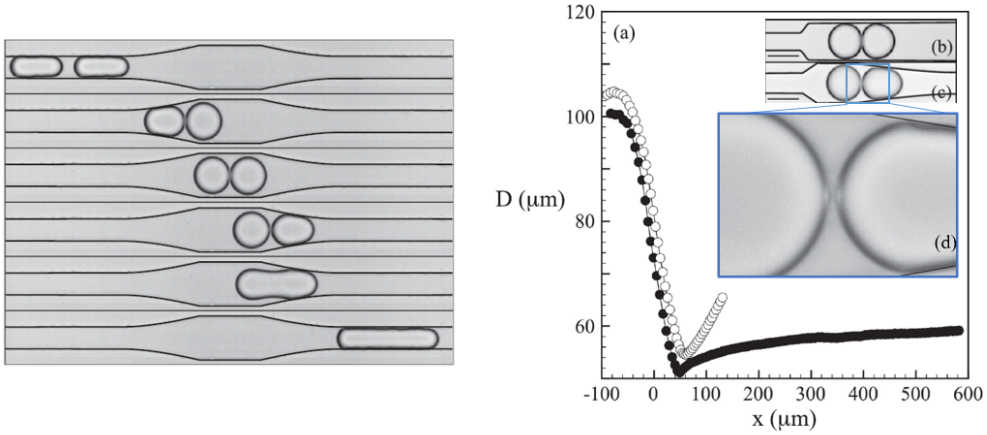

Fig. 4.2 Droplet contact induced by a diverging channel then converging channel and coalescence forced by a subsequent converging channel [15]. The distances travelled by the drops before coalescence with (•, insert 'b') and without (∘, insert 'c') the converging channel are shown in the graph on the right. Channel widths perpendicular to the flows are 36 µm - 72 µm (right). No surfactants were added to the fluid system.

Finally, increasing continuous phase viscosity η_c can invoke longer film-drainage times, meaning droplets must remain in contact with one another for longer if coalescence is to occur. Bibin *et al.* studied coalescence of droplet trains for varying Ca and η and suggested that the film-drainage time-scale τ_{dr} is proportional to the viscous-capillary time-scale $\tau_{cap} = \eta_c h/\gamma$ such that $\tau_{dr} \sim 10^3 \tau_{cap}$ [120].

With Surfactants

In most applications droplets are stabilised by adding stabilising agents such as surfactants. In addition to the information in Section 2.1.2 on surfactants, we will now discuss some of the necessary considerations concerning surfactant stabilisation in micro-scale applications.

One of the primary phenomena for understanding emulsion stabilisation using surfactants is based on the necessary adsorption times (τ_{ads}) such that surfactants may sufficiently cover the interface to provide stability. This means that during, and possibly immediately following, droplet formation the interfaces are not at equilibrium, with a reduced surfactant coverage facilitating their coalescence. In microfluidics, τ_{ads} is not negligible with respect to that of droplet formation (τ_{form}), given by the inverse of the droplet generation frequency and during which fresh interfaces are created. For a typical droplet generation frequency of 1000 Hz, τ_{form} is of the order of 1 ms, which is consistent with that of Bremond *et al.* [15]. We can, therefore, state that:

$$\begin{cases} \tau_{ads} < \tau_{form} : & \text{Suitable for droplet stabilisation} \\ \tau_{ads} \approx \tau_{form} : & \text{Some droplet coalescence} \\ \tau_{ads} > \tau_{form} : & \text{No droplet stabilisation} \end{cases}$$

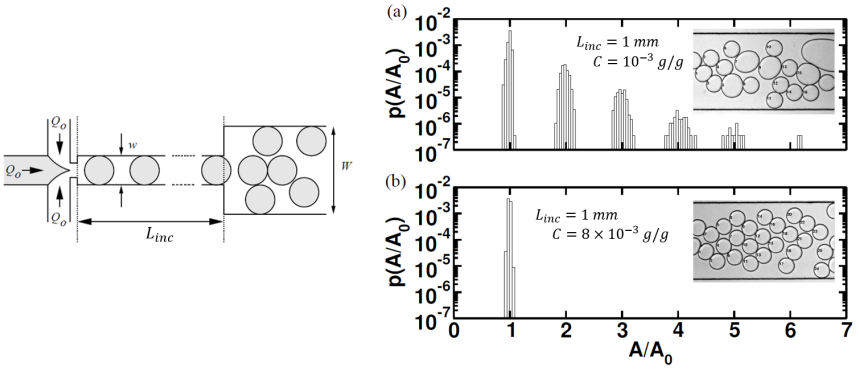

Fig. 4.3 (a) Polydisperse droplet population following coalescence in the case of insufficient surfactant concentration. (b) Monodisperse emulsion stabilised with a sufficient surfactant concentration. Adapted from Baret *et al.* [121].

In order to stabilise droplets, it is crucial to allow an adequate "incubation" time ($> \tau_{ads}$) so that the surfactants can sufficiently coat the surfaces of the droplets before

contacting neighbouring droplets. The necessary incubation time can be reduced by adding a greater surfactant concentration ($\gg CMC$). This situation is illustrated in Figure 4.3 for two different surfactant concentrations following a constant incubation length L_{inc} (Figure 4.3) where $L_{inc} \propto$ time. A very similar figure was also obtained for constant surfactant concentrations but by varying L_{inc} [121]. In their article, Baret *et al.* proposed a stability criterion, formalising the necessity that the incubation time be greater than the adsorption time:

$$L_{inc}C^2 > \frac{f_i^2}{\delta^4 D_m {N_A}^2} \frac{Q_{tot}}{WH} \tag{4.1}$$

where C is the surfactant concentration, f the fraction of the interface covered by surfactant molecules (the minimum necessary coverage for stable droplets depends greatly on the surfactant but can be as low as 10%), δ the lateral dimensions of a molecule at the interface (typically 2 nm), D_m the micelle diffusion coefficient (typically 10^{-12} m^2/s), N_A the Avogadro constant, Q_{tot} the total flow rate, and W and H the width and height of the channel cross-section respectively. For the systems studied by Baret *et al.*, $L_{inc}C^2 = 10^{-9}$ m(g/g)^2 defined the threshold below which coalescence is very unlikely and above which it is very likely. Whilst this threshold may be difficult to calculate in many cases, it nonetheless provides some quantifiable insight into droplet coalescence probability. In the case of the droplets formed in droplet generators in this study, and using $D_{SPAN80} = 10^{-11}$ m^2/s, we get the condition $L_{inc}C^2 > 2 \times 10^{-7}$ and an incubation length of ≈ 5 µm, approximately 7 % of the diameter of the droplets most frequently studied.

It should also be noted that when droplets flow under confinement the concentration of surfactants is not uniform over the surface, as was shown for droplets flowing in a Hele-Shaw cell where surfactants accumulated at the rear of the droplets [82]. Furthermore, when droplets flow through porous media, such as when passing through a constriction, the shape of the interface and thus the surfactant distribution can vary [122]. A good example of this can be seen in the simple geometries of Bremond *et al.* who repeated their experiments discussed above only this time adding a high concentration of surfactant ($\approx 10^2$ CMC) [15]. No coalescence occurred for the purely diverging channel that caused droplet contact (Figure 4.2, right, insert 'b'). For the diverging-converging channel (Figure 4.2, left and right, insert 'b') forced-coalescence still occurred despite the surfactant concentration being 10 times larger than that needed to fully cover the interfaces and $t > \tau_{ads}$. The localised deformation of the

droplets at their contact point (Figure 4.2, right, insert 'd') had a characteristic time that was estimated to be 10 times greater than τ_{ads}. The ensuing local depletion of surfactant molecules at the droplet contact point enabled coalescence to occur. In the case of a train of closely-packed droplets this even had the effect of triggering a cascade of forced-coalescence across all of the droplets. Finally, localised depletions in surfactant concentration could also arise following droplet breakup whilst passing through a porous medium, which we now discuss.

4.1.2 Droplet Breakup in Porous Media

As formalised by Kovscek and Radke [35] there are three fundamental pore-level mechanisms through which a dispersion can be formed in a porous media. These three mechanisms are displayed in Figure 4.4. The first is snap-off where the interface forms a thin finger due to the passage through a pore constriction initially filled with the wetting fluid. Snap-off requires a gently sloped pore with a pore body-to-throat ratio larger than roughly two. The resulting droplets have roughly the same size as the pore bodies. The second mechanism, division, occurs when a translating bubble or droplet encounters a point where the flow branches in two different directions, causing it to split into two separate bubbles or droplets. For this to happen the droplet must have a size larger than that of the pore body. It is also highly dependant on the capillary number of the flow. The resulting droplets can vary in size from one another, depending on the pore geometry and the downstream flows to either side. Finally, the third mechanism is leave behind and occurs when two fluid fingers invade adjacent pores before converging further downstream. In general snap-off is very common amongst trapped droplets whilst division has been most frequently observed for moving droplets [35, 99, 123].

So as droplets or bubbles pass through a porous medium under certain geometric and flow conditions they can continuously divide until reaching a size close to that of the pore body. This continuous breakup has been studied extensively experimentally for foams or emulsions in model porous medium [99–101, 124]. Experiments studying the behaviour of isolated drops in simplified microfluidic geometries consisting of T-junctions [125–130] or channels containing a single obstacle [104, 125, 131] have also allowed for greater understanding of the mechanisms and conditions for droplet breakup. Consequently, the following trends and phase diagrams have been established:

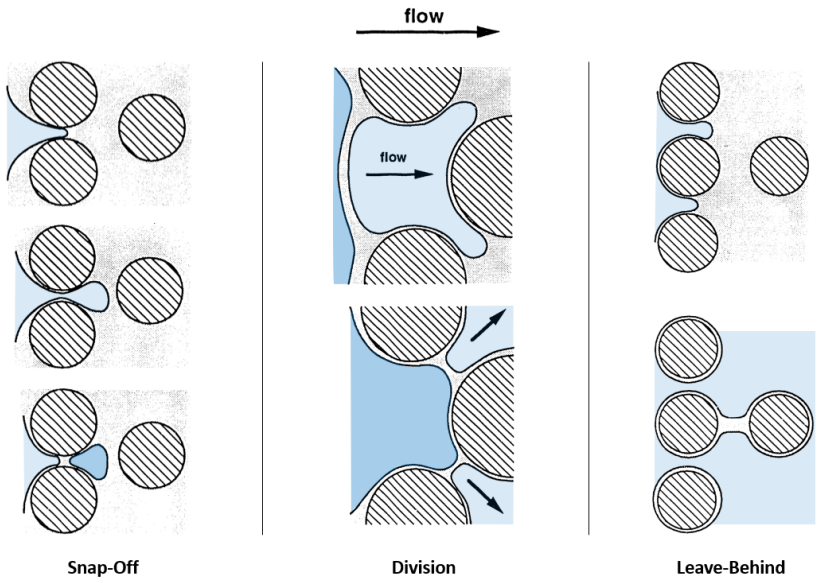

Fig. 4.4 The three classically recognised pore-level mechanisms for droplet/bubble generation in a porous medium (adapted from Kovscek and Radke [35]). The continuous phase is transparent and the continuous, aqueous phase is in blue, different shades of which are solely to enhance visualisation.

- Firstly, the degree of droplet breakup increases with capillary number Ca. Higher Ca means greater pressure and droplet deformability. This increased deformation facilitates snap-off. Also, when droplets encounter any obstacles, they are more likely to diverge around them and divide as opposed to maintaining a spherical form through surface tension and passing to one side of the obstacle. This was quantified by observing the size of droplets leaving the medium at various capillary numbers, for porous media [101] and porous membranes [124]. At low capillary numbers of around $Ca < 10^{-5}$ low levels of droplet breakup are observed and droplet sizes at the outlet are highly polydisperse, reassembling those in Figure 4.6b with a mix of large unbroken droplets and small droplets following breakup. As Ca increases droplet breakup becomes more prominent before reaching a plateau at around $Ca = 10^{-4}$, both in terms of mean droplet diameter and droplet diameter polydispersity at the outlet. Similar variations with Ca were also observed in simplified microfluidic geometries consisting of T-junctions [125–130] or channels containing a single obstacle [104, 125, 131]. In these latter cases, the increase of the upstream pressure has been found to be responsible for droplet breakup [127].

- Secondly, the degree of droplet breakup depends on the diameter of the droplets, or more precisely the ratio of this diameter to the pore spacing, D/d. As mentioned, breakup of moving droplets occurs mainly through division: droplets smaller than the pore body rarely divide, whilst very large droplets may split several times over before arriving at a stable diameter on the order of d [35]. In addition, the final diameter of outlet droplets is not expected to be dependant on inlet droplet diameter [35].

  Phase diagrams, such as that of Jullien *et al.* and Salkin *et al.*, highlighting the dependency on Ca and droplet confinement D/d have been developed [128, 132], as shown in Figure 4.5. Interestingly, for T-junctions all droplets ruptured beyond a critical length [128] whereas in obstacle geometries the Ca required for droplet rupture to occur increased for increasing droplet size [132].

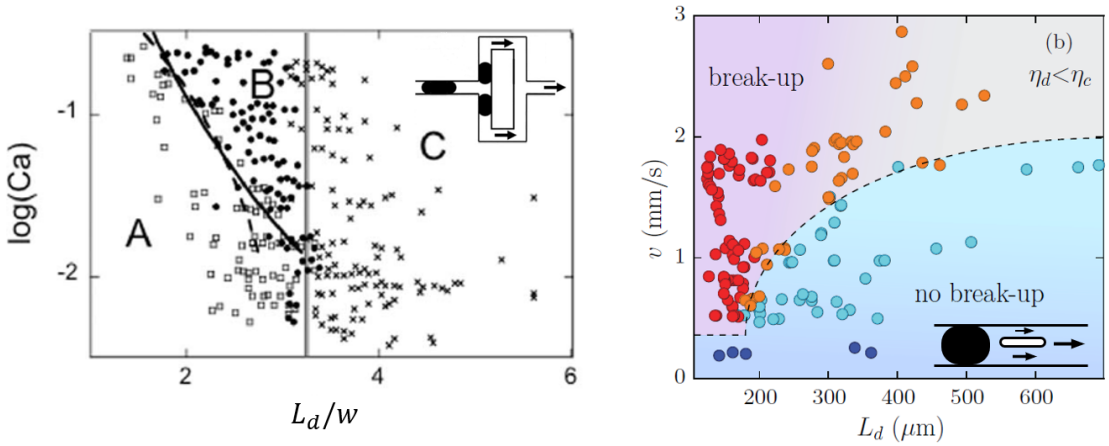

Fig. 4.5 Phase diagrams by Jullien *et al.* (left) and Salkin *et al.* (right) for the passage of isolated droplets through T-junctions or past an obstacle in a channel respectively [128, 132]. Left) Water droplets in hexadecane + SPAN80 with a viscosity ratio between the dispersed (η_d) and continuous (η_c) phases of M=η_d/η_c =0.11. The diagram highlights instances of no droplet breakup (A) and two types of droplet breakup (B and C) as a function of droplet length in the channel. Here, L_d and w are the droplet length and channel width respectively. The solid line separating regimes A and B is the theory of Leshansky and Pismen [127]. Right) Water droplets in a viscous silicone oil, M=0.02. L_d is initial droplet length, and the obstacle had a length of 300 µm. Similar trends were developed for the case where M>1.

- Thirdly, droplet breakup increases with the length of the porous media, i.e. the total distance or the number of obstacles traversed by the dispersion through the porous media. Once again, only this time at constant Ca, droplet diameter and droplet diameter polydispersity were shown to quickly plateau. By studying a simplified system consisting of alternating channels and porous regions, Quennouz *et al.* showed that initially large air bubbles converged on a normalised droplet diameter of 0.44 times that of the post diameter, with a coefficient of variation of 50 %. This was reached after traversing 20 mm of porous media ($>$ 100 times greater than the post diameter) as shown in Figure 4.6 [57]. Most droplet breakup occurs, therefore, in the initial region of a given porous media, as further quantified by Yeates *et al.* who produced probability density functions for droplet diameters at various sections along the porous medium [100]. Similar values for the ratio of the droplet diameter to the pore body width were found elsewhere in the literature, such as by Mauray *et al.* [101]. More generally it has been observed that:

$$\bar{D} = \alpha d \tag{4.2}$$

where $\bar{D}$ is the mean droplet diameter at the outlet of the porous medium, d is the pore body size, and α is a proportionality constant that notably depends on the interfacial tension γ of the fluids considered and the droplet velocity. Gomaa *et al.*, Mauray *et al.*, and Yeates *et al.* all found values of α of around 0.4-1 [101, 100, 133].

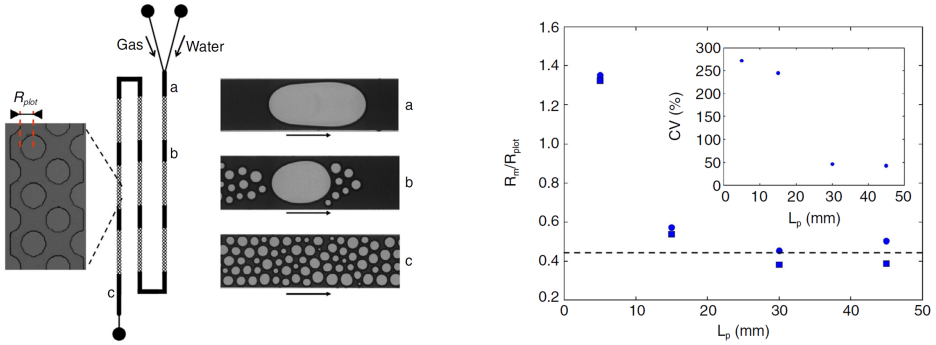

Fig. 4.6 Study by Quennouz *et al.* [57]. Left: Porous medium used for foam generation with snapshots of *in situ* bubbles a three locations in the porous medium. Right: Mean outlet bubble radius R_m normalised by post radius R_{plot} and coefficient of variation in bubble size (inset) as a function of length of the porous medium traversed L_m. Dotted line is at $R_m/R_{plot} = 0.44$

- Lastly, droplet breakup depends on the ratio of the dynamic viscosities of the two phases in the dispersion, M. Jullien *et al.* and Salkin *et al.* also produced similar phase diagrams to those in Figure 4.5 but for the case where $M \gg 1$ [128, 132]. They found that droplet breakup depends greatly on the viscosity ratio of the two phases, with droplet breakup initiating at lower Ca when the dispersed phase is less viscous than the carrier phase.

One final thing to note is that collisions and interactions between droplets can too influence breakup. Droplet collisions have already been shown to govern droplet transport for certain flow regimes in both simplified geometries [70, 85, 86] and porous media [99, 105]. Droplet division has been observed for isolated drops, but can also be forced through collision from a subsequent droplet (as in Figure 4.4). For instance, the influence of a droplet on the local hydrodynamics in a channel also changes following rupture, which can influence the rupture of preceding droplets [104]. Additionally, Liontas *et al.* highlighted two mechanisms by which breakup could be forced through squeezing from neighbouring bubbles, as shown in Figure 4.7 [134]. Droplet concentration, as measured by the volume fraction of the dispersed phase with the total volume, could therefore influence the distance required before a stationary dispersion at the outlet is reached, as a higher droplet concentration would likely lead to more such droplet interactions. To our knowledge, however, no such quantification exists.

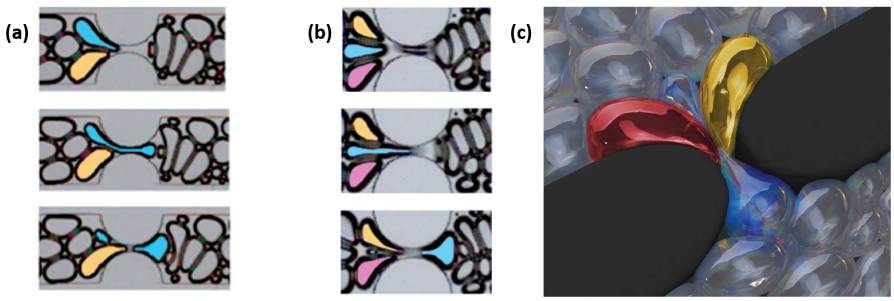

Fig. 4.7 New collective bubble formation mechanisms observed by Liontas *et al.*. Time series of (a) neighbour–wall pinch-off (ΔT = 61 µs) and (b) neighbour–neighbour pinch-off (ΔT = 66 µs) adapted from [134]. (c) 3D schematic drawing of (b). Colours added afterwards to highlight bubbles of interest. Diameter of constriction = 380 µm.

4.1.3 Size Dependant Droplet Transport

When droplets larger than the pore throats and the channel height traverse a porous media, they experience significant friction at their menisci along the channel walls in horizontal and vertical planes. Furthermore, to pass through a pore neck the pressure drop across a given droplet must also overcome the capillary pressure or else the droplet can become trapped, causing intermittent flow. This phenomena is of particular importance at $\overline{Ca} < 10^{-4}$ [101]. On the other hand, droplets smaller than the channel height are much less impacted by wall friction that larger droplets, require less deformation to pass through narrow pore necks, and follow the central streamlines of the Poiseuille flow, thus exhibiting a higher average velocity than the larger droplets.

Given that droplet transport in porous media is a continuous process of repeated droplet breakup and coalescence, the mobility of the droplets is therefore highly dynamic. This has been evidenced experimentally, both from the fluctuating pressure drops measured during dispersion injection in porous media [135] and qualitative observations [99, 100, 136] that dispersion transport is dynamic and unstable.

4.1.4 Conclusion

In summary, the fate of droplets in a porous medium (breakup or not, their mobility, etc.) depends on a vast set of parameters such as the capillary number, droplet size, pore size, length of the porous medium, the nature of the surfactant, surface tension, and the viscosity ratio of the two phases. We want to investigate how the state of the emulsion evolves in the radial injections discussed in Chapter 3 based on the various parameters described above. To do so, we compare the initial monodisperse droplet diameters to those at various locations within the porous media as well as in the outlet channel. We also considered how the continuously evolving diameter and confinement of the droplets in the emulsion influences transport through the porous media in our experiments.

4.2 Results

4.2.1 Initial Observations

We systematically varied the injection capillary number of the emulsion, the size and volume fraction of the droplets and assessed the evolution of droplet size in the various radial geometries from Chapter 3. Observations took place both in the exit channels and at the pore-scale within the porous media.

In this chapter we used the same water-in-oil emulsion as primarily studied in Chapter 3. Before considering the behaviour of the emulsion within the porous media, we first consider its stability at bulk. The emulsion was prepared and collected into a plastic beaker for 30 minutes. Directly after the 30 minutes, the emulsion was stirred to evenly distribute the droplets, and a few drops of the emulsion were placed on a glass microscope slide. The diameters of the droplets were recorded and the observation procedure repeated on a new glass slide twice more, both at 30 minute intervals. The resulting graph in Figure 4.8 shows the coefficient of variation (CV) in droplet diameters, equal to the standard deviation in droplet diameters normalised by the mean droplet diameter. Despite the repeated agitation of the droplets and even after 1 hour, longer than any of the experiments considered in this chapter, the coefficient of variation in droplet diameters didn't surpass 16 %. We can therefore conclude that the emulsion is stable in bulk during at least the first hour.

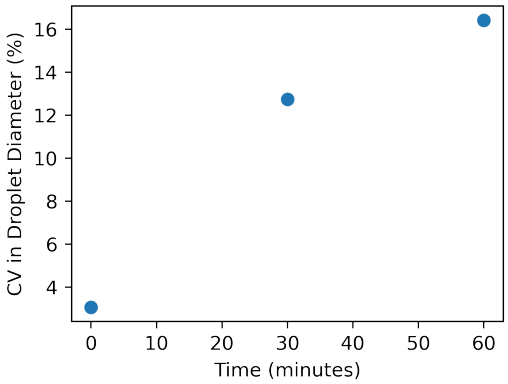

Fig. 4.8 Coefficient of variation in droplet diameters at 30 minute intervals. The emulsion was collected in a plastic beaker and the droplet diameters observed under a microscope after stirring the collected emulsion and placing a few drops of it on a glass slide.

Figure 4.9 shows microscope observations at three locations in the square geometry. These images were also taken approximately 1 hour after initial injection of the emulsion, equivalent to the injection of around 300 pore volumes. In and around the regions of preferential flow, or rather the regions of high tortuosity (Figure 4.9B), we see lots of droplet breakup has taken place, with droplets now having a diameter similar to that of the pore body size. Many droplets can also be seen to overlap which makes automatic droplet detection and size measurement difficult.

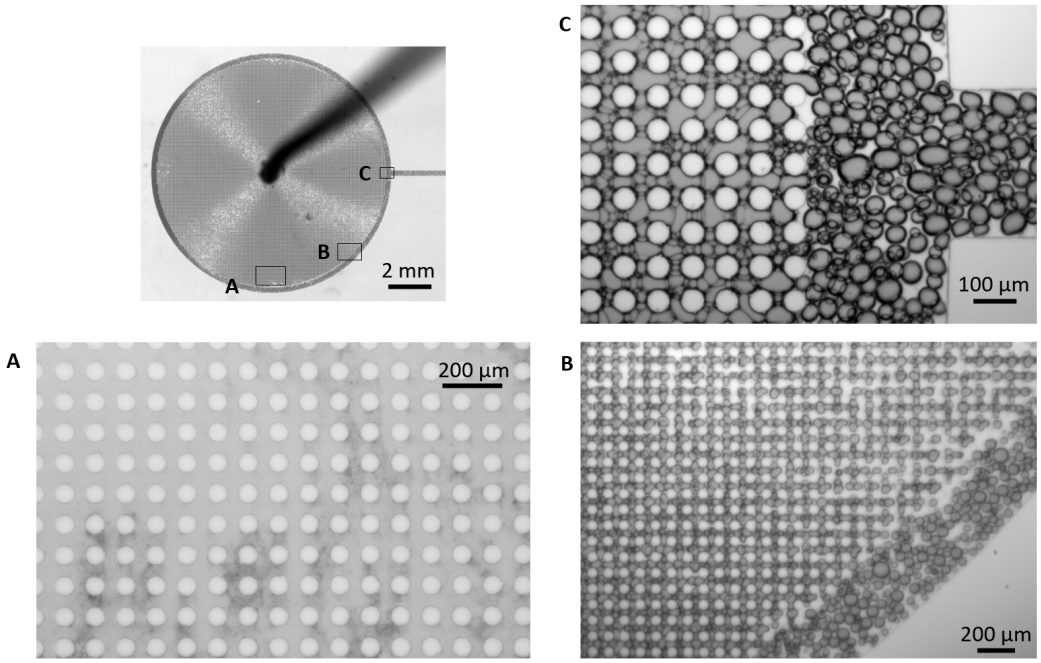

Fig. 4.9 Top left: Macroscopic view of the stationary phase of emulsion injection in a porous medium witch a square lattice geometry of posts. A-C: Microscope images of the flow at three locations within the micromodel.

In the regions of high tortuosity, such as in Figure 4.9C next to the exit channel, we see droplets in the porous region are highly compacted with very little of the continuous phase visible between droplets. However in Figure 4.9A, still in a region of low tortuosity only further away from straight exit channel, extensive coalescence can be observed. Such coalescence renders large regions of the porous media permanently blocked, and was observed for all three regular lattice geometries.

For the remainder of the experiments in this chapter, observations are performed at time intervals ranging from 5 to 30 minutes after initial injection. The exact time

at which observations were performed had negligible influence on the droplet size distribution at the outlet. To quantify this we performed one experiment using the hexagonal geometry - the droplets at the exit were measured to have CVs in their diameter of 17 % after 5 mins and 16 % after 30 mins.

As for the mechanisms of droplet breakup, we primarily observed division which most frequently occurred near the inlet, i.e. for small values of r where r is the radial distance from the central injection point. Figure 4.10 shows an example of division during the filling phase for the hexagonal geometry and for a droplet positioned at around $r/R = 0.25$ where R is the radius of the entire porous region. Snap off was also observed for large coalesced drops at the edge of the porous region, albeit at much lower frequencies. We understand that capillary snap-off is unlikely to occur in a model bearing this geometry, owing to the large aspect ratio necessary in 2-dimensional media [134]. As a result, we chose not to extensively study droplet fragmentation dynamics, unlike in certain other studies [137, 99]. We instead focus more-so on global trends of breakup.

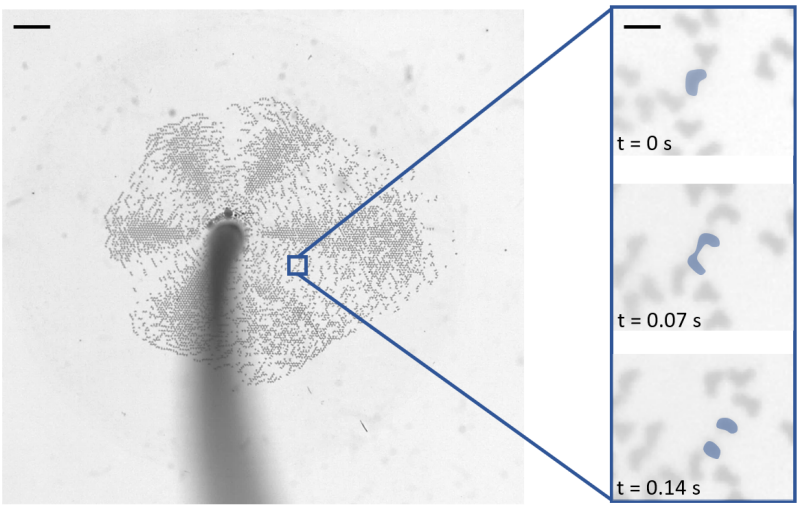

Fig. 4.10 Left: Macroscopic view of the filling phase of emulsion injection in a porous medium witch a hexagonal lattice geometry of posts. Right: Time series of images showing droplet division around a post.

Summary: Initial Observations

- Significant droplet breakup was observed within the porous media, primarily through division and near the inlet.
- The droplets in the emulsion studied are mostly stable in bulk after one hour (droplet diameter CV = 16 %) whereas droplets trapped in the porous medium for the same duration appear to completely coalesce.

4.2.2 Influence of the Injection Capillary Number

The injection capillary number, $\overline{Ca}$, has been shown to play a key role in droplet stability for both simplified geometries and porous media. Furthermore, in the previous section we saw that increasing $\overline{Ca}$ led to a heterogeneous droplet transport through the porous media. These heterogeneities lead to angular variations in the local capillary number, Ca, as evidenced by the large disparities in droplet speeds. In regions of high droplet concentration droplets flow much slower, even to the point of being trapped and eventually coalescing. These blocked regions cause an effective decrease in porosity and subsequent droplets flowing in the remaining preferential paths experience a higher $\overline{Ca}$. A map of the heterogeneities in Ca throughout the porous media at various injection capillary numbers is shown in Figure 3.45.

To study the influence of $\overline{Ca}$ we injected a monodisperse emulsion in the hexagonal geometry at various $\overline{Ca}$ and measured the average apparent diameters of the droplets in the straight exit channel. The emulsion was produced using the same droplet generator and by applying the same flow rates each time. These resulting droplets are larger than the minimal pore spacing such that $D/d \approx 3$. The injection flow rate was then applied before the preformed emulsion was injected into the porous media, as per the method detailed in the previous chapter. For each experiment only one flow rate and thus global Ca was considered. The micromodel was then rinsed with ethanol meaning no residual droplets were left in the porous region between experiments.

The probability density functions (PDFs) of the apparent diameters of the droplets at the exit as a function of $\overline{Ca}$ are shown in Figure 4.11. These were determined by automatically thresholding and analysing several thousand unique droplets at the exits of the porous media, using the methods described in section 3.2.5. The PDF of the

droplets in the droplet generator are also shown for comparison. The same data are shown in both graphs of the figure. For visibility of the data, a secondary y-axis was used for the inlet drops in the graph on the right.

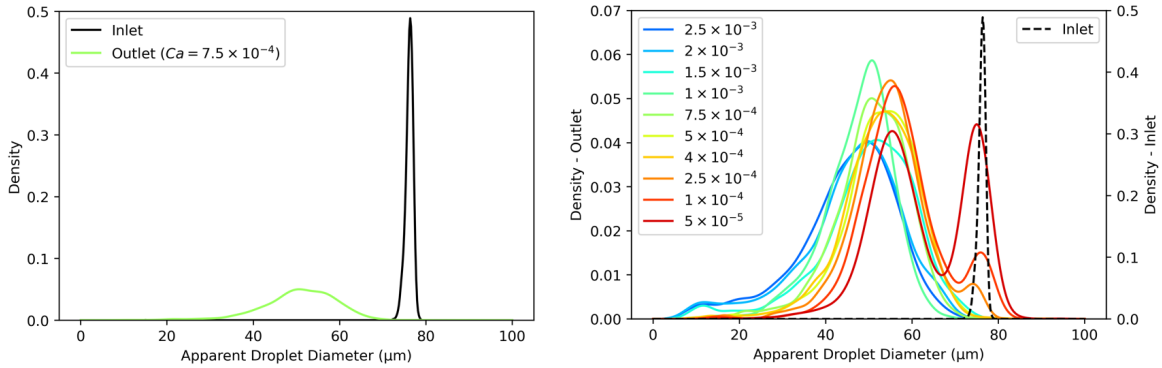

Fig. 4.11 Probability density functions (PDFs) for diameters of droplets at the outlet of the hexagonal porous media at various $\overline{Ca}$ and for $D/d \approx 3$ at the inlet. Note that for the graph on the right, the primary vertical axis is for the outlet droplets and the secondary one is for the inlet droplets and is at least one order of magnitude larger.

For the three lowest $\overline{Ca}$ we see the distributions are bimodal - some droplets are able to travel through the entire porous media without splitting or coalescence. The degree of droplet breakup can be determined from the offset of each peak in the probability distributions from that of the inlet droplets as well as from the width of the distributions. As expected, we see that droplet breakup increases with $\overline{Ca}$. For $\overline{Ca} \geqslant 10^{-3}$ there appears to be little change in droplet size distribution at the outlet, even after further increasing Ca by over two orders of magnitude. The mean droplet size at this plateau is $D/d \approx 2$ and $D/H \approx 1$. It should be noted that coalescence, and thus droplets larger than those initially injected were also observed exiting the porous media, however they remained rare in comparison to smaller droplets.

In order to gain further insight into the nature of the droplet breakup within the porous media, we captured images at four different positions in the micromodel during the stationary phase of flow. The positions are shown on the left of Figure 4.12. Around 100 droplets were considered at each position, the apparent diameters of which are shown in the same figure. At this injection capillary number ($\overline{Ca} = 4.9 \times 10^4$) we find no significant difference between droplet diameters with distance r from the central inlet location, suggesting that the breakup is concentrated near the entrance, as highlighted by Yeates *et al.* among others [100]. This observation is exacerbated

in radial porous media where the local Ca is highest near the central injection point and decreases with r, as highlighted in figure 3.45. Positions A and C correspond to a traversed distance of approximately $50L$ where D/d is the spacing between adjacent posts.

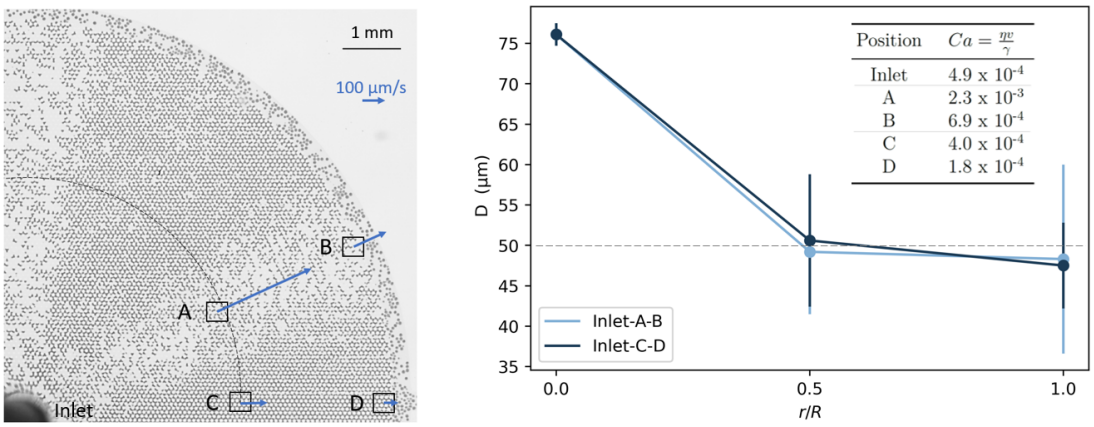

Fig. 4.12 Spatial variations in droplet diameter within the hexagonal porous medium and during the stationary phase ($\overline{Ca} = 4.9 \times 10^4$). Mean apparent droplet diameters (D) and local capillary numbers (Ca) were determined at each of the four locations (A-D) indicated. The local capillary numbers were calculated from average droplet speeds in each of the four positions whilst the global $\overline{Ca}$ was calculated as described in Chapter 2. The dashed grey line at $D = 50$ µm has been added for clarity.

Interestingly, despite the dependence of droplet breakup on $\overline{Ca}$, the droplet diameters weren't influenced by the angular position, i.e. whether they were in a region of fast or slow droplet transport (low or high tortuosity respectively). This would suggest that the heterogeneous nature of the transport doesn't play a role in the breakup of the droplets. It is also consistent with the fact that droplet breakup is largely concentrated at the start of the porous medium.

Summary: Influence of the Injection Capillary number

- Droplet breakup increases with the injection capillary number $\overline{Ca}$ and plateaus for $\overline{Ca} \geqslant 10^{-3}$, at which point the outlet droplets have a mean size such that $D/d \approx 2$ and $D/H \approx 1$.
- Breakup is concentrated near the inlet of the porous medium. Consequently, at the mid-radius and the exit of the porous medium droplet diameters were independent of the path taken through the porous medium.

4.2.3 Influence of D/d

The second, primary parameter of study was the ratio of apparent droplet size to pore spacing, D/d. This can be varied either by altering the size of the droplets or the lattice geometry of the posts. We initially sought to change only the former, however finely tuning droplet size whilst maintaining a constant droplet concentration amongst experiments proved difficult experimentally. Additionally, droplets with a diameter largely inferior to the channel height appear less contrasted and can overlap in the channel, making it difficult to accurately measure droplet diameters at the outlet.

As a result, we conducted two separate experiments. For the first we injected droplets much larger than the post spacing ($D/d \approx 10$) and those injected previously in this chapter ($D/d \approx 3$). For the second, we used a new geometry bearing the same hexagonal lattice geometry and post diameter $2r$, only this time with $d = 75$ µm, three times larger than normal and giving $D/d = 1$. Whilst this geometric modification also increases the porosity and the permeability of the medium, we nonetheless considered it a worthwhile trade-off to allow quantitative study of smaller D/d. In addition to larger post spacing, the porous region was square (not circular, albeit still with a radial flow - see figure 3.20) with the outermost posts open to atmospheric pressure (no exit channel). To avoid capillary end effects the geometry was submerged in a 5 mm deep bath of the continuous phase. The diameters of the droplets around the edge of the geometry were measured and the average diameter calculated.

$D/d = 10$

Figure 4.13 shows the PDFs for the inlet and outlet apparent droplet diameters for the experiment where $D/d \approx 10$. The histograms were created in the same manner as those of Figure 4.11. To create large enough droplets, a droplet generator of height $h = 100$ µm was used. Since the height of the porous medium was 50 µm, the measured apparent droplets diameters D for the inlet droplets were first converted to an equivalent droplet diameter for a droplet of the same volume in a 50 µm channel. The equations for doing so are described in Section 3.2.5.

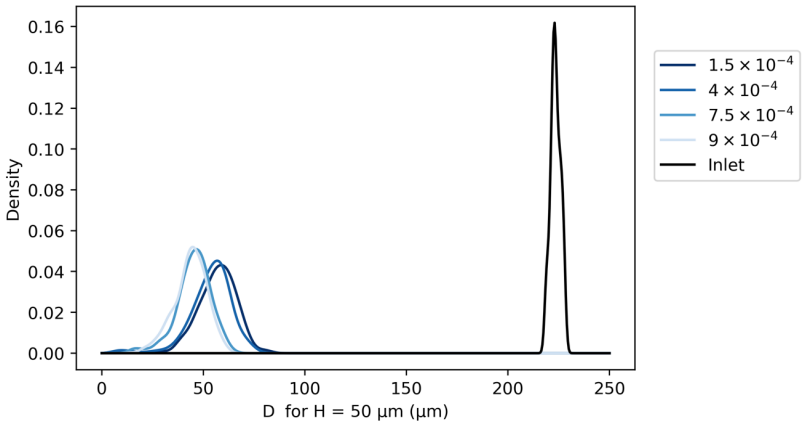

Fig. 4.13 Probability density functions (PDFs) for diameters of droplets at the outlet of the hexagonal porous media at various $\overline{Ca}$ and for $D/d \approx 10$ at the inlet.

Similarly to Figure 4.11, droplet breakup increases with $\overline{Ca}$. The average outlet droplet diameter was around 50 µm, the same as in Figure 4.11 for $D/d = 3$ at the inlet. This is consistent with the literature in that outlet droplet sizes are determined by the post spacing and not the inlet droplet diameter for $D/d \gg 1$. Here, the distributions of the outlet droplets are unimodal at all $\overline{Ca}$ meaning all droplets are broken up to some degree, unlike the bimodal distributions at $\overline{Ca} < 2.5 \times 10^{-4}$ in Figure 4.11 for $D/d = 3$. Outlet droplet diameters appear to plateau around 7.5×10^{-4}, approximately the same order of magnitude at the 1×10^{-3} observed for droplets of relative size $D/d \approx 3$. The mean outlet droplet size at the plateau is $D/d \approx 2$ such that $D/H \approx 1$, the same as for the $D/d \approx 3$ at the inlet. We also note that the same heterogeneous transport was also observed for this larger D/d.

$D/d \approx 1$

For $D/d \approx 1$, one experiment was conducted at $\overline{Ca} = 7.5 \times 10^{-4}$. At this same $\overline{Ca}$ but for $D/d \approx 3$ significant droplet breakup occurred. A comparison of the coefficients of variation in droplet diameters at the inlet and outlet for three initial D/d, as well as the droplet diameter PDFs, are shown in Figure 4.14. As evidenced by this figure, no breakup was observed for $D/d = 0.9$ whilst very little breakup was observed for $D/d = 1.3$ at this $\overline{Ca}$. The heterogeneous transport was once again observed for this experiment at all values of D/d. The droplets in the low tortuosity regions travelled slower and were more densely packed together than those in the high tortuosity regions, however, no blockage occurred.

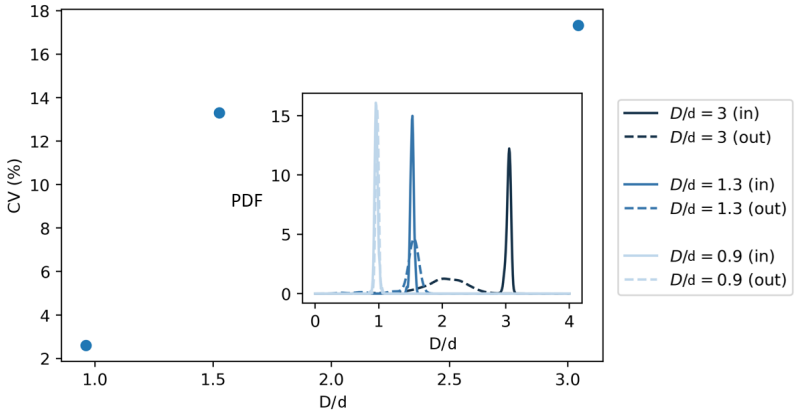

Fig. 4.14 Coefficient of variation in droplet diameters for three different initial values of D/d and for an injection capillary number of $\overline{Ca} = 7.5 \times 10^{-4}$. The insert contains the PDFs of the droplet diameters at the inlet (in) and the outlet (out) normalised by the post spacing D/d.

Summary: Influence of D/d

- For droplets much larger than the pore size ($D/d \approx 10$) breakup was observed at all injection capillary numbers, with the level of breakup plateauing at around $\overline{Ca} \approx 7.5 \times 10^{-4}$. This is of the same order of magnitude as the value for plateauing in the case of $D/d \approx 3$ at the inlet of $\overline{Ca} \approx 1 \times 10^{-3}$. At the outlet, the mean droplet diameter was such that $D/d \approx 2$ and $D/H \approx 1$, the same as when we considered inlet droplets of $D/d \approx 3$.
- For droplets of slightly larger diameter than the pore spacing ($D/d = 1.3$) little breakup was observed at $\overline{Ca} \approx 7.5 \times 10^{-4}$. No droplet trapping occurred under these conditions either, meaning no droplet coalescence was observed.
- For $D/d < 1$ no droplet breakup occurred.

4.2.4 Influence of the Geometry

All of the microfluidics studies discussed in the introduction to this chapter considered a single porous geometry, with one study varying the post spacing [123]. How dependant is droplet breakup on the geometry however, especially when the transport can become highly heterogeneous as discussed in Chapter 3. We considered the two regular geometries (hexagonal and rectangular) as well as two of the random geometries presented in the previous section. All geometries have the same porosity, and the minimal post spacing D/d of the two random geometries match those of the hexagonal (R25, $D/d = 25$ µm) and the rectangular (R15, $D/d = 15$ µm) geometries. Once again, highly monodispersed droplets of constant size and concentration were injected into the porous media, with $\overline{Ca}$ kept constant at $\overline{Ca} = 9 \times 10^{-4}$. Figure 4.15 shows the PDFs of the inlet and outlet droplet diameters.

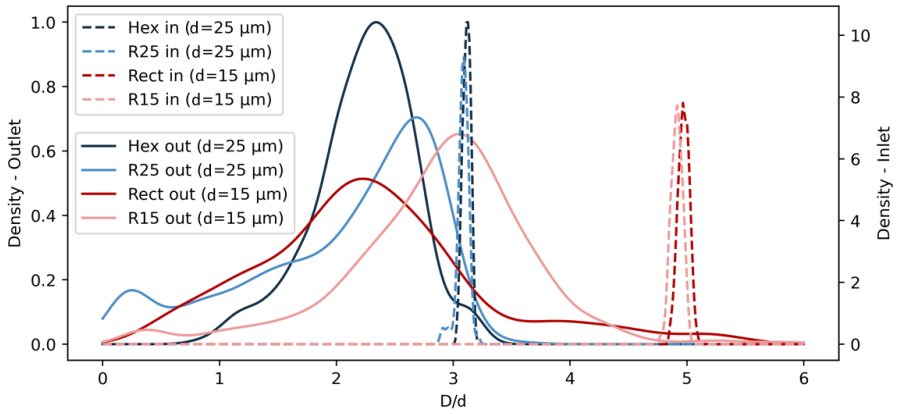

Fig. 4.15 Probability density functions (PDFs) for diameters of droplets D at the outlet of the various porous media, normalised by the minimal post spacing d. Injection $\overline{Ca} = 9 \times 10^{-4}$ and $D/d \approx 3$ for all experiments. R25 and R15 refer to randomly generated geometries (as per Section 3.2.2 with minimal post spacing $D/d = 25$ µm and $D/d = 15$ µm respectively). All geometries have a porosity of ≈ 0.6.

Regular Geometries

If we first consider the regular geometries we see that for the hexagonal and rectangular geometries the curves both have peaks at $D/d \approx 2.5$. The curve for the rectangular geometry was more spread out than in the hexagonal one, with a standard deviation of approximately 0.8 as compared to 0.3 for the hexagonal geometry. This greater spread can be understood by the wider variation in post spacing in the rectangular geometry (15 µm and 25 µm) than in the hexagonal geometry (25 µm).

Random Geometries

The primary reason for including the two random geometries was to compare the degree of droplet breakup between one system with a regular lattice structure and another with a random lattice structure when the porosity and D/d is the same for each. The primary difference, then, between the regular and random geometries is the directions of droplet transport governed by the tortuosity of the porous media. We can therefore compare the results for the hexagonal geometry with those of R25 ($D/d = 25$ µm for each) as well as the results for the rectangular geometry with those of R15 ($D/d = 15$ µm for each). Furthermore, as shown in Figure 3.40 in the previous chapter, droplet transport in R15 is homogeneous whilst it is heterogeneous in R25 due to the posts in the R25

geometry forming a crystalline structure that resembled that of the hexagonal regular geometries. The macroscopic droplet transport could too influence droplet breakup.

Interestingly, in each case we see less droplet breakup in the case of the random geometry. We may imagine that this is due a dispersity in pore diameter distribution that favours fragmentation by the presence of smaller pore sizes in comparison to the regular geometries.

Finally, it is interesting to note that the peak for the R25 curve ($D/d \approx 2.7$) is lower than that for the R15 geometry ($D/d \approx 3$). We would expect the lower minimal post spacing in the R15 geometry to lead to higher shear stresses and thus more breakup. It is possible that in the R15 geometry, which bore a larger variation in post spacing when compared to the almost crystalline geometry of the R25 geometry, the droplets flowed primarily through the larger pores and were trapped at the others. In the R25 geometry, however, the small variation in pore sizes means few preferential paths could be formed.

Summary: Influence of the Geometry

- More breakup is observed in porous media consisting of regular post lattices than in those consisting of random post lattices at constant porosity and minimal post separation distance. This is likely due to a larger dispersity in pore diameter.
- Droplet breakup increased with decreasing minimum post separation distances in regular post lattices. In the random lattice post geometries, however, greater droplet breakup is observed at larger minimum post separation distances.

4.2.5 Influence of Droplet Concentration

The final parameter considered is that of the concentration of the droplets in the emulsion. In the introduction we discussed how pore-level observations showed that collective behaviour between droplets, such as through collisions and blocking neighbouring pores, could lead to droplet breakup. Following these findings it was postulated by Yeates *et al.* that increasing droplet speeds could lead to more such pore-level events and thus increase droplet breakup. Naturally, therefore, one could assume that the number of such droplet interactions be dependant on the concentration of droplets in the dispersion. It remains unclear, however, how the overall level of breakup would be impacted by droplet concentration.

We studied three different dispersions, all with approximately the same initial droplet diameters and injected at the same $\overline{Ca}$. The concentration of the dispersion, V_v, as quantified by the volume fraction of the dispersed phase in the total volume of dispersion, was however varied. Three volume fractions were tested: 0.14, 0.2, and 0.37. The results, displayed in Figure 4.16, show that droplet breakup was slightly greater when the concentration of droplets in the dispersion was largest. The variations in the values of droplet diameter between experiments, however, remain small (roughly 10 % of D). Greater concentrations of droplets were also considered, but the large concentrations of dispersed phase in the exit channel made thresholding and determining the sizes of individual droplets impossible. These results, nonetheless, allow us to postulate that droplet breakup is not affected by volume fraction for $V_v \leqslant 0.2$. At high concentrations the volume fraction shows a slight tendency to lead to smaller droplets and thus more breakup, but the tendency remains within the error bar.

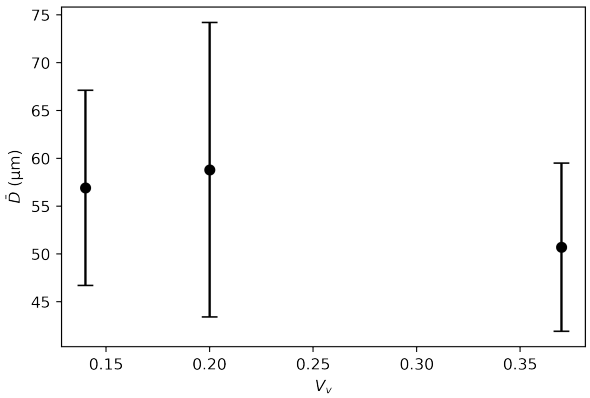

Fig. 4.16 Mean ($\bar{D}$) and standard deviation (error bars) in droplet diameter at the outlet of the hexagonal porous medium for various volume fractions of the dispersed phase with respect to the total dispersion volume (V_v).

Summary: Influence of Droplet Concentration

- For dispersed volume fractions $V_v \leqslant 0.2$ the volume fraction of droplets at constant inlet diameter appears to have no influence on the degree of droplet breakup.
- Higher volume fractions could induce more breakup however our results are not conclusive.

4.3 Discussion

4.3.1 Stationary Droplet Size

We first seek to quantify if the size of the droplets exiting the porous region of the micromodels is independent of their length. We, therefore, compared the length of porous region traversed with the model of Quennouz *et al.* (Figure 4.6) with the radius of our porous media, R. When normalised by the post diameter the model of Quennouz gives a saturation length for droplet breakup of 5.6 mm, slightly less than radius of the circular porous regions in our micromodels of 6.2 mm. Whilst the values are close, we can also postulate that the "very large" bubbles in the study of Quennouz *et al.* (exact size unknown, $D \gg D/d$) would need to separate more times over before reaching a stable size on the order of the pore spacing, and thus to traverse more of the porous medium. We can, therefore, assume the droplet size is stationary upon exiting the porous media for all inlet values of D/d considered. This is consistent with our observations in the case of $D/d \approx 3$, Figure 4.12 showing that even at $r/R = 0.5$ in the porous region, $\bar{D}$ measured inside the porous was already stationary.

To further quantify the nature of the dispersion at the exit of the porous medium, we plotted the mean droplet diameters $\bar{D}$ as a function of $\overline{Ca}$ in Figure 4.17 (left). To capture the shape of the histograms in Figure 4.11 we also plotted the position of the peaks of each of the PDFs as a function of $\overline{Ca}$ (right). For the latter, error bars were added to represent the standard deviation in droplet diameter at each peak. The standard deviations are based on the closest fitting Gaussian curves for each peak of each PDF and were generated using a curve estimation module in plug im!.

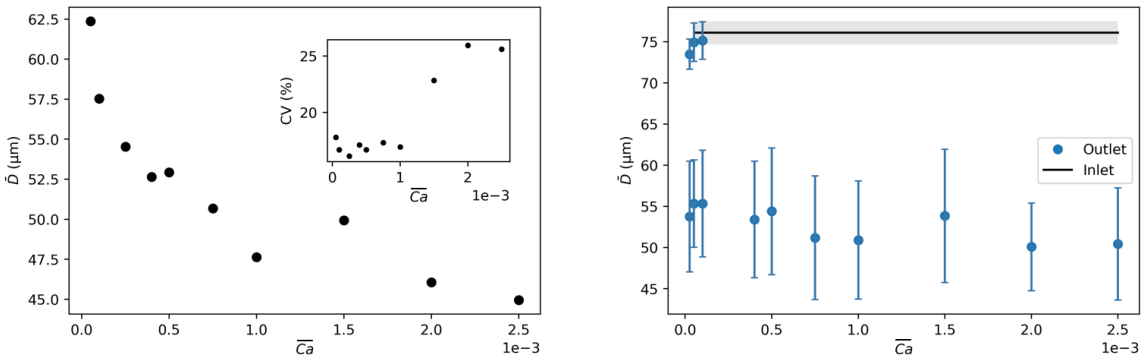

Fig. 4.17 Left: Mean droplet diameter ($\bar{D}$) at the outlet of the hexagonal porous medium as a function of the injection $\overline{Ca}$. Insert shows coefficient of variation (CV) of droplet diameters as a function of $\overline{Ca}$. Right: Positions and standard deviations of the peaks in the PDFs from Figure 4.11

The graph on the right shows that the diameter at which the PDFs peak (or the smaller diameter for PDFs with two peaks) remains approximately constant with respect to $\overline{Ca}$. Interestingly, whilst these peaks show little influence from $\overline{Ca}$, the widths of the curves appear to increase in a steady manner. For instance, if we consider the lowest value of D in Figure 4.11 for each value of $\overline{Ca}$ and at a constant droplet density of 0.02, we can generate the curve in Figure 4.18. This almost linearly decreasing curve with respect to $\overline{Ca}$ indicates a non-symmetrical breakup.

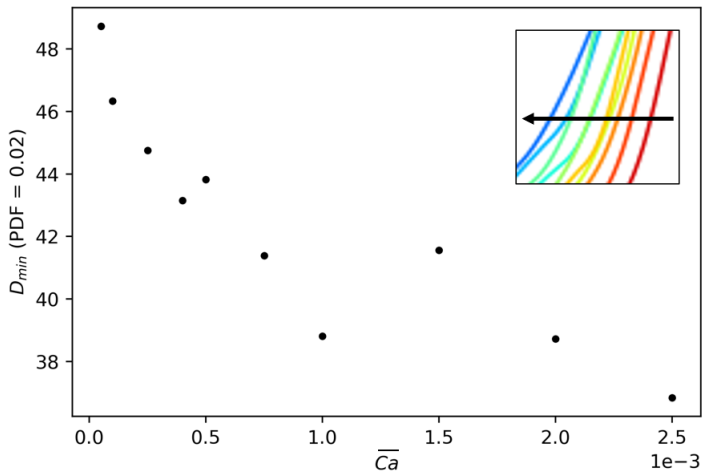

Fig. 4.18 Minimum droplet diameter (D_{min}) intersection density = 0.02 from Figure 4.11 for each $\overline{Ca}$. Insert shows a crop of Figure 4.11 to highlight the region considered.

4.3.2 Stationary Droplet Size Variation

How homogeneous is the dispersion after leaving the porous medium? How does this depend on the initial state of the dispersion? Also, how does it compare to predictions in the literature? It is generally noted in the literature that the droplets become increasingly more homogeneous with distance travelled through the porous medium [57, 101, 124]. As for the influence of $\overline{Ca}$, Mauray *et al.* saw the homogeneity in bubble size converge for $\overline{Ca} > 10^{-4}$ [101]. We see in the inset in the graph on the left of Figure 4.17 that in our study the coefficient of variation (CV) in droplet diameters was constant at $\overline{Ca} \leqslant 10^{-3}$, similar to Mauray *et al.*. However, for $\overline{Ca} > 10^{-3}$ the CV increased by around 80 %. This would suggest that a new regime of droplet breakup became possible at the higher $\overline{Ca}$. If we base our assumption on the phase diagram of Jullien *et al.* (Figure 6 in [128]) there could be a large number of droplets passing from regions A to B with increasing $\overline{Ca}$. Upon close consideration of the curves for $\overline{Ca} > 10^{-3}$ in Figure 4.11 it appears like a new peak begins to form for $D \approx 10$ µm, further suggesting a new mechanism leading to an increasing presence of droplets at that diameter.

On a final note, we analysed the CV for the larger droplets ($D/d = 10$) in Figure 4.13 with those of the droplets just discussed. The graph is displayed as an inset in Figure 4.19. Unfortunately the $\overline{Ca}$ considered were all under the threshold of $\overline{Ca} \leqslant 10^{-3}$ so we cannot know if the same trend at higher $\overline{Ca}$ would arise. However, we are able to see that the CV was similar for both D/d at the $\overline{Ca}$ considered, and that CV remains relatively constant in both cases.

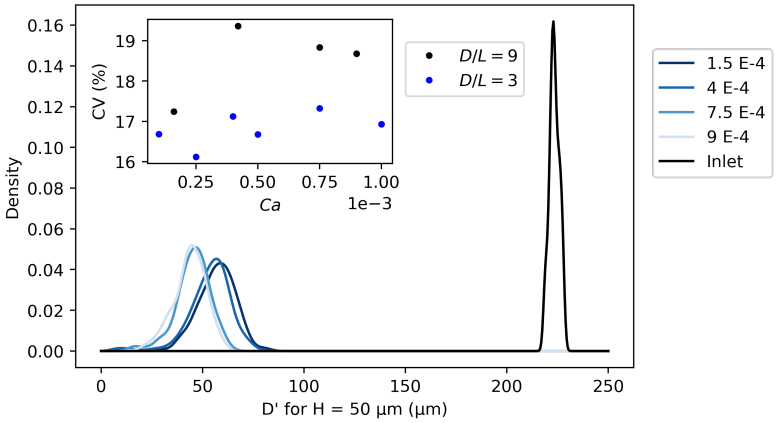

Fig. 4.19 Probability density functions (PDFs) for diameters of droplets at the outlet of the hexagonal porous media at various $\overline{Ca}$. $D/d \approx 10$. Insert shows coefficient of variation (CV) in droplet diameters as a function of $\overline{Ca}$ for $D/d \approx 3$ and $D/d \approx 9$.

4.4 Conclusions and Perspectives

We studied the stability of water-in-oil emulsions whilst traversing radial model porous media consisting of lattices of cylindrical posts. We observed that the breakup of the droplets was concentrated near the central injection point, as evidenced by the plateau in mean droplet diameters observed at the mid-radius, equivalent to a distance traversed of approximately 50 pore lengths. Interestingly, the angular heterogeneities in droplet speed within the porous medium had no noticeable influence on the droplet diameters in our measurements. It is likely, then, that the stable outlet diameter was reached at a distance less than 50 pore lengths from the central injection point. Coalescence was observed at high injection capillary numbers ($\overline{Ca} \geqslant 10^{-3}$) in the low tortuosity regions where droplets became trapped near the exit of the porous medium, as in Figure 4.9. Finally, the outlet droplet diameter was studied for several porous media geometries, consisting of either regular or random lattices of posts. Greater droplet breakup was observed for the regular geometries at constant minimal pore spacing and porosity.

Future work could seek to apply an empirical model of droplet breakup, such as Taylor's law, to predict the droplet size distribution as a function of the geometry and the fluid flow parameters. Further pore-scale observations under a microscope, at varying positions within the porous region and at different flow properties, could provide further insights into the spatial distribution of droplet sizes throughout the porous media. Pore-scale observations could also allow for greater links between the microscopic pore structure and the level of droplet breakup or coalescence to be correlated. Finally, during this study we attempted to use Reflection Interference Contrast Microscopy (RICM) to observe the drainage of the film separating trapped droplets that coalesced. The image sequence in figure 4.20 of the coalescence of two adjacent droplets was captured. Future work, could, therefore, use this method to systematically observe the positions and conditions at which droplet coalescence occurs. To effectively use the RICM, however, it is necessary to employ a micromodel consisting of a glass slide of thickness 100 µm, and thus the study of an oil-in-water system would be more suited to do so.

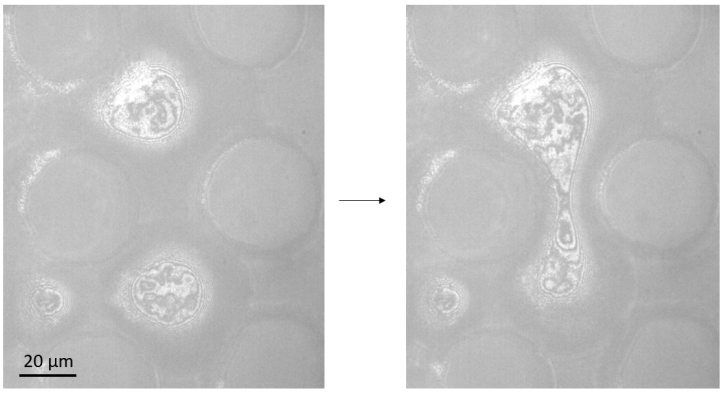

Fig. 4.20 RICM capturing coalescence of two adjacent droplets. Flow direction is from right to left.

Chapter 5

Influence of the Wettability

5.1 Introduction

As mentioned in previous chapters, fluid-fluid displacement in porous media is commonly encountered in both natural and industrial processes. Examples include CO_2 sequestration, groundwater remediation, soil wetting and drying, as well as the dyeing of paper or textiles. To study such porous systems we have employed micromodels, simplified porous media allowing us to precisely control the geometrical parameters and easily visualise the resulting flow. In most micromodels the internal channels have homogeneous wettability. Real porous media, on the contrary, vary spatially not just in their geometry but also in their wettability. Figure 5.1 highlights the wide range of wettability distributions in the case of a Ketton limestone as determined by Mascini *et al.* [138]. At the scale of pores in rocks (µm), surface forces due to wettability play a predominant role in multiphase flows. Our aim is to move closer to modelling such real porous media by adding localised heterogeneities in wettability to micromodels.

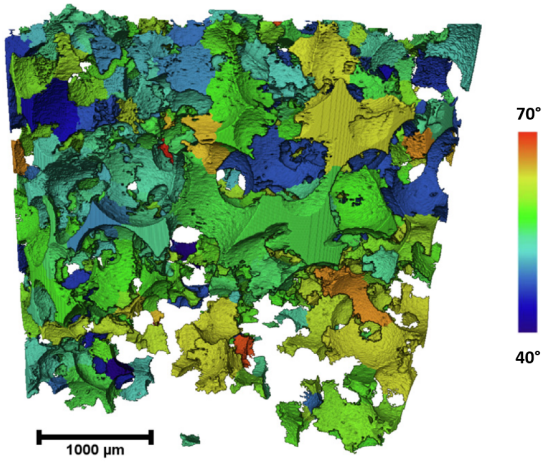

Fig. 5.1 Rendering of the 3D distribution of the contact angle for each pore in a sample of Ketton Limestone. The contact angles were determined by analysing time-resolved micro Computed Tomography data of fluid invasion events during drainage (injection of a non-wetting phase) [138].

To achieve this goal, we developed a procedure for manufacturing micromodels from a different polymer, cyclic olefin copolymer (COC). Unlike PDMS, which has been used for fabricating all previous micromodels in this work, COC allows for lasting modifications of its surface wettability. The experimental study presented in this chapter addresses several aspects, including the fabrication of the micromodels using various materials, surface treatments adapted to each material, and the observation

and characterisation of the resulting multiphase fluid flows. The work presented was primarily conducted during the internship of Camille Brigodiot, as part of her ENSCP engineering cycle and the Master 2 Microfluidics course at PSL University, taking place from February to August 2022. Her experimental procedures and results are presented here with her permission.

In this introduction, we will begin by discussing the various existing methods for modifying wettability in microfluidic systems. We will then present the literature on single-phase fluid displacement of a second, immiscible phase in such systems, considering varying (homogeneous) wettabilities. Finally, we will discuss the influence of wettability heterogeneities, both in the context of single-phase fluid displacement and emulsion flow.

5.1.1 Surface Treatment Methods

Most microfluidic devices are constructed using glass or transparent polymers. As mentioned in Chapter 2, polydimethylsiloxane (PDMS) quickly gained popularity in microfluidics following its development by Duffy *et al.* in the late 1990s [139]. PDMS is favored for its transparency, biocompatibility, relatively low cost, and the ability to fabricate devices in a matter of hours. It is also the material that has been used for all the micromodels up to this point. Therefore, the simplest approach would be to continue using PDMS for the micromodels in this chapter. In this section, we will present various techniques for modifying the wettability of PDMS surfaces and discuss our attempts to utilize them.

Nonetheless, PDMS is inherently hydrophobic, with a contact angle θ_c of around 110°. Surface treatments seeking to render it hydrophilic have typically shown limited durability, which restricts its use in studies requiring micromodels with precise and controllable wettability.

Numerous methods for altering surface wettability, transitioning from hydrophobic to hydrophilic and vice versa, have been extensively explored in the literature. For PDMS, one of the most prevalent approaches involves surface functionalisation, which entails attaching hydrophilic groups to the surface through polymerisation. Researchers such as Hu, Ren *et al.* have leveraged the hydrophilic properties of compounds like poly(ethylene glycol) (PEG), acrylamide, or acrylic acid (AA) by conducting a UV-

initiated radical polymerisation reaction [140–143]. This technique was subsequently replicated by Schneider *et al.* and Ramirez-Gutiérrez *et al.*, who used AA to achieve adjustable and long-lasting contact angles as low as 40-45° for water droplets on PDMS, representing a reduction of 65-70° [144, 145]. We attempted to apply the method developed by Ramirez-Gutiérrez *et al.*, along with several minor variations, to flat PDMS surfaces. Unfortunately, we were unable to reproduce their results. Details of the tests conducted and the outcomes obtained are discussed in Appendix D.

An alternative approach for treating PDMS surfaces involves exposure to UV, UVO (ozone treatment) [146], or plasma. Since Langmuir's pioneering work in the 1920s on ionized gases, plasma technology has become a well-established technique for surface treatment [147]. Plasma is an ionized gas consisting of various charged species (electrons, ions) that are highly reactive but overall neutral. Plasma can be generated by energizing a gas (e.g., Ar, O_2, air) with a power source such as alternating current, radio frequency waves, or even microwaves. When plasma interacts with a surface, it increases its surface energy, facilitating surface functionalisation [148] or the deposition of thin layers from a precursor (Figure 5.2).

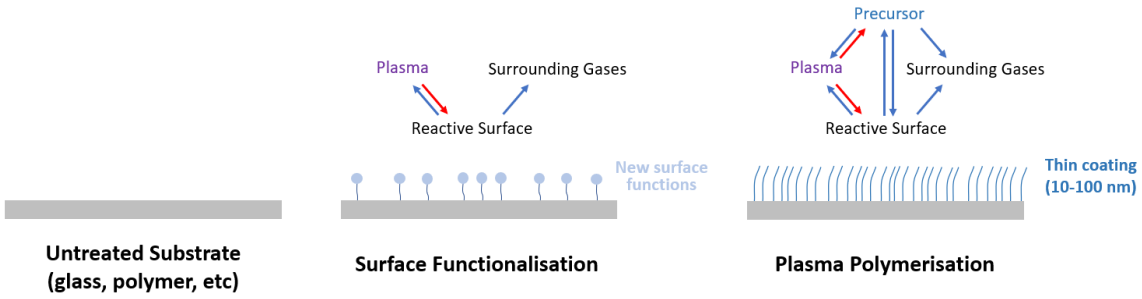

Fig. 5.2 Interactions between the different compounds during functionalisation and plasma polymerisation. Diagram adapted from the Plasmas, Processes, Microsystems (2PM) department at the Institut Pierre-Gilles de Gennes (IPGG).

To achieve uniform surface treatments efficiently and rapidly, plasma polymerization has become a widely-used method for rendering PDMS or other materials hydrophilic. Low-pressure plasmas are typically employed for thin film deposition, especially on PDMS. Precursors such as hydrophilic monomers like PEG or AA are utilised in this process [149–151]. Additionally, atmospheric pressure plasmas have been developed, allowing for the deposition of silica-like layers using organosilicate precursors like hexamethyldisiloxane (HMDSO) or tetraethyl orthosilicate (TEOS). Atmospheric pressure

plasmas offer the advantage of providing uniform hydrophilic treatments without the need for low-pressure experimental conditions [152–156]. These techniques, known as Polymer Enhanced Chemical Vapor Deposition (PECVD) or plasma polymerization, have proven to be exceptionally durable on thermoplastics like polymethyl methacrylate (PMMA) or cyclic olefin copolymer (COC). These treatments can last for several days or even weeks, making them increasingly popular in microfluidics applications. Moreover, these techniques can be readily adapted to confine the treatment to specific discrete areas, as will be discussed in Section 5.2.2.

5.1.2 Influence of Wettabilities on Porous Media Fluid Flow

Single Phase Fluid Injection

The displacement of one stationary fluid phase by another injected phase in porous media is classically described by the diagrams of Lenormand. Flow behavior is found to be contingent on two key parameters: the viscosity ratio between the fluids, denoted as M, and the injection capillary number, $\overline{Ca}$, which defines the relative significance of viscous and capillary forces [157]. The resulting morphology of the displacement front can vary from a stable, circular one to a highly heterogeneous one consisting of complex preferential paths, as illustrated in Figure 5.3. Recent studies, both experimental and numerical, have underscored the pivotal role of wettability. These investigations, often employing pore-network models, have extended the Lenormand diagrams to encompass finer variations in wettability [158–162]. Moreover, they have elucidated novel mechanisms of pore invasion and highlighted the intrinsically three-dimensional nature of such multiphase flows, even in quasi-2D micromodel experiments.

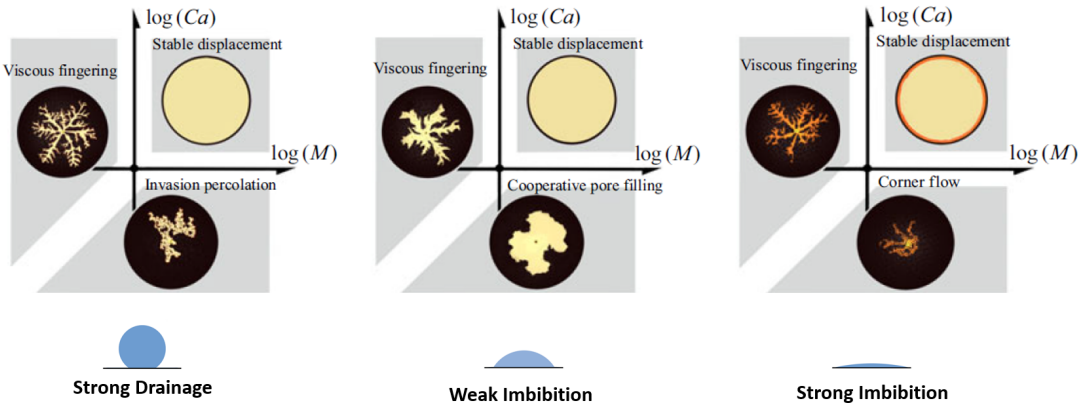

Fig. 5.3 Simplified extended Lenormand diagrams for the five principal flow regimes within the M–$\overline{Ca}$–θ_c parameter space: viscous fingering, stable displacement, invasion percolation, cooperative pore filling, and corner flow. The stationary phase is in black and the injected phase is in colour, with the darker colours in the strong imbibition diagram (bottom) representing partial pore filling. Diagrams adapted from Primkulov *et al.* [162].

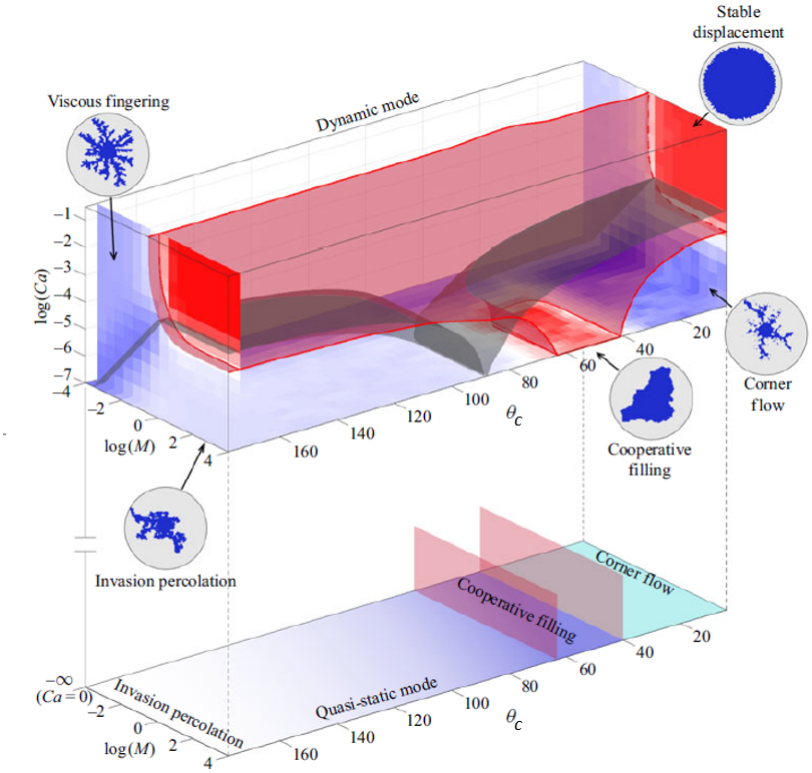

Fig. 5.4 Complete extended Lenormand diagrams for the five principal flow regimes within the M–$\overline{Ca}$–θ_c parameter space. Stationary phase in the individual flow diagrams is grey and the injected phase is blue. Diagrams adapted from Primkulov *et al.* [162].

Nevertheless, our comprehension of multiphase flow in porous media with heterogeneous wettability remains less comprehensive. Experimental investigations have been conducted on diverse geometries characterised by mixed-wettability, including sandpacks [157, 163] and reservoir rocks [138, 164–170]. The flow behaviour observed in these mixed-wet porous media varied significantly from homogeneously-wet counterparts, such as less residual trapping in CO_2-saturated mixed-wet core samples and greater oil displacement for imbibition in oil-saturated mixed-wet core samples.

Micromodels featuring discrete zones of modified wettability have also been utilised to establish direct correlations between observations of interfacial fluid dynamics and local wettability conditions [144, 161, 171–174]. The spatial distributions of the mixed-wettability zones at the pore-scale was shown to greatly impact the resulting fluid flows [173]. The influence of wettability heterogeneities diminishes with increasing $\overline{Ca}$ as viscous effects played a greater role and the thickness of the lubrication film surrounding the injected phase increased as per Bretherton's law in Equation 3.2 [172].

Interestingly, Irannezhad *et al.* injected water into an oil-filled porous media and observed that invading water preferentially filled strongly water-wet zones ($\theta = 30°$) but completely avoided weakly water-water ones ($\theta = 60°$) in an otherwise oil-wet micromodel, as shown in Figure 5.5 [161]. This behaviour contradicted the trend predicted by the Lenormand diagram for a flow under the same conditions at low Ca, where capillary forces dominate, and was attributed to the complex curvature of the interface in mixed-wet pores. Another study provided numerical evidence of the influence of mixed-wet pores and pore structure tortuosity on the stability of the fluid front [175]. Further systematic investigations are needed to gain a better understanding of how continuously varying wettabilities can influence fluid flow properties.

Emulsion Injection

All the studies discussed so far have focused on the injection of a single fluid phase into a porous medium filled with another immiscible phase. Few studies have explored the impact of wettability heterogeneities on the transport and stability of foams or emulsions.

In general, microfluidic devices are made from a material that is wetting for the continuous phase. Flowing droplets are then surrounded by a lubrication film of the

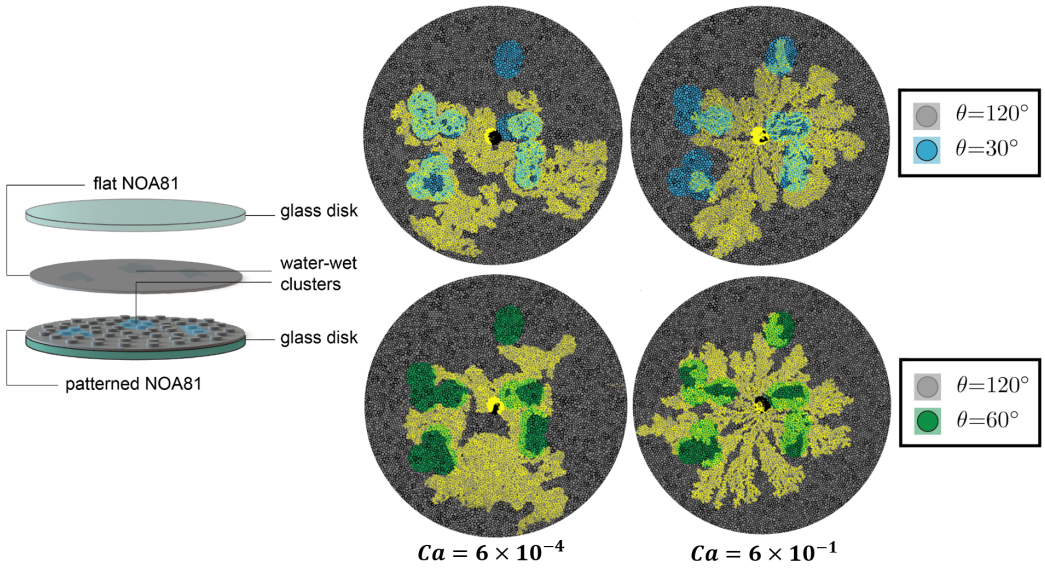

Fig. 5.5 Experimental displacement patterns of water (yellow) displacing silicone oil (black) in mixed-wet microfluidic flow cells at two capillary numbers. Most of the flow cell is oil-wet (grey, $\theta_c = 120°$). Clusters of either strongly water-wet posts (blue, $\theta_c = 30°$) or weakly water-wet posts (green, $\theta_c = 60°$) were added. The invading water saturates the strongly water-wet clusters (top row), but encircles the weakly water-wet clusters (bottom row). On the left is a schematic of the flow cell geometry and materials. Adapted from Irannezhad *et al.* [161].

continuous phase, as seen in Figure 3.4, preventing the emulsion droplets from adhering to the channel surfaces or even breaking up. The mobility of the emulsion flowing in a straight channel, therefore, depends on the thickness of this lubrication film. For droplets of diameter greater than the channel dimensions, the film thickness increases with the capillary number, as per the relation determined by Bretherton and discussed in Section 3.1.

One study considered the influence of droplet confinement and the homogeneous contact angle of the continuous phase on the stability of a flowing emulsion [176]. The contact angle was varied not through surface treatment but instead by adding varying surfactant concentrations to the dispersed phase. Whilst droplets remained stable in the case of complete wetting of the continuous phase, intermittent adhesion of droplets to the channel walls was observed in the case of partial wetting. Some studies have also considered emulsion flow in straight channels of variable wettability and in the absence of surfactants [177, 178]. It was observed that below a critical droplet speed, an unfavourable surface wettability could induce the instability of the lubrication film

and thus induce an inversion of the emulsion, as shown in Figure 5.6. Chen *et al.* also observed an influence of the droplet confinement between the four walls of the channel, deriving a relation between droplet size and the critical capillary number for the droplet to remain stable as:

$$Ca = k\left(\frac{A}{\gamma d^2}\right)^{3/8}\left(\frac{L_d}{w}\right)^{3/4} \tag{5.1}$$

where L_d is the length of the droplet, w the inner dimension of the microchannel, γ the interfacial tension of the two immiscible phases, $A = 1$ x10^{-19} J the Hamaker constant, and k a constant (k = 2.5 when fitted to their data) [177]. These findings have, however, not been related to droplet flow in porous media.

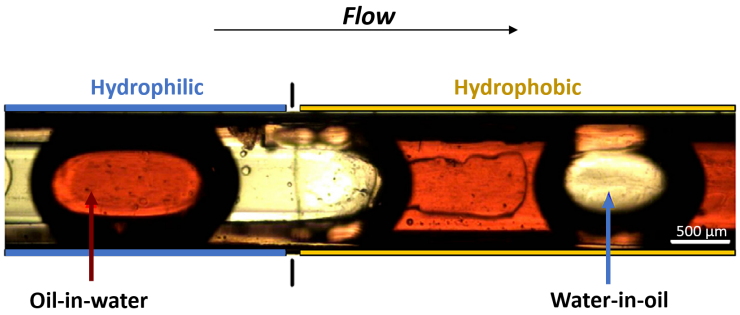

Fig. 5.6 The inversion of an emulsion from water-in-oil to oil-in-water observed inside a glass capillary, immediately after a sudden transition in wettability from hydrophilic (left, untreated) to hydrophobic (right, coated with OTS). The contact angles of the hydrophilic and hydrophobic sections were 11° and 90°, respectively. The oil phase was dyed red for visibility. Scale bar is 500 µm. Adapted from Chen *et al.* [177].

5.2 Materials and Methods

Our main objective was to produce oil-wet porous media patterned with discrete water-wet clusters of controlled wettability and position within the porous media. The experimental work carried out involved three primary steps: the systematic quantification of the surface treatment methods, the manufacture of the micromodels with modified wettability, and the injection of fluids into the micromodels. Two surface treatments methods were considered: UV-initiated radical polymerisation (as in [140, 144, 145]) and plasma-initiated TEOS depositing (as in [154, 179]). The former was performed at IFPEN while the latter at the Institut Pierre-Gilles de Gennes (IPGG) using atmospheric pressure plasma technology in the Plasmas, Processes, Microsystems (2PM) department. Both methods were first tested on flat surfaces to systematically quantify the effectiveness and durability of each. Two different materials used in micromodel fabrication were tested: PDMS, as in the previous chapters, and COC, as currently developed at the Chemistry Research Institute of Paris (IRCP).

For the **PDMS micromodels**, the fabrication method was the same as described in Section 3.2.4. However, the micropatterned PDMS bodies were instead plasma-bonded to a glass slide, rendering the micromodels hydrophilic. New PDMS micromodels were fabricated for each experiment to maintain consistent wettability. Immediately following plasma bonding the PDMS-on-glass micromodels were flushed with a 1 wt% SDS in water solution, and experiments were performed within 10 minutes of plasma bonding to maintain hydrophilicity. The PDMS micromodels are only further discussed for emulsion injection in Section 5.3.3.

The slightly different method for the **COC micromodels**, performed at IPGG, is described below in Section 5.2.1. The work in this chapter primarily concerned the COC micromodels which were used for all the single-phase fluid injections in Section 5.3.3 and most of the emulsion injections in Section 5.3.3.

5.2.1 Making the COC Micromodels

The fabrication of the COC microfluidic devices was undertaken in the grey room at IPGG to prevent any impurities from contaminating the surface. All of the main steps are also summarised in Figure 5.7 below. The same micromodel geometries as discussed in Chapters 2 and 3 were used, opting only for the **square lattice** post geometry throughout this chapter.

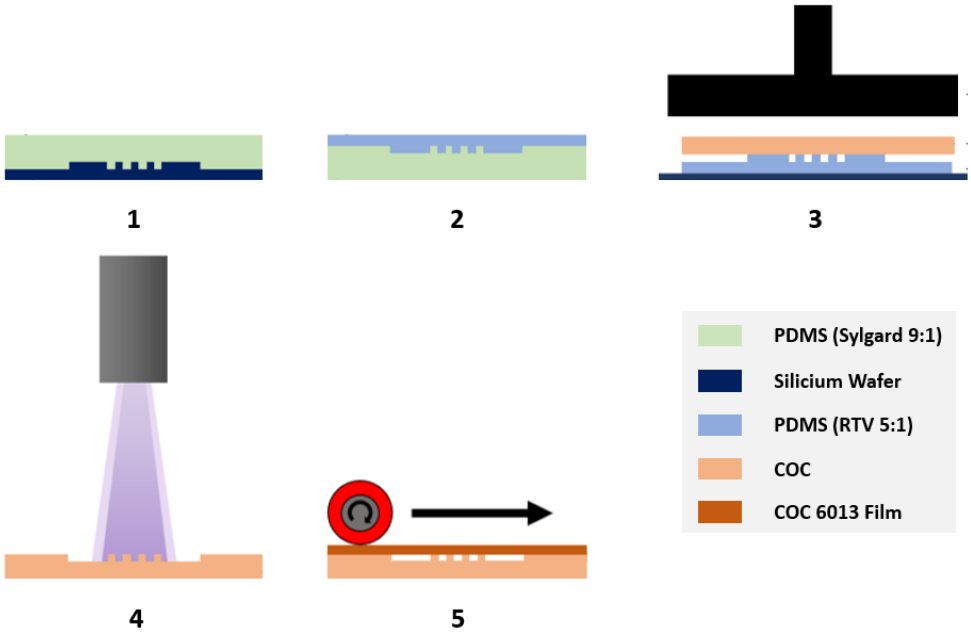

Fig. 5.7 Schematic summary of the COC microfabrication procedure. 1) Sylgard PDMS counter mould. 2) Replication of the microstructure of the silicon wafer on an RTV PDMS membrane. 3) Hot pressing of COC to impart microstructure. 4) Deposition of a thin TEOS layer with an atmospheric plasma. A mask can be positioned over the COC to limit the treatment to precise zones. 5) Closing of the microfluidic device.

In step 1 of Figure 5.7, a micropatterned disk of PDMS (Sylgard, 9:1) with a thickness of approximately 5 mm was made from the original silicon wafer following the process described in Section 3.2.1 which was then treated with an O_2 plasma and silanised. 50 mL of a second PDMS mix (RTV, 5:1) was then degassed and deposited on the Sylgard PDMS block by spin-coating (500 rpm, 40 s, 10 rpm/s at the beginning). The whole assembly was then placed in an oven at 70 °C for at least 2 hours, but ideally overnight. Afterwards, the PDMS system, along with a second silicon wafer, were treated with an O_2 plasma, before bonding the PDMS to the wafer, RTV PDMS

side down. Any air bubbles trapped beneath the membrane were immediately removed before placing the wafer with the PDMS system in an oven at 90 °C for 15 minutes. Using isopropanol, the Sylgard PDMS can be separated from RTV PDMS membrane. The wafer bearing the RTV PDMS membrane is then overbaked for at least 3 hours on a hot plate at 250 °C. The membrane/wafer system is then ready to be used as a mould for COC embossing, a procedure that can be repeated several times for a given membrane.

Step 3 involves the hot embossing of a COC wafer onto the membrane using a 3-tonne SCAMEX press. In all of our work, we used 3 mm thick COC 6013 (ChipShop) with a glass transition temperature T_g of 140 °C. The temperatures and duration applied during this step were optimised to prevent the formation of air bubbles within the COC during the hot embossing process, which would hinder experimental observations. Based on previous work carried out at the IPGG technology platform and several iterations during this study, the optimised protocol is as follows:

1. Pre-heat the two plates of the press to 50 °C.
2. Position the wafer with the RTV membrane on the lower plate before placing a good-sized plate of COC 6013 on it (3.5 cm x 5 cm for the micromodels produced during this study).
3. Set the temperature of the lower and upper plates to 180 °C and 140 °C respectively.
4. As soon as the lower plate has reached its control temperature, after approximately 10 minutes of heating, initiate the press at a pressure of 3 bars.
5. Leave the press engaged for 12 minutes before decreasing the temperature of both plates to 50 °C. The COC plate bearing the desired pattern can then removed from the press.

In the case of the TEOS deposition method adopted in this study, the embossed COC block is then treated following the procedure described in Section 5.2.2. To finish, the microsystem can be completed by sealing the embossed COC with a film of COC 6013. To do so, the embossed COC was preheated to 140 °C, the temperature of the laminator used in this study. The COC 6013 film was placed on a block of PDMS saturated with hexadecane for 4 minutes to enhance adhesion during lamination. Excess hexadecane was removed from the film, which was then placed on the embossed

COC and laminated, with extra force applied to the patterned areas.

It should be noted that the surface treatments were only applied to the embossed COC and not the film used to seal the micromodels. Treating both sides would have added complexity and uncertainty, having to perform the localised surface treatments on both sides before precisely aligning the two during sealing. Given that out of the four surfaces of the channels formed in the micromodels three will have received the surface treatment, we deemed this sufficient for our preliminary study.

In order to characterise the quality of the micropattern replication in the COC, several techniques are used such as SEM or optical profilometer, as shown in Figure 5.8. The topographical characterisations of the micromodels were carried out before the chips were sealed. We see that the posts appear to have been very reliably reproduced, and that the 50 µm height of the posts has been well respected. Upon emulsion injection, as discussed in Chapter 2, the same patterns of heterogeneous droplet transport were observed at the same experimental conditions, further indicating a reliable reproduction of the geometry. Finally, to verify that all of the posts were well adhered to the flat COC surface closing the micromodel a water and fluorescein mixture was injected into the hydrophilic porous media. During this test the fluorescein was only observed around the posts, suggesting they were well adhered.

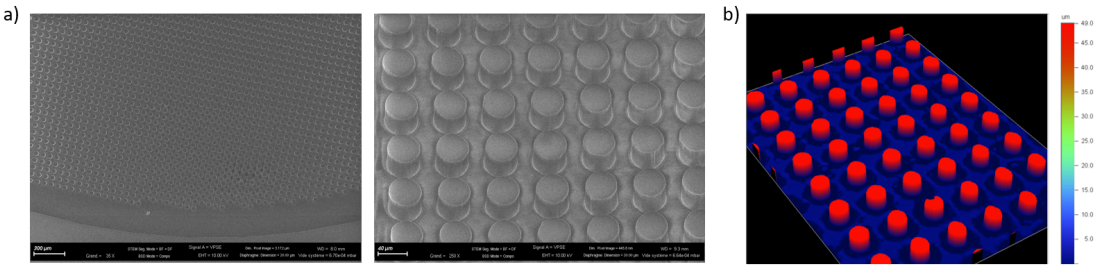

Fig. 5.8 a) SEM photos of a COC micromodel. Left: scale bar is 300 µm, 35× zoom. Right: scale bar is 40 µm, 250× zoom, 29° tilt. b) Optical profilometer images of a COC micromodel, 10× zoom. All images were taken before the embossed COC was sealed.

5.2.2 COC Surface Treatment Methodology

Method of depositing SiO_2-type TEOS on COC substrates

In order to render certain areas hydrophilic, a thin layer of silica was deposited on the micropatterned COC substrates by an atmospheric plasma system (AcXys Technologies) consisting of three control modules and a movable nozzle (Figure 5.9). The tetraethylorthosilicate (TEOS) deposition procedure adopted was originally presented in [154, 179]. An AcXys ULS (ultra light system) module allows the power and frequency of the atmospheric plasma to be set, as well as the flow rate of the carrier gas (air). The position of the atmospheric plasma nozzle is controlled by an AcXys Quickset module, allowing precise movements in all three xyz axes at a constant speed of up to 150 mm/s.

The first step is an air plasma pre-treatment to efficiently clean the surface of each sample. The air plasma used had a power between 600 W and 720 W and a gas flow rate of 32 L/min - 35 L/min. For the silica deposition step, the pre-treatment plasma was reproduced and this time an organosilicate precursor (TEOS) was also introduced at a flow rate between 100 µL/min and 500 µL/min, controlled by a flow meter. The carrier gas vaporises the liquid precursor at a flow rate between 5 L/min and 25 L/min.

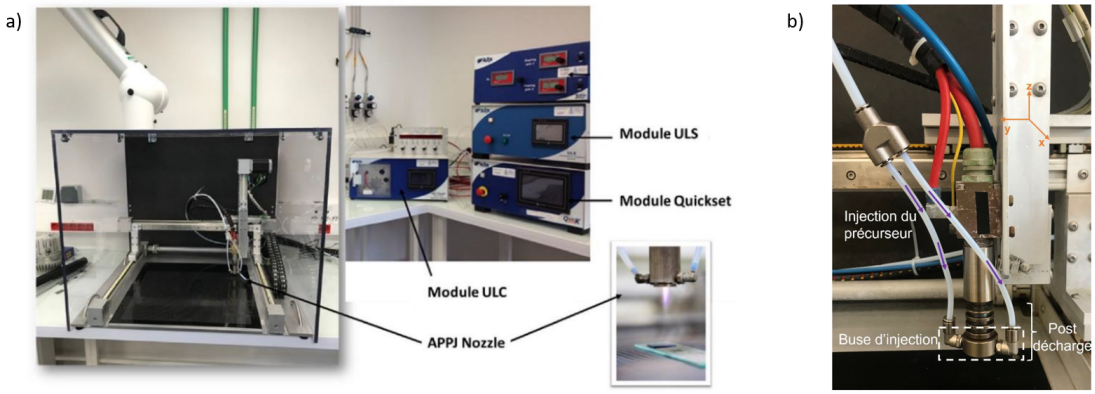

Fig. 5.9 a) Photo of the AcXys plasma torch and ULS system. b) Annotated photo of the plasma nozzle

After optimisation of the various plasma parameters (Section 5.3.1) on flat surfaces as a function of the resulting contact angles, the surface treatments could be applied to the micromodels. This silica deposition can easily be limited to certain zones of the surface by using a mask with holes for the plasma to pass through above these zones, or even by simply covering the other zones with a piece of cellotape. Some example

patterns are shown in Figures 5.10 and 5.11 below. In this study, PDMS masks around 3 mm thick were used as masks: they were first cut according to the desired geometry and deposited directly on the micromodels before applying the surface treatment.

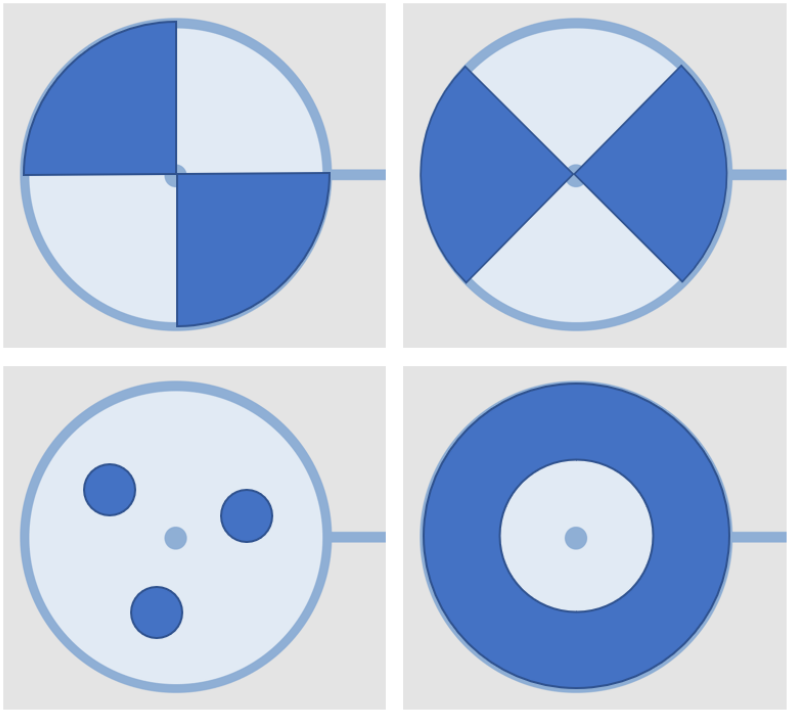

Fig. 5.10 Examples of the localised surface treatment patterns explored in the research. Zones in dark blue are those rendered hydrophilic.

Contact Angle Measurements

In order to characterise the hydrophilic or hydrophobic character of the material, contact angle measurements were carried out. The measurements were made by placing a drop of distilled water on the sample otherwise exposed to air. The two angles were averaged and the average for five drops at different positions on the same sample was then taken. In addition, the durability of the hydrophilic treatment was evaluated by repeating the contact angle measurements over time periods ranging from several hours to several weeks. Static measurements were carried out either using a camera and image processing with ImageJ, or with the Krüss device at IRCP. The results did not vary between the two methods.

Performing contact angle measurements allowed us to quantify the influence of the various surface treatment parameters. Once the relevant parameters were optimised, the contact angles measurements were repeated using the fluids to be used in the fluid injection. The results are presented in Section 5.3.2.

Further Characterisation of TEOS deposition on COC

In addition to quantifying the hydrophobicity induced by the TEOS deposition through contact angle measurement, we can also characterise the TEOS deposition using infrared spectroscopy (FTIR) [154, 179]. The resulting FTIR spectra are presented in Appendix D.

Furthermore, our objective was not just to apply a homogeneous surface modification but also to generate discrete water-wet zones within the micromodels. By performing energy dispersive spectroscopy (EDS) using a scanning electron microscopy (SEM) we can detect the locations of TEOS depositions. Doing so also allows us to verify that the resulting TEOS deposits are true to the intended mask designs. The results for two different mask designs are shown in Figure 5.11 below.

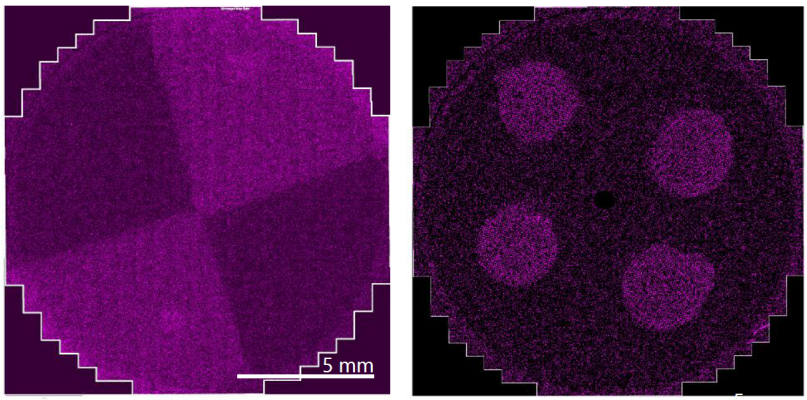

Fig. 5.11 SEM EDS photos for two examples of localised SiO_2 deposition (in light pink) on COC micromodels.

5.3 Results

5.3.1 Quality of the surface treatments

Preliminary study: Comparing PDMS and COC

As previously mentioned, the study of wettability heterogeneities was carried out in PDMS and COC micromodels. The contact angles formed by a water drop in air for each of the materials are 110° and 86° respectively, demonstrating their low affinity for water in air. The goal, therefore, was to render the materials hydrophilic in a controllable and durable manner. For this purpose, a preliminary study on flat, unpatterned samples was carried out. Water in air contact angles were measured for both materials in both their intrinsic state and after surface treatment. For contact angles of water droplets in the continuous oil phase, see section 5.3.2.

PECVD Method

The PDMS and the COC samples were both treated using the atmospheric plasma as well as the TEOS deposition technique from Section 5.2.2. For these initial tests we used the same parameters as in Bourg *et al.* only with a slightly lower power. These parameters were: air flow rate of 33 L/min, plasma power of 667 W, torch-surface distance of 15 mm, and torch speed of 150 mm/s [179]. Two pre-treatment passes were performed before depositing the TEOS. For deposition, the precursor flow rate is 109 µL/min, with a carrier gas at 9 L/min. The resulting contact angles were measured again at several points across the following 24 hours and are presented in Figure 5.12 below.

Immediately following the treatment the average contact angle remains much higher on the PDMS than on the COC. Moreover, the PDMS regains its hydrophobicity a few hours after the treatment whilst the COC maintained a contact angle less than 30° even after 96 hours. It is, therefore, clear that these surface treatments were much more effective on the COC than on the PDMS.

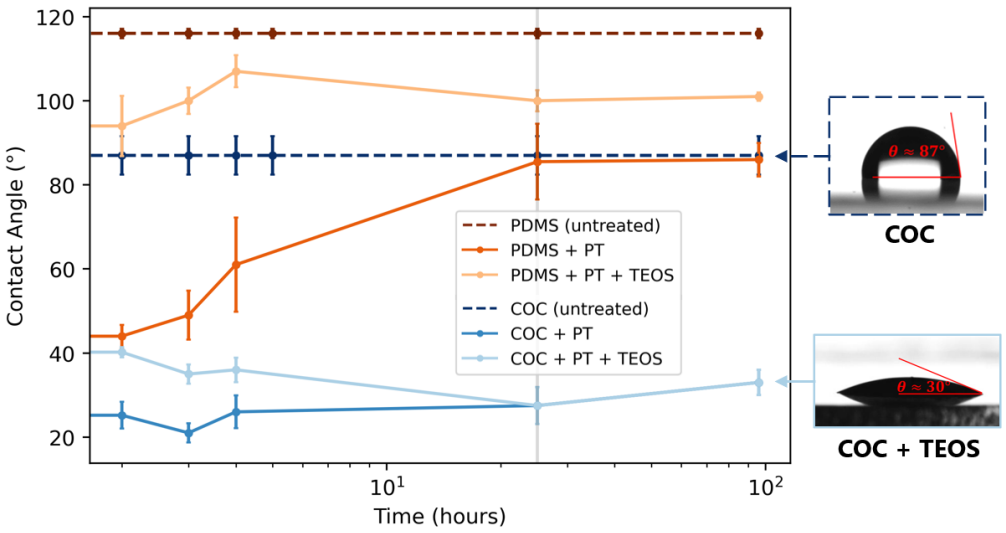

Fig. 5.12 Durability of the PECVD surface treatment and pre-treatment (PT) as well as with TEOS deposition (TEOS) for PDMS and COC flat surfaces. Pre-treatment: 2 passes with 33 L/min flow rate, 80 kHz, 653 W. TEOS deposition: 4 passes; precursor flow rate 200 µL/min; carrier gas flow rate 12 L/min. Torch to surface distance: 15 mm. Torch speed: 150 mm/s.

AA Method

Surface treatments through UV-initiated surface functionalisation, as performed by Schneider *et al.* as well as Ramirez-Gutierrez *et al.* were also tested on the PDMS [144, 145]. The results obtained, however, varied significantly from those in the literature. Little to no variations in water-in-air contact angles arose, despite varying several times over the power of the UV lamp, as measured using a Hamamatsu C9386 UV light checker at the position of the sample, the proportions of chemicals used, and the duration of imbibition in the various chemical baths. The full experimental procedure along with the measured contact angles are included in Appendix D. Given these results, the remainder of this section focuses on the PECVD method on the COC.

Summary: Comparing PDMS and COC

- PECVD Method:
  - Surface treatments of both PDMS and COC were performed.
  - COC maintained a contact angle of less than 30°, even 96 hours after surface treatment.
  - PDMS wettability was quickly reversed, regaining its hydrophobicity a few hours after treatment.
- AA Method:
  - Little to no influence on the contact angle of the PDMS, even when tested immediately after treatment.
- We, therefore, pursue the PECVD method on the COC.

Optimising the Plasma Procedure: COC

We now seek to vary the parameters of the plasma deposition on the COC in order to reliably produce the lowest and most durable contact angles. We performed three series of tests, concentrating on the following variables: the number of passages of TEOS deposit for the initial parameters [179], the distance between the torch and the COC substrate, and the different possible post-treatments. The final parameters used throughout the remainder of this chapter are then listed.

Influence of the Number of Passages During TEOS Deposition

The results of the optimisation of the number of torch passes for TEOS deposition are shown in Figure 5.13. The sample names correspond to the number of torch passes during TEOS deposition. The two graphs correspond to two different distances between the torch and the COC surface: 15 mm (left) and 31.5 mm (right). With a distance of 15 mm, and for all samples bar sample 12, the wettability trend is the same. Immediately after the treatment the contact angles are around 50°. In the first few days after, we observe further decrease in the contact angles to around 20°. Finally, from the fourth day onward the contact angles increased before plateauing at around 45-55° after around 15 days. Conversely, the contact angles on the surface treated with 12 passes increased immediately following the treatment and after 5 days they were

very similar to that of the untreated COC. We can, therefore, assume that at some point between 8 and 12 passes the plasma modifies the surface to such an extent that the deposit is no longer hydrophilic. Consequently, we decided upon using 4 passes for the TEOS deposit throughout the remainder of the study.

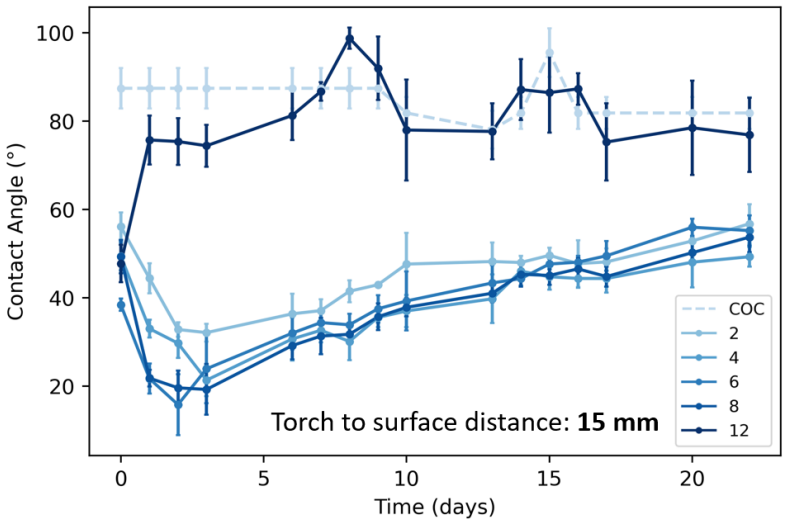

Fig. 5.13 Durability of the PECVD surface treatment with TEOS deposition for COC samples. The number associated with each data series corresponds to the number of TEOS deposition passes. Pre-treatment: 2 passes with a flow rate of 32 L/min, 80 kHz, 667 W. TEOS deposition: precursor flow rate 109 µL/min; carrier gas flow rate 9 L/min. Torch speed: 150 mm/s.

Influence of the Torch-to-Surface Distance

In addition to observing the resulting contact angles, the structure of the treated surface was also considered. With the plasma torch within 15 mm of the sample surface (Figure 5.15, left) cracks were observed on the surface of the treated COC. These were likely due to the high temperature of the plasma torch during the treatment (> 600 °C) and have been displayed in Figure 5.14. Therefore, in order to avoid potential alteration of the surface condition, we performed a new series of tests with a new separation distance of 31.5 mm (Figure 5.15). Once again we see that the contact angle of a water droplet in air first decreases after the first day before increasing. Furthermore, we see that 4 passes of the TEOS deposition were sufficient to obtain a hydrophilic surface with a contact angle of around 40° after 2 weeks. We, therefore, use a torch-to-surface distance of 31.5 mm for the all subsequent treatments.

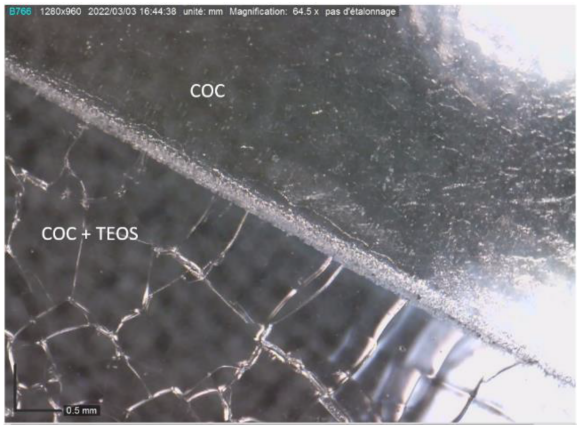

Fig. 5.14 Surface condition of untreated COC (COC, top right) and COC after 4 torch passes of TEOS deposition (COC + TEOS, bottom left) at a distance of 15 mm.

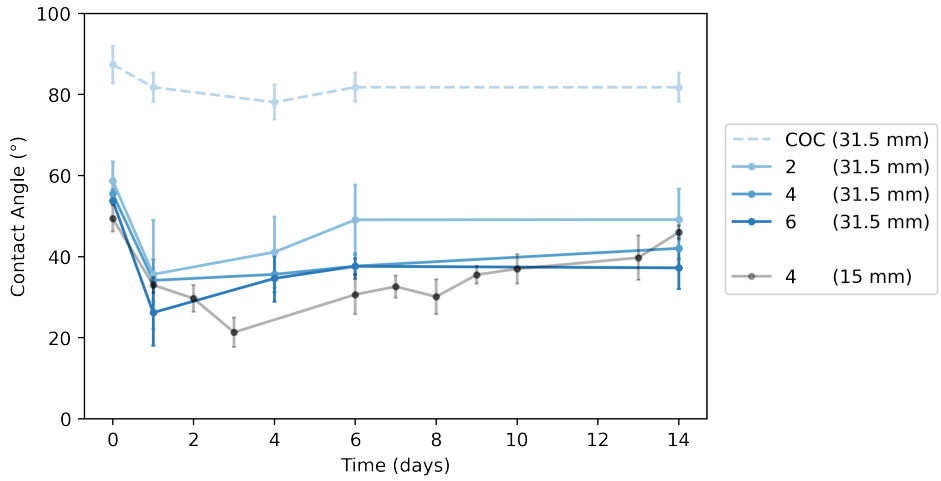

Fig. 5.15 Influence of the distance between the torch and the COC surface on the durability of the PECVD surface treatment with TEOS deposition for COC samples. The number associated with each data series corresponds to the number of TEOS deposition passes. Pre-treatment: 2 passes with flow rate of 32 L/min, 80 kHz, 667 W. TEOS deposition: precursor flow rate 109 µL/min; carrier gas flow rate 9 L/min. Torch to surface distance indicated in brackets in the legend. Torch speed: 150 mm/s.

Influence of Different Surface Post-treatments

Finally, the influence of several common post treatments following the TEOS deposition on the resulting contact angle and its stability in time was tested. The post treatments were with the air plasma, varying once again the number of passages, and rinsing in water.

As Figure 5.16 demonstrates, all post treatments led to an increase in the contact angle after 12 days when compared to the TEOS-coated COC without any post treatments. In addition, increasing the number of passes of the plasma torch significantly increased the resulting contact angle, effectively counteracting the effects of the TEOS deposition on the substrate. We therefore decided to not perform any post treatments on the samples in order to keep the lowest possible contact angles.

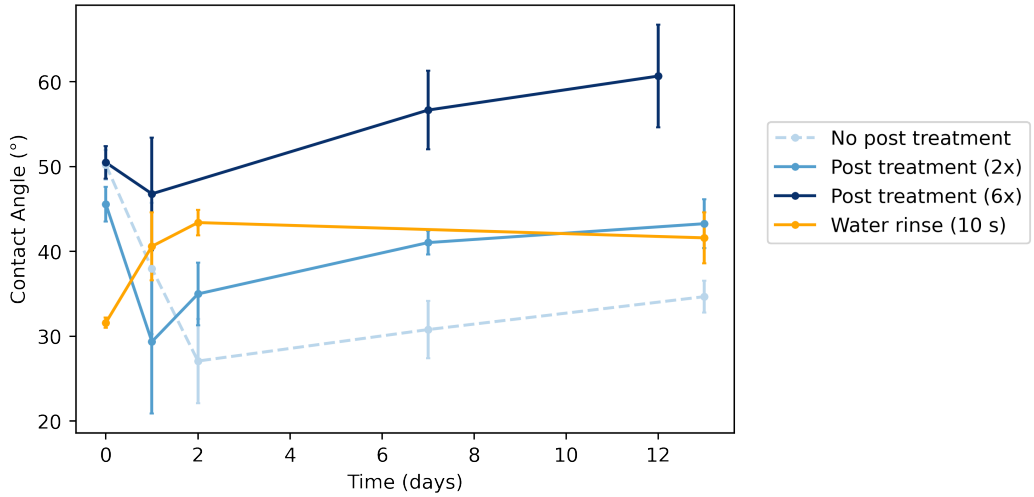

Fig. 5.16 Comparison of the effects of various PECVD post treatments on COC. Each TEOS deposit is preceded by a pre-treatment with an atmospheric air plasma: 2 passes with a flow rate of 32 L/min, 80 kHz, 667 W. TEOS deposition: precursor flow rate 109 µL/min; carrier gas flow rate 9 L/min. Torch to surface distance: 31.5 mm. Torch speed: 150 mm/s. Water wash with distilled water at plasma outlet for 10 s. Post-treatment: air flow rate 32 L/min, 80 kHz, 667W, performed for two passes (2x) and 6 passes (6x).

Summary: Optimising the Plasma Procedure on COC

Final parameters for PECVD TEOS-deposition treatments used for the remainder of this chapter:

- Torch to surface distance: 31.5 mm
  - At 15 mm surface cracks were observed, reducing the reliability of the treatment.
- Pre-treatment with atmospheric air plasma (2 passes, 32 L/min, 667 W, 80 kHz)
- 4 passes of TEOS deposition with a precursor flow rate of 100 µL/min and a carrier gas flow rate of 10 L/min.
  - 6-8 passes produced negligible improvement of the contact angle, whilst further passes rendered the treatment reversible after a few hours.
- No post treatment
  - All post treatments tested led to an increase in contact angle.

5.3.2 Final Contact Angles

The contact angle measurements carried out so far have been done using drops of distilled water in air. However, the objective of the second part of this chapter was to inject different types of fluids into the micromodels, such as water, mineral oil or a water-in-oil emulsion (as in Chapters 2 and 3). Specifically, we used the same fluids as in Section 3.2.3. The oil phase consisted of mineral oil (Alfa Aesar) with 1 wt% SPAN 80. We measured the contact angles for drops of oil in air and drops of water in oil on both untreated COC and on a COC substrate following TEOS deposition with the previously optimised parameters. The resulting droplet shapes and the corresponding contact angles are displayed in Figure 5.17

It should be mentioned that all fluid injections in the micromodels were performed several days after manufacture of the surface-treated micromodels. Consequently, the contact angles presented here were also measured several days after treatment to most

accurately assess the experimental conditions.

In the continuous oil phase with the surfactant, a droplet of water did not wet the untreated COC, forming a contact angle of 140°. After the surface was treated with TEOS and rendered hydrophilic, the water in the oil spreads and partially wets the surface of the solid. A contact angle of about 70° is formed, a reduction of 70°. This angle is also around 30° larger than that for a water droplet in air. It is interesting to note that while the treatment is hydrophilic, it is not lipophobic. The deposition of SiO_2 even slightly improves the spreading of the oil on the surface from 30° to 20°.

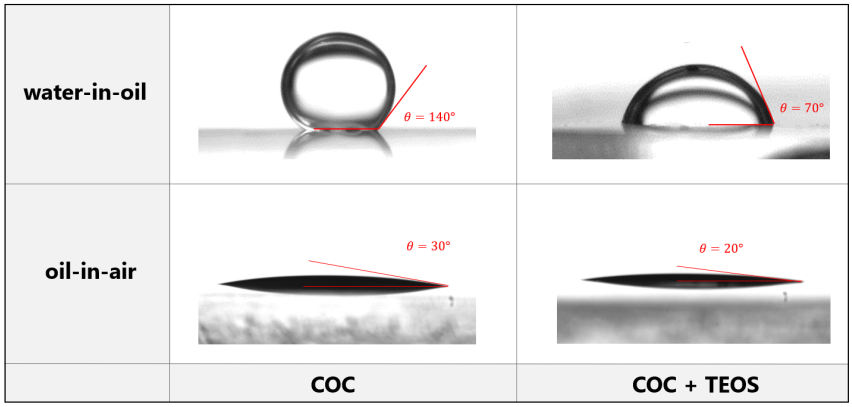

Fig. 5.17 Comparison of the contact angles of water droplets in oil (top) and oil droplets in air (bottom) on flat substrates of COC (left) and COC + SiO_2 (right). The oil phase consists of mineral oil (Alfa Aesar) with 1 wt% SPAN 80.

5.3.3 Fluid Flow in Micromodels with Variable Wettability

As discussed in the previous section, we developed a methodology for creating COC micromodels of which we could modify the wettability. We now discuss the impact these changes in wettability had on the resulting fluid flows, both in the case of homogeneous and heterogeneous wettabilities. Whilst the study of emulsion flow in model porous media remains the primary topic of interest, as in the work of previous chapters using homogeneous oil-wet micromodels, single-phase injections were too considered and are briefly presented below.

Single-phase Fluid Injection: COC

Injection tests were performed in the micromodels, first filling the empty micromodels with water (plus 1 g/L of blue methylene) before injecting high purity mineral oil (Alfa Aesar, J62592) into the water filled system. Untreated, homogeneously treated, and heterogeneously treated micromodels were studied for comparison. All micromodels bore the same microstructure. The flows were performed at low pressures and controlled using Fluigent tools (Flow EZ 2000 mBar). Pictures of the fluid interfaces for the different experiments are presented in Figure 5.18. All experimental images in Figure 5.18 represent the final, stationary phase.

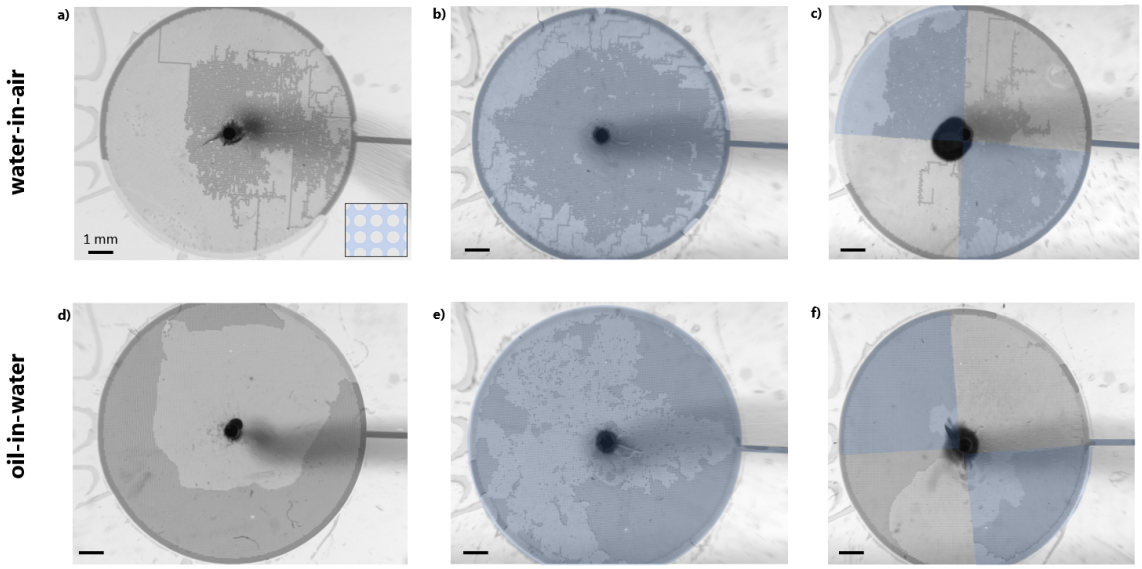

Fig. 5.18 Injection of water + blue methylene (1 g/L) and injection of mineral oil (Alfa Aesar) in micromodels pre-filled with air and water respectively. Micromodels are made from COC (contact angle 86°) and consist of square lattices of posts of diameter 50 µm (see bottom-right insert in 'a'). Zones coloured in blue correspond to areas rendered hydrophilic (contact angle approximately 40°) through SiO_2 deposition.

In the untreated COC micromodel (hydrophobic, Figure 5.18a) the water has difficulty in flowing and passes through a limited number of preferential paths (percolation). Afterwards the water continues to flow through these established paths without forming new ones. In the uniformly-treated micromodel however (hydrophilic, Figure 5.18b) the water flows more easily and homogeneously. The formation of preferential paths after the water propagation front is still noticeable and is likely due to the reduction in Ca with radius given the radial nature of the flow. Once percolation has occurred, following

the established paths presents less resistance than establishing new percolation route, and as such the flow pattern becomes stable. As expected, the water injection in the mixed-wettability micromodel (Figure 5.18c) flows preferentially in the areas treated by the TEOS deposition, i.e. in the hydrophilic areas. In fact, the behaviour in each quadrant is the same as that in the micromodel (Figure 5.18a or b) bearing the same wettability.

In the case of oil injection in the water-filled porous media in Figure 5.18(d-f), we first observe a somewhat uniform front in the case of the untreated COC (Figure 5.18d). This was expected given the favourable viscosity ratio M between the invading and defending phases of $M = 18$. As was the case for water injection, the front becomes less compact with distance from the central injection point. For the uniformly hydrophilic system (Figure 5.18e) the front is less homogeneous and we observe residual water trapped behind the advancing oil front. Finally, in the case of a mixed wettability (Figure 5.18f), we see that the oil initially flows solely in hydrophobic zones in a stable manner. In the upper right quadrant (hydrophobic) the water is completely drained, however in lower left quadrant (also hydrophobic) only the half of the quadrant closest to the exit channel is drained. We can deduce that this is an influence of the position of the sole exit channel. Consequently, in later experiments on emulsion injection (Section 5.3.3) additional exit channels were added to mitigate this effect.

Summary: Single-phase Fluid Injection

- For water injection in the air-filled porous media, the water preferentially flows in the hydrophilic sections, as expected.
- For injection of the oil and surfactant mix in the water-filled porous media, the oil preferentially drains the hydrophobic zones. The macroscopic flow behaviour is also influenced by the position of the single exit channel.

Emulsion Injection: PDMS and COC

A water-in-oil emulsion, generated using a droplet generator as described in Section 3.2.2, was then injected at a constant total flow rate into different micromodels pre-filled with the continuous phase. The experimental system, including the tubing and the syringe pumps for controlling the flow rate, were the same as used in Chapters 2 and 3.

All images below were taken once the steady state was reached.

PDMS micromodels

Two PDMS geometries were considered, both of which were made by binding the micro-patterned PDMS to a second block of PDMS using an air plasma after rinsing with isopropanol. PDMS plasma bonding leaves the surfaces highly hydrophilic, with a contact angle of around 25°, but which increases rapidly following the bonding. The micromodels were therefore filled with distilled water and 1 wt% SDS immediately after plasma bonding and the experiments were then conducted within ten minutes, before the hydrophilicity of the surfaces wore off. The first geometry was a straight channel of width 300 µm and height 50 µm whilst the second bore the porous geometry as before with a square lattice of posts.

In the case of the straight channel, the water-in-oil emulsion was injected at a total flow rate of 15 µL/min. We can see in Figure 5.19a that at this flow rate and given the small size of the water droplets within the channel geometry they did not adhere to the hydrophilic surface (Figure 5.19a, bottom). When the same emulsion was injected into the porous media with the same uniform hydrophilicity, however, the water droplets adhered to the PDMS within traversing the first few posts, as can be clearly seen in Figure 5.19b. The droplet are larger than the minimal pore spacing between the posts of the porous region such that $D/d \approx 4$. Within the distance of a few more posts the emulsion had completely inversed, as observed in a simple channel by Chen *et al.* [177]. Some water-in-oil-in-water double emulsion droplets were also observed to form in the porous media, as demonstrated by Schneider *et al.* with simple T-junctions [144].

Beyond the first few rows of posts in the porous media the inversed emulsion flowed largely in the directions of low tortuosity. Further away from the central injection point the transport of the emulsion became highly ramified, with most of the oil droplets trapped in position and just a few paths open to droplet flow. Figure 5.20 highlights this behaviour at two points around the edge of the porous medium, with the trapped droplets in black/dark blue and the moving droplets in yellow/red/white.

COC micromodels

Finally, we consider the emulsion injections in the COC micromodels bearing the same microstructure but of mixed wettability. The resulting flow patterns are shown below in Figure 5.21. As mentioned, additional exit channels were added to avoid the location

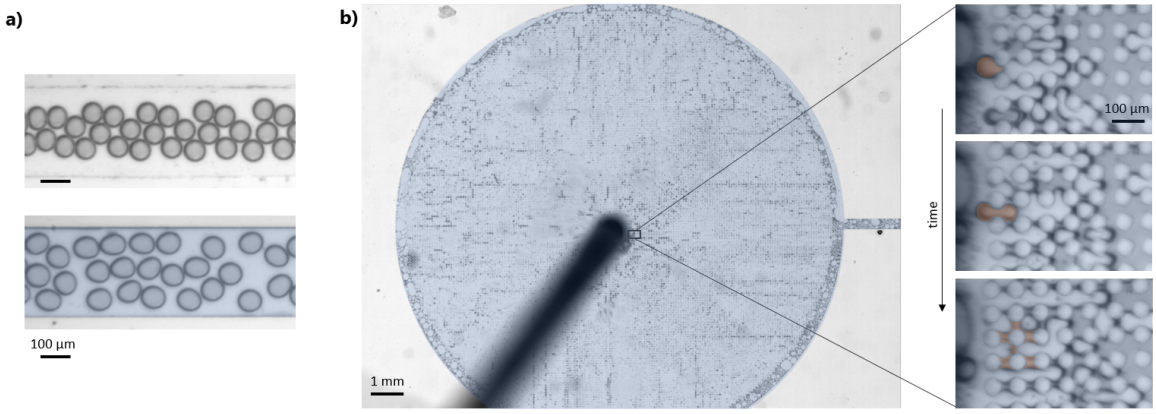

Fig. 5.19 a) Transport of water droplets (grey) in a continuous mineral oil phase (clear) in channels of width 300 µm and height 50 µm made of PDMS. b) Injection of the water-in-oil emulsion from 'a' (top) into a PDMS porous media micromodel consisting of a square lattice of posts of diameter 50 µm. The images in the time series on the right were taken 1 second apart. One droplet has been coloured in orange for visibility. In both cases the water phase was dyed with blue methylene (1 g/L) whilst the mineral oil phase contains 1 wt% SPAN 80. The emulsion was injected at 15 µL/min, giving $\overline{Ca} \approx 1.5 \times 10^{-3}$. The droplet diameters are larger than the minimal post spacing such that $D/d \approx 4$. Zones coloured in blue have been treated with an air plasma to render them hydrophilic ($\theta \approx 25°$).

of the exit channels influencing the transport of the emulsion through the porous media. Once again the total injection flow rate was kept constant throughout the duration of the experiment. For the COC experiments a total flow rate of 7.5 µL/min was used, corresponding to $\overline{Ca} = 3.5 \times 10^{-4}$.

In the case of the homogeneously hydrophobic porous structure (Figure 5.21a) we observe the same droplet transport patterns as in the PDMS models discussed in Section 3.3 and Figure 3.37. In the case of the geometries with mixed wettability (Figure 5.21b-c), the flow pattern greatly depended on placement of the zones rendered hydrophilic. In the case of Figure 5.21b the limits of the hydrophilic zones intersect the lines of preferential droplet flow and we see that the flow in the untreated zones (hydrophobic) appears to be identical to the equivalent zones in the uniformly hydrophobic micromodel. In the remaining hydrophilic zones the droplets are largely broken up and their path selection is unclear.

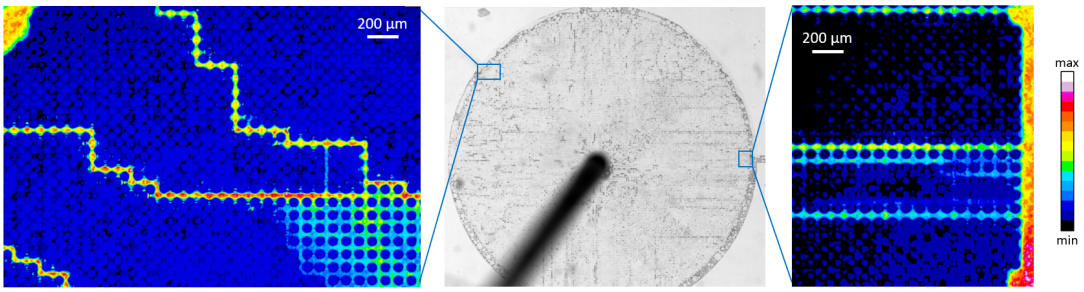

Fig. 5.20 The result of differencing 200 experimental images taken using an optical microscope at intervals of 1 second and then taking the average of the 199 resulting images. The differencing is calculated by subtracting the intensity of each pixel in one image from the intensity of the corresponding pixels in the second. The scale is from black (min, no difference between any of the 40 images) to white (max, greatest variation in pixel intensity across all 40 images). It becomes clear that most of the oil droplets are immobile. Most of the image including the posts is blue, not black, due to the very slight oscillation of the camera lens during the experiment. The experimental photo is the same as that of Figure 5.19

.

However, in Figure 5.21c we no longer observe the four distinct lines of preferential flow from the hydrophobic model. Large degrees of coalescence occur in the hydrophilic zones, as observed by the very large droplets in the circular exit channels at the edge of these zones. Flow occurs preferentially in the hydrophilic zones, with most of the droplets in the hydrophobic zones remaining stuck in place and only a few percolation paths opening up intermittently. As a result, very few droplets exit the porous region through the hydrophobic quadrants. The positioning of the hydrophilic zones, and not just their size or contact angle, has a strong influence on the nature of the droplet transport.

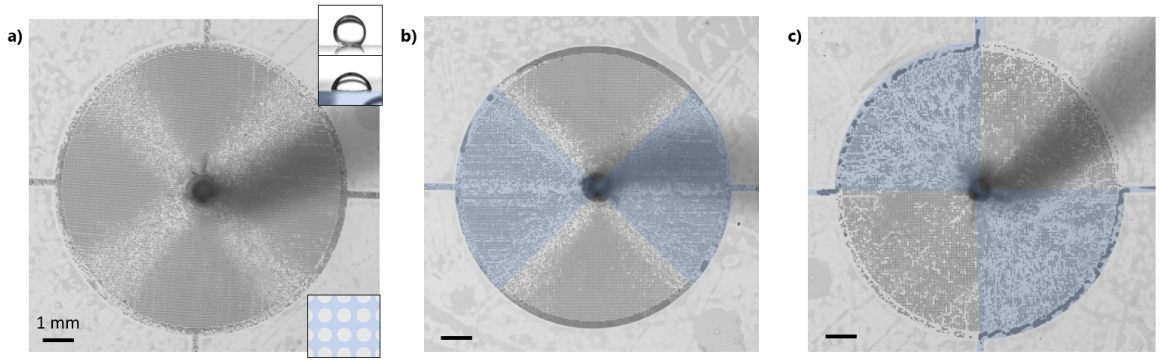

Fig. 5.21 Injection of a water-in-oil emulsion in a COC micromodel of variable wettability: uniformly hydrophobic ('a', contact angle 86°) and mixed ('b-c'). Hydrophilic zones (contact angle approximately 40°) have been coloured in blue in the images.

Summary: Emulsion Injection

- A PDMS micromodel was plasma-treated to render it homogeneously hydrophilic. The water-in-oil emulsion injected inversed while traversing the first few posts of the porous region. At the borders of the porous region the flow was highly ramified with just a few percolation paths being established.
- A COC micromodel bearing the same square post lattice was also studied. The flow patterns for the homogeneously hydrophobic micromodel were the same as for the PDMS geometries bearing the same lattice. Distinct hydrophilic zones were also added to the geometries in the form of quadrants. In all cases droplets coalesced in the hydrophilic zones. The disruption of the flow patterns was more severe when the hydrophilic zones fully encompassed two of the four preferential flow paths. When the borders of the quadrants only overlapped the preferential flow paths, the flow was undisturbed in the hydrophobic zones.

5.4 Discussion

Single-phase Fluid Injection

We can use the contact angles discussed in Section 5.3.2 to compare the various flow patterns to the extended Lenormand diagrams of Figure 5.4. The water-in-air injection in our experiments appears to vary from invasion percolation (hydrophobic, Figure 5.18a) to a more cooperative pore-filling method (hydrophilic, Figure 5.18b). This behaviour is as predicted in the phase diagrams of Figure 5.4, as well as that of Zhao *et al.* for $M >> 1$, when passing from neutral wetting ($\theta = 87°$) to weak imbibition ($\theta = 30°$).

As for the oil injection in the water-filled micromodels, it is harder to correlate the flow patterns to the Lenormand diagrams having not determined the contact angle of water-in-oil for the treated and untreated COC. Given that the contact angle of oil-in-air varies little after the surface treatment (from 30° to 20°) whilst the contact angles of water-in-oil decrease significantly (from 140° to 70°), we can postulate that the contact angle of water-in-oil may slightly increase after the treatment.

As for the experiments in the mixed wettability micromodels, the flow patterns in the hydrophilic and the hydrophobic quadrants remain the same as homogeneous hydrophilic and hydrophobic micromodels respectively. In both cases, and unsurprisingly, the injected water and oil show a great preference for flowing in the hydrophilic or hydrophobic zones respectively. The invading oil phase has a greater ease in displacing the defending water phase from the hydrophobic zones.

Emulsion Injection

As illustrated in Figure 5.19a, the water-in-oil emulsion remained stable when flowing through a straight rectangular channel. The lubrication film is, therefore, thick enough to prevent the van der Waals interactions from coming into play. Using Equation 5.1 from Chen *et al.*, we arrive at a critical capillary number for droplet adhesion to occur in a straight channel of $\approx 1 \times 10^{-1}$ which is much greater than the capillary number of the experiment of $Ca \approx 3.5 \times 10^{-4}$ [177].

We see, however, that when the droplets pass through the porous region the emulsion inverses within traversing a few posts. Given that $D/d \approx 4$, the droplets are under severe confinement when traversing each pore. It is possible that the added

resistance the posts add slows the droplets sufficiently such that the film thins to the point of emulsion inversion occurring. Furthermore, the deformation of the droplet to pass through the pores may leads to a surfactant depletion, leading to a change in the critical capillary number for droplet adhesion from Equation 5.1.

The behaviour of the emulsion varied greatly between all of the wettabilities considered. The most severe droplet breakup was observed for the plasma bonded PDMS micromodel, as this was the only instance where the emulsion was inversed upon injection. Whilst the water-in-oil contact angle has not been measured for this surface, the water-in-air contact angle was on the order of 15°, as was also observed by Ginn *et al.* [149]. The water, therefore, has a far greater affinity for the PDMS in this condition than for the COC as used in the remaining emulsion injection experiments (water-in-air contact angle of 40°). In both the COC micromodels of mixed-wettability studied, the emulsion remained water-in-oil despite have the same injection conditions and a hydrophilic surface treatment. This could be due to the larger contact angle for the treated COC, as well as the fact that only the micropatterned side of the COC was modified.

As mentioned for the emulsion injection in the mixed-wettability COC micromodels, the positioning of the surface-treated quadrants greatly impacted the resulting droplet transport. We can try to relate this behaviour to the droplet transport discussed in Chapter 2 and the angular variations in tortuosity. We see that in Figure 5.21b the borders of the surface treated zones fall on the regions of high tortuosity whilst those in Figure 5.21c fall on the regions of low tortuosity. This suggests that more systematic studies should be performed where the heterogeneities in wettability and correlated to preferential flow directions.

5.4.1 Summary and Perspectives

In this chapter we presented an experimental system for the manufacture of mixed-wet micromodels. Model porous media consisting of cylindrical posts with a spacing of 20 µm were accurately reproduced in COC from existing PDMS models. Controllable surface treatments were then performed using PECVD-based silica coating to produce precise local heterogeneities in wettability, as quantified using sessile drop contact angle measurements. These devices allow us to better understand and model multiphase flows in real porous media consisting of largely heterogeneous wettabilities.

For the COC substrates with an intrinsic contact angle for a water drop in air of 86°, the surface treatments allowed us to drop to as low as 20°, with stable contact angles of 40° several weeks after the treatment. Intermediate contact angles could be achieved in several ways, allowing for a more continual variation of wettability or even devices bearing several different wettabilities. It is unclear whether varying the PECVD parameters discussed previously yield different contact angles whilst still producing a homogeneous surface modification. However, post treatments such as a water-rinse were observed to immediately increase the contact angle and could also be applied between two series of TEOS depositions to produce distinct locations with different contact angles (cf Figure 5.16). Furthermore, performing two TEOS depositions on two distinct zones several days apart after varying time intervals.

As for perspectives in the fluid flow studies, a more systematic variation of the transport of the emulsion for varying injection capillary numbers or droplet sizes could be performed, similar to in Chapter 2, allowing the stability and the transport of the emulsion with respect to the models wettability to be better understood. It would also be interesting to observe the flows under a microscope in order to study the interfaces at the pore-scale to better understand the origin of the patterns observed. Finally, the injection of an oil-in-water emulsion could also be considered. In the experiments studied for water-in-oil emulsions the oil had a viscosity 20 times that of water resulting in the oil film separating the drops from the treated surface was undoubtedly more stable than with a direct oil-in-water emulsion. We can more easily achieve destabilisation of a water film in the oil-in-water case and therefore observe a more marked influence of wettability.

Conclusion

We have presented a primarily experimental study on the transport of emulsions in 2D porous media. Our main objective was to study the influence of the heterogeneities of the media, both in terms of the geometry and the surface wettability, on the resulting transport. Furthermore, the experimental conditions, such as the injection flowrate, as well as the properties of the emulsion, in terms of the size and volume fraction of the dispersed droplets, were varied systematically.

In Chapter 2, we observed preferential flow paths that arose within the porous media when droplets were under confinement ($D/d \ll 1$, $\psi > 1$) and the capillary numbers, measured at the mid-radius of the porous regions, $\overline{Ca} \geqslant 10^{-3}$. For the regular geometries, these paths arose systematically in the directions of high geometric tortuosity, a counterintuitive result. High concentrations of droplets converged on the low tortuosity directions, and the confinement of these droplets led to an increase in the hydrodynamic resistance of these paths, rendering them less favourable for subsequent droplets to flow through.

However, at $\overline{Ca} \approx 10^{-4}$, for emulsions with a droplet volume fraction $V_v < 0.2$, and for droplets of diameter $D < d$ and $\psi < 1$, the droplets filled the porous media homogeneously. We attribute the homogeneous transport under the three above conditions respectively to the following:

- At $\overline{Ca} \approx 10^{-4}$ confined droplets have greater difficulty overcoming the capillary pressure necessary to pass through pore constrictions, and the resulting collective droplet behaviour leads intermittent flows and a uniform filling of the porous media.
- At $V_v < 0.2$ the lower concentration of droplets adds less resistance in the congested paths of low tortuosity, and the dipolar perturbations generated by each droplet likely act to spread them out more uniformly.

- The unconfined droplets generate neither a Bretherton pressure drop nor must they overcome a capillary pressure to pass through posts and act more like tracers in a Newtonian fluid.

For the random geometries preferential flow paths were only observed in the pseudo-crystalline geometries that most resembled the regular lattices. Furthermore, a CNN-based analytical tool was employed to quickly map the local velocities of the thousands of droplets throughout the model porous media.

In Chapter 3, the experiments of Chapter 2 are re-examined, this time with the aim of assessing the stability of the emulsions. The distributions in droplets diameters, both at the outlet of the porous media and a specific locations within the porous media, were studied as a function of the injection and geometric parameters. We find that the mean diameter of the droplets exiting the porous media plateau at $\overline{Ca} \approx 10^{-3}$, regardless of the mean droplet diameter at the inlet in the case where droplets diameters are much larger than the pore widths. However, little to no breakup occurs when the droplets are smaller than the pore width.

Finally, in Chapter 4, we proposed a new methodology for fabricating micromodels containing discrete zones of modified wettability. The models were made from COC, a transparent and naturally hydrophobic polymer with an initial contact angle of $\sim 30°$, and treated using a TEOS deposition with an atmospheric pressure plasma. The resulting contact angles were quantified for flat COC substrates as a function of the experimental parameters of the surface treatment. Contact angles of a water droplet in air as low as 20° were achieved, with contact angles of 40° remaining several weeks after the treatment. Fluid injections, both of single immiscible phases and water-in-oil emulsions were then performed. Notably, the transport of the emulsion was highly dependent on the position of the hydrophilic zones with respect to the positions of the preferential transport paths discussed in Chapter 2.

The transport of an emulsion, even in simplified channel geometries or porous media, is highly complex and difficult to model. For instance, recent studies have shown that even the number of carbon atoms in the surfactant molecules can drastically impact the speed of a droplet with respect to that of the continuous phase [72]. As such, emulsion and droplet transport remains an active field of research.

The visualisation of the flow behaviour within transparent micromodels, allowing the microscopic geometry to be related to the macroscopic flow behaviour, presents an excellent opportunity to improve our understanding of emulsion flows. Further quantitative analysis is required if we want to predict the flow behaviour based on the geometric properties of the micromodel and the flow parameters of the injected emulsion, the flow parameters of the injected emulsion, and the physico-chemical properties of the working fluids (viscosities, surface tension, surfactant used). Such analyses include quantifying the resistance added to a flow path by a series of droplets in a simple obstacle network. Future analyses could also benefit, at least from a qualitative perspective, from considering the geometric tortuosity of the porous media, as the preferential flows paths and the regions of droplet blockages were dictated by the directions of high and low geometric tortuosity respectively. Furthermore, the ability to determine in an iterative manner the geometric tortuosities as a function of the droplets already present in the porous media could allow for the transitions in preferential flow paths, such as from the filling to stationary phases in Chapter 2, to be identified.

Appendix A

Angular Variations in the Permeability of Regular Porous Media

A.1 Introduction

The porous geometries of all the micromodels considered in this manuscript have consisted of regular lattices of posts and are homogeneous at a macroscopic scale. However, we have seen that in the case of radial outward flows from the centre of these porous media, preferential flow directions can arise. These preferential directions are determined by the microscopic pore structure, arising in the angular directions where the posts align, producing low tortuosity streamlines. As discussed in Chapter 2, porous media micromodel studies have shown that preferential flow directions primarily arise in directions of high permeability. It was unclear to us how the alignment of the posts influenced the permeability of a regular porous media and in turn the development of preferential flow directions. Furthermore, given that permeability is a macroscopic property, does it even make physical sense to discuss an angular permeability?

Fluid flow in the Stokes regime through periodic and random arrays of aligned cylinders has been widely considered in theoretical and computational studies, notably by Sangani and Acrivos [180, 181]. Koch and Ladd stated that the permeability k is isotropic in the case of isotropic media [182]. This is due to the linearity of the Stokes equations - the mean flow velocity $\bar{v}$ must be proportional to the applied pressure gradient. As a result, the proportionality constant, k/η, must be a scalar in the case of

isotropic media. This reasoning was also extended to simple square arrays of cylinders owing to the principle of linear superposition, as well as to random geometries. It was unclear to us, however, whether hexagonal lattice arrays could be considered isotropic, and as such whether the permeability is this array could be considered isotropic.

Some relations, such as the Kozeny–Carman law, have been derived to predict the links between porosity, tortuosity, and the resulting permeability of a porous medium. The permeabilities of geometries have been considered, such as systems of parallel capillaries (k_{cap}) or packed beds of spheres (k_{sph}).

$$k_{cap} = \frac{\phi D_h^2}{96 T_G} \tag{A.1}$$

$$k_{sph} = \phi_s^2 \frac{\phi^3 D_g^2}{180(1-\phi^2)} \tag{A.2}$$

where D_h is the hydraulic diameter of the capillary, T its tortuosity, D_g the mean diameter of the spherical grains, ϕ_s their sphericity ($\phi_s = 1$ for perfect spheres). As a general trend, the permeability increases with increasing porosity and decreasing tortuosity. However, for more complex geometries no exact relations exist. We can, nonetheless, calculate a rough approximation using Equation A.1 and setting $T_G = 1$ as well as $D = \sqrt{\frac{4HL}{\pi}}$ where H and L are the height of the channels and the minimum inter-post spacing for each of the geometries. Doing so gives us values of k = 10.3 darcy for the hexagonal geometry, 8.2 darcy for the square geometry, and a variation between 6.2 and 10.3 darcy for the rectangular geometry at 0° and 90° respectively (see below for significance of these angles).

Furthermore, Tamayol and Bahrami considered the permeability of square lattices of cylinders at 0° and for various porosities and post diameters [183, 184]. They subsequently derived the following equation for such calculations:

$$\frac{k}{D^2} = \left\{ \frac{12\left(\sqrt{\epsilon'}-1\right)}{\epsilon'\sqrt{\epsilon'}} \left[\frac{2-g(\phi)}{2}\right] + \frac{18+12\left(\epsilon'-1\right)}{\sqrt{\epsilon'}\left(1-\epsilon'\right)^2} + \frac{18\sqrt{\epsilon'}\left[\tan^{-1}\left(\frac{1}{\sqrt{\epsilon'}-1}\right)\right]}{\left(\epsilon'-1\right)^{\frac{5}{2}}} \right\}^{-1} \tag{A.3}$$

where D is the post diameter, ϕ the porosity of the structure such that $\phi = 1 - \pi D^2/4(L+D)^2$, $\epsilon = 1 - \phi$, $\epsilon' = \pi/4\epsilon$, and $g(\phi) = 1.274\phi - 0.274$. However, this equation accounts only for the resistance added by the posts and not that added by the walls enclosing the porous region which for this porosity can still be significant [185]. To account for the wall effects as per Brinkman's law, Tamayol and Bahrami proposed a correction using an effective viscosity $\eta_e = \eta/\phi$. For the dimensions of our square porous media this relation with the corrections gives a permeability of 25.7 darcy, over three times greater than the value determined by the Kozeny–Carman law.

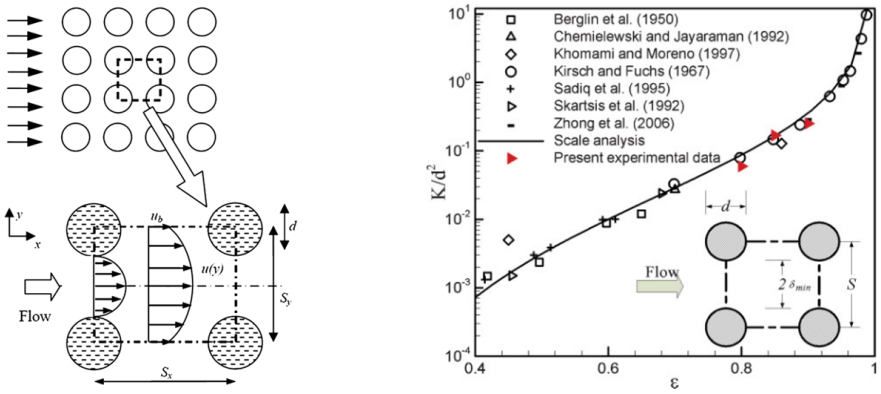

Fig. A.1 Left) Rectangular lattice of cylinders and the considered unit cell. For the square lattice $S_x = S_y = S$. Right) Comparison of the model in Equation A.3 proposed by Tamayol and Bahrami for square arrangements at 0° and comparison with experimental data from several sources [183, 184].

Consequently, in order to determine permeabilities at intermediate rotations we pursued two different methods of measuring permeability: experimental measures using specially adapted micromodels, and numerically, using both finite element (COMSOL) and Lattice Boltzmann simulations. For each method we first determined the permeability of a straight, rectangular channel, allowing us a comparison with the theoretical permeability of the geometry, as calculated following Equation 2.8. With this base-point established, we then studied Hele-Shaw cells, the dimensions of which varied based on the method used, that were transposed with the lattices of posts from previous chapters. To mimic the angular variations in the alignment of the posts, as seen by the fluid when flowing outward in the radial geometries, the post lattices were rotated in increments of 5°. Figure A.2 highlights the resulting lattice geometries at 0° (in line with the exit channel), 15° and 30°. The size of the porous geometry remained fixed for all experimental measurements whilst for the numerical methods

the dependence of the permeability measures on the dimensions of the geometry were studied. For the latter the influence of mesh size (COMSOL) and other such numerical parameters were also considered.

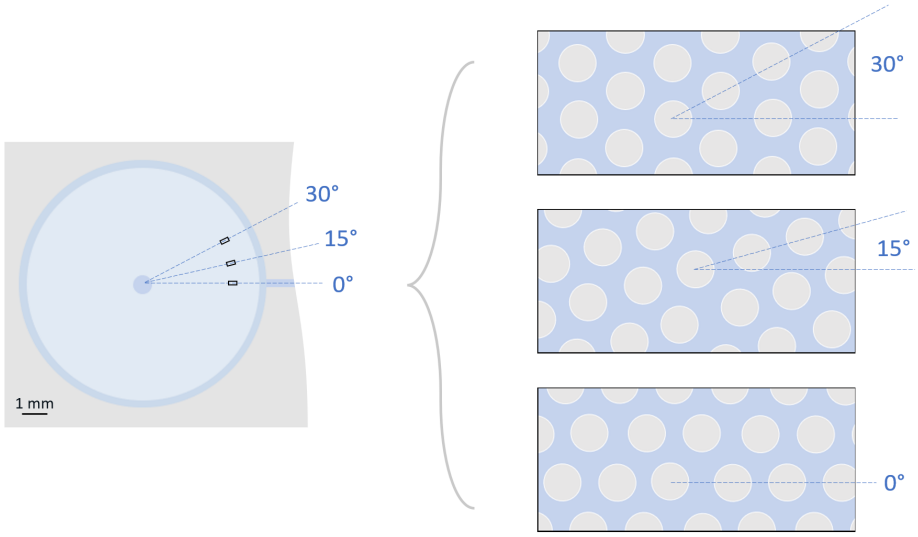

Fig. A.2 Schematic of the radial porous media (left) and the resulting variations in the orientation of the posts (right) in the case of the hexagonal lattice symmetry. All the posts have a diameter of 50 µm.

It was mentioned in Chapter 1 that a single-phase Stokes flow is linear and as such an analogy of Ohm's law can be made to correlate the pressure difference across a fluid system, ΔP, and the corresponding flow rate, Q, using a hydrodynamic resistance, R. With R determined, the permeability of the system k can be calculated by rearranging Darcy's law in Equation 2.21:

$$k = \frac{L\eta}{RA} \tag{A.4}$$

where η is the viscosity of the fluid, L the length of the fluid system, and A its cross-sectional area. The resulting permeability, of dimensional units length^2, is commonly converted to the darcy whereby 1 darcy is equivalent to 0.987 µm^2.

A.2 Experimental Measures

The experimental set-up used to measure the permeabilities of the porous media of our micromodels is shown below in Figure A.3. Water at room temperature (21 °C) was transported through the porous media at various inlet pressures by means of a pressure controller (Fluigent Flow EZ 2000 mbar) and the resulting flow rate was measured with a flow meter (Fluigent M Flow Unit). Prior to injection in the porous media the flow was left to run for several minutes so that any air bubbles in the system were flushed out. An initial series of measures were then performed to determine the resistance added by the various components such as the flow meter, the PFTE tubing, and the straight channels either side of the porous region within the model porous media. The permeability of a single straight rectangular channel was also measured to provide a comparison point with theoretical values. With the measures performed for the various lattice configurations, the initial values could be subtracted, given the linearity of Stokes flow, and the permeability of each porous media determined using Equation A.4.

A second series of micromodels were also developed as a means to measure the permeabilities. The geometries feature the same lattices of posts, but they were instead confined to a rectangular channel, inducing a linear flow. The rectangular section containing the lattice of posts has a length of 12 mm, equal to the diameter of the circular porous region in the radial geometries, and a width of 3.6 mm. The resistance added by these rectangular channels was calculated experimentally and subtracted from the global resistance measures when determining the permeabilities of the porous media. At either extremity of the porous region is an additional space of length 0.3 mm to allow the dispersion to enter the lattice of posts evenly across the width. The rectangular channels are each 9 mm in length, the same as the exit channel of the radial geometries. One variable that didn't remain constant, however, was the height of the channels, determined during the fabrication of the mould whereby a tolerance of ± 10 % exists. The geometries for all of the various porous media in this chapter were spread across three moulds of heights 45, 45, and 53 µm. Given the dependence of the hydrodynamic resistance on the height of the channel to the power 3, expressed in Equation 2.8, the influence of this variation in height will be explored in this section.

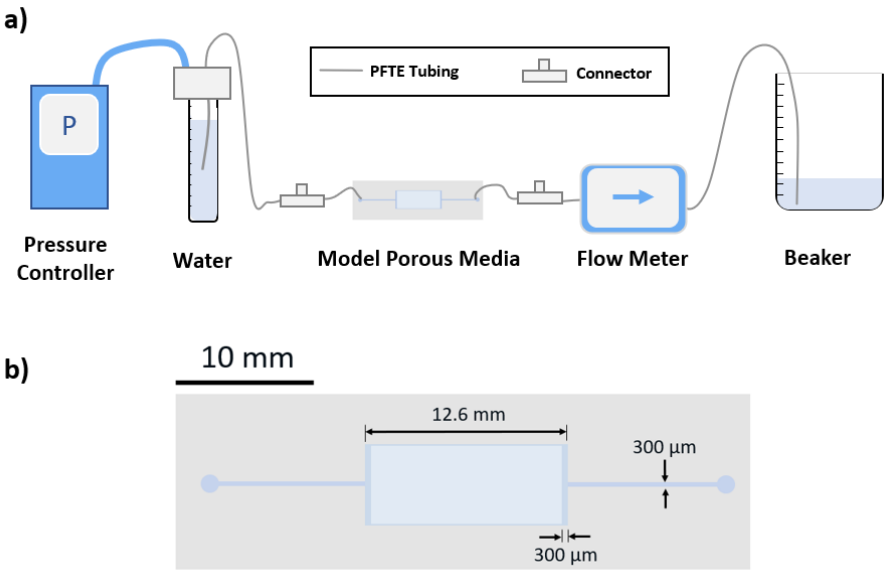

Fig. A.3 (a) Experimental set-up for permeability measurements. (b) The porous geometry of the PDMS porous media used for the permeability measurements.

A.2.1 Straight Channel

The hydrodynamic resistance of the entire fluidic system was first measured by replacing the model porous media of Figure A.3 and the two 10 cm tubes either side of it with a single 20 cm tube of the same material and internal diameter. A channel of dimensions 18 mm x 300 µm x 50 µm was connected in the position of the model porous media and the new resistance determined. The various measures taken of the applied pressure and the measured flow rate are for this experiment are shown in Figure A.4. With the difference between the two measures, i.e. the hydrodynamic resistance of the channel, the channel's permeability was determined to be 166.2 darcy. With a theoretical permeability of 154.8 darcy we have an overestimation by around 7 %.

A.2.2 Porous Media Measurements

The results for the experimental measures on the angular dependence of the permeability of the porous media are shown in Figure A.5. For each geometry a minimum of three angles were considered so as to allude to a trend in the measurements. The permeabilities bearing a square lattice geometry were rather constant at 16.3 ± 1.5 darcy. The global trend for the rectangular geometries, increasing with the angle of

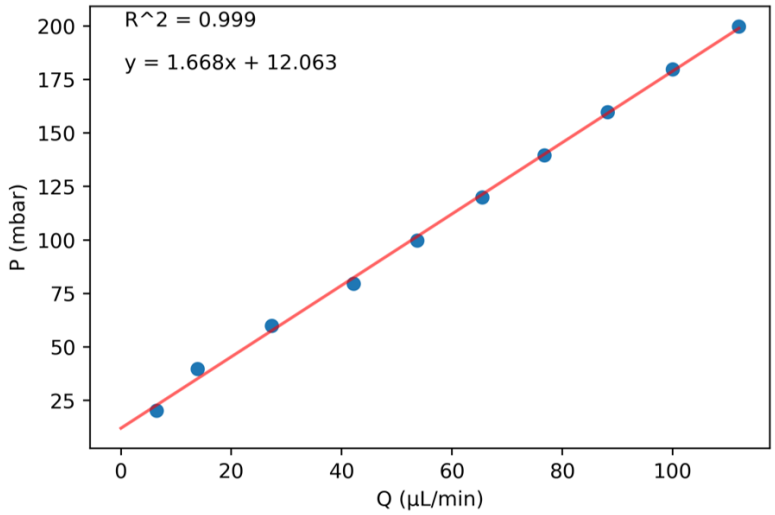

Fig. A.4 Plot of the applied pressures and corresponding measured flow rates for water in a straight rectangular channel of dimensions 18 mm x 300 µm x 50 µm using the set-up in Figure A.3.

rotation, appears reasonable given that the post spacing is lowest at 0° (15 µm) and highest at 90° (25 µm). However, we would therefore expect the permeability measured for the rectangular lattice geometry at 90° (14.0 Darcy) to be greater than that of the square lattice geometry (15.6 Darcy) where the alignment of the posts is the same but with an inter-post spacing of just 20 µm. Finally, the hexagonal geometry was the most varied of the three. In fact, the angles producing both the highest and the lowest permeabilites were those with the larger channel height of 53 µm (outlined in red in Figure A.5). Correcting these values to account for the increased channel height would likely significantly decrease the resulting permeability measurements. In order to obtain permeability measures for more angles between 0-90°, and in a manner requiring much lest time and materials to do so, we next decided to perform numerical permeability measures, as described in the following two sections.

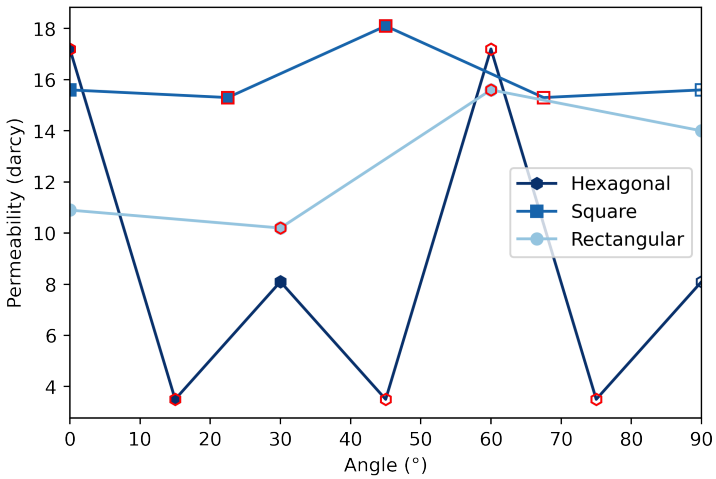

Fig. A.5 Results from the experimental measures on the angular dependence of the permeability of the porous media. The porous media consisted of three regular lattice geometries: hexagonal, square, and rectangular. Unfilled points in the graphs indicate values that were assumed due to symmetry of the regular geometries. Points with a red outline were performed on geometries with a height of 53 µm whilst the rest had a height of 45 µm.

A.3 Numerical Measures: COMSOL

COMSOL Multiphysics is a commercially available simulation software package based on the finite-element method. The simulations presented this chapter were performed using COMSOL 5.5 on a dedicated computer having 60 Gb of RAM and a 3.5 GHz Intel Xeon processor. All COMSOL simulations were performed on 3D geometries by resolving the equations of Stokes and mass-conservation. The fluid of study in each case was water ($\eta = 1$ mPa.s). With this system the duration of each the simulations on the porous media of this study was approximately 4 hours.

A.3.1 Straight Channel

As with the experimental measures of the permeability, our methodology was first checked by considering a straight, rectangular channel. The channel had dimensions of length 1 mm, width 300 µm, and height 50 µm. Several triangular meshes were tested, all generated automatically by COMSOL using the method “Meshing controlled by the Physics” and with element sizes of ‘Normal’, ‘Fine’, and ‘Finer’. The ratio of element size to channel height (the smallest length dimension) ranged from 0.14 for ‘Normal’

element sizes to 0.08 for 'Finer'. A pressure difference was applied across the channel and no-slip boundary conditions were applied to all of its internal surfaces. Using the calculated flow-rates we calculated the permeability of the channel to be 189 darcy for all meshes studied. This is in excellent agreement wit the theoretical value given by Equation 2.8, presenting an error of just 0.2 %.

A.3.2 Size Invariability and Mesh Dependence

Next, we created a Hele-Shaw geometry interspersed with the various lattices of posts from previous chapters and studied the smallest representative elementary volume (REV) as well as the dependence on the fineness of the mesh. For the following tests in this chapter the hexagonal lattice geometry at 30° was used each time. By starting with a Hele-Shaw of dimensions 750 x 225 x 50 µm, we reduced the size of this volume by half several times and measured the permeability for each geometry. The manner in which the geometry was halved, as well as the resulting permeability measures for each geometry, are shown in Figure A.6. For this first test the 'Normal' mesh size was used for each measurement.

The permeability appeared to be unaffected by variations in the length of the channel and to only drop by approximately 10 % between those of width 225 µm and those with half that width. As a result, we kept the largest dimensions studied of 750 x 225 x 50 µm for all remaining COMSOL simulations. Since the permeability still appeared to vary with the width of the porous media, we would have like to increase the width for remaining tests. However, when adopting larger geometries our simulations failed to converge despite many attempts to vary the convergence requirements. With ?? meshes in the 750 x 225 x 50 µm, it appeared we were unable to perform simulations on geometries larger than this.

As for the dependence on the mesh fineness, we tested the four finest meshes default meshes available in COMSOL. Between the coursest ('Normal') and the finest ('Extra Fine') of them the resulting permeability of the porous geometry varied by just 1 % (Figure A.6, right) whilst computational times increased considerably. We hence adopted the 'Normal' mesh fineness for the remainder of the COMSOL simulations.

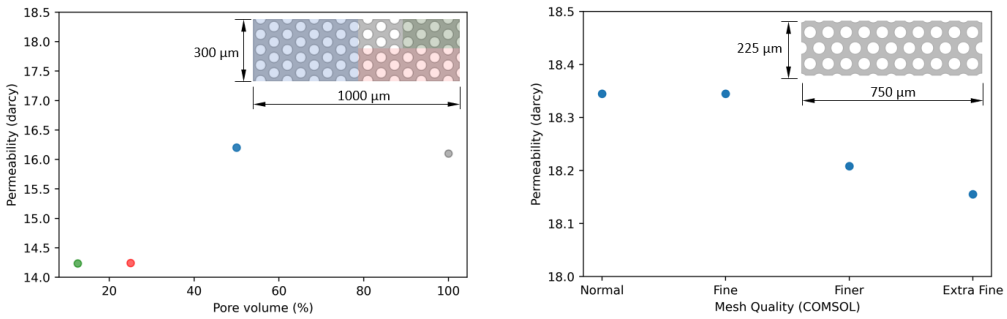

Fig. A.6 Influence of the size of the porous media (left, hexagonal at 30°) and the mesh fineness (right, hexagonal at 0°) on the permeability measures for the hexagonal lattice geometry at 0°.

A.3.3 Porous Media Measurements

With the porous media size and mesh fineness determined, the influence on the permeability of the rotation of the three regular lattice geometries was studied. A pressure gradient was imposed across the porous media and a no-slip boundary condition applied to all internal surfaces. The results of the simulations are shown in Figure A.7.

It should be noted that each of the regular geometries are cyclically symmetrical, with periods of 30°, 45° and 180° respectively for the hexagonal, square, and rectangular geometries respectively. Furthermore, the exact overlap of the cylindrical pillars within the rectangular frame can naturally be varied. Hence, in cases where the point on a graph in Figure A.7 or thereon after is filled the simulation was performed for a unique geometry bearing that angle of rotation. Taking the hexagonal geometry in A.7a, this means that whilst at 0° and 60° the alignment of the posts is the same, the exact positioning of the posts varied. However, in cases where the point on a graph is unfilled, such as for the square geometry at 50-90° in Figure A.7a, the permeability shown was simply assumed through symmetry.

We see in Figure A.7a that for the hexagonal and the square geometries, the permeability remains relatively constant throughout, as predicted by Koch and Ladd [182]. In an attempt to explain the spikes in the permeability at various points, such as at 0° and 60° for the hexagonal geometry, we plotted the porosities of each of the porous media considered, calculated directly in COMSOL. Permeability measured should be performed on representative elementary volumes (REV) of the porous media whereby the porosities should be constant with a value of 0.597, the macroscopic porosity of all

three geometries. However, as shown in Figure A.7c, the porosities deviate from the macroscopic porosity by up to 5 %. Furthermore, these variations appear correlated to the spikes in permeability. We can therefore deduce that the volumes considered are not large enough to be true REVs. However, as mentioned previously, we were unable to perform simulations on geometries larger than these for computational reasons.

Finally, we can consider the speed maps shown in Figure A.7b. Whilst the streamlines appear well predicted, we can see that the no-slip boundary conditions on the side walls (top and bottom in the flow maps) reduces flow near these walls and as such as periodic or other such boundary condition may have been better suited to these geometries.

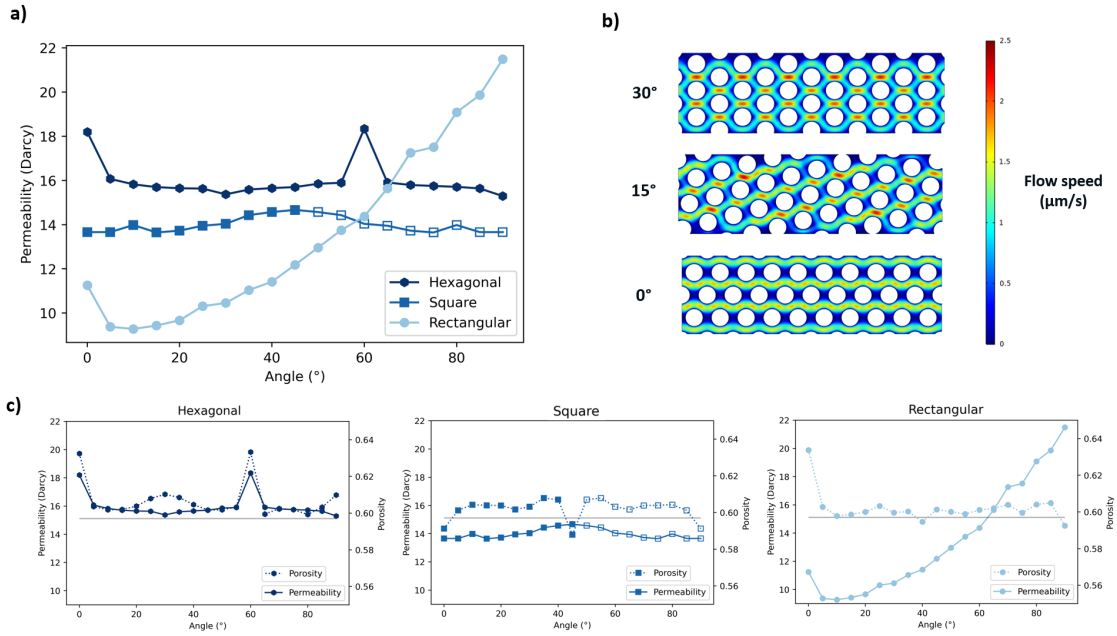

Fig. A.7 (a) Results from the COMSOL simulations on the angular dependence of the permeability of the porous media. The porous media consisted of three regular lattice geometries: hexagonal, square, and rectangular. (b) The speed maps for three of the hexagonal lattice geometries considered in 'a'. The posts have a diameter of 50 µm. (c) From left to right, the variations of the permeability and the porosity for the hexagonal, square, and rectangular lattice geometries respectively. Unfilled points in the graphs indicate values that were assumed due to symmetry of the regular geometries. The grey horizontal lines in each graph indicates the macroscopic porosity (0.597) of each of the three porous media geometries, highlighting the large variations in porosity observed in the modelled geometries.

A.4 Numerical Measures: Lattice Boltzmann

It became apparent that the simulations using COMSOL presented two main problems. Firstly, we were unable to simulate the flow within geometries large enough to be considered as REV. Secondly, creating the geometries was time consuming and significant difficulties with the meshing was encountered, meaning the geometry creation could not be automated. As a result, we decided to use the Lattice Boltzmann Method (LBM). The LBM is used to derive the solutions of macroscopic thermodynamics equations, such as the Navier-Stokes equations or the Advection-Diffusion equation, based on statistical considerations [186]. This method is relatively complex and as such the aim of this section is by no means to detail it precisely. Simulations with this method are highly efficient, using the binary images of the geometries directly as the input, and are not as constrained by meshing as with finite element analyses. All LB simulations were performed on a Dell Precision 5540 laptop running Windows 10 and containing 6 cores, an Intel(R) Core(TM) i7-9850H CPU (2.60GHz) processor and 16 GB of RAM.

The simulations were run using an in-house LBM code implemented in 'plug im!'. For every simulation the input was a 3D binary image with the pores in black (voxel value 0) and the posts in white (voxel value 255, 8-bit encoding). The precision of LBM depends directly on the resolution of the base images. The output of every simulation was the average interstitial velocity of the fluid within the pore space $\bar{j}$. The permeability, k, could then be calculated using the equation:

$$k = \bar{j}\phi\eta^* \frac{\Delta P^*}{L} \tag{A.5}$$

where ϕ is the porosity of the geometry, η^* the numerical fluid viscosity, ΔP^* the numerical pressure drop across the geometry, and L the length of the geometry in the direction of the flow in voxels. The preceding numerical parameters are the given as inputs for each simulation and influence the required convergence time. More precisely, the available input parameters were $\Lambda_E = 3\eta$, $\Lambda_O = 3\Lambda_E/16$, and $\rho^*_{in} - \rho^*_{out} = \Delta P^*/{c^*}^2$. Here, ρ^*_{in} and ρ^*_{out} are the numerical fluid densities at the inlet and outlet respectively and c^* is the numerical speed of sound (0.33 for all simulations).

A.4.1 Straight Channel

A single-phase Stokes was simulated in a rectangular straight channel of cross-sectional dimensions 436 x 100 µm and length 715 µm. As mentioned for the previous meth-

ods, comparison with a simple geometry allows for a comparison with theoretical permeabilities so as to estimate the accuracy of the method. Numerous numerical viscosities were studied to find the fastest convergence time for the system. The simulations were then run until the variation in permeability between iterations was on the order of 10^{-5}, for this test and for all subsequent tests. A no-slip boundary condition was also applied to the internal surfaces for all tests. The permeabilities calculated were all 179.0 darcy giving an error of less than 1 % from the theoretical value.

A.4.2 Size Invariability

As for the COMSOL studies, before simulating the various porous media at all angles, the dependence of the permeability on the size of the geometry was first investigated. Unlike with the COMSOL simulations, the various geometry sizes maintained a constant aspect ratio of 3.3 and a voxel-to-µm ratio of approximately 0.55. The lengths considered ranged from 200 voxels to 3600 voxels. For these dimensions it was not possible to have a channel height equivalent to exactly 50 µm, and so two different heights were considered for each geometry: 27 voxels (49.2 µm) and 28 voxels (51.0 µm). Finally, for each geometry size four different randomly generated posts placements were considered. The resulting average permeabilities, plotted against the pore volumes of the geometries, is shown in Figure A.8.

The permeabilities appeared to plateau at around 20 darcy for pore volumes greater than 10^8 µm^3, corresponding to a length of 1600 voxels or around 2900 µm. In subsequent studies, geometries with the same aspect ratio and a length of 2901 µm were used. Furthermore, a new technique for creating the binary images allowed us to achieve a voxel-to-µm ratio of 1, meaning the geometries studied had a greater number of pixels than that of the 1600 voxel geometry here. Furthermore, this allowed us to generate a height of 50 µm exactly, halving the number of required simulations.

A.4.3 Porous Media Measurements

The results from the LBM simulations on the angular dependence of the permeability of the porous media for the same three regular lattice geometries are shown in Figure A.9. For the hexagonal lattice geometry at 25° four random lattice positions were considered independently, all of which led to permeabilities of 14.8 ± 0.01 darcy. Given

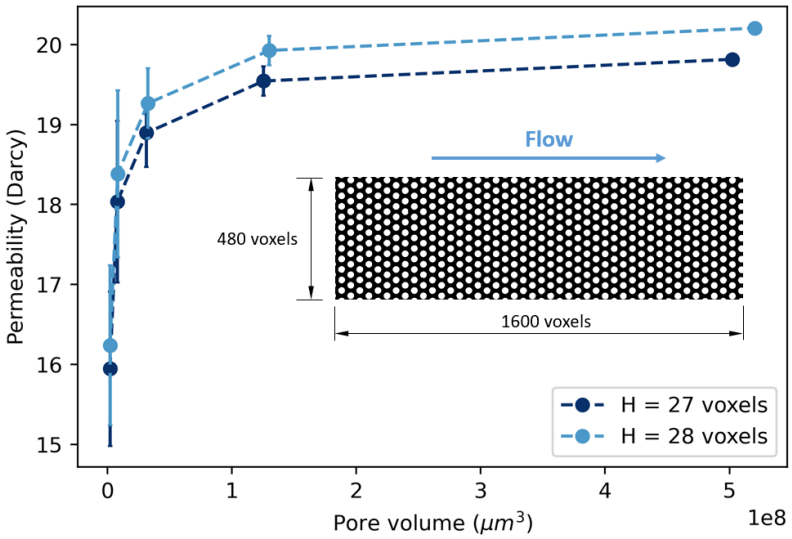

Fig. A.8 Influence of the size of the porous media on the permeability measures for the hexagonal lattice geometry at 30°. One of the geometries corresponding to the second largest pore volume studied, L = 1600 voxels, is shown as an insert.

the invariability of the permeability of these porous media with lattice positioning, all subsequent simulations were performed for one random lattice positioning at each angle. Unlike with the COMSOL simulations, the porosities of all geometries considered were constant at $\phi = 0.59$. All geometries were of dimensions 2901 x 871 x 50 voxels.

We find very similar trends in the curves and similar permeability values as for the COMSOL simulations in Section A.3.3. Once again, the results for the hexagonal and square lattice geometries appear rather constant at all angles, as predicted by Koch and Ladd [**?**], whilst those of the rectangular geometry pass from a minimum around 0° to a maximum at 90°. Interestingly, we also find the similar spikes in the permeability values, such as at 0° for the for all three lattices.

Comparing the permeabilities of the hexagonal lattice geometry in Figures A.8 and A.9 we find average values of approximately 20 darcy and 15 darcy respectively. We are unsure exactly what caused such a discrepancy. Despite the permeability not varying maintaining a constant value of 14.8 darcy for the hexagonal lattice geometry at 25°, regardless of lattice positioning, we decided to once again investigate the invariability of the permeabilities with the geometry size. This time, the width of the geometries remained constant at 871 voxels whilst the length varied from 500 to 4500 voxels. The results, shown in Figure A.10, suggest that the geometries studied in Figure A.9 may

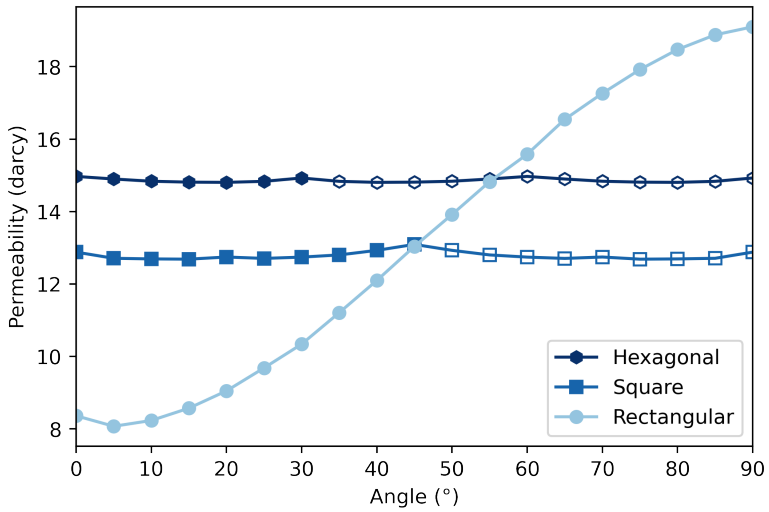

Fig. A.9 Results from the LBM simulations on the angular dependence of the permeability of the porous media. The porous media consisted of three regular lattice geometries: hexagonal, square, and rectangular. All porous media were of dimensions 2901 x 871 x 50 voxels. Unfilled points in the graph indicate values that were assumed due to symmetry of the regular geometries.

not have been REVs, given that the measured permeabilities continue to vary when the size of the porous medium is increased. However, we were unable to simulate larger geometries due to computing time consideration.

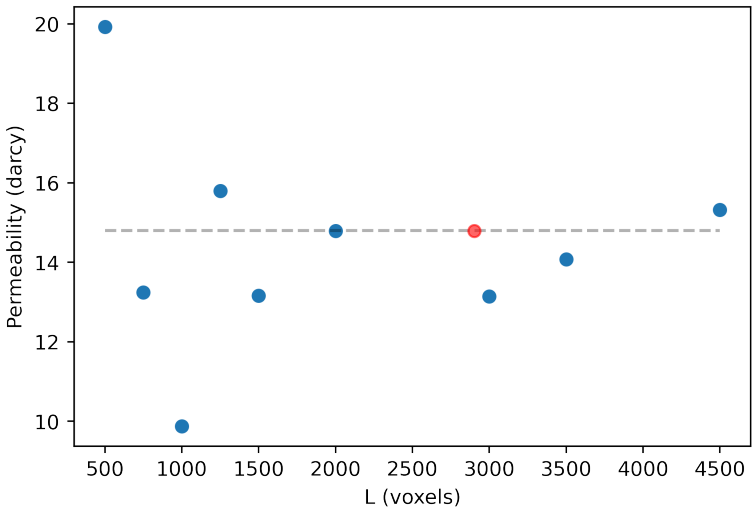

Fig. A.10 Results from the LBM simulations on the variability of the permeability with the length of the hexagonal porous media at 25° for constant cross-sectional dimensions. The red point represents the permeabilities of the four different geometries of length 2901 voxels studied, and the dotted grey line at 14.8 darcy their mean permeability.

A.5 Discussion

Three methods were used to determine the possible variations in permeability for three periodic lattices of cylindrical posts. The results from the various methods for each geometry are displayed in Figure A.11. The results for the square and rectangular geometries present very similar trends and average values across all three methods. It is unclear, however, what caused the larger disparities for the hexagonal geometry between experimental and numerical measures that did not arise for the other two geometries. It would therefore be advised to repeat the experimental permeability measurements several times to produce an average value, however when considering tens of geometries this method is much more time consuming than the numerical measurements.

The accuracy of the experimental measurements could also have been improved by measuring the pressure difference uniquely across the porous region, reducing possible sources of error, and repeating the measurements several times over. The geometries considered for both numerical methods were significantly smaller than the experimental ones, and by adopting smaller geometries for the experiments it may have been possible to produce them all with just one mask. This would further eliminate error sources

through variations in channel heights.

This being said, it still remains unclear for both numerical methods whether the geometries are significantly large to be considered REVs. In particular, the LBM should be further developed for its rapidity and ease of use.

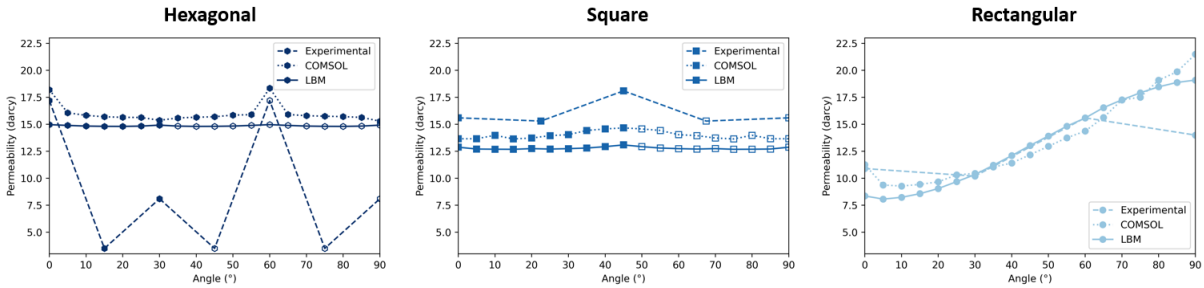

Fig. A.11 Comparison of the angular variations in permeability measures for the three lattice geometries.

Appendix B

Droplet Formation and Injection: Experimental Procedure

In Chapter 2, the experimental procedure presented allowed for fine tuning of the size and volume fraction of the droplets in the emulsion using a microfluidic droplet generator. The pre-formed emulsion could then be injected into the microfluidic porous media at the controlled capillary number as determined by the total injection flow rate. The experimental apparatus is shown in the schematic of Figure B.1. Table B.1 summarises the sequential opening and closing of the vannes in Figure B.1 throughout a typical experiment.

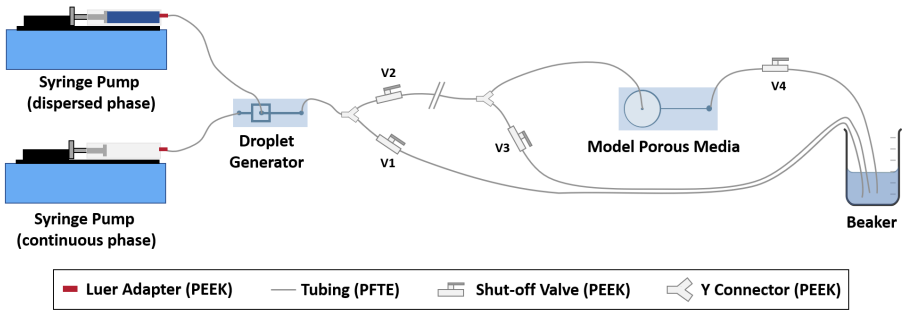

Fig. B.1 Schematic of the experimental set-up employed for the experiments in Chapters 3 and 4. The experimental apparatus is not shown to scale.

Droplets were initially directed towards the waste beaker by opening valves V1 and V3 and closing valves V2 and V4. After a minimum of ten minutes, the size and volume fraction of the droplets being formed were considered stable and emulsion could

Experimental Step	**Shut-off Valve**			
	V1	V2	V3	V4
Filling system with the continuous phase	**C**	**O**	**C**	**O**
Emulsion Testing → Beaker	**O**	**C**	**O**	**C**
Emulsion Preparation → Beaker	**C**	**O**	O	C
Emulsion Injection → Porous Medium → Beaker	C	O	**C**	**O**

Table B.1 Positions of the shut-off valves ('O' = open, 'C' = closed) during the various experimental steps for the injection of an emulsion in the porous medium. Values in bold are ones that have been modified from the previous step.

be redirected towards the porous medium.

Care had to be taken during redirection of the emulsion: even slight touches of the tubing could lead to rupture of the travelling droplets, especially at low flow rates. The injection was, therefore, performed in two steps. V2 was opened and V1 closed to first fill the intermediate tubing between V2 and Y2, with any ruptured drops being filtered out at Y2. Depending on the flow rates chosen, the filling of the intermediate tubing could last up to one hour. The diameter and volume of the droplets could be remeasured during this time to verify that the modified hydrodynamic resistance of the system had no noticeable influence on the emulsion being produced.

To redirect the produced emulsion towards the porous medium V4 was opened and V3 gently closed. At this point, the injection flow rates could be modified so as to apply the desired injection capillary number $\overline{Ca}$.

Appendix C

Morphological Modelling of Random Lattice Geometries

When creating the random lattice geometries of cylindrical posts, as discussed in Section 3.2.2, two distinct cases can be considered, depending on whether posts can overlap one another or not.

- In the case where the posts can overlap, Boolean models based on a Poisson point process can be used to determine their positions [187, 111]. Points within the defined geometry are randomly allocated, whilst the number of points to be placed follows a Poisson law. The density of points δ can be defined based on the desired porosity ϕ. In the case of a cylindrical post of constant cross-sectional area A:

$$\delta = \frac{-ln(\phi)}{A} \tag{C.1}$$

  Each post can then be positioned independently of all previously positioned posts following a Poisson point process until the required density is achieved. An example geometry is shown in Figure 3.18.

- In the case where posts should not overlap, a minimal inter-post spacing can be defined to allow for comparison with the other regular geometries. Additionally, due to manufacturing tolerances, spacing may be required to ensure all posts are well defined once moulded. To avoid overlapping of posts Random Sequential Addition (RSA) processes can be employed [188]. Posts are sequentially placed in random positions fulfilling the required separation from all other, previously positioned posts. Certain variants also allow for a more iterative approach whereby previously positioned posts can be repositioned or removed entirely to

allow for more efficient packing [189]. Recently, [190] proposed a packing model with variable compactness available from plug im! (IFP Energies nouvelles). The geometry is constructed by sequential addition, assigning a placement probability to possible points based on "concave points", leading to compact clusters, and "non concave" points, leading to loose structures. The concave points closest to the centre of mass of the cluster are also used, where the maximum compactness is reached. This model is used with a maximum compactness parameter by specifying the post diameter, the desired porosity, and the minimum inter-post spacing. For large values of the minimal inter-post spacing, fewer options remained to achieve the required porosity, and the organisation of the posts formed a quasi-crystalline structure partially resembling the hexagonal lattice geometry.

The parameters for the creation of the geometries were the post size which remained constant, the minimum inter-post spacing, and the compacity of the posts. With the first two selected for a given geometry, the latter was varied continuously until arriving as close as possible to the desired porosity, that of the regular geometries (0.6). The output of plug im! was a text file containing the centres of all of the posts, which was then imported in CleWin using a short python code.

Appendix D

Chapter 4: Additional Information

D.0.1 Additional TEOS Deposit Characterisation

Flat COC samples following different surface treatments were characterised by ATR-FTIR (attenuated total reflection Fourier-transform infrared spectroscopy) in the 2PM laboratory at Chimie Paris. As shown in figure D.1 below, the characteristic band of SiO_2-type thin film deposition is located at around 400 cm^{-1}, as shown previously by Bourg *et al.* [179]. This band is not present on the spectrum for untreated COC. It is interesting to note that the intensity of this characteristic peak is higher when the PECVD treatment is followed by a rinsing step with water. The effect this rinsing step had on the stability of the subsequent contact angles was discussed in section 5.3.1 and with figure **??**.

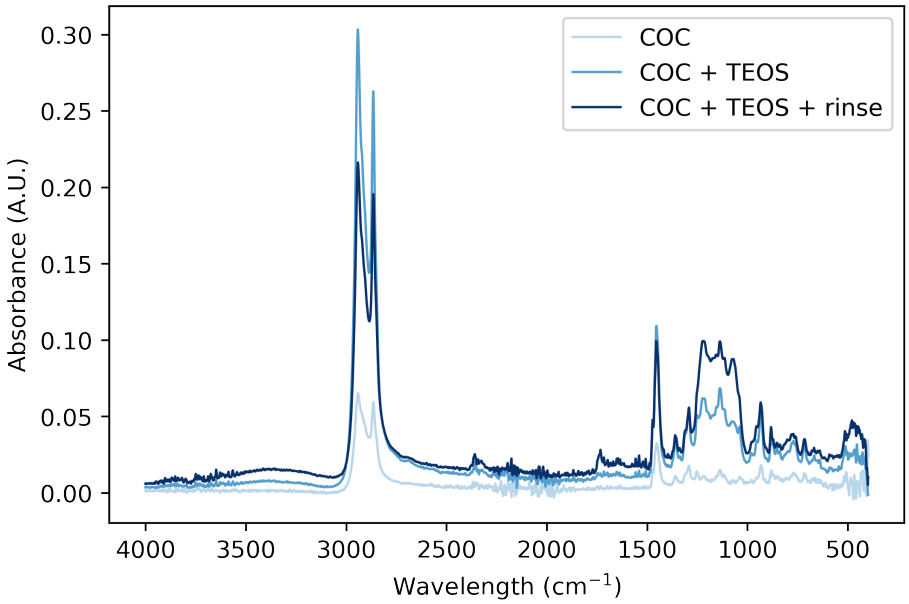

Fig. D.1 COC substrate characterisations by ATR-FTIR. Three different samples were considered: untreated COC (COC), COC with 4 passes of TEOS (COC + TEOS), and COC with 4 passes of TEOS then rinsed with water for 10 s (COC + TEOS + rinse).

D.0.2 Protocol and Results: AA photo-polymerisation on PDMS

Photopolymerisation experiments with acrylic acid (AA) on PDMS were carried out according to the protocol of Ramirez *et al.* [145]. For flat PDMS samples approximately 3 mm thick and 4 cm² in size, the experimental protocol was as follows: *

1. Immerse the samples for 2 min (or 15 min) in a 10 wt% solution of benzophenone in acetone (solution A).

2. Rinse with water, then with ethanol.

3. Immerse the samples in a 10 wt% solution of acrylic acid in distilled water (solution B) and expose them to UV for 300 s using a lamp at a distance of 25.5 cm.

For the UV lamp used, 90% corresponds to 19.6 mW/cm² and 60% to 13.5 mW/cm². The results are quite different from those obtained in the literature and it seems that the part for which the treatment is most effective is the side of the sample not directly exposed. All the angles measured in the figure below are taken from the unexposed

side except for the sample whose contact angle is 107.5°.

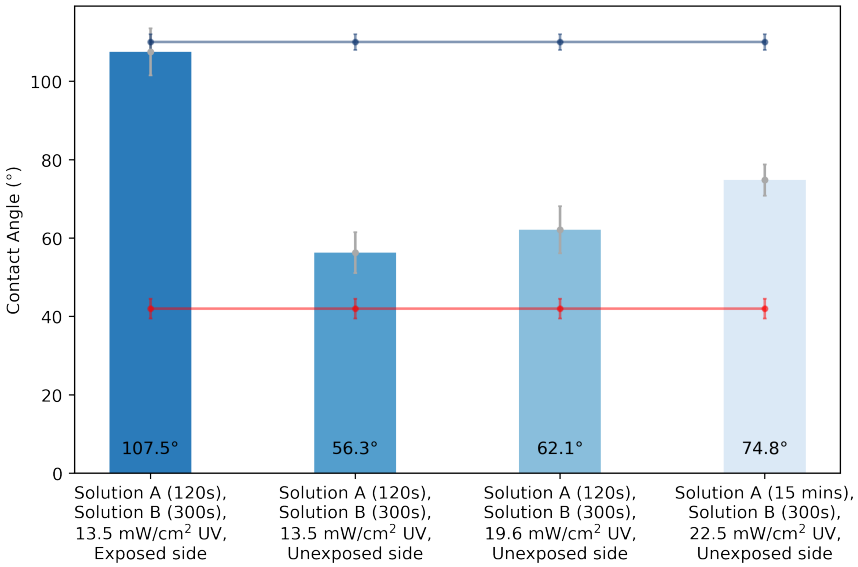

Fig. D.2 Comparison of the different conditions for photo-polymerisation of AA on PDMS. The dark blue line represents untreated PDMS whilst the red line represents the results of Ramirez-Gutierrez *et al.* [145].

References

[1] https://nextbillion.ai/route-optimization api.

[2] Oasys. Massmotion: Human movement simulation tool.

[3] M. Wetzel, T. Kempka, and M. Kühn. Diagenetic trends of synthetic reservoir sandstone properties assessed by digital rock physics. *Minerals*, 11(2):151, 2021.

[4] P. Kelemen, S. M. Benson, H. Pilorgé, P. Psarras, and J. Wilcox. An overview of the status and challenges of co2 storage in minerals and geological formations. *Frontiers in Climate*, 1, 2019.

[5] J. Stark and Manga M. The motion of long bubbles in a network of tubes. *Transport in Porous Media*, 40:201–218, 2000.

[6] Y. Tao, R. W. J. Edwards, D. L. Mauzerall, and M. A. Celia. Strategic carbon dioxide infrastructure to achieve a low-carbon power sector in the midwestern and south-central united states. *Environmental science & technology*, 55(22):15013–15024, 2021.

[7] S.-S. Kim, S.-J. Han, and Y.-S. Cho. Electrokinetic remediation strategy considering ground strate: A review. *Geosciences Journal*, 6(1):57–75, 2002.

[8] A. Ajdari. Microfluidique pour la physique: Quelques pistes. *Reflets de la physique: Bulletin de la Société Française de la Physique*, 7:5–9, 2008.

[9] N. Convery and N. Gadegaard. 30 years of microfluidics. *Micro and Nano Engineering*, 2:76–91, 2019.

[10] Berkeley Engineering. Microfluidic chip for single cell analysis.

[11] A. Folch. https://theconversation.com/microfluidics-the-tiny-beautiful-tech-hidden-all-around-you-160436.

[12] A. Jain, A. Graveline, A. Waterhouse, A. Vernet, R. Flaumenhaft, and D. E. Ingber. A shear gradient-activated microfluidic device for automated monitoring of whole blood haemostasis and platelet function. *Nature Communications*, 7(1):10176, 2016.

[13] Weizmann Institute of Science. Microfluidics methods.

[14] T. Moragues, D. Arguijo, T. Beneyton, C. Modavi, K. Simutis, A. R. Abate, J.-C. Baret, A. J. deMello, D. Densmore, and A. D. Griffiths. Droplet-based microfluidics. *Nature Reviews Methods Primers*, 3(1):32, 2023.

[15] N. Bremond, A. R. Thiam, and J. Bibette. Decompressing emulsion droplets favors coalescence. *Physical Review Letters*, 100(2), 2008.

[16] J. McGrath, M. Jimenez, and H. Bridle. Deterministic lateral displacement for particle separation: a review. *Lab on a chip*, 14(21):4139–4158, 2014.

[17] T. Krüger, D. Holmes, and P. V. Coveney. Deformability-based red blood cell separation in deterministic lateral displacement devices-a simulation study. *Biomicrofluidics*, 8(5):054114, 2014.

[18] Projet Lutetium. Aventures microfluidiques #3 : Les puces microfluidiques.

[19] E. Guyon, J.-P.. Hulin, and L. Petit. *Hydrodynamique physique*. Savoirs actuels. Physique. EDP sciences and CNRS, Les Ulis and Paris, 3e édition edition, 2012.

[20] M. van Dyke. *An Album of Fluid Motion*. Parabolic Press, Stanford (Calif.), 1982.

[21] H. Bruus. *Theoretical microfluidics*, volume 18. Oxford University Press, USA, 2008.

[22] P.-G. de Gennes, F. Brochard-Wyart, and D. Quéré. *Capillarity and wetting phenomena: Drops, bubbles, pearls, waves*. Springer, New York, 2004.

[23] H. J. Butt, K.. Graf, and M. Kappl. *Physics and chemistry of interfaces*. Physics Textbook. Wiley-VCH, Weinheim, second, revised and enlarged edition edition, 2006.

[24] University of Stuttgart. Institute of interfacial process engineering and plasma technology.

[25] T. Young. An essay on the cohesion of fluids. *Philosophical Transactions of the Royal Society of London*, 95:65–87, 1805.

[26] H.-E. Wagner, R. Brandenburg, K. V. Kozlov, A. Sonnenfeld, P. Michel, and J. F. Behnke. The barrier discharge: basic properties and applications to surface treatment. *Vacuum*, 71(3):417–436, 2003.

[27] M. Reysatt, L. Courbin, E. Reyssat, and H. A. Stone. Imbibition in geometries with axial variations. *Journal of Fluid Mechanics*, 615:335–344, 2008.

[28] Lotus leaf on a pond.

[29] W. Barthlott and C. Neinhuis. Purity of the sacred lotus, or escape from contamination in biological surfaces. *Planta*, 202(1):1–8, 1997.

[30] J. Jurin. An account of some experiments shown before the royal society; with an enquiry into the cause of the ascent and suspension of water in capillary tubes. *Philosophical Transactions of the Royal Society of London*, 30:739–747, 1719.

[31] W. Wick. *A Drop of Water: A Book of Science and Wonder*. Scholastic, New York, 1997.

[32] Covid-19 test.

[33] P. Marmottant and J.-P. Raven. Microfluidics with foams. *Soft matter*, 5(18):3385–3388, 2009.

[34] Derjaguin B.V. and Obuchov E. Ultramicrometric analysis of solvate layer and elementary expansion effects. *Acta Physicochimica URSS*, 5, 1936.

[35] A. R. Kovscek and C. J. Radke. Fundamentals of foam transport in porous media. In *Schramm (Ed.) 1993 – Foams*, volume 242, pages 115–163.

[36] A. Emadi. *Enhanced heavy oil recovery by water and carbon dioxide flood*. Phd in petroleum engineering, Heriot-Watt University, Edinburgh, 2012.

[37] L. Louis, P. Baud, and T.-F. Wong. Characterization of pore-space heterogeneity in sandstone by x-ray computed tomography. *Geological Society, London, Special Publications*, 284(1):127–146, 2007.

[38] M. Han, M. Fleury, and P. Levitz, editors. *Effect of the pore structure on resistivity index curves*, 2007.

[39] F. A. L.. Dullien. *Porous media: Fluid transport and pore structure*. Academic press, San Diego and New York and Boston etc, 2e édition edition, 1992.

[40] G. V. Chilingar. Relationship between porosity, permeability, and grain-size distribution of sands and sandstones. In L.M.J.U. van Straaten, editor, *Developments in Sedimentology : Deltaic and Shallow Marine Deposits*, volume 1, pages 71–75. Elsevier, 1964.

[41] M. Kozeny. Uber kapillare leitung des wassers im boden. *Sitzber. Akad. Wiss. Wein, Math-naturw*, 136:Abt. II a, 277, 1927.

[42] P. C. Carman. Fluid flow through granular beds. *Transactions of the Institution of Chemical Engineers*, 15:150–166, 1937.

[43] M. N. Panda and L. W. Lake. Estimation of single-phase permeability from parameters of particle-size distribution. *0149-1423*, 78:7, 1994.

[44] B. Zinszner and F. Pellerin. *A geoscientist's guide to petrophysics*. IFP publications. Éd. Technip, Paris, 2007.

[45] R. A. Freeze and J. A. Cherry. *Groundwater*. Prentice-Hall, Englewood Cliffs (N. J.), 1979.

[46] O. Ozsun, V. Yakhot, and K. L. Ekinci. Noninvasive measurement of the pressure distribution in a deformable micro-channel. *Journal of Fluid Mechanics*, 734:538, 2013.

[47] I. C. Christov, V. Cognet, T. C. Shidhore, and H. A. Stone. Flow rate–pressure drop relation for deformable shallow microfluidic channels. *Journal of Fluid Mechanics*, 841:267–286, 2018.

[48] A. Martínez-Calvo, A. Sevilla, G. G. Peng, and H. A. Stone. Start-up flow in shallow deformable microchannels. *Journal of Fluid Mechanics*, 885, 2020.

[49] C. Lantuejoul and S. Beucher. On the use of the geodesic metric in image analysis. *Journal of Microscopy*, 121(1):39–49, 1981.

[50] J. Chaniot, M. Moreaud, L. Sorbier, T. Fournel, and J. M. Becker. Tortuosimetric operator for complex porous media characterization. *Image Analysis & Stereology*, 38(1):25, 2019.

[51] J. Chaniot, M. Moreaud, L. Sorbier, D. Jeulin, J. M. Becker, and T. Fournel. Heterogeneity assessment based on average variations of morphological tortuosity for complex porous structures characterization. *Image Analysis and Stereology, International Society for Stereology*, 39(2):111–128, 2020.

[52] C. Yeates, S. Youssef, and E. Lorenceau. Accessing preferential foam flow paths in 2d micromodel using a graph-based 2-parameter model. *Transport in Porous Media*, 133(1):23–48, 2020.

[53] M. Matyka, A. Khalili, and Z. Koza. Tortuosity-porosity relation in porous media flow. *Physical review. E, Statistical, nonlinear, and soft matter physics*, 78, 2008.

[54] J. Bear. *Dynamics of Fluids in Porous Media*. American Elsevier Publishing Company, New York, 1972.

[55] M. A. Knackstedt and X. Zhang. Direct evaluation of length scales and structural parameters associated with flow in porous media. *Physical Review E*, 50(3):2134–2138, 1994.

[56] Y. Sugiyama, M. Fukui, M. Kikuchi, K. Hasebe, A. Nakayama, K. Nishinari, S. Tadaki, and S. Yukawa. Traffic jams without bottlenecks—experimental evidence for the physical mechanism of the formation of a jam. *New Journal of Physics*, 10(3):033001, 2008.

[57] N. Quennouz, R. Maciej, J.-F. Argillier, B. Herzhaft, Y. Peysson, and N. Pannacci. Microfluidic study of foams flow for enhanced oil recovery (eor). *Oil & Gas Science and Technology – Revue d'IFP Energies nouvelles*, 69(3):457–466, 2014.

[58] W. Engl, M. Roche, A. Colin, P. Panizza, and A. Ajdari. Droplet traffic at a simple junction at low capillary numbers. *Physical review letters*, 95(20):208304, 2005.

[59] N. Champagne, R. Vasseur, A. Montourcy, and D. Bartolo. Traffic jams and intermittent flows in microfluidic networks. *Physical review letters*, 105(4):044502, 2010.

[60] R. C. V. Coelho, D. P. F. Silva, A. M. R. Maschio, M. M. T. Da Gama, and N. A. M. Araújo. Collective transport of droplets through porous media. *Physics of Fluids*, 35(1):013304, 2023.

[61] A. Averchi. Traffic modelling.

[62] C. N. Baroud, F. Gallaire, and R. Dangla. Dynamics of microfluidic droplets. *Lab on a chip*, 10(16):2032–2045, 2010.

[63] W. Choi, M. Hashimoto, A. K. Ellerbee, X. Chen, K. M.J. Bishop, P. Garstecki, H. A. Stone, and G. M. Whitesides. Bubbles navigating through networks of microchannels. *Lab on a chip*, 11(23):3970–3978, 2011.

[64] D. A. Sessoms, M. Belloul, W. Engl, M. Roche, L. Courbin, and P. Panizza. Droplet motion in microfluidic networks: Hydrodynamic interactions and pressure-drop measurements. *Physical review. E, Statistical, nonlinear, and soft matter physics*, 80(1 Pt 2):016317, 2009.

[65] M. Schindler and A. Ajdari. Droplet traffic in microfluidic networks: a simple model for understanding and designing. *Physical Review Letters*, 100(4):044501, 2008.

[66] S. Jakiela, S. Makulska, P. M. Korczyk, and P. Garstecki. Speed of flow of individual droplets in microfluidic channels as a function of the capillary number, volume of droplets and contrast of viscosities. *Lab on a chip*, 11(21):3603–3608, 2011.

[67] N. Champagne. *Dynamique de trafic dans les réseaux microfluidiques modèles : Embouteillages, chocs et avalanches.* PhD thesis, 2011.

[68] A. Amon, A. Schmit, L. Salkin, L. Courbin, and P. Panizza. Path selection rules for droplet trains in single-lane microfluidic networks. *Physical review. E, Statistical, nonlinear, and soft matter physics*, 88(1):013012, 2013.

[69] O. Cybulski, P. Garstecki, and B. A. Grzybowski. Oscillating droplet trains in microfluidic networks and their suppression in blood flow. *Nature Physics*, 15(7):706–713, 2019.

[70] V. Hourtané. *Écoulement de mousse dans des modèles de milieux poreux.* PhD thesis, 2014.

[71] P. Panizza, A. Amon, and L. Courbin. Comment circulent des gouttes dans un laboratoire sur puce ? *Reflets de la physique*, (36):4–9, 2013.

[72] J.-T. Baué. *Rôle de la chimie des surfactants dans la dynamique de gouttes confinées dans une cavité microfluidique.* PhD thesis, Université de Rennes, 13/04/2023.

[73] F. P. Bretherton. The motion of long bubbles in tubes. *Journal of Fluid Mechanics*, 10(02):166, 1961.

[74] J. Ratulowski and H.-C. Chang. Transport of gas bubbles in capillaries. *Physics of Fluids A: Fluid Dynamics*, 1(10):1642–1655, 1989.

[75] S. R. HODGES, O. E. JENSEN, and J. M. RALLISON. The motion of a viscous drop through a cylindrical tube. *Journal of Fluid Mechanics*, 501:279–301, 2004.

[76] M. J. Fuerstman, A. Lai, M. E. Thurlow, S. S. Shevkoplyas, H. A. Stone, and G. M. Whitesides. The pressure drop along rectangular microchannels containing bubbles. *Lab on a chip*, 7(11):1479–1489, 2007.

[77] H. Wong, C. J. Radke, and S. Morris. The motion of long bubbles in polygonal capillaries. part 2. drag, fluid pressure and fluid flow. *Journal of Fluid Mechanics*, 292:95–110, 1995.

[78] H. Wong, C. J. Radke, and S. Morris. The motion of long bubbles in polygonal capillaries. part 1. thin films. *Journal of Fluid Mechanics*, 292:71–94, 1995.

[79] B. J. Adzima and S. S. Velankar. Pressure drops for droplet flows in microfluidic channels. *Journal of Micromechanics and Microengineering*, 16(8):1504–1510, 2006.

[80] V. Labrot, M. Schindler, P. Guillot, A. Colin, and M. Joanicot. Extracting the hydrodynamic resistance of droplets from their behavior in microchannel networks. *Biomicrofluidics*, 3(1):12804, 2009.

[81] A. Huerre, M-C Jullien, O. Theodoly, and M-P Valignat. Absolute 3d reconstruction of thin films topography in microfluidic channels by interference reflection microscopy. *Lab on a chip*, 16(5):911–916, 2016.

[82] B. Reichert, A. Huerre, O. Theodoly, M.-P. Valignat, I. Cantat, and M.-C. Jullien. Topography of the lubrication film under a pancake droplet travelling in a hele-shaw cell. *Journal of Fluid Mechanics*, 850:708–732, 2018.

[83] B. Reichert, I. Cantat, and M.-C. Jullien. Predicting droplet velocity in a hele-shaw cell. *Physical Review Fluids*, 4(11), 2019.

[84] J. Y. Moon, S. Kondaraju, W. Choi, and J. S. Lee. Lattice boltzmann-immersed boundary approach for vesicle navigation in microfluidic channel networks. *Microfluidics and Nanofluidics*, 17(6):1061–1070, 2014.

[85] M. Belloul, W. Engl, A. Colin, P. Panizza, and A. Ajdari. Competition between local collisions and collective hydrodynamic feedback controls traffic flows in microfluidic networks. *Physical Review Letters*, 102(19), 2009.

[86] M. Belloul, L. Courbin, and P. Panizza. Droplet traffic regulated by collisions in microfluidic networks. *Soft matter*, 7(19):9453, 2011.

[87] T. Beatus, T. Tlusty, and R. H. Bar-Ziv. Phonons in a one-dimensional microfluidic crystal. *Nature Physics*, 2(11):743–748, 2006.

[88] L.H.P. Cunha, I. R. Siqueira, E. L. Albuquerque, and T. F. Oliveira. Flow of emulsion drops through a constricted microcapillary channel. *International Journal of Multiphase Flow*, 103:141–150, 2018.

[89] S. Liu, X. Dou, Q. Zeng, and J. Liu. Critical parameters of the jamin effect in a capillary tube with a contracted cross section. *Journal of Petroleum Science and Engineering*, 196:107635, 2021.

[90] E. Benet and F. J. Vernerey. Mechanics and stability of vesicles and droplets in confined spaces. *Physical review. E*, 94(6-1):062613, 2016.

[91] H. Chio, M. J. Jensen, X. Wang, H. Bruus, and D. Attinger. Transient pressure drops of gas bubbles passing through liquid-filled microchannel contractions: an experimental study. *Journal of Micromechanics and Microengineering*, 16(1):143–149, 2006.

[92] S. Cobos, M. S. Carvalho, and V. Alvarado. Flow of oil–water emulsions through a constricted capillary. *International Journal of Multiphase Flow*, 35(6):507–515, 2009.

[93] D.J.E. Harvie, M. R. Davidson, J. J. Cooper-White, and M. Rudman. A parametric study of droplet deformation through a microfluidic contraction: Low viscosity newtonian droplets. *Chemical Engineering Science*, 61(15):5149–5158, 2006.

[94] M. J. Jensen, G. Goranovi, and H. Bruus. The clogging pressure of bubbles in hydrophilic microchannel contractions. *Journal of Micromechanics and Microengineering*, 14(7):876–883, 2004.

[95] A. Z. Zinchenko and R. H. Davis. Motion of deformable drops through porous media. *Annual Review of Fluid Mechanics*, 49(1):71–90, 2017.

[96] W. L. Olbricht. Pore-scale prototypes of multiphase flow in porous media. *Annual Review of Fluid Mechanics*, 28(1):187–213, 1996.

[97] D. R. GRAHAM and HIGDON J. J. L. Oscillatory flow of droplets in capillary tubes. part 1. straight tubes. *Journal of Fluid Mechanics*, 425:31–53, 2000.

[98] A. Mauray, M. Chabert, and H. Bodiguel. Yield stress fluid behavior of foam in porous media. *Physical Review Fluids*, 5(9), 2020.

[99] B. Géraud, S. A. Jones, I. Cantat, B. Dollet, and Y. Méheust. The flow of a foam in a two-dimensional porous medium. *Water Resources Research*, 52(2):773–790, 2016.

[100] C. Yeates. *Multi-Scale Study of Foam Flow Dynamics in Porous Media*. PhD thesis, Sorbonne université, 2019.

[101] A. Mauray. *Etude des propriétés de transport de mousse dans des modèles de milieux poreux*. Phd in physics, Université Grenoble Alpes, 2017.

[102] L. Nguyen, M. Hang, W. Wang, Y. Tian, L. Wang, T. J. McCarthy, and W. Chen. Simple and improved approaches to long-lasting, hydrophilic silicones derived from commercially available precursors. *ACS applied materials & interfaces*, 6(24):22876–22883, 2014.

[103] P. Garstecki, I. Gitlin, W. DiLuzio, G. M. Whitesides, E. Kumacheva, and H. A. Stone. Formation of monodisperse bubbles in a microfluidic flow-focusing device. *Applied Physics Letters*, 85(13):2649–2651, 2004.

[104] L. Salkin. *Création, stabilité et rupture d'interfaces fluides.* Dynamique des fluides, Université Rennes 1, 2014.

[105] C. Yeates, S. Youssef, and E. Lorenceau. New insights of foam flow dynamics in a high-complexity 2d micromodel. *Colloids and Surfaces A: Physicochemical and Engineering Aspects*, 575:184–198, 2019.

[106] D. Jeulin. *Morphological models of random structures*, volume 53 of *Interdisciplinary applied mathematics.* Springer Nature, 2021.

[107] W. D. Bancroft. The theory of emulsification, v. *The Journal of Physical Chemistry*, 17(6):501–519, 1913.

[108] D. W. Scott. *Multivariate density estimation: theory, practice, and visualization.* John Wiley & Sons, 2015.

[109] National Institutes of Health. Imagej.

[110] IFP Energies nouvelles. plug im ! signal and image processing software.

[111] J. Serra. *Image Analysis and Mathematical Morphology.* Academic press, 1982.

[112] D. Ershov, M-S. Phan, J. W. Pylvänäinen, S. U. Rigaud, L. Le Blanc, A. Charles-Orszag, J. R. W. Conway, R. F. Laine, N. H. Roy, D. Bonazzi, G. Duménil, G. Jacquemet, and J.-Y. Tinevez. Trackmate 7: integrating state-of-the-art segmentation algorithms into tracking pipelines. *Nature Methods*, 19(7):829–832, 2022.

[113] G. Haskins, U. Kruger, and P. Yan. Deep learning in medical image registration: a survey.

[114] X. Wang, Y. Liu, D. Liu, X. Ge, L. Li, and T. Qiu. Droplet breakup in the square microchannel with a short square constriction to generate slug flow. *AIChE Journal*, 68(8), 2022.

[115] Juan C. O.-A., Oscar V.-C., and Sergio I. M.-M. 3.15 - fundamentals of high-pressure homogenization of foods. In Kai K. and Kasiviswanathan M., editors, *Innovative Food Processing Technologies*, pages 244–273. Elsevier, Oxford, 2021.

[116] Y. Wang, S. Yang, J. Zhang, Z. Chen, B. Zhu, J. Li, S. Liang, Y. Bai, J. Xu, D. Rao, L. Dong, C. Zhang, and X. Yang. Scalable and switchable co2-responsive membranes with high wettability for separation of various oil/water systems. *Nature communications*, 14(1):1108, 2023.

[117] H. Gu, M. H. G. Duits, and F. Mugele. Droplets formation and merging in two-phase flow microfluidics. *International journal of molecular sciences*, 12(4):2572–2597, 2011.

[118] B-J Jin, Y. W. Kim, Y. Lee, and J. Y. Yoo. Droplet merging in a straight microchannel using droplet size or viscosity difference. *Journal of Micromechanics and Microengineering*, 20(3):035003, 2010.

[119] X. Niu, S. Gulati, J. B. Edel, and A. J. deMello. Pillar-induced droplet merging in microfluidic circuits. *Lab on a chip*, 8(11):1837–1841, 2008.

[120] B. M. Jose and T. Cubaud. Droplet arrangement and coalescence in diverging/converging microchannels. *Microfluidics and Nanofluidics*, 12(5):687–696, 2012.

[121] J.-C. Baret, F. Kleinschmidt, A. El Harrak, and A. D. Griffiths. Kinetic aspects of emulsion stabilization by surfactants: a microfluidic analysis. *Langmuir*, 25(11):6088–6093, 2009.

[122] F. de Soete, L. Delance, N. Passade-Boupat, M. Levant, E. Verneuil, F. Lequeux, and L. Talini. Passage of surfactant-laden and particle-laden drops through a contraction. *Physical Review Fluids*, 6(9), 2021.

[123] M. Lv, Z. Liu, L. Jia, and C. Ji. Visualizing pore-scale foam flow in micromodels with different permeabilities. *Colloids and Surfaces A: Physicochemical and Engineering Aspects*, 600:124923, 2020.

[124] G. Vladisavljevic, M. Shimizu, and T. Nakashima. Preparation of monodisperse multiple emulsions at high production rates by multi-stage premix membrane emulsification. *Journal of Membrane Science*, 244(1-2):97–106, 2004.

[125] D. R. Link, S. L. Anna, D. A. Weitz, and H. A. Stone. Geometrically mediated breakup of drops in microfluidic devices. *Physical review letters*, 92(5):054503, 2004.

[126] L. Ménétrier-Deremble and P. Tabeling. Droplet breakup in microfluidic junctions of arbitrary angles. *Physical review. E, Statistical, nonlinear, and soft matter physics*, 74(3 Pt 2):035303, 2006.

[127] A. M. Leshansky and L. M. Pismen. Breakup of drops in a microfluidic t junction. *Physics of Fluids*, 21(2):023303, 2009.

[128] M.-C. Jullien, M.-J. Tsang M. C., C. Cohen, L. Menetrier, and P. Tabeling. Droplet breakup in microfluidic t-junctions at small capillary numbers. *Physics of Fluids*, 21(7):072001, 2009.

[129] A. Carlson, M. Do-Quang, and G. Amberg. Droplet dynamics in a bifurcating channel. *International Journal of Multiphase Flow*, 36(5):397–405, 2010.

[130] P. Kumari and A. Atta. Droplet breakup in a parallel microchannel with asymmetrical geometric constraints. *Chemical Engineering Research and Design*, 184:13–23, 2022.

[131] S. Protière, M. Z. Bazant, D. A. Weitz, and H. A. Stone. Droplet breakup in flow past an obstacle: A capillary instability due to permeability variations. *EPL (Europhysics Letters)*, 92(5):54002, 2010.

[132] L. Salkin, L. Courbin, and P. Panizza. Microfluidic breakups of confined droplets against a linear obstacle: The importance of the viscosity contrast. *Physical review. E, Statistical, nonlinear, and soft matter physics*, 86(3 Pt 2):036317, 2012.

[133] H. G. Gomaa and R. Sabouni. Interfacial phenomena and droplet size of particle stabilized emulsions in oscillatory shear. *AIChE Journal*, 62(8):2902–2911, 2016.

[134] R. Liontas, K. Ma, G. J. Hirasaki, and S. L. Biswal. Neighbor-induced bubble pinch-off: novel mechanisms of in situ foam generation in microfluidic channels. *Soft matter*, 9(46):10971, 2013.

[135] R. F. Li, W. Yan, S. Liu, G. J. Hirasaki, and C. A. Miller. Foam mobility control for surfactant enhanced oil recovery. *SPE Journal*, 15(04):928–942, 2010.

[136] H. Nguyen. Random sets. *Scholarpedia*, 3(7):3383, 2008.

[137] W. R. Rossen. Comment on "verification of roof snap-off as a foam-generation mechanism in porous media at steady state". *Colloids and Surfaces A: Physicochemical and Engineering Aspects*, 322(1-3):261–269, 2008.

[138] A. Mascini, V. Cnudde, and T. Bultreys. Event-based contact angle measurements inside porous media using time-resolved micro-computed tomography. *Journal of colloid and interface science*, 572:354–363, 2020.

[139] D. C. Duffy, J. C. McDonald, O. J. A. Schueller, and G. M. Whitesides. Rapid prototyping of microfluidic systems in poly(dimethylsiloxane). *Analytical chemistry*, 70(23):4974–4984, 1998.

[140] S. Hu, X. Ren, M. Bachman, C. E. Sims, G. P. Li, and N. Allbritton. Surface modification of poly(dimethylsiloxane) microfluidic devices by ultraviolet polymer grafting. *Analytical chemistry*, 74(16):4117–4123, 2002.

[141] S. Hu, X. Ren, M. Bachman, C. E. Sims, G. P. Li, and N. Allbritton. Cross-linked coatings for electrophoretic separations in poly(dimethylsiloxane) microchannels. *Electrophoresis*, 24(21):3679–3688, 2003.

[142] S. Hu, X. Ren, M. Bachman, C. E. Sims, G. P. Li, and N. Allbritton. Surface-directed, graft polymerization within microfluidic channels. *Analytical chemistry*, 76(7):1865–1870, 2004.

[143] S. Hu, X. Ren, M. Bachman, C. E. Sims, G. P. Li, and N. Allbritton. Tailoring the surface properties of poly(dimethylsiloxane) microfluidic devices. *Langmuir : the ACS journal of surfaces and colloids*, 20(13):5569–5574, 2004.

[144] M. Schneider. *Wettability Patterning in Microfluidic Systems and Applications in the Petroleum Industry*. Phd thesis, fluid dynamics, Université Pierre et Marie Curie - Paris VI, 2011.

[145] D. Ramírez-Gutiérrez, C. Nieto-Draghi, N. Pannacci, L. V. Castro, F. Álvarez-Ramírez, and B. Creton. Surface photografting of acrylic acid on poly(dimethylsiloxane). experimental and dissipative particle dynamics studies. *Langmuir : the ACS journal of surfaces and colloids*, 31(4):1400–1409, 2015.

[146] K. Efimenko, W. E. Wallace, and J. Genzer. Surface modification of sylgard-184 poly(dimethyl siloxane) networks by ultraviolet and ultraviolet/ozone treatment. *Journal of colloid and interface science*, 254(2):306–315, 2002.

[147] E. M. Liston. Plasma treatment for improved bonding: A review. *The Journal of Adhesion*, 30(1-4):199–218, 1989.

[148] S. Hemmilä, J. V. Cauich-Rodríguez, J. Kreutzer, and P. Kallio. Rapid, simple, and cost-effective treatments to achieve long-term hydrophilic pdms surfaces. *Applied Surface Science*, 258(24):9864–9875, 2012.

[149] B. T. Ginn and O. Steinbock. Polymer surface modification using microwave-oven-generated plasma. *Langmuir*, 19(19):8117–8118, 2003.

[150] V. Sharma, M. Dhayal, Govind, S. M. Shivaprasad, and S. C. Jain. Surface characterization of plasma-treated and peg-grafted pdms for micro fluidic applications. *Vacuum*, 81(9):1094–1100, 2007.

[151] K. M. Kovach, J. R. Capadona, A. S. Gupta, and J. A. Potkay. The effects of peg-based surface modification of pdms microchannels on long-term hemocompatibility. *Journal of biomedical materials research. Part A*, 102(12):4195–4205, 2014.

[152] V. Barbier, M. Tatoulian, H. Li, F. Arefi-Khonsari, A. Ajdari, and P. Tabeling. Stable modification of pdms surface properties by plasma polymerization: application to the formation of double emulsions in microfluidic systems. *Langmuir*, 22(12):5230–5232, 2006.

[153] D. Lee and S. Yang. Surface modification of pdms by atmospheric-pressure plasma-enhanced chemical vapor deposition and analysis of long-lasting surface hydrophilicity. *Sensors and Actuators B: Chemical*, 162(1):425–434, 2012.

[154] B. Da Silva, M. Zhang, G. Schelcher, L. Winter, C. Guyon, P. Tabeling, D. Bonn, and M. Tatoulian. Study of the stability and hydrophilicity of plasma-modified microfluidic materials. *Plasma Processes and Polymers*, 14(3):1600034, 2017.

[155] C. Huang, C.-H. Liu, C.-H. Su, W.-T. Hsu, and S.-Y. Wu. Investigation of atmospheric-pressure plasma deposited siox films on polymeric substrates. *Thin Solid Films*, 517(17):5141–5145, 2009.

[156] D. Magni, Ch Deschenaux, Ch Hollenstein, A. Creatore, and P. Fayet. Oxygen diluted hexamethyldisiloxane plasmas investigated by means of in situ infrared absorption spectroscopy and mass spectrometry. *Journal of Physics D-Applied Physics*, 34(1):87–94, 2001.

[157] R. Lenormand. Liquids in porous media. *Journal of Physics: Condensed Matter*, 2(S):SA79–SA88, 1990.

[158] R. Holtzman and E. Segre. Wettability stabilizes fluid invasion into porous media via nonlocal, cooperative pore filling. *Physical Review Letters*, 115(16), 2015.

[159] B. Zhao, C. W. MacMinn, and R. Juanes. Wettability control on multiphase flow in patterned microfluidics. *Proceedings of the National Academy of Sciences of the United States of America*, 113(37):10251–10256, 2016.

[160] C. Odier. *Imbibition forcée en milieu poreux*. PhD thesis, Lyon, 2017.

[161] A. Irannezhad, B. K. Primkulov, R. Juanes, and B. Zhao. Fluid-fluid displacement in mixed-wet porous media. *Physical Review Fluids*, 8, 2023.

[162] B. K. Primkulov, A. A. Pahlavan, X. Fu, B. Zhao, C. W. MacMinn, and R. Juanes. Wettability and lenormand's diagram. *Journal of Fluid Mechanics*, 923, 2021.

[163] J-M. Lombard. *Influence de micro-hétérogénéités de mouillabilité sur les déplacements en milieu poreux*. Phd in petroleum science, L'Université de Paris VI, 1992.

[164] A. Scanziani, Q. Lin, A. Alhosani, M. J. Blunt, and B. Bijeljic. Dynamics of fluid displacement in mixed-wet porous media. *Proceedings. Mathematical, physical, and engineering sciences*, 476(2240):20200040, 2020.

[165] J. P. Stokes, D. A. Weitz, J. P. Gollub, A. Dougherty, M. O. Robbins, P. M. Chaikin, and H. M. Lindsay. Interfacial stability of immiscible displacement in a porous medium. *Physical Review Letters*, 57, 1986.

[166] M. Cieplak and M. O. Robbins. Dynamical transition in quasistatic fluid invasion in porous media. *Physical Review Letters*, 60, 1988.

[167] Q. Lin, B. Bijeljic, S. Berg, R. Pini, M. J. Blunt, and S. Krevor. Minimal surfaces in porous media: Pore-scale imaging of multiphase flow in an altered-wettability bentheimer sandstone. *Physical review. E*, 99(6-1):063105, 2019.

[168] A. S. Al-Menhali and S. Krevor. Capillary trapping of co2 in oil reservoirs: Observations in a mixed-wet carbonate rock. *Environmental science & technology*, 50(5):2727–2734, 2016.

[169] A. Mascini, M. Boone, S. van Offenwert, S. Wang, V. Cnudde, and T. Bultreys. Fluid invasion dynamics in porous media with complex wettability and connectivity. *Geophysical Research Letters*, 48(22), 2021.

[170] M. Amirmoshiri, X. Wang, C. Bai, D. T. Raj, S. X. Xie, Ridhwan Z.K. B., P. M. Singer, R. Farajzadeh, S. L. Biswal, and G. J. Hirasaki. Distinguishing the effect of rock wettability from residual oil on foam generation and propagation in porous media. *Energy & Fuels*, 35(9):7681–7692, 2021.

[171] C. Laroche, O. Vizika, and F. Kalaydjian. Network modeling as a tool to predict three-phase gas injection in heterogeneous wettability porous media. *Journal of Petroleum Science and Engineering*, 24:155–168, 1999.

[172] C. Chang, T. J. Kneafsey, J. Wan, T. K. Tokunaga, and S. Nakagawa. Impacts of mixed–wettability on brine drainage and supercritical co 2 storage efficiency in a 2.5–d heterogeneous micromodel. *Water Resources Research*, 56(7), 2020.

[173] C. Chang, T. J. Kneafsey, T. K. Tokunaga, J. Wan, and S. Nakagawa. Impacts of pore network–scale wettability heterogeneity on immiscible fluid displacement: A micromodel study. *Water Resources Research*, 57(9), 2021.

[174] A. M. Saad, M. P. Yutkin, C. J. Radke, and T. W. Patzek. Pore-scale spontaneous imbibition at high advancing contact angles in mixed-wet media: Theory and experiment. *Energy & Fuels*, 36(11):5647–5656, 2022.

[175] Z. Diao, S. Li, W. Liu, H. Liu, and Q. Xia. Numerical study of the effect of tortuosity and mixed wettability on spontaneous imbibition in heterogeneous porous media. *Capillarity*, 4(3):50–62, 2021.

[176] R. Dreyfus, P. Tabeling, and H. Willaime. Ordered and disordered patterns in two-phase flows in microchannels. *Physical Review Letters*, 90(14):144505, 2003.

[177] H. Chen, E. Dong, J. Li, and H. A. Stone. Adhesion of moving droplets in microchannels. *Applied Physics Letters*, 103(13):131605, 2013.

[178] Q. Meng, Y. Zhang, J. Li, R. G. H. Lammertink, H. Chen, and P. A. Tsai. Altering emulsion stability with heterogeneous surface wettability. *Scientific Reports*, 6:26953, 2016.

[179] S. Bourg, S. Griveau, F. d'Orlyé, M. Tatoulian, F. Bedioui, C. Guyon, and A. Varenne. Surface functionalization of cyclic olefin copolymer by plasma–enhanced chemical vapor deposition using atmospheric pressure plasma jet for microfluidic applications. *Plasma Processes and Polymers*, 16(6):1800195, 2019.

[180] A. Sangani and Acrivos A. Slow flow through a periodic array of spheres. *International Journal of Multiphase Flow*, 8:343–360, 1982.

[181] A. Sangani and Acrivos A. Slow flow past periodic arrays of cylinders with application to heat transfer. *International Journal of Multiphase Flow*, 8:193–206, 1982.

[182] D. L. Koch and A. J. C. Ladd. Moderate reynolds number flows through periodic and random arrays of aligned cylinders. *Journal of Fluid Mechanics*, 349:31–66, 1997.

[183] A. Tamayol and M. Bahrami. Analytical determination of viscous permeability of fibrous porous media. *International Journal of Heat and Mass Transfer*, 52(9-10):2407–2414, 2009.

[184] A. Tamayol and M. Bahrami. Transverse permeability of fibrous porous media. *Physical review. E, Statistical, nonlinear, and soft matter physics*, 83(4 Pt 2):046314, 2011.

[185] T. Hulikal Chakrapani, H. Bazyar, R. G. H. Lammertink, S. Luding, and W. K. den Otter. The permeability of pillar arrays in microfluidic devices: an application of brinkman's theory towards wall friction. *Soft matter*, 19(3):436–450, 2023.

[186] S. Chen and G. D. Doolen. Lattice boltzmann method for fluid flows. *Annual Review of Fluid Mechanics*, 30(1):329–364, 1998.

[187] G. Matherton. *Random Sets and Integral Geometry*. J. Wiley, New York, 1975.

[188] B. Widom. Random sequential addition of hard spheres to a volume. *The Journal of Chemical Physics*, 44(10):3888–3894, 1966.

[189] A. Delarue and D. Jeulin. Multi-scale simulation of spherical aggregates. *Image Analysis & Stereology*, 20(3):181, 2001.

[190] G. Ferri, M. Moreaud, S. Humbert, M. Digne, and J.-M. Schweitzer. Simulation of large aggregate particles system with a new morphological model. *Image Analysis & Stereology*, 2021.

COLLEGE DOCTORAL BRETAGNE
SCIENCES DE LA MATIERE DES MOLECULES ET MATERIAUX

Université de Rennes

Titre : Transport d'émulsions en milieux poreux bidimensionnels : Effets d'hétérogénéités de géométrie et de surface

Mots clés : émulsion, micromodèle, poreux, tortuosité, transport, stabilité

Résumé : Les écoulements multiphasiques dans les milieux poreux déterminent divers processus naturels et industriels, comme la séquestration géologique du CO_2, la remédiation des sols, et la filtration de particules. Toutefois, des questions subsistent concernant l'effet du confinement et de la géométrie des milieux poreux sur le transport des émulsions. Nous explorons ces questions par des expériences utilisant des milieux poreux transparents et contrôlés, appelés micromodèles. Au sein de ces micromodèles, composés de réseaux de plots cylindriques, nous injectons une émulsion d'eau dans de l'huile.

Notre étude révèle que l'alignement radial des plots, en lien avec la tortuosité géométrique du réseau, varie périodiquement en fonction de l'angle et exerce une influence significative sur le transport des gouttes, en créant des chemins préférentiels.

En manipulant de manière systématique la configuration des plots, le nombre capillaire d'injection, la taille des gouttes, leur concentration et la mouillabilité des surfaces, nous caractérisons le transport des gouttes ainsi que leurs conditions de rupture.

Lorsque le nombre capillaire est faible, le transport radial des gouttes est homogène. Cependant, à mesure que le nombre capillaire augmente, les gouttes empruntent initialement les chemins les moins tortueux avant de passer à un régime d'écoulement stable, privilégiant les chemins les plus tortueux. En effectuant un suivi de gouttes à grande échelle, nous mettons en évidence l'influence de la tortuosité géométrique du milieu sur les motifs d'écoulement des gouttes, révélant des réponses contre-intuitives.

Title: Emulsion Transport in Two-dimensional Porous Media: Influence of Geometric and Surface Heterogeneities.

Keywords: emulsion, micromodel, porous, tortuosity, transport, stability

Abstract: Multiphase flow in porous media is widely studied and impacts countless applications in natural and industrial processes, such as geologic CO_2 sequestration, groundwater remediation, and particle filtration. However, many questions remain, in particular regarding the effect of the confinement and the geometry of the porous medium on the transport of emulsions. We address these issues experimentally using transparent, controlled porous media: micromodels. Within these micromodels, composed of arrays of cylindrical posts, we inject a water-in-oil emulsion.

Our study reveals that the radial alignment of the posts, i.e. the geometric tortuosity of the network, varies angularly in a periodic manner and plays a key role in droplet transport by generating reproducible preferential paths. By systematically varying the geometrical configuration of the posts, injection capillary number, droplet size, droplet concentration, and surface wettability, we characterise the droplet transport and the conditions for droplet breakup.

At low capillary numbers, radial droplet transport is homogeneous. By increasing the capillary number, droplets initially follow the least tortuous paths before transitioning to a stable flow regime whereby droplets flow primarily in the most tortuous paths. Through large-scale droplet tracking, we highlight the influence of the geometric tortuosity of the media on the resulting droplet flow patterns and the counter-intuitive responses that can arise.